THESE DE DOCTORAT DE

L'UNIVERSITE
DE BRETAGNE OCCIDENTALE

ECOLE DOCTORALE N° 598
Sciences de la Mer et du littoral
Spécialité : Mécanique, génie mécanique, m*écanique des fluides et énergétique*

Par

Vanilla TEMTCHING TEMOU

Etude Expérimentale et Numérique des Interactions Fluide-Structure sur des Hydrofoils Flexibles en Composite

Rapporteurs avant soutenance :

Christophe BALEY   Professeur des universités, Université de Bretagne Sud
Antoine DUCOIN   Maître de conférences-HDR, École Centrale de Nantes

Composition du Jury :

Président du : Jean-Yves BILLARD   Professeur des universités, Ecole Navale
Jury

Examinateurs : Antoine DAZIN   PU, Resp. Laboratoire de mécanique des fluides de Lille aux Arts et Métiers
                Marianna BRAZA   Directrice de Recherche CNRS, Institut de Mécanique des Fluides de Toulouse
                Stéphane SIRE   Maître de conférences-HDR, Université de Bretagne Occidentale

Rapporteurs :   Christophe BALEY   Professeur des universités, Université de Bretagne Sud
                Antoine DUCOIN   Maître de conférences-HDR, École Centrale de Nantes

Dir. de thèse : J. André ASTOLFI   Professeur des universités, Directeur de l'IRENAV
Co-dir. de thèse : Gilles AUSIAS   Maître de conférences-HDR, Université de Bretagne Sud
Encadrant de thèse : Benoit AUGIER   Docteur- Chercheur, Responsable du bassin de Brest IFREMER

Invité
M. Benoit LEQUIN   Ingénieur chef de projet chez SEAIR

Acknowledgements

Last but no least, I dedicate this thesis to my family, to my mother who is always kind to me, to my brothers and sisters, to all of you whom I love very much, you who are my strength and motivation on a daily basis, to my friends and to beloved fiance, who gave me enormous advices and unconditional support.
Thank you all for being there for me and helping me all along.

Table des matières

List of figures

List of tables

Nomenclature

u_e Edge velocities [m/s]

[ε]   Matrix of strains [%]

[σ]   Matrix of stress [Pa]

[K]   Stiffness matrix

α [%]   bend-twist Coupling percentage

α [°]   Angle of Attack

$α_e$ Effective angle of Attack [°]

$α_i$ Induced angle of Attack [°]

Γ   Vorticity [m^2/s]

μ   Dynamic viscosity of the fluid [P$a.s$]

$μ_t$ Turbulent dynamic viscosity of the fluid [P$a.s$]

ν   [$m^2.s^{-1}$] kinematic viscosity of the fluid

ν   [] Poisson coefficient of a material

$ν_f$ Poisson coefficient of the fiber []

$ν_{lt}$ Poisson coefficient of the ply in direction lt []

$ν_m$ Poisson coefficient of the resin []

ω   Relaxation factor []

ρ   Density [kg/m^3]

$τ_w$ shear stress [Pa]

θ   Twist angle of a hydrofoil or orientation of a ply in a layup [°]

B   Span dimension [m]

C   Chord of a profile [m]

C_D Drag coefficient []

C_f Friction coefficient []

C_L Lift coefficient []

D   Drag force [N]

E   Young modulus of a material [Pa]

E_f Young modulus of the fiber [Pa]

E_l Young modulus of a ply in longitudinal direction [Pa]

E_l Young modulus of the ply in longitudinal direction [Pa]

E_m Young modulus of the resin [Pa]

E_t Young modulus of a ply in transverse direction direction [Pa]

E_t Young modulus of the ply in transverse direction direction [Pa]

e_p Thickness of a ply [m]

G_m Shear modulus of the resin [Pa]

G_{lt} Shear modulus of the UD in direction lt [Pa]

G_{lt} Shear modulus of the ply in direction lt [Pa]

L   Lift force [N]

l, t Longitudinal l and transverse t direction of a ply

Re Reynolds number []

S   Surface [m^2]

U   Velocity [m/s]

V_∞ upstream [m/s]

V_f[%]   Volume of fiber in the composite

y^+ Dimensionless wall distance []

Abbreviations

AoA	Angle of Attack
Aster	Analyses des Structures et Thermomécanique pour des Études et des Recherches
BEM	Boundary Element Method
BTC	Bend twist coupling
CALFEM	Computer Aided Learning of the Finite Element Method
CFD	Computational Fluid Dynamic
CSD	Computational Structure Dynamic
CV	Control Volume
DES	Detached Eddy Simulation
DSBT	Differential Stiffness Bend-Twist
FE	Finite element approach
FE-BTC	Finite element with BTC implemented
FFT	Fast Fourier Transform
FSI	Fluid-structure Interactions
IFREMER	Institut Français de Recherche pour l'Exploitation de la MEr
IRDL	Institut de Recherche Dupuy De Lôme
IRENav	Institut de Recherche de l'Ecole Navale
LES	Large Eddy Simulation
LT	Laminate Theory
PAC	Passive Adaptive Composites
POM	PolyOxymethylene material
NACA	National Advisory Council for Aeronautics (actuel NASA)
NASA	National Aeronautical and Spatial Agency
OpenFoam	Open Field Operation and Manipulation
RANS	Reynolds Averaged Navier-Stokes
SALOME	Simulation numérique par Architecture Logicielle en Open source et à Méthodologie d'Évolution
UD	Unidirectional ply in a composite layup
VAM	Variational Asymptotic Method
VLM	Vortex Lattice Method
VOF	Volume Of Fluid

Introduction

For the top high performance yacht design, the foiling technology has become a key issue in order to increase the boat 's performances and reduce its energetic consumption. It consists in the design of a lifting surface, the "hydrofoil" that generates a lifting force, which pulls the hull of the boat out of the water and thus reducing the resistance against the boat advancement as shown in figure 1.

FIGURE 1 – AC45 of the Emirates Team New Zealand, challenger for the 34rd America's Cup.

This thesis is a CIFRE collaboration between the foil resource center SEAIR in Lorient, the French Naval Research Institute IRENAV in Brest, the Research Institute Dupuy de Lôme, IRDL in Lorient and the French Research Institute for Exploitation of the Sea, IFRE-MER in Brest.
SEAIR is a foil designer known since 2016 for its flying 6.50 scow bow, the "MINI 747" (see figure 2). The company has become a key player in the nautical industry as an expert of the "flying function" on yachts and motorboats.

1

Its constant innovations aim to develop components designed to make the "flying function" a simple and affordable tool that democratizes the use of hydrofoil.

SEAIR is interested in this **"numerical and experimental study of fluid-structure interactions on flexible hydrofoils in composite"** in one hand, to increase its knowledge on the behavior of the hydrofoils. On the other hand, the company wants to develop internal skills, through the creation of numerical tools with various levels of fidelity that model the hydro-elastic response of hydrofoils working in a fluid domain.

The concept of hydrofoil has been the subject of multiple researches since the dawn of hydrodynamic sciences. The first examples are the work of Thomas MOY (1861) who tested a hull equipped with three lifting surfaces on a canal and observed a dynamic lift-off and drag reduction. In 1905, Professor Enrico Forlanini built a hydrofoil and performed tests in the Lake Maggiore (Italy). The hydrofoil helped the boat to reach a top speed of 68 kilometres per hour and elevate to half a metre above the water surface of the lake.

The technology has gradually become more popular over the past 20 years in several marine applications : commercial ships, military applications and racing yacht (America's cup, Vendée globe),...

The hydrofoils are submitted to hydrodynamic loading and experience a lot of fluid phenomena such as, cavitation, ventilation or free surface effects, that impact their performances.

Indeed, they are nowadays mostly manufactured in composite material ensuring a good balance between strength and weight, that revolutionized their development. The characteristics of these materials lead to deformable hydrofoils that experience Fluid-Structure Interactions (FSI) with the loading created by a dense fluid such as water. The anisotropic behavior of the composite materials also creates internal couplings in the structure such as bend-twisting coupling (BTC).

Marimont [59] highlighted the possibility of designing a structure that is able to change its angle of attack in a range of loading conditions with a good tailoring of the composite materials. The design of a hydrofoil is therefore, a complex combination of free surface analysis, hydrodynamic simulations, material behavior and fluid-structure interactions.

This thesis thus links the industrial point of view of understanding and modeling the behavior of a hydrofoil by developing a high-fidelity FSI tool, and the need to analyze new aspects on Fluid-Structure Interactions at the IRENAV laboratory, through experiments. IRDL center being specialized in structures and materials, IFREMER with its hydrodynamic flume and, the IRENAV with its expertise in hydrodynamics and previous work in FSI, coupled with the foil designer SEAIR, make this CIFRE collaboration a closed-loop study with a direct application.

Among the recent works carried out at the IRENAV center on hydrofoils :
(Ducoin, 2008) [45], highlighted the appearance of a twist angle on flexible hydrofoils due to the variation of the section 's thickness in the chord-wise, that changes the distribution of the pressure field along the chord.

(Gaugain,2013) [55] studied numerically and experimentally the FSI on a flexible hydrofoil to predict its hydro-elastic response in non-cavitationg and cavitating flow.

(Delafin,2014) [39] performed a transitional flow analysis on a hydrofoil, applied to transverse axis tidal turbines with active control of the pitch angle.

(Lelong, 2016) [86], observed the decrease in the performances of a flexible hydrofoil

made of isotropic material compared to a rigid profile, when the angle of incidence increases.

A parallel study simultaneously conducted at IRENAV on the morphing of hydrofoils (Mohamed F., 2020) investigates the effect of internal pressure on a deformable composite hydrofoil to design a smart structures that optimize their geometries according to loading conditions.

With the development of computational codes in fluid mechanics and the increase in computer resources, numerical simulation has become an interesting and complementary alternative for the study of fluid-structure interactions.

Thus, the goal of this thesis is to set up for SEAIR numerical tools modeling FSI on flexible composite hydrofoils. The starting case is the hydrofoil of the MINI 747 (see figure 2), which is a surface piercing hydrofoil with a large aspect ratio, experiencing very large displacements.
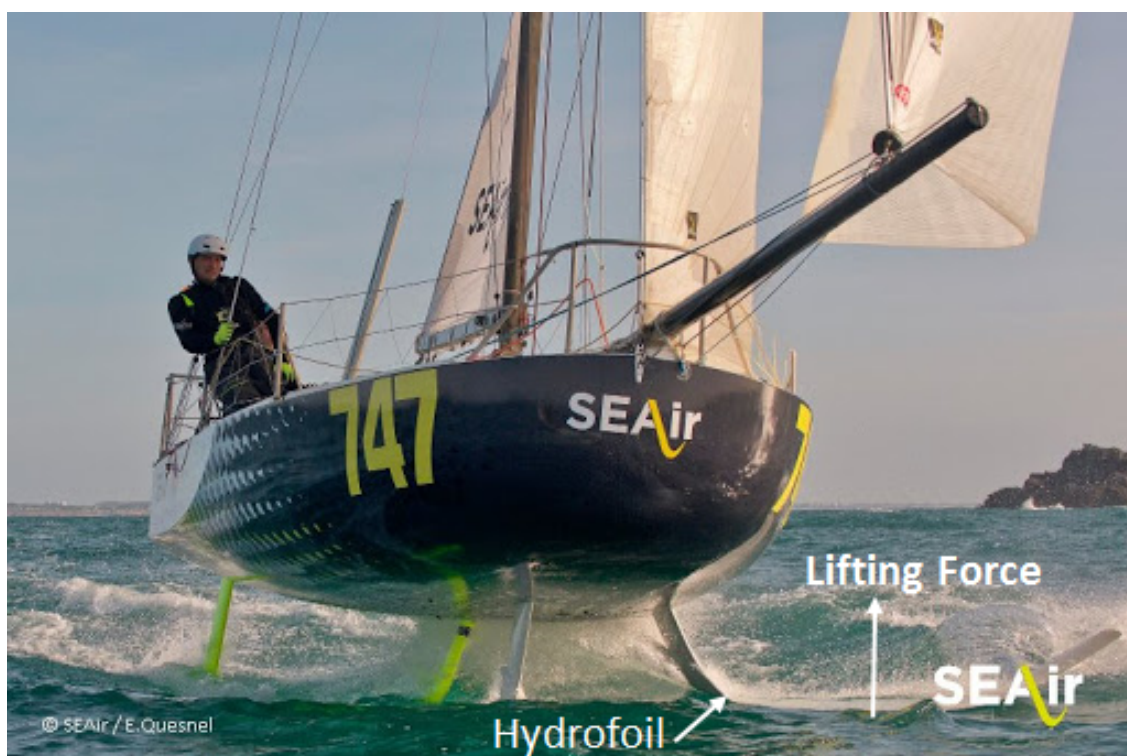
FIGURE 2 – Flying scow bow MINI 747.

Multiple commercial tools are available to perform studies on hydrofoils. One of the best known for hydrodynamic simulations is FineMarine, a commercial software developed by Centrale Nantes and Numeca. It is mainly dedicated to CFD computations that use the fluid solver "ISIS-CFD" and, it is also able to perform FSI simulations but, it is necessary to give as input the modal forms of the structure, previously calculated from a structural software. Thus, FineMarine is not by itself a complete software allowing FSI studies.

Another commercial tool suitable for this application is STAR-CCM++, its V10.04 release in 2015 solves problems involving the flow of fluids and solids in a single, fully integrated environment. STAR-CCM+ offers an efficient way for modeling FSI in a single environment, the main limitation of this tool is the expensive cost of its licence.

Another solution to numerically study FSI on hydrofoils is to couple a tool analyzing the fluid dynamic to another tool analyzing solid dynamics.

Gaugain [55], developed at IRENAV, a coupling between the commercial tool ABAQUS that

3

solves solid dynamics with the commercial tool CFX specialized in fluid dynamic, to studied FSI on a flexible hydrofoil in sub and cavitating flow.

Developing internal tools that do not require commercial licenses and that can be tailored for suitable applications is an increasingly need in the field of research and innovation. Several studies conducted on the subject have led to good results on high-fidelity and low-fidelity couplings such as finite element method couplings solving both the structural and fluid parts [95].
Balze, [13] developed during his thesis at Centrale Nantes, the tool SOPHIA which is based on an LLT (Lifting Line Theory) method and an in-house FEM (Finite element Model) code developed at GSEA design. The robustness of their tool is linked to the gigantic database they have built up on composite materials as well as their expertise in mechanics.
EDF (Electricité de France) performed high-fidelity coupling between their CFD (computational Fluid Dynamics) code Saturne and the CSD (Computational Solid Dynamics) Code_Aster, that they develop internally. A first coupling [37] between these 2 codes was unable to run on multiple processors, the parallelization of the calculations led to bugs and errors.
A recent research work in collaboration with the CEFRACS (Centre Européen de Recherche et de Formation Avancée en Calcul Scientifique), gave rise to new coupling algorithms (Claire BREGMAN, 2018) [29]. The implementation of a new coupling of code Saturne and Code_Aster is part of the ongoing work of EDF.

In the present study, we are interested in a fluid-structure coupling, based on open source tools : OpenFoam for the resolution of the fluid domain and Code_Aster for the resolution of the solid domain. Code_Aster has already proven to give great results in many studies (Julan, 2014) [81] and is now a good reference in terms of CSD tools in the field of openSource. (Suraj & al., 2012) [115] shows excellent results with good accuracy on the OpenFoam solver, "interFoam" in a simulation with free surface.
A manual coupling was performed between OpenFoam and Code_Aster for propeller applications (M. Eichhorn & al. 2016), [47] : a CFD calculation was performed on OpenFoam and the loads were extracted, then, a second calculation was performed on Code_Aster taking the loads as input.
(Yvin,2010) [135] has implemented a partitioned coupling algorithm between OpenFoam and Code_Aster that has been tested on a cavity with a flexible bottom and gave good results. These studies show on the one hand the good individual performances of the two codes calculations, and on the other hand their ability to be coupled together.

Two main aspects are addressed in this research work. On one hand, experiments are essential to analyze the loading that the hydrofoil experiences, their hydro-elastic response under hydrodynamic loading, the internal coupling in composite materials such as bend-twist coupling, the free surface effect. Model-scale hydrofoils made at the image of the MINI 747 's hydrofoil and composite hydrofoils in scale 1 with the same characteristics of MINI 747 's hydrofoil are manufactured. Mechanical characterization and, investigations of FSI are experimentally performed.
On the other hand, numerical development are carried out into two stages to reduce the complexity of the problem, leading to two coupling tools :

- A low-fidelity coupling, FS6R : The first development aims to design a quick and easy to use coupling tool, dedicated to pre-design projects. The coupling solves the fluid domain with a vortex lattice method and the structural part by finite elements.

It should predict the forces and displacements on the hydrofoil with good accuracy.

- A high-fidelity coupling, FOAM-Aster : The coupling between OpenFoam and Code_-Aster. It is a more complete and complex tool, designed for complete studies on various hydrofoil geometries and considering free surface and fluid phase change. The tool is based on advanced numerical scheme for structural and fluid analysis that allow to construct the field of all different variables in the flow.

The innovative character of this research is in the benchmark performed on many hydrofoils (isotropic and composite materials) in both numerical and experimental studies. Moreover, it is difficult to find in the literature direct applications of the coupling OpenFoam-Aster to composite materials.
This work answers the need to create experimental data of reference including the free surface analysis, the composite sandwich structure and the bending-twisting coupling (BTC) behavior.

This manuscript is divided into five chapters :

Chapter 1 : The first chapter is the bibliographical study, it starts with a brief description of the different types of hydrofoils and the fluid interactions that these appendices encounter. The composite materials and FSI phenomena are discussed in the second part of the chapter and the last part presents a state of the art of the coupling methods available to model the FSI.

Chapter 2 : This chapter describes the hydrofoils used in this study and the experimental tests performed. Model-scale and real-scale hydrofoils are investigated. The chapter is divided into three parts : the first part describes the model-scale hydrofoils, the mechanical tests and hydrodynamic tests are described with their experimental setups.
The second part described the real-scale composite hydrofoils, it starts with the design and the manufacturing of the foils. Then, the mechanical characterization of the structures, the hydrodynamic tests and the experimental setups are presented. For the real-scale hydrofoils, free surface effects and structural behavior such as bend-twist coupling are investigated.
The last part presents the post-processing methods used on the different measurements.

Chapter 3 : This chapter concerns the numerical methods, the numerical tools developed in this research work. The low-fidelity coupling FS6R and the high-fidelity coupling FOAM-ASTER are presented. The fluid and structural code are described for each part and their coupling algorithms are also presentedd.

Chapter 4 : The objective of this chapter is to understand the behavior of the hydrofoils studied on on hand and to validate the low-fidelity tool FS6R on the other hand. The chapter is divided into two mains parts.
The first part is the the model-scale hydrofoils : the mechanical characterization of the structure is presented and the hydro-elastic response of the hydrofoils during the tests are also analyzed. The last section compares the simulations of FS6R with the experiments.
The second part of the chapter concerns the real-scale hydrofoils. The mechanical characterization of the different hydrofoils are presented. The investigation of the bend-twist coupling in static and dynamic tests is also discussed in this part. The hydro-elastic behavior of this foils are well understood and the validation of FS6R is performed through

comparisons of the experimental results.

Chapter 5 : The aim of this chapter is to validate the high-fidelity coupling FOAM-ASTER. A comparison of the simulations with the results of the model-scale hydrofoils is first performed.
Then a static analysis of the real-scale hydrofoils helps to validate Code_Aster on the bend-twist coupling behavior. The following step is the comparison the hydro-elastic response of the real-scale hydrofoils to the simulations of the numerical tool and, the both high-fidelity and low-fidelity coupling are compared each other on the results of the real-scale hydrofoils.

CHAPTER 1

State of the art of fluid-structure coupling on composite hydrofoils

« *The foil is not a "miracle solution" or a "revolution", it is one of the components of a boat, an evolution among others.* »

Antoine MAINFRAY, Naval
Architect

Contents

This chapter presents a state of the art that first describes the different types of hydrofoils, their evolution, design variation and some application cases. The fluid phenomena occurring during the hydrofoils operation are also presented in the first part. In the second part, a brief description of the composite materials used for the manufacturing of the hydrofoils is presented.

The third part of the chapter is dedicated to the fluid-structure interaction phenomena and the last part presents an overview of the different coupling methods for FSI analysis.

1.1 Hydrofoils

Hydrofoils are water wings, used in boats to generate a lifting force that creates balance in the boat. They are also used as an anti-drift surface to partially or totally relieve the weight of the boat and a positive effect is the reduction of the water resistance on the hull by reducing water friction and wave resistance against the boat motion.

Indeed, hydrofoils generate in the water a hydrodynamic lifting force that is transmitted to the boat and allows its rise out of the water. They also impact the overall equilibrium of the boat and improve stability and comfort when sailing ([22],[122], [52]).

Figure 1.1 shows the balance equilibrium of an Imoca 60 sailboat, heeling to the port side and using a hydrofoil as an anti-drift device. The first step is to tilt the keel to starboard and its weight will partially straighten the boat. The second step consist to deploy the foil downwind on the port side in the water. The vertical component of the hydrodynamic force (creating the lifting effect) will create a righting moment opposite to the heeling that will straighten the boat and it will gradually regain its horizontal position on the water.
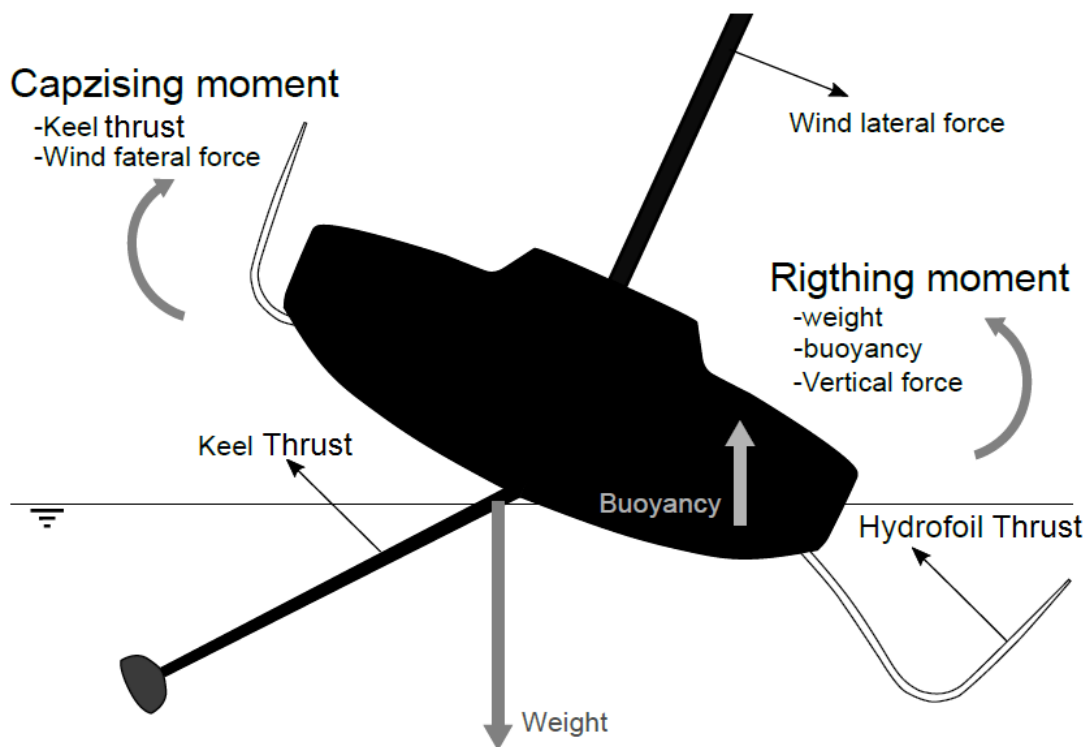
FIGURE 1.1 – Equilibrium of a modern 60 Imoca foiling yacht. Inspired from VPLP [122].

The hydrofoil has two major effects on the sailing boat : the lift force reducing the surface of the hull underwater and thus the drag force and the righting moment leading to a good

equilibrium and a more powerful boat.

There are several types of hydrofoils that can be divided into 2 categories and their shapes vary according to the application : submerged hydrofoils or active control hydrofoils and the hydrofoils piercing the free surface.

1.1.1 Hydrofoils piercing the free surface

These are the first generation of hydrofoils that appeared in the late 19th and early 20th centuries, they are also called V-foils.
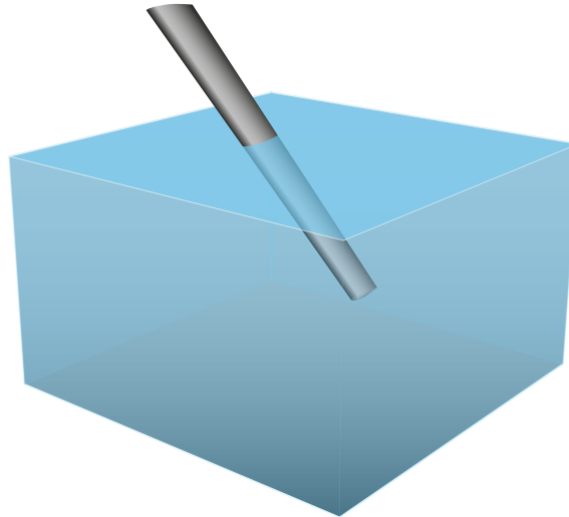
FIGURE 1.2 – Hydrofoil piercing the free surface [101]

These category of hydrofoils are piercing the free surface : one part works in the air and the other works in the water (figure 1.2). Only the part underwater part creates the lifting force.

As the speed of the boat increases, the lift forces increases too, resulting in an elevation of the boat.

The design of a V-Foil allows to reduce the submerged surface when the velocity rises, creating a constant lift force and therefore a stabilization of the boat's flying height : the equilibrium between low speed-high submerged surface and, high speed-low submerged surface, maintain the lift force constant.

The first type of V-Foil were created between 1911-1922 by the scientists Baldwin & Bell, they were made up of overlapping of planes and the geometry had the form of ladders (figure 1.3).

Figure 1.3 shows the Canadian Navy's experimental hydrofoil "the KC-B" : which made the cover of Life magazine in 1954. This flying boat used a ladder hydrofoil design after Alexander Graham Bell [18]. The foils pierce the free surface and are made up of a super-position of flat bearing surfaces that form ladders.

The recent design of V-Foil are continuous geometries with shapes similar to the letters C, I, or J, as shown in figure 1.4, 1.5, 1.6, 1.7.

The C foil are easy to install but are unstable in heave. The J foils are similar to C foils, but the maximum lift remains even when the foils are partially retracted (less potential drag). They are also unstable in heave. The L foil can regulate the heave without control.

FIGURE 1.3 – LIFE MAGAZINE SEPT 1954 - KC-B, the Canadian Navy's experimental hydrofoil, could do 96 km/h. [96]

When the boat goes up, the lateral area gets smaller and the boat starts slipping sideways. The horizontal part of the foil moves toward its own low pressure field and the lift decreases leading to a settle of the boat and the lateral area increases again, the leeway decreases and the vertical lift rises again. The L-foils are harder to build.

1.1.1.1 V-Foil advantages

— Self-regulation : Flight height regulation is achieved by reducing the surface area which avoid the use of a regulation system that may be difficult to implement

— The retraction system is easier to design on V-foils
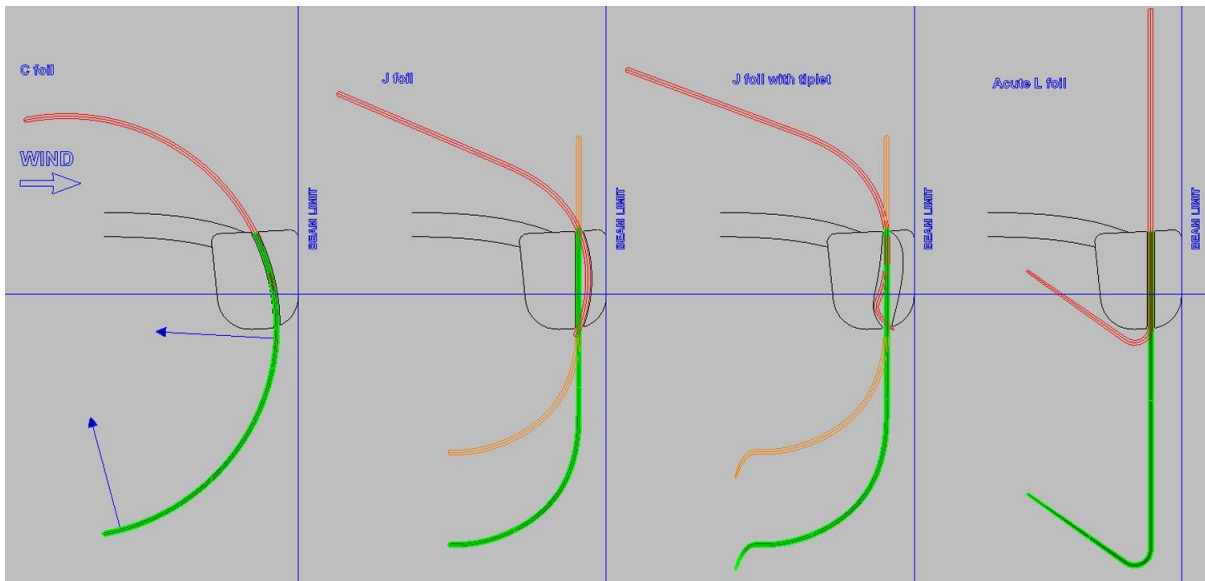
FIGURE 1.4 – "C", "J", "L" Foils [8].

1.1.1.2 V-Foil disadvantages

— V-shaped foils piercing the free surface have interactions with the free surface at the air/water interface, it increases the risk of ventilation. This requires designers to use systems (such as fences) preventing air from flowing down the profile.

— The force lifting the boat is created by effective surface foil projected on the horizontal plane. For the same efficiency as T-shaped foils, V-foils must be longer.

— Due to their longer length, the moment experience by V foil are higher.

FIGURE 1.5 – SEAIR's flying rib : foiling motor boat with J foil, [109]

FIGURE 1.6 – Alain THEBAULT's hydrofoil 'Rocket' type I with fences to avoid ventilation. [118]

FIGURE 1.7 – Racing catamaran Nacra F20 FCS equiped with L-Foil, [107]

1.1.2 Submerged hydrofoils or active regulation hydrofoils

These hydrofoils also called T-Foils appeared in 1945, 50 years after the passive foils, during the researches of the scientists Christopher Hook and A. C. Kermode, on solving ventilation problems by developing servo foils on motor boats ([73], [72]). The main difference with the first hydrofoil category is the need of regulation for T-Foils.
Figure 1.8 shows a submerged hydrofoil, it is composed of a vertical support piercing the free surface and a horizontal lifting surface, fully submerged.

T-Foils regroup all the hydrofoils requiring servoing regulation, several geometries are developed on this principle with the shape of the letters : T, L, Y and U.
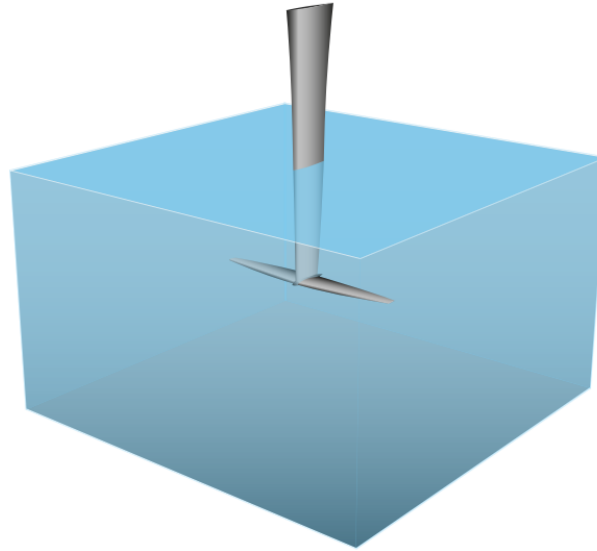
FIGURE 1.8 – Submerged Hydrofoil [101]

Nowadays, the regulation can be performed by a system tailoring the foil incidence in real time : a mechanical device such as a sensor wand is used to detect the flying height of the boat and then sensor acts of the rake of the foil (see figure 1.9).
Figure 1.10a shows the T foil used on the racing moth Exocet, an example of L-foil designed by G. Ketterman (sailboat designer) in 2005 is presented in figure 1.10b. The SEAIR's moth, flying on a T-foil is shown in figure 1.11.
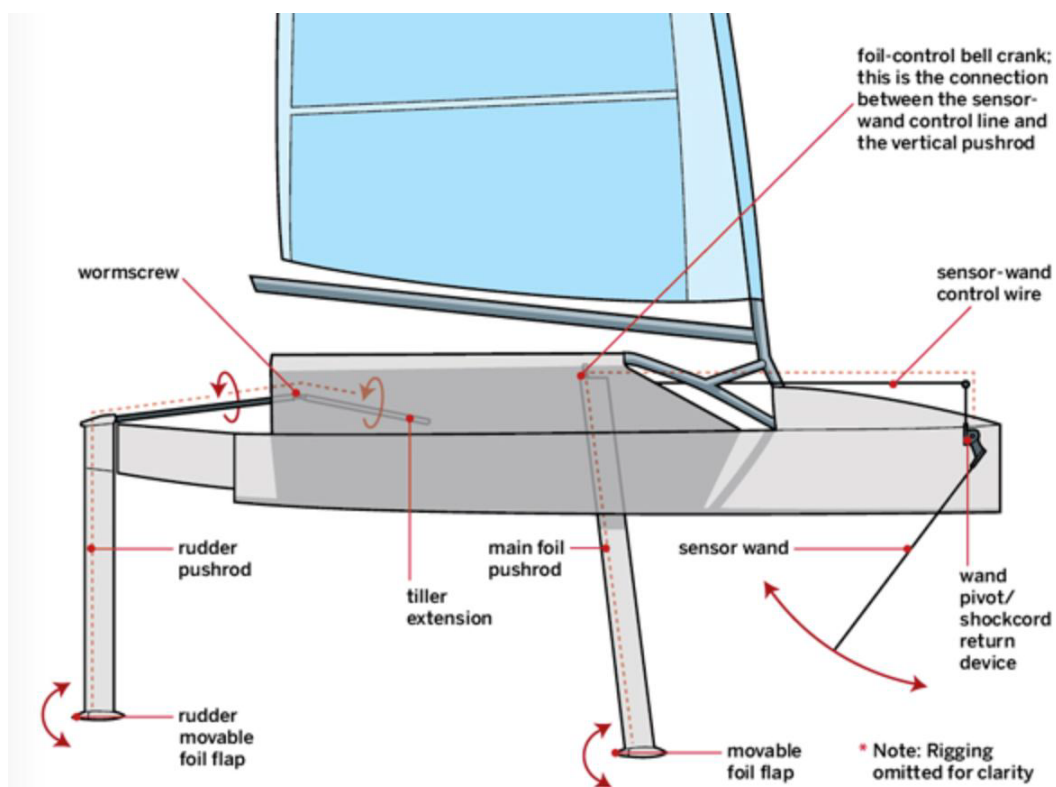
FIGURE 1.9 – Description of the active control of submerged hydrofoils [8].

(a) T-foil of Exocet's Moth.[25]

(b) L-foil, G. Ketterman 2005. [84]

FIGURE 1.10 – T and L hydrofoils

FIGURE 1.11 – Moth on a T foil, SEAIR.

1.1.2.1 Advantages

— The lifting plane operates at the same depth along the span when there is no heel, all its sections see the same phenomena.

— Being fully submerged, the lifting surface does not interact with the free surface.

— The lifting force is transmitted to the boat through the vertical support, thus the hydrofoil architecture is rigid.

1.1.2.2 Disadvantages

— The need to implement a regulation system.

— The motion of the lifting surface (during the regulation) can lead to stall angle if the

angle of attack becomes too high.

— A retraction system is very complicated to implement, especially for the geometry T.

1.1.3   Fluid instabilities

This part describes the fluid instabilities that impact the hydrofoil performances and that should be considered during the design process.

1.1.3.1   Free surface effects

The fluid flow around hydrofoils near the free surface generates waves which strongly influence its performances. Figure 1.12 shows the deformation of the free surface, creating waves which are responsible for the drag increase and also modify the pressure field. H. Ghassemi et al. [57] show that the effect of immersion on the hydrodynamic performance is significant when the hydrofoil is located near the free surface.
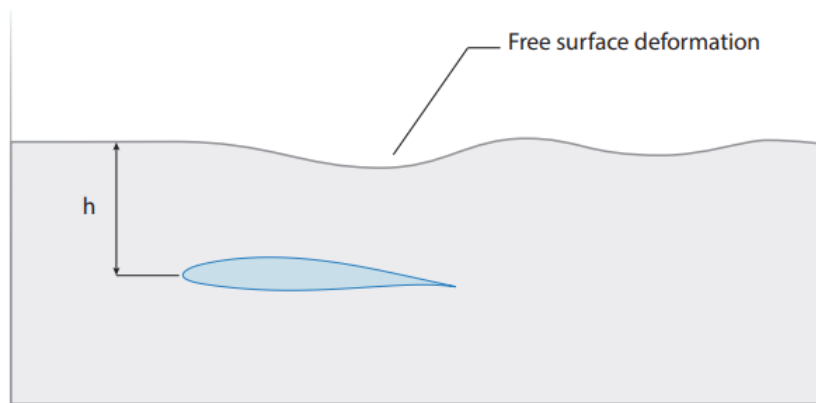
FIGURE 1.12 – Free surface deformation when hydrofoil moves in its vicinity : wave generation

Many studies have been carried out to study the impact of the free surface on the hydrodynamic coefficients and the literature is very well documented concerning hydrofoil fully submerged. That influence became strong when the immersion depth h of the hydrofoil is small.

Figure 1.13 from [74] shows the evolution of the lift coefficient with the submerge Froude number $F_{nh} = \frac{U}{\sqrt{gh}}$ for several immersion depth ratio h/c. U is the flow velocity, h the immersion depth, g the gravitational acceleration and c the hydrofoil's chord.

The results show a decrease of the lift coefficient when the foil gets close to the free surface (when the ratio h/c decreases), this decrease is amplified for lower Fnh.

S. Bal [11] studied the free surface effect on a 3D NACA0015 extruded for several immersion depth. Figure 1.14 shows the distribution of the pressure coefficient around the profile at the same Froude number for two immersion depth ratio :$h/c = 0.1$, $h/c = 0.5$. The two cases are compared to the red curve showing the distribution for an unbounded flow domain : the depth immersion is so high that there is no free surface effect.

The differences between the three curves highlight the influence of the free surface on the pressure coefficient. For $h/c = 0.5$, the difference with the red curve is barely observable, there is a slight decrease in the amplitude, the two curves have the same trend and $h/c = 0.5$ is slightly shifted down.
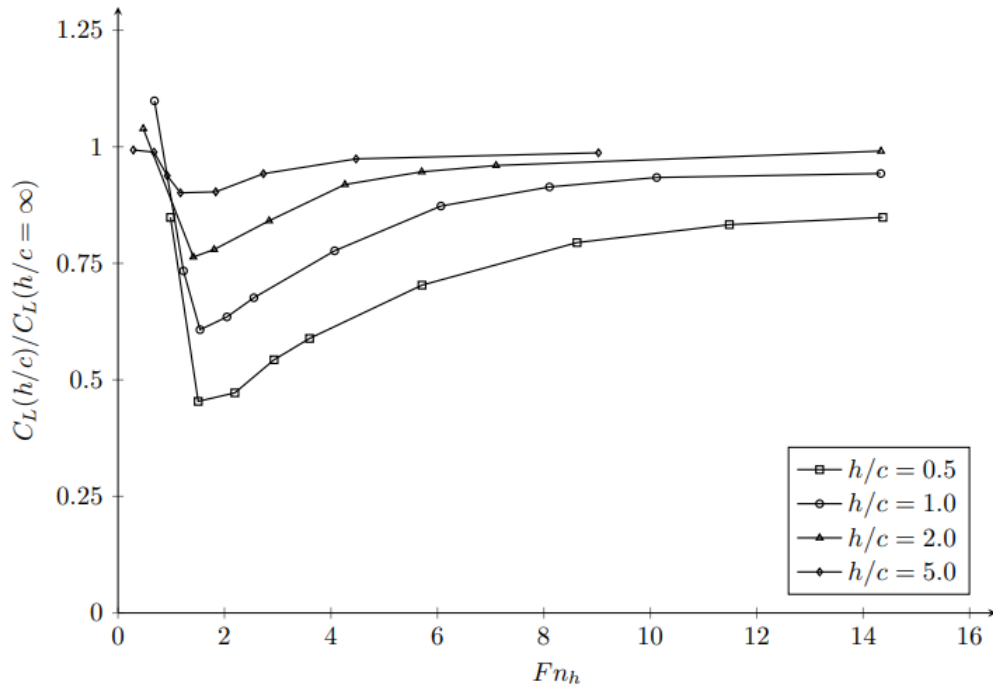
FIGURE 1.13 – Evolution of lift coefficient with Froude number Fnh for several immersion depth ratio h/c. [74]

For $h/c = 0.1$, modifications are observable in the amplitude and the shape of the curve. The effect of free surface is larger on the high pressure side than the low pressure side, in both cases.
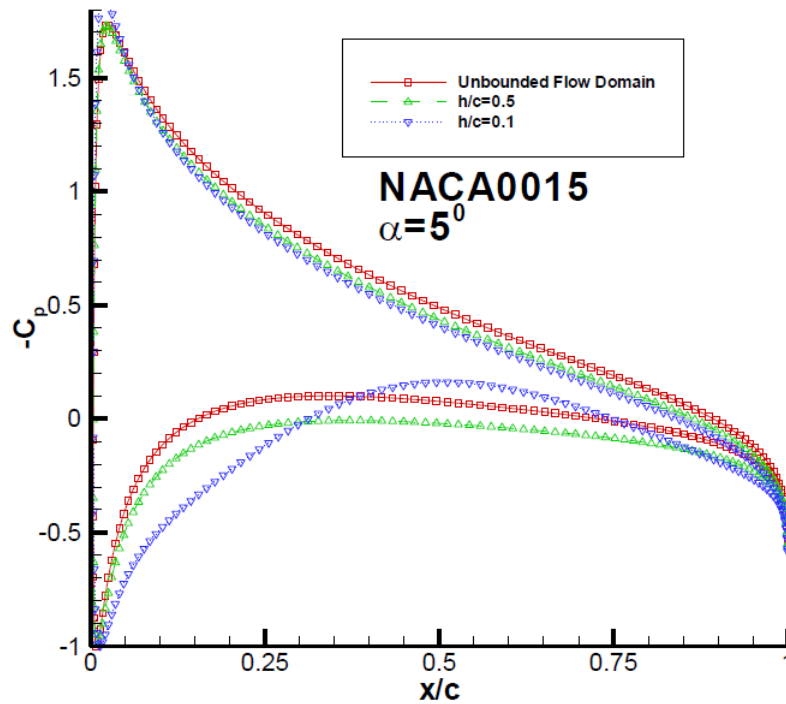
FIGURE 1.14 – Distribution of the pressure coefficient along the profile for different immersion depth, NACA0015. [11]

1.1.3.2 Ventilation

S.F. Hoerner [71] defines the ventilation as "the formation of a more or less steady cavity which is connected to the atmosphere, past or behind a surface piercing body ..." Wetzel [128] states that, it is the formation at a certain speed of "an air pocket... that will expose part or all of the rear portion of the surface piercing body to the atmosphere."
J. Breslin and R. Skalak2. [30] define ventilation as "the occurrence of atmosphere connected cavities, usually on one side of a moving, surface piercing body. "
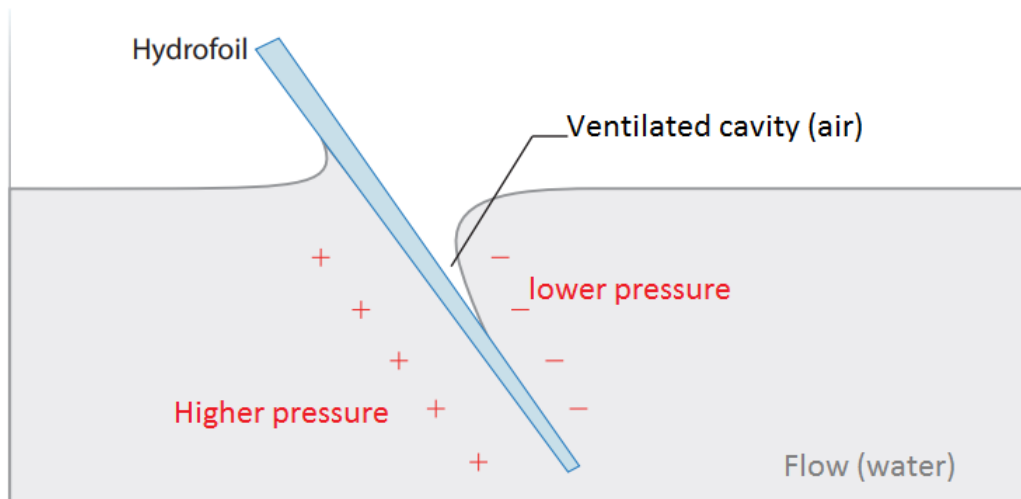
FIGURE 1.15 – Ventilation phenomenon [101]

The ventilation is another limiting phenomenon that appears when the hydrofoil pierces the free surface. If the low pressure generated by the flow on the suction side of the lifting surface becomes lower than the atmospheric pressure, it creates a suction of air in the water at the free surface interface (figure 1.15). An amount of air is sucked in the water flow, creating a cavity that replace the flowing water and causes a loss of lift because of the difference of the fluid density (air/Water).

FIGURE 1.16 – Ventilation phenomenon on a surface piercing A-class catamaran hydrofoil [1]

Figure 1.16 shows the ventilation well developed on a hydrofoil piercing the free surface. The profile is a Selig/Donovan SD7032-099-88, the hydrofoil is tested in a cavitation

tunnel at 10 m/s and $\alpha = 4°$.

Young et al.[131] reviewed the fundamental physics driving ventilation and its impact upon the hydrodynamic and structural response of a lifting body in steady and unsteady flow regimes. They observed that natural ventilation occurs when the flow around a body forms a cavity that is open to the free surface and for flexible structures, flow-induced deformations can increase the loading and the size of cavities. The ventilation in unsteady regime creates fluctuations of added mass that can change the structural frequencies of resonance, the damping of the structure, and may accelerate the hydro-elastic instabilities.
R. S. Rothblum [106] investigated the methods of delaying and controlling the ventilation on surface piercing structures and shows that the ventilation can be prevented or controlled by using : fences, roughness, tapered hydrofoils.

The most common method to prevent ventilation effect in practice is the use of "fences", small horizontal plates designed to limit the area of low pressure upwards (see figure 1.6). Fences are also used on motor boats to prevent ventilation. They must be perfectly aligned with the flow to avoid drag increase or structural problems.

1.1.3.3 Cavitation

Cavitation is a purely hydrodynamic phenomenon which occurs at a constant temperature and depends on the pressure variations. It is the vaporization of a liquid when its pressure decreases under the vapour saturated pressure at constant temperature. It can also appear in a fluid at rest under the action of a shock. Figure 1.17 shows the phase diagram of water that allows to understand the phenomenon.
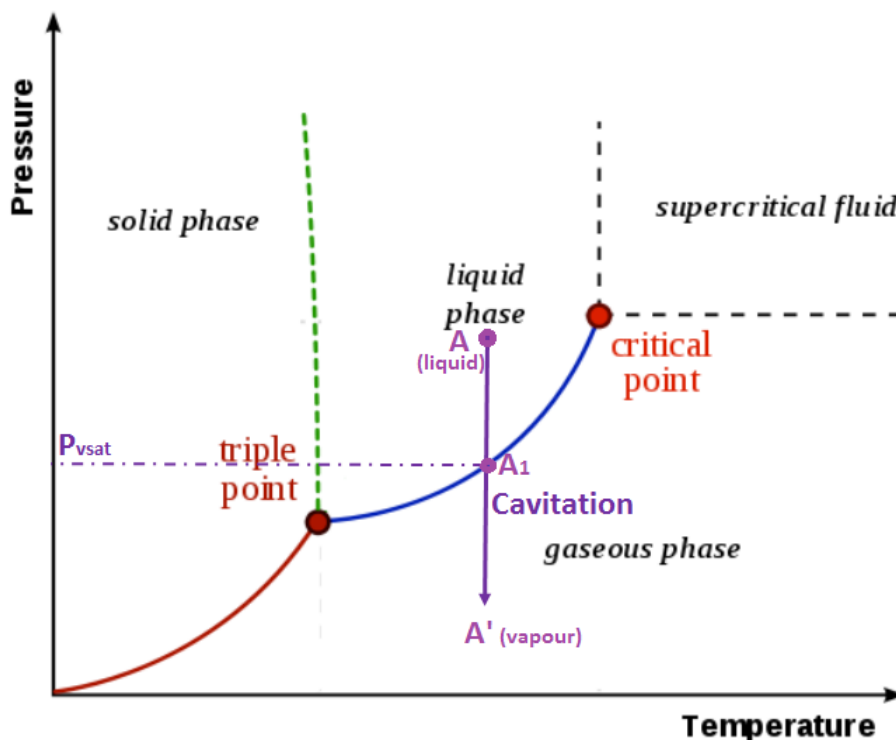
FIGURE 1.17 – Phase diagram of water.

The cavitation phenomenon can occur in different forms, the three main ones (figure figure 1.18) described in [6] are :

— **Vortex cavitation** : this type of cavitation generally appears first. It occurs in areas of high vorticity when the pressure at the center of the vortex is low enough (such as at the tip of propeller blades).

— **Bubble cavitation** : vapour bubbles appear at several points in the structure, they originate from cavitation nucleus contained in the fluid. When a cavitation nuclei moves into the fluid, it grows and becomes a bubble that grows and moves to the re-compression area. These bubbles implode during pressure variations and emit an acoustic wave. This phenomenon has highly erosive nature.

— **Sheet cavitation or partial cavitation** : the steam appears in the form of a pocket attached to the structure. It develops from the leading edge and can appear during the separation of the laminar boundary layer. This type is less noisy than bubble cavitation but causes vibrations that induce fluctuations in the loading on the structures (the pocket can cover a large area of the lifting surface and strongly impacts the loading). Studies show that they reduced the performances of propulsive systems and that as soon as the cavitation pocket reaches the trailing edge, the hydrodynamic performances of the structures collapse [12].
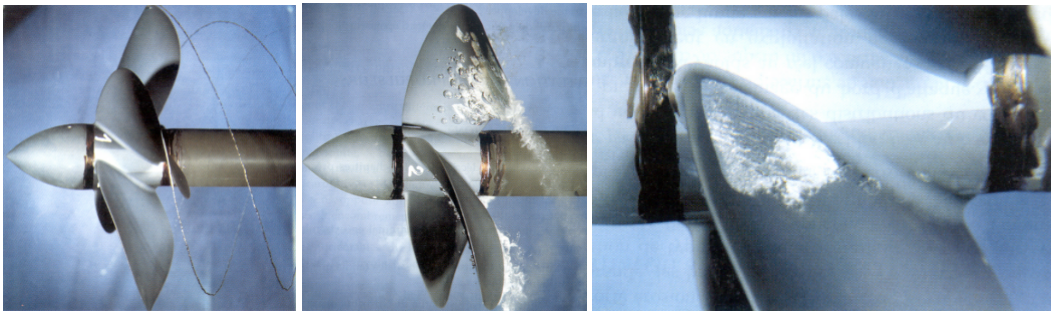
FIGURE 1.18 – Cavitation types shown on a propeller : a)Vortex cavitation, b) Bubble cavitation, c) Partial cavitation

Two non-dimensional numbers describing the pressure distribution can be used to predict the cavitation appearance in a flow : the number of cavitation σ and the pressure coefficient C_p.

$$\sigma = \frac{P_0 - P_V}{0.5\rho U^2} \quad C_p = \frac{P - P_0}{0.5\rho U^2} \quad C_{p_{min}} = \frac{P_{min} - P_0}{0.5\rho U^2} \tag{1.1}$$

ρ is the fluid density
U is the flow velocity
P_0 is the hydro-static pressure that varies with the immersion depth
P is the total pressure
P_V is the vapour saturated pressure
Looking at the distribution of the pressure coefficient around a lifting profile, $C_{p_{min}}$ is the minimum value. The limit condition for cavitation occurrence is $P_{min} = P_V$, the minimum pressure coefficient is equal to the opposite of the cavitation number.In a global approach, a comparison of σ and $-C_{p_{min}}$ can help to define the cavitation appearance.

Figure 1.19 shows the distribution of the pressure coefficient C_p as a function of the reduced abscissa x/c (c is the chord length of the profile and x the position along the x-axis).

The figure is plotted for a NACA0015 profile at $Re = 3 \times 10^5, \alpha = 3°$.
Depending on σ value, three cases are possible :

— $-\sigma_1 < C_{p_{min}}$: the minimum pressure is higher than the vapour saturated pressure, there is no cavitation

— $-\sigma_2 = C_{p_{min}}$: There is a possible start of the cavitation. It depends on the water quality, the roughness on the profile, turbulence in the flow or nucleus that can initiate the cavitation,([36], [54]), [53].

— $-\sigma_3 > C_{p_{min}}$: The minimum pressure is lower than the vapour saturated pressure, the cavitation is developed.
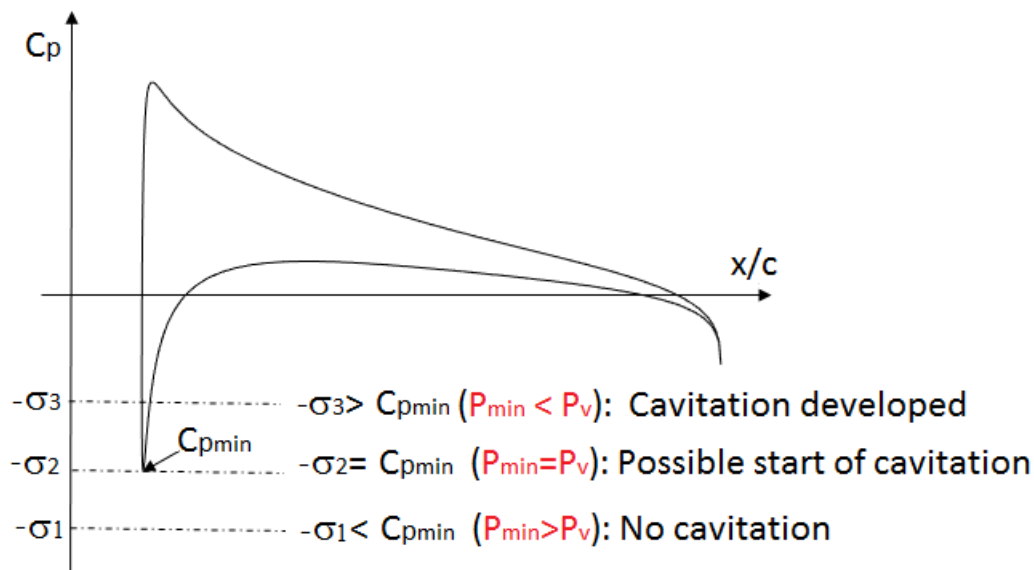
FIGURE 1.19 – Pressure coefficient on a NACA0015 profile at $Re = 3 \times 10^5, \alpha = 3°$

Cavitation leads very often to harmful consequences that degrade the hydrodynamic performance of the lifting surfaces and reduce the durability of the materials :

— **Erosion** : Steam bubbles can be convected by a flow to areas of higher pressure, causing implosion. Erosion of structures is caused by high pressure peaks,that create a local destruction of the surface walls. These damages can be observed on propeller blades, hubs or control surfaces as shown in figure 1.20.

(a) Pump rotor destroyed by cavitation erosion.

(b) propeller blade destroyed by cavitation erosion.

FIGURE 1.20 – Cavitation erosion [68].

— **Performances drop** : cavitation has negative effects on the loading of structures, it can create load fluctuations and performances decrease. Shen et al. [110] studied the influence of surface cavitation on hydrodynamic forces of a cambered two-dimensional NACA 66 (MOD) wing section in a high-speed water tunnel. They observed a significant increase in lift with increasing cavity length.

Tolag and al. [3] examine the effect of turbulent and cavitating flow on the hydroelastic response and stability of a hydrofoil, the results show that cavitation tends to : reduce the mean lift, increase the mean drag and lower the mean deformations.

Considering the cavitation phenomenon is an important step in the design of lifting structures and propulsion systems. The purpose of hydro design is to delay the cavitation as much as possible. The numerical modelling of this phenomenon is also a challenge (Gaugain [55], Ducoin [45]).

Figure 1.21 shows a hydrofoil in a cavitating flow for R$e = 3 \times 10^5$, $\sigma = 0.6$ at 4° and 5° of incidence. For $\alpha = 4°$ the vortex is well developed in the wake and the cavitation patches emerge from the tip of the foil. At $\alpha = 5°$ the vortex has grown and the cavitation patches have developed from the tip to the root of the foil.
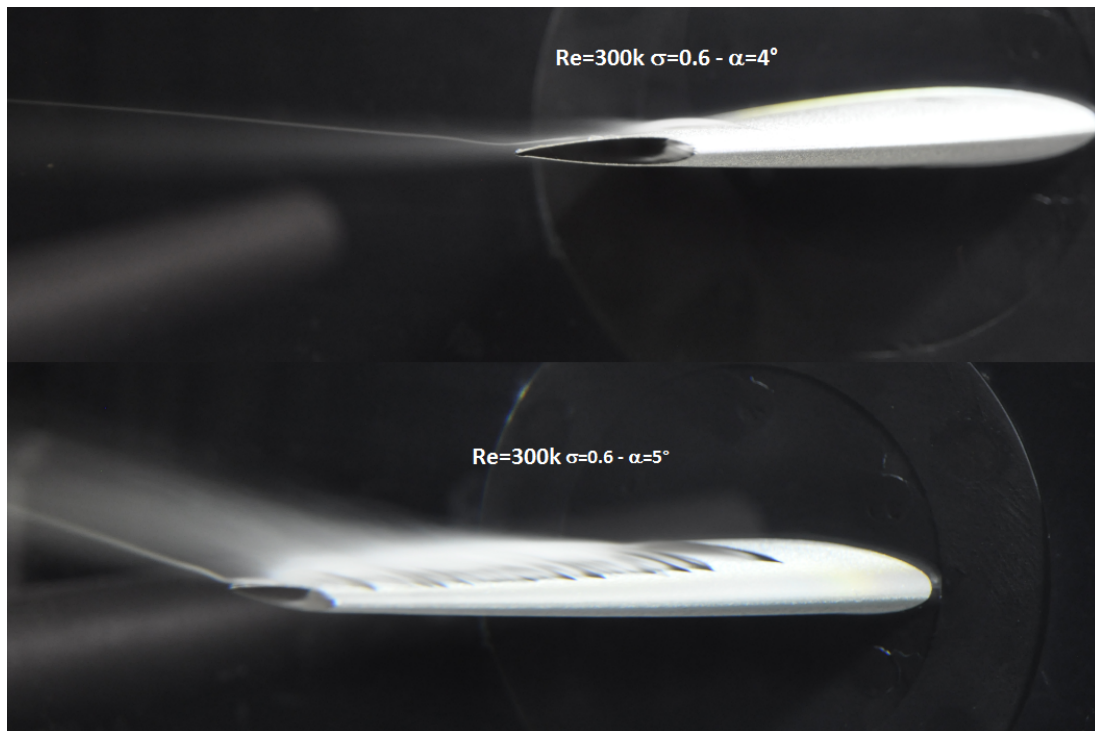
FIGURE 1.21 – Cavitation flow in the cavitation tunnel of IRENAV. Hdrofoil in POM material, NACA 0015, $\sigma = 0.6$, R$e = 3 \times 10^5$

Lelong [86] studied a rigid isotropic hydrofoil in a cavitating flow. The results showed an increase in the bending frequency of the profile as the cavitation number decreases, which implies a decrease in the fluid added mass to the profile.

Lianzhou Wang and al.[126] analyzed the performance of an oscillating propeller in cavitating flow. The propagation of unsteady flow fields and the propeller's rotations and oscillations were coupled in a numerical study. They investigated the hydrodynamic behaviour of propellers in oscillatory conditions and came out with significant results for propeller design and optimization.

Ducoin et al[45] studied, both experimentally and numerically, the displacement of the

tip of a hydrofoil under different flow conditions. They showed that the movements of the sections were influenced by unstable cavity pockets while the small stable cavities had a negligible effect.

Bertetta and al. [20] proposed different setting of picth angle of a CPP (controllable pitch propeller) to reduce the cavitating phenomena and presented a method, based on the coupling between a multiobjective optimization algorithm and a panel code to model the cavitation.

After considering the fluid phenomena and its impact on the hydrodynamic performances of lifting structures, the design process consider the material behavior which strongly influences the hydro-elastic response of the structures.

1.2 Mechanic of composite materials

Composite materials are increasingly used in the manufacturing of hydrodynamic lifting surfaces due to their higher specific strength, their light weight and favorable fatigue properties. The complex behavior of these materials induces complexity in the design and performance prediction of the structures.

Composite materials are made of at least two different materials : a high-performance and fragile reinforcement such as fibers (glass, carbon, kevlar,...) and a low modulus and more ductile matrix, typically a resin. The basic combination of these two materials is called a ply : it is composed of long fibers of high elastic modulus, bounded together with a ductile resin. Figure 1.22 shows a unidirectional ply, all the fibers are oriented in the same direction.
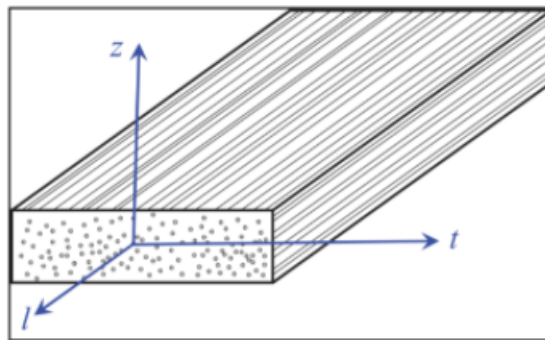
FIGURE 1.22 – unidirectional (UD) ply, and its reference system (l,t,z). [28].

The composite ply is commonly manufactured within three main types (see figures 1.22 and 1.23) : **unidirectional ply** (all the fibers are oriented in the same direction), **bias ply**(the ply is composed of an equilibrium of fibers oriented at 45° and −45°), **balanced ply** (the ply is composed of an equilibrium of fibers oriented at 0 and 90°).

Composite structures consist of a stack of plies in various orientations and the resulting properties depend mainly on the characteristics of each ply and the different orientations in the layup.

They first appeared in aeronautics and aerospace for these lightweight properties and are now widely used in other applications such as wind turbines and, marine appendices and constructions.

Barbero [14] describes three scales for composite material analysis : micro-mechanics, lamina level and laminate level. The behaviour at these different scales is governed by
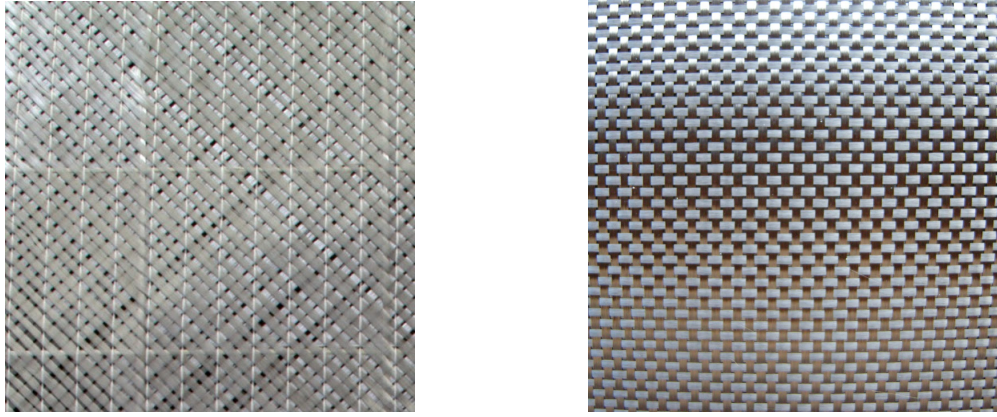
(a) Bias ply composed of 45° and −45° fibers.

(b) Balanced ply composed of 0° and 90° fibers.

FIGURE 1.23 – Bias and balanced composite plies.

composite materials theory : **the laminate theory** [56], [80], [136], [28].
This section summarily presents the basic characteristics of a ply. The behaviors of a ply and a laminate layup are described with the laminate theory. For more details on the different types of composite materials, reinforcements, resin types and derived products, readers should refer to [56].

1.2.1 Homogenization method : properties of a ply

The properties of a ply combine the strength of the fibers and the ductile nature of the resin. This section describes the mechanical characteristics of a ply.
In the reference system (l,t,z) of an unidirectional ply (see 1.22), the direction of the fibers is the longitudinal direction "l", the other in-plane direction perpendicular to "l" is the transverse direction "t" and "z" is the out of plane direction.
[56] proposed a mixing law (equations 1.2-1.6) that calculates the mechanical properties of a ply : the modulus of elasticity in the longitudinal direction E_l and in the transverse direction E_t, the shear modulus G_{lt} and Poisson coefficient ν_{lt}, based on the properties of the fiber and the resin.
V_f is the volume of fiber in the ply, M_s the mass of the ply per unit of area, ρ_f is the density of the fiber. The variables indexed with "f" stand for the fiber and the ones indexed with "m" stand for the resin. e_{ply} is the thickness of the ply.
E_f, E_m are respectively the modulus of elasticity of the fiber and the resin and, G_m is the shear modulus of the resin.

$$V_f = \frac{M_S}{\rho_f \times e_{ply}} \tag{1.2}$$

$$E_l = E_f V_f + E_m (1 - V_f) \tag{1.3}$$

$$E_t = E_m \left[\frac{1}{(1 - V_f) + \frac{E_m}{E_f} V_f} \right] \tag{1.4}$$

$$\nu_{lt} = \nu_f V_f + \nu_m (1 - V_f) \tag{1.5}$$

$$G_{lt} = G_m \left[\frac{1}{(1 - V_f) + \frac{G_m}{G_f} V_f} \right] \tag{1.6}$$

23

1.2.2   Unidirectional ply behavior

To design a structure, it is necessary to characterize the stress [σ] and strain tensor [ϵ]. The following assumptions are made [21] :

— The thickness of a ply is very small

— The stresses and strains are in-plane, the out of plane component are zero

— The material is elastic : the deformations are reversible

— The deformations are small and linear

— The material behavior is in agreement with the Hooke 's law

Equation 1.2.2 gives the components of the stress matrix of a ply in its reference system (l,t,z). The components related to the out-of-plane direction "z" are zero. Only tensile or compression stresses in the longitudinal direction σ_l or in the transverse direction σ_t and, the shear stress τ_{lt} are not zero.

$$\left[\sigma\right] = \begin{bmatrix} \sigma_l & \tau_{lt} & 0 \\ \tau_{lt} & \sigma_t & 0 \\ 0 & 0 & 0 \end{bmatrix}_{(l,t,z)} \tag{1.7}$$

The in-plane strain field consists of tensile-compression strains in the longitudinal direction ϵ_l, in the transverse direction ϵ_t and shear strain γ_{lt}.
According to the Hooke's law, the in plane strains for tensile-compression are linked to the stresses by the equations 1.8 and composed of :

$$\begin{cases} \epsilon_l = \underbrace{\dfrac{\sigma_l}{E_l}}_{\text{El}astic} - \underbrace{\nu_{tl}\dfrac{\sigma_t}{E_t}}_{Poisson} \\[3em] \epsilon_t = \dfrac{\sigma_t}{E_t} - \nu_{lt}\dfrac{\sigma_l}{E_l} \\[2em] \gamma_{lt} = \dfrac{\tau_{lt}}{G_{lt}} \end{cases} \tag{1.8}$$

— Elasticity component : the strain in direction "l" is linearly linked to the stress in direction "l" by the elastic modulus in that direction. Same for direction "t".

— Poisson effect component : a stress in the direction "l" creates a strain in direction "t" linked in a linear relation with the Poisson coefficient ν_{lt} and vice versa for the direction "t".

— The shear strain γ_{lt} is linked to the strain stress in a linear relation with the shear modulus G_{lt}.

In a general representation (using the Voigt representation), the stress tensor [σ] is linked to the strain tensor [ϵ] by the stiffness matrix [Q] of the ply, defined in the orthotropic reference by equation 1.9.

$$\begin{cases} [\sigma] = [Q].[\epsilon] \\\\ \begin{bmatrix} \sigma_l \\ \sigma_t \\ \tau_{lt} \end{bmatrix} = - \underbrace{\begin{bmatrix} \beta.E_l & \beta.\nu_{lt}.E_t & 0 \\ \beta.\nu_{lt}.E_t & \beta.E_t & 0 \\ 0 & 0 & Glt \end{bmatrix}}_{[Q]} \begin{bmatrix} \epsilon_l \\ \epsilon_t \\ \gamma_{lt} \end{bmatrix} \\\\ with \\ \beta = \frac{1}{1-\nu_{lt}.\nu_{tl}} \end{cases} \quad (1.9)$$

The elastic properties of a ply can thus be defined by five components : $\{E_l, E_t, G_{lt}, \nu_{lt}, \nu_{tl}\}$. The definition of the stiffness matrix of a ply [Q] in any reference system (x,y,z) is named $[Q']$ and expressed in equation 1.10. It is a combination of the stiffness matrix [Q] expressed in (l,t,z), the change-of-basis matrix from coordinate (l,t,z) to (x,y,z) [T] ([129]) and its transpose $[T^t]$. "c" is the cosine of the ply orientation measured in the reference (x,y,z) and "s" is the sine.

$$\begin{cases} \begin{bmatrix} \sigma_x \\ \sigma_y \\ \tau_{xy} \end{bmatrix}_{(x,y)} = \begin{bmatrix} Q'_{11} & Q'_{12} & Q'_{16} \\ Q'_{21} & Q'_{22} & Q'_{26} \\ Q'_{31} & Q'_{32} & Q'_{36} \end{bmatrix}_{(x,y)} \begin{bmatrix} \epsilon_x \\ \epsilon_y \\ \gamma_{xy} \end{bmatrix}_{(x,y)} \\\\ [Q']_{(x,y)} = [T^t]_{x,y}.[Q]_{(lt)}.[T]_{(x,y)} \\\\ [T]_{(x,y)} = \begin{bmatrix} c^2 & s^2 & 2.s.c \\ s^2 & c^2 & -2.s.c \\ -s.c & s.c & (c^2 - s^2) \end{bmatrix}_{(x,y)} \\\\ [T^t]_{x,y} = \begin{bmatrix} c^2 & s^2 & -s.c \\ s^2 & c^2 & s.c \\ 2s.c & -2s.c & (c^2 - s^2) \end{bmatrix}_{(x,y)} \end{cases} \quad (1.10)$$

1.2.3 Laminate in bending and in-plane loading

A composite structure called laminate is made of a stacking of plies bounded with resin as shown in figure 1.24. The numbering of the plies is done from bottom to top : each ply "k" has its orientation θ_k, a thickness e_k and, the reference z=0 is set at the medium plane of the stack. The entire structure is studied in the global reference (x,y,z) ; the reference (l,t,z) is only related to a ply.

Figure 1.25 shows the forces on the laminate subjected to membrane and bending loading, presented in the medium plane.

The membrane loading create forces in the medium plane : the normal force flux N_x, N_y and the shearing force flux T_{xy}. The bending loading are the loads normal to the medium plane which creates the bending moment M_x, M_y and the warping moment M_{xy}. They are linked to the stresses and the thickness in equation 1.11.
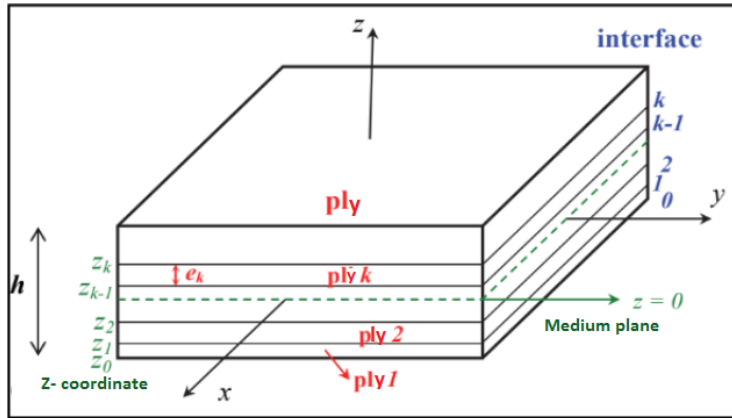
FIGURE 1.24 – Stacking of plies in a laminate composite. [28]
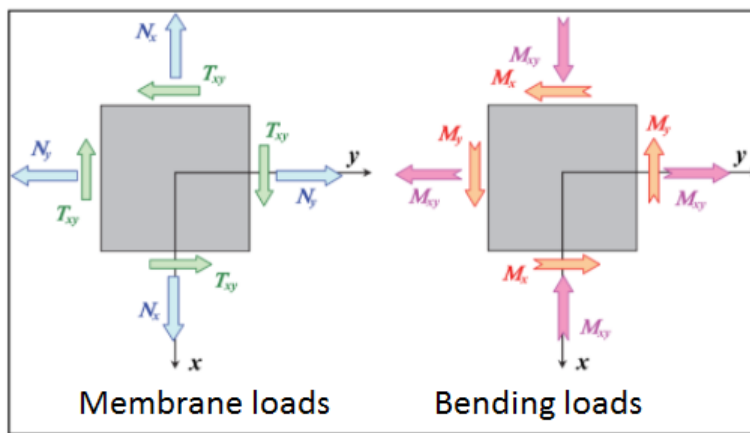
FIGURE 1.25 – Forces on the laminate under to membrane and bending loading, in the medium plane of the laminate. [28]

$$
\begin{cases}
N_x = \int_{-h/2}^{h/2} \sigma_x . dz \\[2mm]
N_y = \int_{-h/2}^{h/2} \sigma_y . dz \\[2mm]
T_{xy} = \int_{-h/2}^{h/2} \tau_{xy} . dz \\[2mm]
M_x = \int_{-h/2}^{h/2} z . \sigma_x . dz \\[2mm]
M_y = \int_{-h/2}^{h/2} z . \sigma_y . dz \\[2mm]
M_{xy} = \int_{-h/2}^{h/2} z . \tau_{xy} . dz
\end{cases}
\tag{1.11}
$$

h is the thickness of the laminate, and z the out-of-plane direction.

The stains at a point with coordinates (x,y,z) are defined in figure 1.26 as membrane strains : ϵ_x^0 , ϵ_y^0 , $\gamma_{x,y}^0$ and the bending strains k_x^0, k_y^0 and $k_{x,y}^0$.

The membrane strains are the first derivatives of the displacements (induced by the membrane loading) in x-direction , $u_0(x, y)$ and in y-direction , $v_0(x, y)$.

The bending strains which are the curvature of the laminate due to the bending loading are the second derivatives of the displacement $w_0(x, y)$ in z-direction, induced by the bending loading.

$$
\begin{bmatrix} \varepsilon_x \\ \varepsilon_y \\ \gamma_{xy} \end{bmatrix} = \begin{bmatrix} \varepsilon_x^0 \\ \varepsilon_y^0 \\ \gamma_{xy}^0 \end{bmatrix} + z \begin{bmatrix} \kappa_x^0 \\ \kappa_y^0 \\ \kappa_{xy}^0 \end{bmatrix},
$$

$$
\varepsilon_x^0 = \frac{\partial u_0}{\partial x}(x, y), \quad \varepsilon_y^0 = \frac{\partial v_0}{\partial y}(x, y), \quad \gamma_{xy}^0 = \frac{\partial u_0}{\partial y} + \frac{\partial v_0}{\partial x},
$$

$$
\kappa_x^0 = -\frac{\partial^2 w_0}{\partial x^2}(x, y), \quad \kappa_y^0 = -\frac{\partial^2 w_0}{\partial y^2}(x, y), \quad \kappa_{xy}^0 = -2\frac{\partial^2 w_0}{\partial x \partial y}(x, y).
$$

FIGURE 1.26 – Components of the strains in the medium plane for membrane and bending loading. [21]

Considering equation 1.9 linking the stress field to the strain field and, a combination of equations 1.11 and the expression of the strains, the flux forces and moments are linked to the strains by a stiffness matrix in equation 1.12. The terms of the matrix are expressed below.

$$
\begin{cases}
\begin{bmatrix} N_x \\ N_y \\ T_{xy} \\ M_x \\ M_y \\ M_{xy} \end{bmatrix} = \begin{bmatrix} A_{11} & A_{12} & A_{16} & B_{11} & B_{12} & B_{16} \\ A_{21} & A_{22} & A_{26} & B_{21} & B_{22} & B_{26} \\ A_{16} & A_{26} & A_{66} & B_{16} & B_{16} & B_{66} \\ B_{11} & B_{12} & B_{16} & D_{11} & D_{12} & D_{16} \\ B_{21} & B_{22} & B_{26} & D_{21} & D_{22} & D_{26} \\ B_{16} & B_{26} & B_{66} & D_{16} & D_{26} & D_{66} \end{bmatrix} \begin{bmatrix} \epsilon_x \\ \epsilon_y \\ \gamma_{xy} \\ k_x \\ k_y \\ k_{xy} \end{bmatrix} \\[4em]
A_{ij} = \sum_{k=1}^{n} Q_{ij}'^k \cdot (z^k - z^{k-1}), i, j = 1, 2, 6 \\[1.5em]
B_{ij} = \sum_{k=1}^{n} Q_{ij}'^k \cdot \frac{(z^k)^2 - (z^{k-1})^2}{2}, i, j = 1, 2, 6 \\[1.5em]
D_{ij} = \sum_{k=1}^{n} Q_{ij}'^k \cdot \frac{(z^k)^3 - (z^{k-1})^3}{3}, i, j = 1, 2, 6
\end{cases}
\tag{1.12}
$$

$[A_{ij}]$ is the in-plane stiffness of the laminate, $[B_{ij}]$ is the coupling stiffness between extension and bending and, $[D_{ij}]$ is the bending stiffness of the laminate.
In the case of unbalanced laminates, the terms D_{16} and D_{26} are non zero and a bending motion (k_x, k_y) creates a twisting moment M_{xy} : this is the **bend twist coupling (BTC)** effect of composite materials.

1.2.3.1 Equivalent properties of a laminate

In a simplified approach, the laminate can be studied with isotropic material laws when the equivalent properties of the laminate have been defined beforehand. In (x,y,z), three quantities are used : modulus of elasticity in the x-direction E_x, modulus of elasticity in the y-direction E_y and shear modulus G_{xy}.

$$
\begin{bmatrix} \epsilon_x \\ \epsilon_y \\ \gamma_{xy} \end{bmatrix} = h \times \begin{bmatrix} A_{11}^{-1} & A_{12}^{-1} & A_{16}^{-1} \\ A_{21}^{-1} & A_{22}^{-1} & A_{26}^{-1} \\ A_{16}^{-1} & A_{26}^{-1} & A_{66}^{-1} \end{bmatrix} \begin{bmatrix} \sigma_x \\ \sigma_y \\ \tau_{xy} \end{bmatrix}
\tag{1.13}
$$

Equation 1.13 is a reformulation of equation 1.12, considering equation 1.11, for the in plane strains. It links the strain field to the stress field with the inverse of the membrane stiffness matrix $[A^{-1}]$ and the laminate thickness h.

Considering the Hooke 's law linking the strain to the stress with the elasticity modulus, the equivalent properties of the laminate are expressed in equation 1.14.

$$\begin{cases} E_x = \frac{1}{h \times A_{11}^{-1}} \\\\ E_y = \frac{1}{h \times A_{22}^{-1}} \\\\ G_{xy} = \frac{1}{h \times A_{66}^{-1}} \end{cases} \tag{1.14}$$

The terms of the matrix [A] are expressed in 1.12. Its uses the stiffness matrix $[Q'^k]$ (defined in equation 1.10) of the ply "k" expressed in (x,y,z) coordinates.

$$\begin{cases} Q_{11}'^k = \beta.E_l.c_k^4 + \beta.E_t.s_k^4 + 2.(\beta.\nu_{lt}.E_t + 2.G_{lt}).c_k^2.s_k^2 \\ Q_{22}'^k = \beta.E_l.s_k^4 + \beta.E_t.c_k^4 + 2.(\beta.\nu_{lt}.E_t + 2.G_{lt}).c_k^2.s_k^2 \\ Q_{66}'^k = (\beta.E_l + \beta.E_t - 2.(\beta.\nu_{lt}.E_t + G_{lt})).c_k^2.s_k^2 + G_{lt}.(c_k^4 + s_k^4) \\ c_k = cos(\theta_k) \\ s_k = sin(\theta_k) \end{cases} \tag{1.15}$$

For the ply numbered k, the terms $Q_{11}'^k$, $Q_{11}'^k$, $Q_{11}'^k$ are expressed in equation 1.15 using the properties of a ply in the longitudinal and transverse reference, and its orientation θ_k. The expression of β is given in equation 1.9.

The laminate composed of N-number of ply having each their orientation, and various properties of each ply, is equivalent to a material characterized by E_x, E_y and G_{xy} expressed in equation 1.14.

1.2.3.2 Labeling of a laminate

The labeling of a composite stack is illustrated as follows :

Figure B.7 shows an example of laminate composed of a stack of five plies. The code of this example is [90/45/0/45/90], it consists of a succession of the orientations of the plies contained in the stack.

If the stack has a symmetry plane, only one half of its layup is written and the symmetry is specified by the index S at the end of the brackets. In our example, the writing becomes $[90/45/0_{0.5}]_S$, the index 0.5 on the middle ply oriented at 0° means that the symmetry plane divides that ply.

If in the stack there is a consecutive succession of the same fold, its orientation is noted once in the code and the number of occurrences is indexed.

Example : $[90_3/45_2/0]_S$ is the same notation as [90/90/90/45/45/0/45/45/90/90/90].

1.2.3.3 Manufacturing process of composite materials

Depending on the manufacturing process, it is possible to manufacture complex geometric parts at one time, for example by layer-by-layer or by Liquid Composite Molding (LCM) using molds or counter molds. The number of parts used and the complexity of assembly is therefore reduced, thus reducing the mass of the structure.
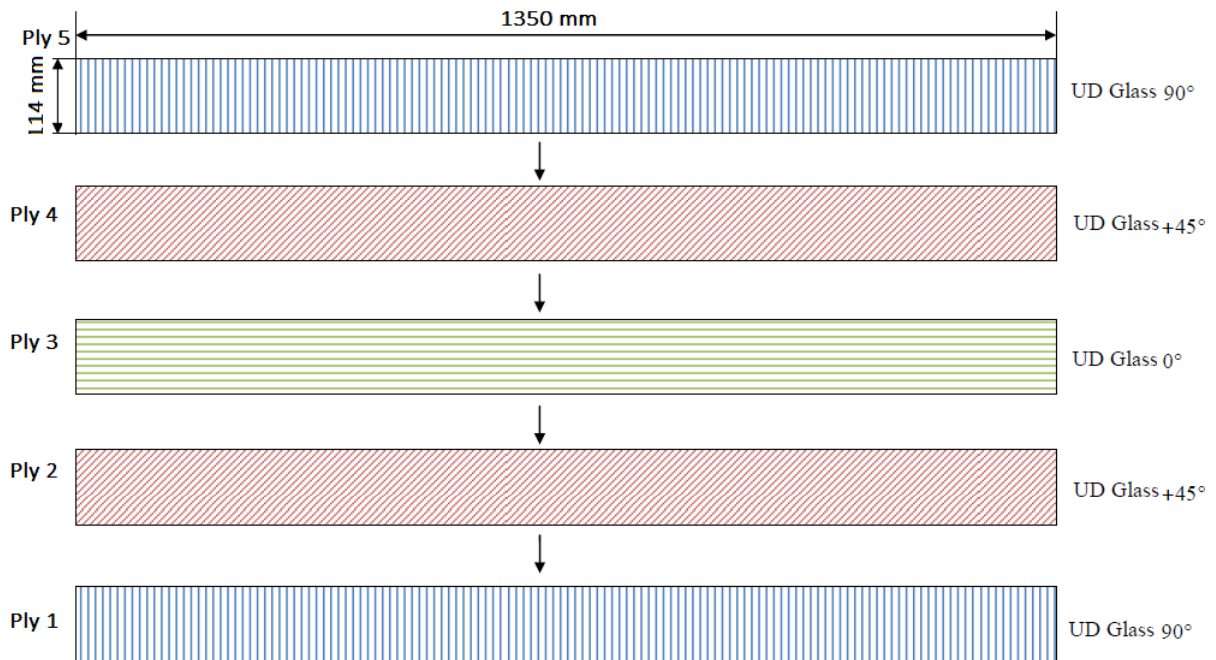
FIGURE 1.27 – Example of a stacking of plies [90/45/0/45/90].

This section is inspired from [34].

There are three types of composite manufacturing processes : open molding, closed molding and cast polymer molding. Cast polymers materials are unique in the composites industry : they typically don't have fiber reinforcement and are designed to meet specific strength requirements of an application. There different processing methods of the open molding and close molding are presented below.

— **Open molding** : Resins and fiber reinforcements are exposed to air as they cure or harden. This molding utilizes different processes (figure 1.29).

Hand lay-up is the most common and least expensive open-molding method because it requires the least amount of equipment. Fiber reinforcements are placed by hand in a mold and resin is applied with a brush or roller.

Spray-up is similar to hand lay-up but uses special equipment—most notably a chopper gun—to cut reinforcement material into short fibers, add them to resin and deposit the mixture (called chop) on to a molding surface. Spray-up is more automated than hand lay-up and is typically used to produce large quantities.

Filament winding is an automated process that applies resin-saturated, continuous strands of fiber reinforcements over a rotating cylindrical mold.

FIGURE 1.28 – Open molding processes

— **Closed molding** : Fibers and resin cure inside a two-sided mold or within a vacuum

bag (shut off from air). Closed-molding processes are usually automated and require special equipment.

Vacuum bag molding improves the mechanical properties of open-mold laminates. This process can produce laminates with a uniform degree of consolidation, while at the same time removing entrapped air, thus reducing the finished void content.

Vacuum infusion processing is a variation of vacuum bagging in which the resin is introduced into the mold after the vacuum has pulled the bag down and compacted the laminate.

Resin transfer molding (RTM) is an intermediate volume molding process for producing composites. In RTM, resin is injected under pressure into a mold cavity. This process produces parts with two finished surfaces.

Other processes exist in this category such as, Compression Molding, Pultrusion and Reinforced Reaction Injection Molding.
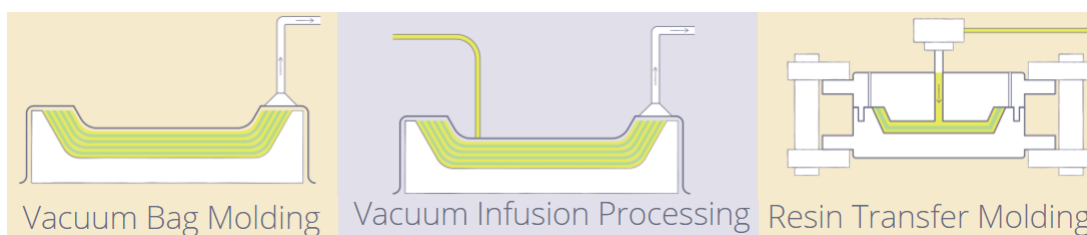
FIGURE 1.29 – Closed molding processes

Composite materials have a very good performance/mass ratio and very good fatigue resistance but, the design of lightweight hydrofoils lead to structures with enough stiffness to resister the hydrodynamic loading but not stiffer enough to exhibit a rigid behavior in a heavy fluid such as water. Therefore, the hydrofoils are deformables and they experience fluid-structure interactions in water.

1.3 Exploring the Fluid-Structure Interaction (FSI)

This section presents an introduction to fluid structure interactions with some applications. The second part describes the influence of bend-twist coupling on FSI on lifting surfaces in composite materials.

1.3.1 Description of the Fluid Structure Interaction

Fluid-structure interaction is an exchange of energy between a fluid domain and a solid domain : the movement of one will influence the behavior of the other and the action can be reciprocal depending on the interaction type.

This phenomenon can be observed in several applications such as the aero-elastic flutter ([41], [23]) in aeronautics : a coupling is created between a fluid instability and the proper modes of the structure which generate self-sustained oscillations. The fluid gives energy to the structure and amplifies the oscillations that grow and may lead to the structure destruction. A well-known incident is the destruction of the Tacoma Bridge in 1940 ([4], [82]). Fluid-structure interactions are also found in human health applications such as Arterial Blood Flow ([75]) and heart valves ([17]).

FSI phenomena can be classified according to two criteria, based on the nature of the fluid flow or based on the strength of the coupling involved.

The criterion based on the nature of the fluid [48], regroups the interactions into two categories :

— Static phenomena : the motion of the fluid is negligible compared to the motion of the structure, the deformation of the structure results from hydro-static forces. These phenomena are very important and can cause damage or even destruction of the structure. Example : the deformation of a dam under the static pressure of water at rest.

— Dynamic phenomena : The motion of the fluid is predominant and the phenomena evolve in time :

— Self-maintained phenomena : After a disturbance, the fluid system gives energy to the structure and the structure moves and remains in motion. An example of this type is aero-elastic flutter.

— Forced phenomena : these phenomena are generally found in systems subject to turbulence. An example is the case of aircraft whose control surfaces are subject to forced oscillations.

The criterion based on the strength of the coupling defines two types :

— Weak coupling : when the effects of one medium are dominant over the other. This is the case of a rigid hydrofoil subjected to a flow, the deformation of the structure due to hydrodynamic forces is very low and the modification it creates in the flow field is therefore low.

— A strong coupling : In this coupling, each domain significantly impacts the other. In the case of a flexible hydrofoil subjected to flow, the structure will deform under the effect of hydrodynamic forces and modify the flow field and vice versa until equilibrium is reached. The fluid strongly influences the response of the structure and vice versa.
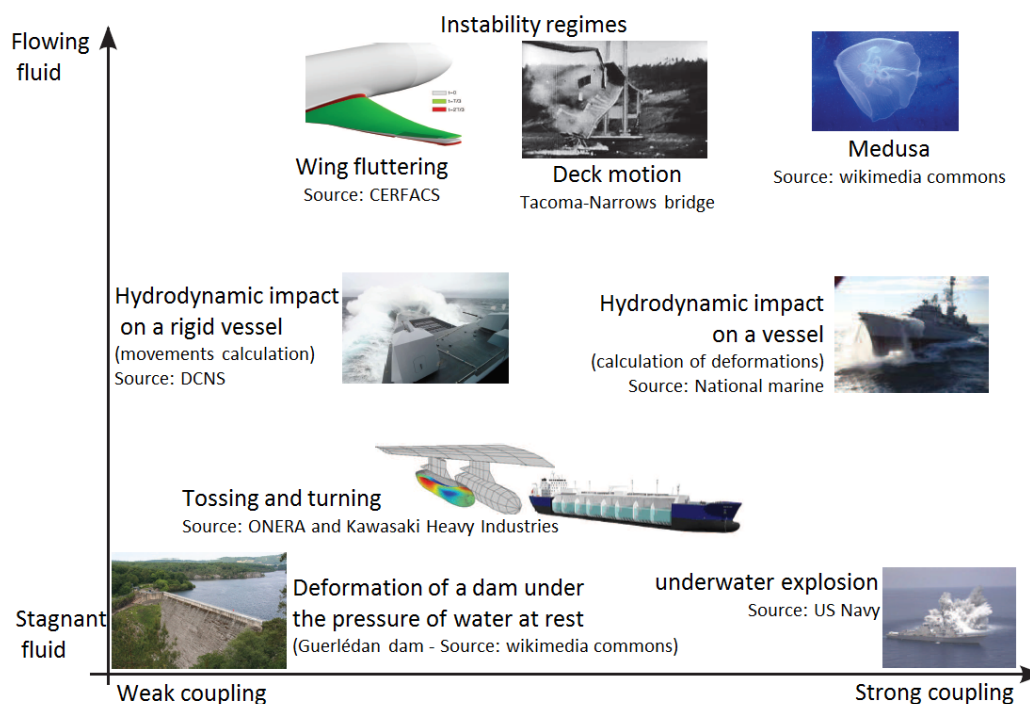
FIGURE 1.30 – Example of fluid-structure interaction problems depending on the nature of the flow and the force of the interaction. (Inspired from [55])

Figure 1.30 show some FSI problems classified with the type of fluid and the type of coupling. For example, the motion of Tacoma bridge was a dynamic interaction (moving fluid), the coupling was strong and led to the destruction of the structure. the deformation of a dam under the pressure of the fluid at rest is a static and weak interaction.

For hydrofoil application, coupled studies of FSI (instead of solving each problem separately) is most likely dedicated to flexible structure in dynamic coupling (moving flow). The lightweight structures strongly interact with the dense fluid, the water, in a strong and dynamic coupling.

Ducoin [46] investigated numerically and experimentally the behavior of a flexible hydrofoil in a flow. They observed that for low incidence and low velocity configurations, the effect of FSI was negligible on the structural response of the hydrofoil and its hydrodynamic performances. Therefore a non-coupled analysis was enough to solve the problem. Moreover, for higher incidences and high flow speed, the interactions are strong and a coupled approach is needed to analyse the behavior of the hydrofoil.

Gaugain [55] studied numerically and experimentally a flexible NACA66-312 (mod.) hydrofoil in polyacetate with a partitioned coupling. The displacement was predicted with good accuracy. An investigation of the behavior of the foil in a cavitating flow shows that the oscillations created by the cavitation phenomena may interact with the proper modes of the structures. Moreover, they found out the same conclusions as [46].

The flexibility of the structure is a very important parameter in the fluid structure interactions. Pernod and al. [103] investigate numerically and experimentally the fluid-structure interaction on a flexible composite hydrofoil under viscous flows and show a very strong hydro-elastic response, with a structural resonance due to the high flexibility of the structure. The case of composite materials add more complexity to the problem due to the anisotropic behavior of the composite which add internal couplings in the structure such as **bend-twist coupling**.

1.3.2   Impact of Bend Twist Coupling (BTC) in FSI

Bend-twist coupling (BTC) in a structure creates a coupling between bending motion and the twisting motion. This structural coupling can arise from the geometry of the structure (a curved geometry which induces additional torsion when the structure is loaded) or from the anisotropic properties of the composite material by changing the fibers orientations. Figure 1.31 shows the BTC mechanism in a composite beam.
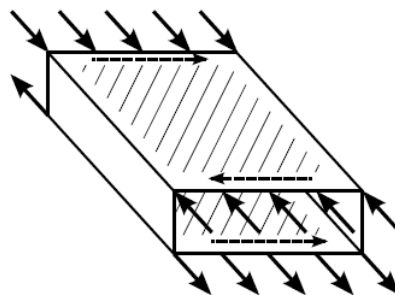
FIGURE 1.31 – BTC mechanism in a composite beam. [51]

With tailored fibers orientations, a bending moment applied to the beam creates compression on the top of the beam and tension on the bottom. It's followed by shear deformation on both top and bottom which lead to a twist of the beam.

In the literature, BTC of beams is mainly considered in the aeronautical and wind energy domains. Kayran and al. [97], investigated the effect of this coupling on natural frequencies and mode shape to improve the design and the control of composite structures. Panda and Chopra [99] investigated the aeroelastic stability of coupled helicopter composite blades using an eigenvalue approach and highlighted the great potential of bending-twisting coupling for rotor stability and vibration level.

Bend twist coupling is used in fluid structure interaction to strongly influence the structural response of the lifting bodies. The aerodynamic forces induce bending in the structure and the BTC creates a twist which modifies the angle of attack and thereby the aerodynamic forces. This loop enables the structure to self-alleviate sudden inflow changes when twisting towards a lower angle of attack, leading to a reduction in ultimate and fatigue loads. It is possible to improve the performances of a structure and its lifetime by designing a structure which deformed in a desired manner when loaded.

The introduction of bend–twist coupling in wind turbine applications firstly investigated twisting towards a larger angle of attack to reduce lift by stalling the aerofoil blade :**twist towards stall** (see figure 1.32a). The development of pitch-regulated turbines introduces investigations on the twisting towards a smaller angle of attack to reduce the lift force :**twist towards feather** (see figure 1.32b).

(a) Twist towards stall. (b) Twist towards feather.
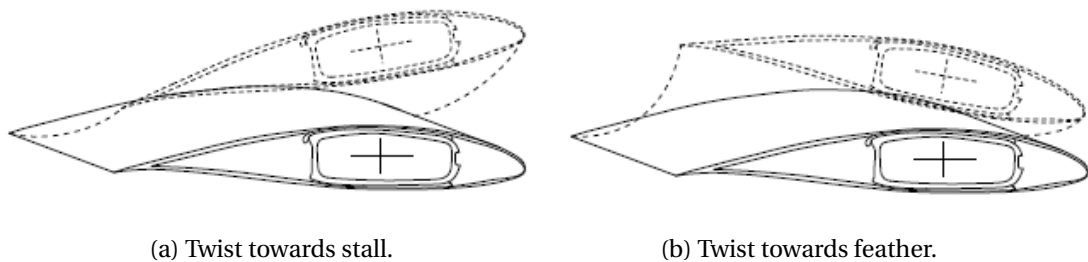
FIGURE 1.32 – Aeroelastic response of a bend twist coupled wind turbine blade to bending load. [50]

BTC is a good approach to control the lifting force through FSI with a passive adaptive method, the target is to reduce the loads by reducing the incidence at the tip. The regulation of the angle of incidence can thus be performed with the coupling twist towards feather, [112].

[69] tested various orientations in the laminate layup of the blade to study the effect of BTC on wind turbine efficiency and came out with an increase of 10% in the wind turbine efficiency without changing the velocity nor the angle of attack.
[89], [26], [88], [123] perform several studies on load alleviation of wind turbine blade with BTC. Fatigue load reduction on wind turbines in a range of 10-20% were highlighted with twist to feather coupling.

The coupling being influenced by the material properties and the section geometry, it is important to have an accurate composite theory able to calculate the equivalent stiffness matrix considering the BTC and the deformations for an arbitrary cross section.
[116], [114] developed a high-order composite beam theory which does not consider the homogenization of the composite material's properties. An out of plane wrarping func-

tion is introduced in the displacement field and a 2D finite element method is used to determine the unknown coefficients needed to solve the problem. The theory gives good results but is limited to straight beams with no twist and the warping calculation is not accurate.

[32] proposed a Variational Asymptotic Beam Sectional (VABS) analysis which uses the variational asymptotic method [125] to split a three-dimensional nonlinear elasticity problem into a two dimensional linear cross-sectional analysis and a one-dimensional, nonlinear beam problem. VABS computes the constants of the one-dimensional cross-sectional stiffness, with transverse shear for initially twisted and curved beams with arbitrary geometry and material properties. [127]presents a validation of VABS and, a comparison with one dimension and three dimension analysis performed on the commercial tool ABAQUS show excellent results. [134] present the last updates of the VABS method.

Lobitz and Veers [121] introduced a coupling coefficient g in the stiffness matrix to consider BTC. Equation 3.39 shows a simplified relation between the torsion and bending moments M_t, M_b to the bending and torsion response of a cross section k_b, k_t. EI is the bending stiffness, GJ is the torsion stiffness.

$$\begin{bmatrix} M_b \\ M_t \end{bmatrix} = \begin{bmatrix} EI & -g \\ -g & GJ \end{bmatrix} \begin{bmatrix} k_b \\ k_t \end{bmatrix} \tag{1.16}$$

The normalized bend twist coupling coefficient α is defined by 3.40.

$$\alpha = \frac{g}{\sqrt{EIGJ}} \qquad -1 < \alpha < 1 \tag{1.17}$$

Hartvig and al. [113] perfomed a modal analysis and studied the stability of BTC in wind turbine blades. From the coupling method of Lobitz and Veers [121], they implemented the coupling in the aero-servo-elastic analysis tool HAWCStab2 by modifying the coupling terms D_{16} and D_{26} in the cross-section stiffness matrix. A validation against test cases in the literature shows good results.

Regarding hydrofoil application,[58] has recently described the use of different techniques for bending-twist coupling as Passive Adaptive Composites (PAC) that tailors the response of a structure by changing the orientation of the composite plies [121] and Differential Stiffness Bend-Twist (DSBT) that utilizes the internal stiffness of a structure to change the aero-hydrodynamic response to fluid load [105]. They have shown that the PAC can be used to control the lift response to hydrodynamic load in the case of a composite structure [60] including by decreasing the tip load. Young and al. [132] also studied the effect of bend-twist coupling on the hydro-elastic response of a composite hydrofoil in a cavitation tunnel with different plies orientations.

1.4 Coupling methods for FSI analysis

This section presents an overview of some methods developed to analyse FSI. Three types of coupling available in the literature are presented and some implemented coupling algorithms are also presented.

Several numerical coupling methods have been developed to predict the behaviour of structures experiencing FSI ([133], [42], [48], [102], [33], [15]).

In a general approach, the structural solution is solved with a classical formulation in Finite Element Method (FEM). The problem of coupling the fluid to the structure consists in looking for a solution to the fluid problem. Once this solution is found, it is necessary to couple it with the finite element formulation to solve the interaction problem.

Young and al. [44] carried out simulations with a model combining Boundary Element Method (BEM) (for fluid analysis) and FEM methods (for structural analysis), to analyse the behaviour of turbines in variable flow with FSI, applicable in both air and water. The comparison of these results with experimental data is satisfactory for structures of many scales.

[58] coupled the Finite Element Analysis (FEA) structural code Abaqus 6.14 to the Computational Fluid Dynamics (CFD) code Star-CCM+ to numerically analyse FSI on hydrofoil experiencing BTC. An experimental investigation in a wind tunnel was performed and numerical-experimental comparison proved good fidelity in the prediction of the developed tool.

1.4.1 Coupling methods

This part focuses on three coupling approaches to assess strong or weak interactions.

1.4.1.1 Partitioned approach

The partitioned coupling separates the FSI problem into a fluid part and a structural part, each of them being solved by a dedicated code. Figure 1.33 shows the communication of the different domains interacting in the partitioned coupling. The two codes communicate with each other to exchange information quantities : the pressure on the structure is calculated by a CFD tool and used as input in a CSD (Computational Solid Dynamics) tool which computes the displacement of the fluid-structure interface. The numerical tracking of moving boundaries is captured with a CMD (Computational Meshing Dynamic) solver ; the three problems are solved separately (fluid, solid, mesh).
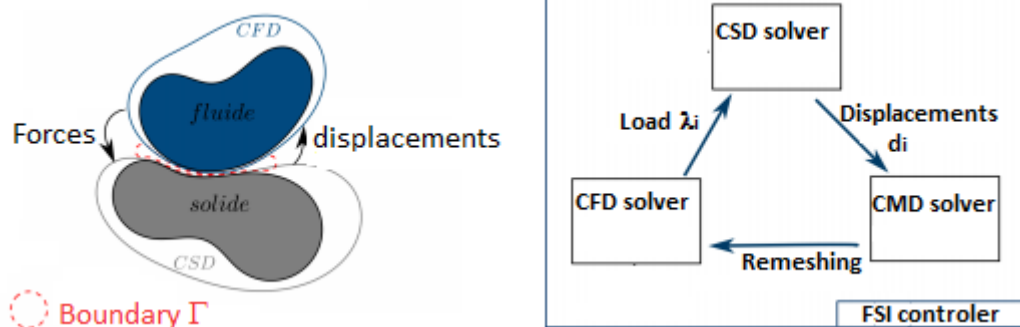
FIGURE 1.33 – Partitioned coupling [135].

The boundary conditions for one system are given by the state of the other system. Therefore, there is a time lag between the boundary conditions and the system which de-

creases the accuracy of the solution.

In order to refine the accuracy of the calculation, internal iterative loops at each time step allow the exchanged quantities to converge between the fluid and structure solvers.

The use of two codes allows the most appropriate resolution methods to be used to fluid and structural problems as well as to exploit existing tools dedicated for each domain. The difficulty of these methods are based on the quality of the coupling between the solvers and on the good convergence of all solvers.

Partitioned coupling eliminates the difficulties of a direct coupling, and reduces the modelling complexities for each domain. [124] proposed a new algorithm technique to use a partitioned solver for very strongly coupled FSI problems.

1.4.1.2 Quasi-direct Coupling

Figure 1.34 presents the flow chart of a quasi-direct coupling. The algorithm solves the fluid and the structural problems in a direct coupled approach and an iterative procedure is implemented to couple with the mesh problem and fully solve the complete FSI.

For each time step, we solve the coupled fluid-solid system, update the mesh displacements, and iterate on these two solvers until convergence is reached. This method is implemented with space–time algorithms [117].
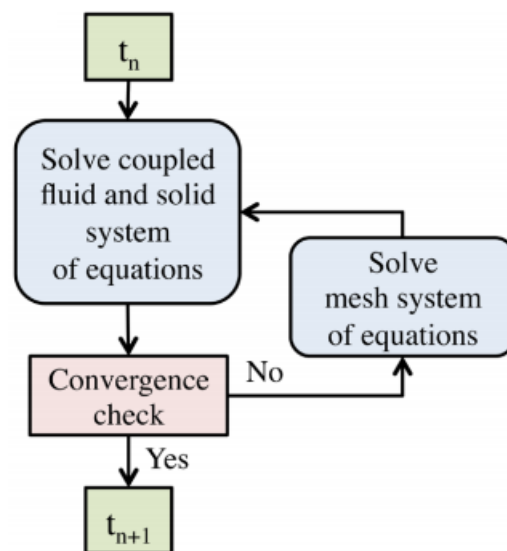
FIGURE 1.34 – Flowchart demonstrating a quasi-direct method. [78]

The quasi-direct and direct coupling techniques give more robust algorithms than the partitioned coupling. The results are more accurate but the implementation is more complex and the CPU time calculation is reduced with the fluid-solid problem solved at the same time.

1.4.1.3 Monolithic approach

Monolithic approaches ([65], [24]) consist in solving the problems in a single block, the fluid, the structural part and the mesh are solved simultaneously in time. The challenge for monolithic methods lies in the correct mathematical formulation of the system. Figure 1.35 shows the flow chart of a monolithic approach.

The problem is solve with two solution types : the monolithic formulation of the monolithic resolution.
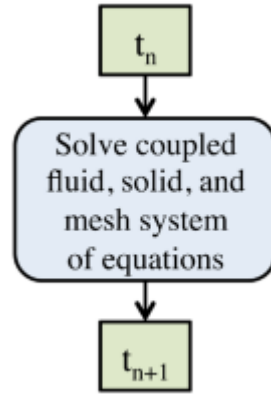
FIGURE 1.35 – Flowchart demonstrating a monolithic method.[78]

The monolithic formulation combines and solves the fluid, solid and mesh problems into a single system. The solution is very close to the physical problem to be solved but is also the most difficult to formulate and solve.

The methods generally used are based on fictitious domains or the method of penalties and immersed boundary methods [95].

Both solutions are particularly well suited to very strongly coupled cases. However, their implementation is complex and to date has not been implemented or validated in a robust and available code : these methods remain in the field of research. Approaches, known as mesh-less approaches, of the SPH type are also used for the resolution of fluid-structure interaction [94].

In the present work, the solutions implemented for FSI analysis are based on partitioned approach.

1.4.2 Coupling algorithms

In order to achieve a partitioned coupling, it is necessary to have, in addition to the fluid solver and the structural solver, coupling algorithms between these two codes. These algorithms must allow the synchronization of solvers and the exchange of data. We are interested in time coupling algorithms that can lead to two types of couplings : weak coupling (**explicit algorithm**) or strong coupling (**implicit algorithm**).

These algorithms are used with a displacement predictor to reduce the error generated when exchanging information between the fluid part and the structure part.

1.4.2.1 Explicit algorithm with predictor

Figure 1.36 shows the flow chart of a synchronised explicit algorithm using a displacement predictor. The algorithm is synchronized because the fluid and the structure are solved at the same time step, between t(n) and t(n+1) as shown on the figure.

At time $t(n+1)$, the calculation starts with the prediction of the interface displacement d_{n+1}^{P} :

$$d_{n+1}^{\mathrm{P}} = d_n + \alpha_0.\Delta t.\dot{d}_n + \alpha_1.\Delta t.(\dot{d}_n - \dot{d}_{n-1}) \tag{1.18}$$

Δt is the time interval, d_i is the displacement at time t(i) and $\dot{d}_i$ is the local velocity of the structure at time t(i) calculated by [135] :
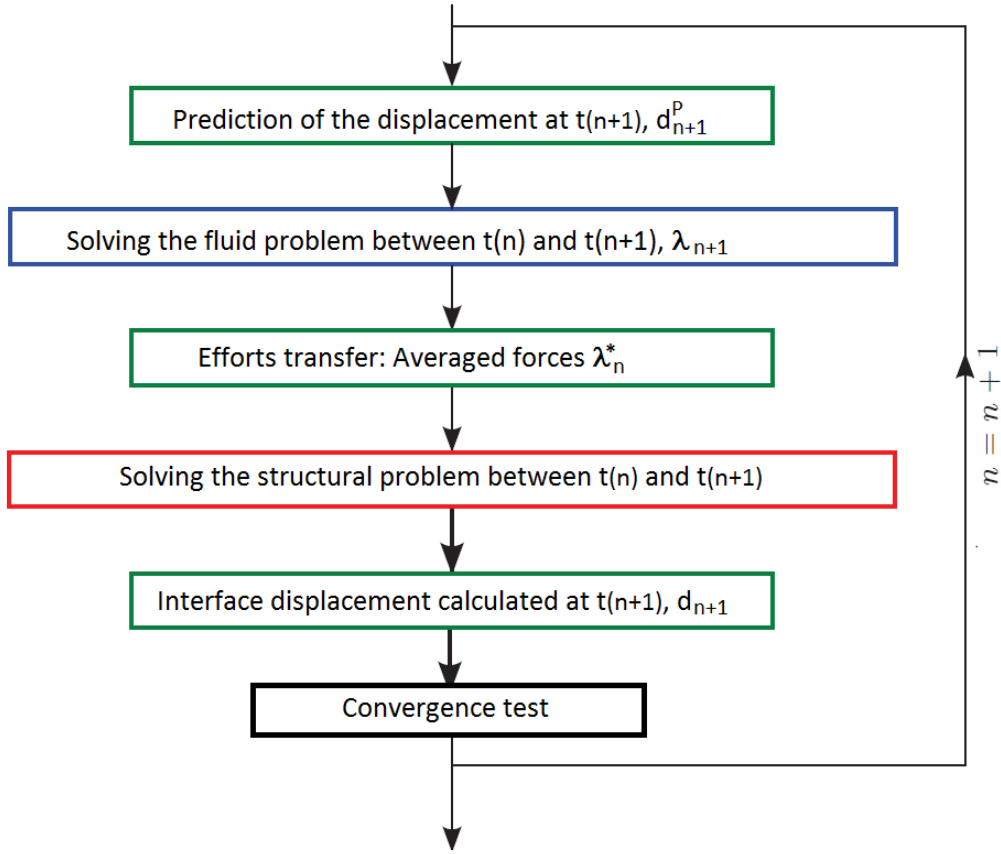
FIGURE 1.36 – Explicit algorithm with predictor.

$$\dot{d}_i = \frac{d_i - d_{i-1}}{\Delta t} \tag{1.19}$$

The initial conditions are set to : $d_0 = 0$, $\dot{d}_0 = 0$.
α_0 and α_1 are coefficients that vary the order of the algorithm :

— **Zero-order prediction** : $\alpha_0 = 0$ and $\alpha_1 = 0 \rightarrow d_{n+1}^P = d_n$
— **First-order prediction** : $\alpha_0 = 1$ and $\alpha_1 = 0 \rightarrow d_{n+1}^P = d_n + \Delta t.\dot{d}_n$
— **Second-order prediction** : $\alpha_0 = 1$ and $\alpha_1 = 0.5 \rightarrow d_{n+1}^P = d_n + \frac{1}{2}\Delta t.(3\dot{d}_n - \dot{d}_{n-1})$

[111] presents the variation of the accuracy and stability of the models with α_0 and α_1.

The fluid solver of the system uses the predicted displacement and computes the force λ_{n+1}. Before transferring the force to the structural code, an average of the fluid forces λ_n^* [135], between t(n) and t(n+1) is computed. This helps to reduce the dissipation of energy at the interface due to an existing difference between the predicted displacement d_{n+1}^P and the real displacement d_{n+1}.

$$\lambda_n^* = \frac{\lambda_n + \lambda_{n+1}}{2} \tag{1.20}$$

Benaouicha [19] presents a panel of method to compute λ_n^*.
There are explicit algorithms for which fluid and structural iterations are calculated at different time steps, the prediction of displacement is then made for an intermediate time with a method similar to the previous one. These are called asynchronous algorithms with predictor.

1.4.2.2 Implicit algorithm with predictor

The implicit algorithm allows to correct the explicitness of the previous algorithm which is accompanied by a loss of energy due to the difference between the predicted displacement given as input to the CFD code and the displacement actually calculated by the CSD software. The figure 1.37 shows the flowchart of an implicit algorithm with predictor.
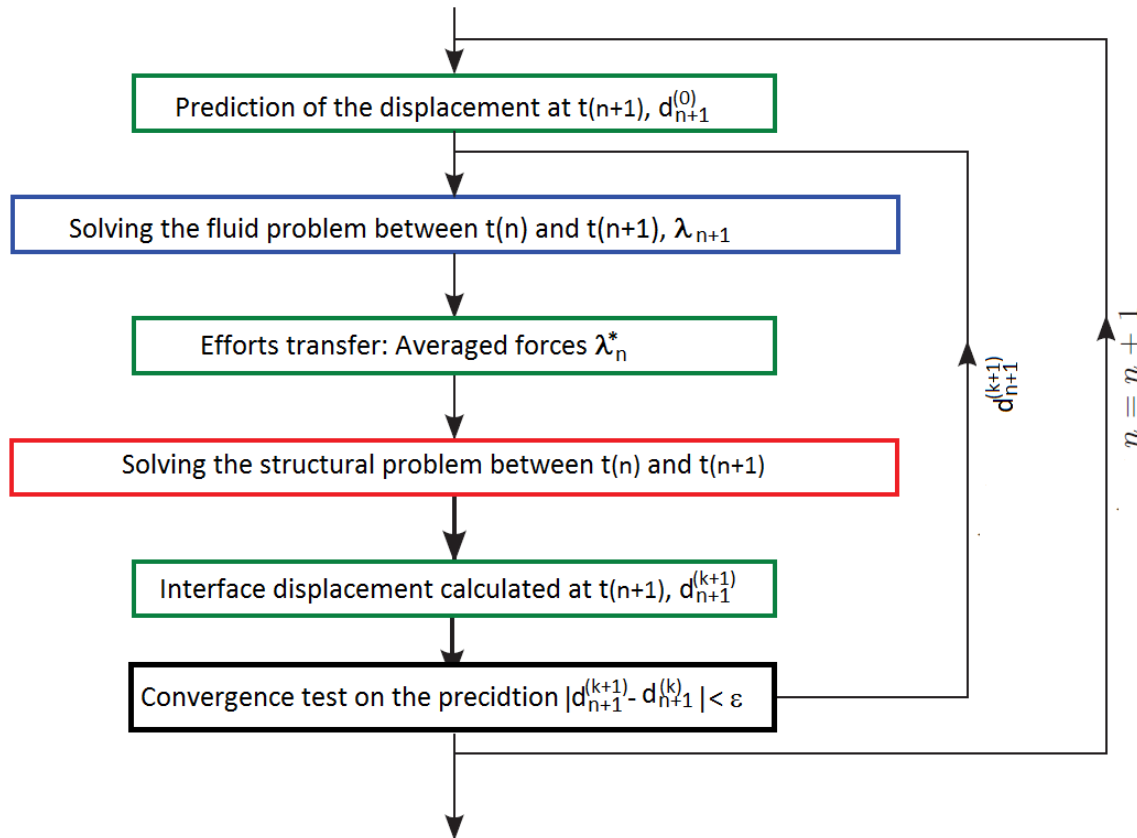
FIGURE 1.37 – Implicit algorithm with predictor.

To overcome this problem of energy loss, at each calculation between the time step t(n) and t(n+1), the implicit algorithm adds an iterative loop on k to verify the convergence between the displacement $d_{n+1}^{(k)}$ given as the input of the CFD solver and the displacement $d_{n+1}^{(k+1)}$ at the output of the CSD solver.

The initiation of the displacements $d_{n+1}^{(0)}$ at the beginning of the internal loop, is done using the predictor defined above.

Errors due to the prediction are strongly reduced but calculation time increases even more as the convergence criterion ϵ is get smaller. This solver could be more precise than explicit schemes.

To accelerate the convergence of this method, relaxation methods can be introduced on the displacements ([83], [120]).

1.5   Summary of the chapter

This chapter starts by presenting the two main categories of hydrofoils : the submerged or active control hydrofoils and the hydrofoils piercing the free surface. They have two major advantages : the lift force that pulls the hull of the boat out and reduce the drag

force and, the righting moment that ensures a good balance of the boat and more power on the foiling yacht.

The main fluid phenomena to consider when designing hydrofoils are the free surface effect, the cavitation and the ventilation.

The second part of the chapter presents the composite materials, their basic properties and their behavior when subjected to bending loading or in-plane loading. A mixing law is proposed to homogenize the properties of a ply (based on the properties of the fibers and the resin) and the laminate theory is used to calculate the equivalent properties of a stack of plies.

The coupling terms in the stiffness matrix D_{16} and D_{26} are identified as responsible of the BTC phenomenon and methods in the literature propose a calculation of these terms to predict the BTC.

In the third section, fluid-structure interactions are discussed. The flexibility of the structures is highlighted as an important parameter in the phenomena and the anisotropy of the composite material appears to strongly impact FSI through the bend-twist coupling of passive adaptive structures (PAC).

The last part is dedicated to the coupling methods to analyze FSI. The monolithic and the partitioned approaches are presented and the monolithic approach seems to be the more accurate but that method is still in the field of research due to the complexity of its implementation.

The implicit and the explicit algorithms to implement a partitioned coupling were also presented.

In this work, the numeric development will derived from partitioned method with explicit algorithms.

The next chapter presents the hydrofoils studied in this research work and the experimental tests performed are described : the hydrofoils geometry, the materials, their manufacturing, the experimental setup are presented and, the post-processing methods are described.

CHAPTER 2

Hydrofoils description and experimental methods

Contents

This chapter presents on the one hand the different foils used in this study to analyze the fluid-structure interactions and on the other hand it describes the experimental setup and the different tests performed.

In this study we chose to progressively increase the complexity based on 3 criteria :

— Geometry : the study begins with the analysis of hydrofoil scale-models then, with reals cale hydrofoils.

— Material behavior : the analysis focuses first on isotropic materials and then on composite materials.

— Type of fluid phenomena involved : to get rid of ventilation or free surface effects, the first hydrodynamic experiments are carried out on submerged hydrofoils and the second campaign, investigated hydrofoils piercing the free surface.

   Thus, the study starts with investigations on three model-scale hydrofoils made of isotropic materials that undergo FSI in a fully submerged configuration. One of the structures is an existing model-scale hydrofoil used in previous research works and the two others are manufactured, inspired from the hydrofoil of the MINI 747 shown in figure 2.1. The purpose of this investigation is to conduct experiments on structures whose behaviour would be representative of the MINI747 hydrofoil.
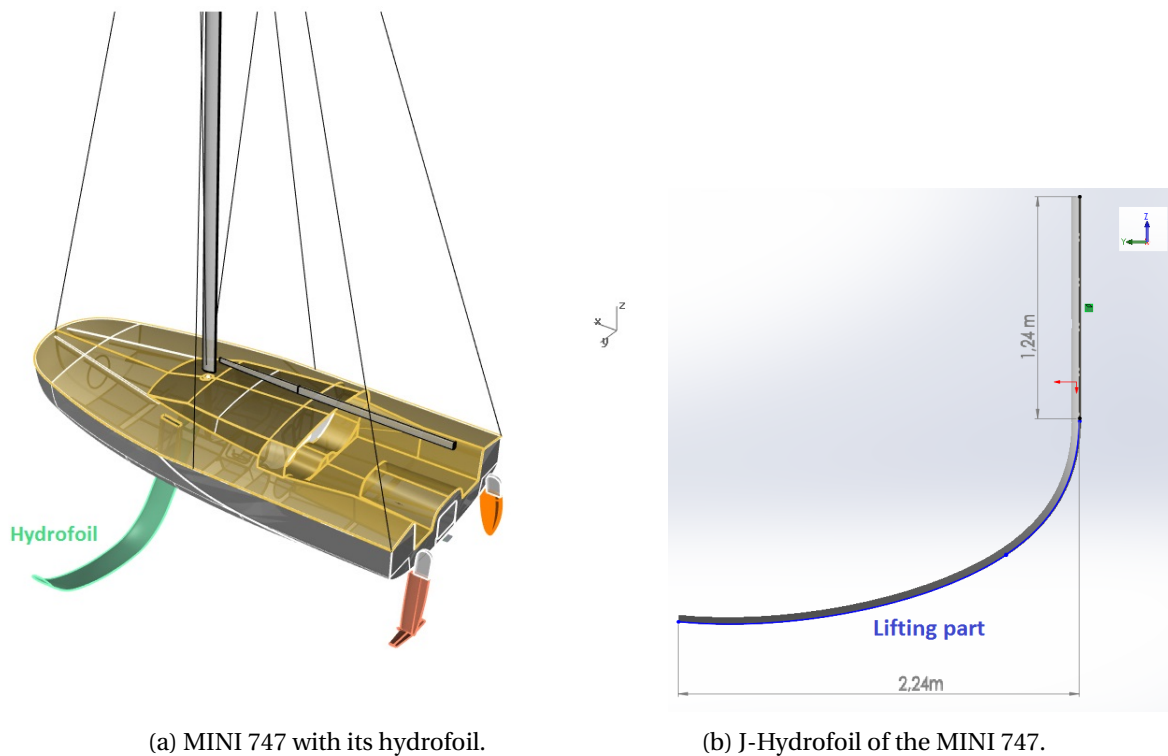
(a) MINI 747 with its hydrofoil.   (b) J-Hydrofoil of the MINI 747.

FIGURE 2.1 – Hydrofoil of the scow bow MINI 747 of SEAIR.

   The hydrofoil of the SEAIR 's Scow bow MINI 747 is a J-foil of around 4m in unfolded length. To simplify the geometry of the model-scale hydrofoils, they are derived of the lifting part of the hydrofoil as shown in figure 2.2.

The lifting part of the hydrofoil is a curved geometry of 2.24m projected span. The section is constant along the hydrofoil and the profile is presented in figure 2.2c. It is an asymmetric profile of $4200mm$ chord and $50mm$ thick.

In the second part of the study, real scale hydrofoils, made of composite materials and piercing the free surface are investigated.

(a) Lifting part of the foil-working configuration.

(b) Lifting part of the foil- side view.

(c) Section of the hydrofoil.
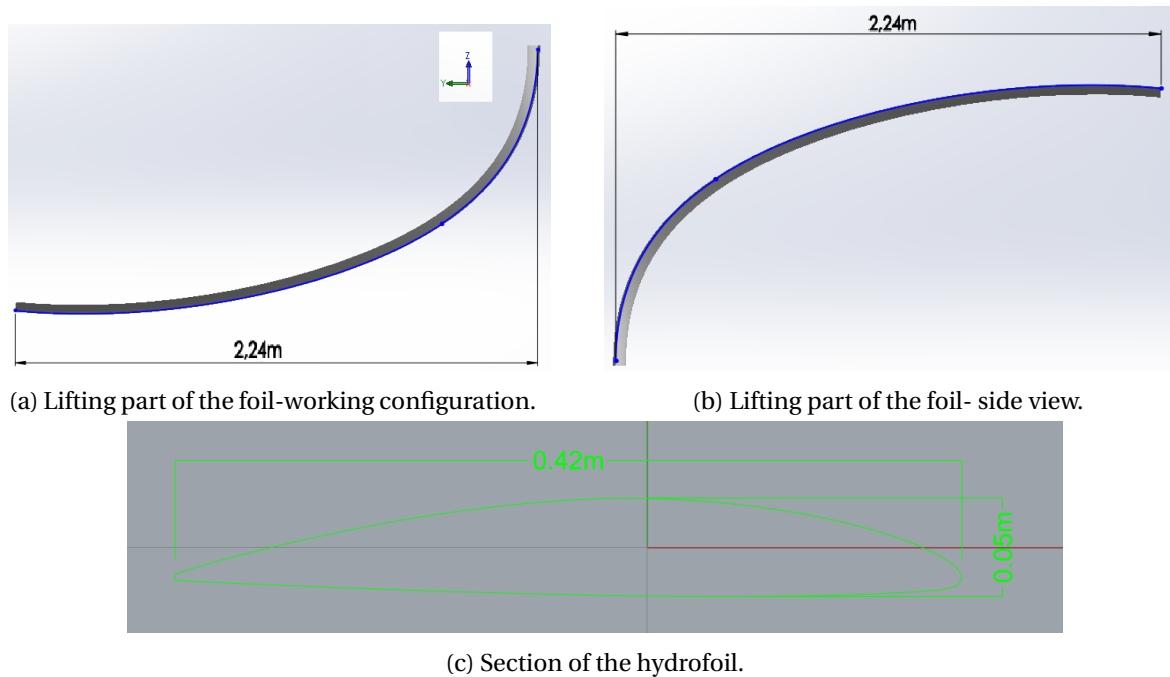
FIGURE 2.2 – Lifting part of the hydrofoil- MINI 747 of SEAIR.

The first part of this chapter describes the model-scale hydrofoils, the static experiments to characterize their mechanical properties and the hydrodynamic tunnel of IRENAV used to perform the hydrodynamic tests.

The second part of this chapter describes the real-scale composite hydrofoils, the different mechanical characterization tests and the test flume of IFREMER used to perform the hydrodynamic tests, are presented.

The last part of this chapter presents the methods for post-processing the measurements.

2.1 Model scale hydrofoils and experimental setups

Two main types of experiments are performed : the first are static tests to assess the mechanical properties of the hydrofoils and the second are hydrodynamic tests which investigate FSI on the structures. Three different hydrofoils are investigated : the first two are manufactured by 3D printing with Kevlar and carbon fibers and the third one is made up of a polymer, the PolyOxyMethylene (POM).

This part starts with the description of the hydrofoils, followed by the mechanical characterization and the description of the hydrodynamic tunnel. The different configurations tested are presented and the last section shows the experimental results.

Looking at these results, the 3D printed kevlar and carbon hydrofoils have not been very suitable for the FSI investigations and are presented for a sake of clarity. Only the POM hydrofoil will be used for the FSI analysis and the numerical validation of the tools.

2.1.1 Hydrofoils description

2.1.1.1 Kevlar hydrofoil

This hydrofoil is the first model-scale investigated in this study. Its geometry is inspired from the MINI 747 and it is manufactured in a 3D printing process at the platform

COMPOSITIC in Lorient. A scale of 1/12 is chosen to have a geometry close to the dimensions of the section of the hydrodynamic tunnel of IRENAV (192mm).

The manufactured geometry is presented in figure 2.3, the kevlar hydrofoil is 187mm projected span, 35mm chord and 4.16mm maximum thickness. From the root to the tip, the sections of the hydrofoil have a lateral offset as shown in figure 2.3c and the offset at the tip is 13.8mm. The figure shows the foil and an embedding base added to the geometry to fix the structure in the boundary condition cantilever for experiments (figure 2.3a). The working configuration of the hydrofoil on the boat is shown in figure 2.3b.

(a) 3D printed kevlar hydrofoil.

(b) working configuration.

(c) dimensions of the section and offset at the tip.
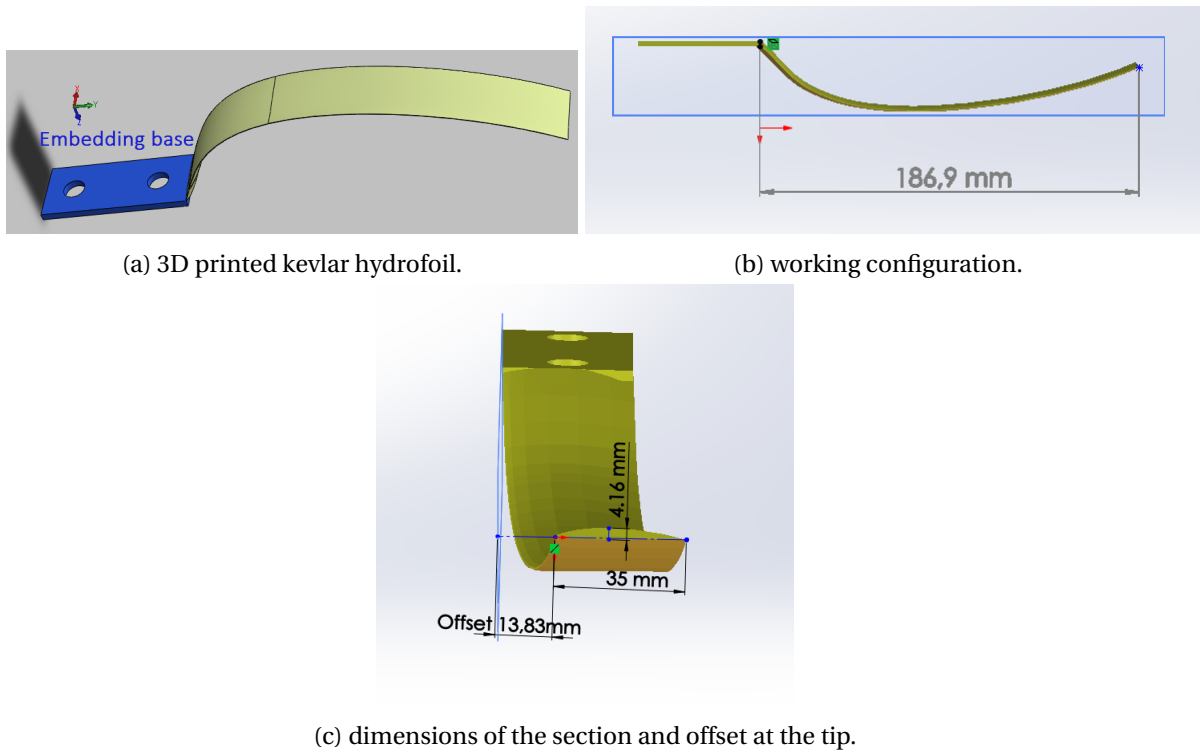
FIGURE 2.3 – Model-scale kevlar hydrofoil.

Kevlar (Aramid) fibers colored in yellow are chosen for the material to have a flexible structure able to experience FSI and light enough to enhance its visibility in the hydrodynamic tunnel which has a black back wall.

The material is made up of reinforced aramid fibers ABS (Acrylonitrile Butadiene Styrene) used in 3D printers. It is a thermoplastic polymer composite material, compose of ABS and aramid fibers. Its theoretical properties are given in table 2.1 but since mechanical properties of 3D printed structure is sensitive to the process, structural tests are performed on the hydrofoil to asses its real properties.

Density [g/cm^3]	1.08
Elastic Young modulus E [MPa]	2400
Elongation at break [%]	7.5

TABLE 2.1 – Mechanical properties of reinforced aramid fibers ABS for 3D printers. (Appendix A)

2.1.1.2 Carbon hydrofoil

The carbon hydrofoil is the following generation of the kevlar foil in order to have a stiffer structure. The possibilities of having a stiffer foil are :

— Keeping the same geometry parameters and use a stiffer material

— Modify the geometry by increasing its section inertia (chord, thickness)

A trial of the first option using the reinforced carbon fibers ABS (properties described in table 2.2) shows some limitations of the 3D printing process with carbon fibers : the thickness of the hydrofoil section are not consistent with the minimum dimensions required (>3mm) to have a good surface roughness with this process, when using carbon fiber.
The second option is performed and the manufacturing process of the section starts from the section shape of the kevlar and makes a filament winding around its geometry to have a chord of 40 mm and a thickness of 5.6 mm.
The global shape of the hydrofoil is also modify to obtain an "L" shape, curved at the root and straight to the tip as shown in figure 2.4.

Density [g/cm^3]	1.08
Elastic Young modulus E [MPa]	2700
Elongation at break [%]	10

TABLE 2.2 – Reinforced carbon fibers ABS for 3D printers. (Appendix A)

White lines are drawn on the span of the hydrofoil, and the tip section is colored in white to enhances its visibility in the tunnel with a black back wall.

(a) 3D printed carbon hydrofoil.

(b) Dimensions of the hydrofoil.
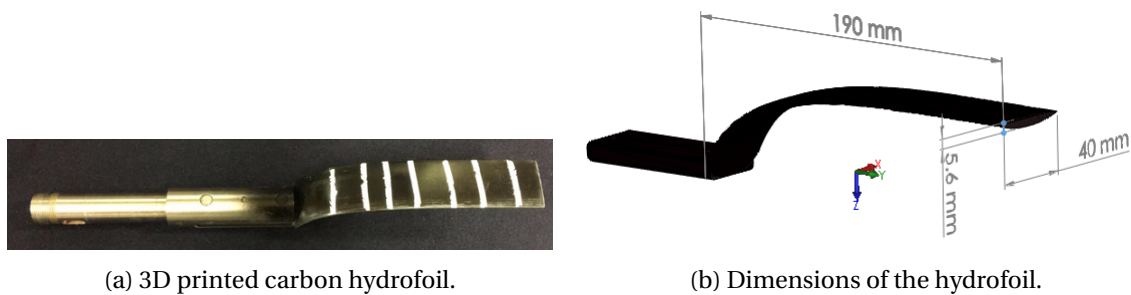
FIGURE 2.4 – 3D printed carbon hydrofoil.

Figure 2.5 compares the kevlar and carbon hydrofoil, the global geometries and the sections are presented. The carbon hydrofoil looks stiffer than the kevlar and is less curved. The comparison of the sections shows a difference in the shape, the chord and the thickness.

(a) Kevlar and carbon hydrofoils.

(b) Comparison of the sections of the kevlar and carbon hydrofoils.
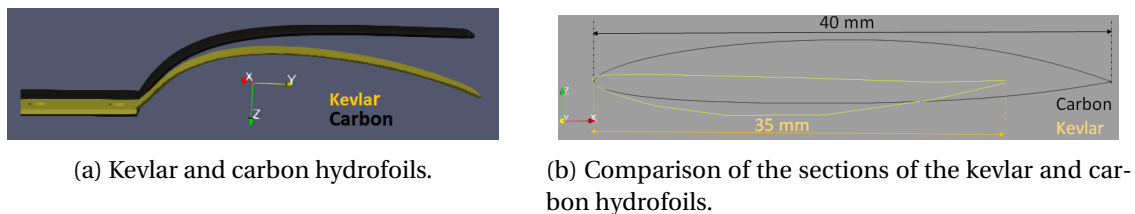
FIGURE 2.5 – Comparison of the model-scale kevlar and carbon hydrofoils.

2.1.1.3 Hydrofoil in POM (PolyOxyMethylene) material

This foil has an extruded geometry, that allows beam assumptions and is made of POM material with isotropic properties widely characterized in the literature. POM material

has been used in several works at the IRENAV to investigate the hydro-elastic behavior of flexible hydrofoils as the recent work of Lelong,2016 [86].

The geometry is a trapezoidal plan form of $150mm$ span, using a NACA0015. The chord is $100mm$ at the root and $30mm$ at the tip.

This geometry shows in figure 2.6 helps to get rid of confinement effects which occurs in the tunnel for longer structures as the kevlar and the carbon hydrofoils and, it allows 3D effects on the hydrofoil.

The manufacturing process is the machining and the material properties are given in table 2.3.

Density [g/cm^3]	1.41
Elastic Young modulus E [MPA]	3000
Poison [ ]	0.3

TABLE 2.3 – Mechanical properties of POM. (Appendix A)

The hydrofoil geometry is presented in figure 2.6. It is a one piece machining including a disk at the root to ensure a rigid clamped condition. However, this specific mounting is not adapted to the hydrodynamic balance of the tunnel and the forces on the hydrofoil were not measured during the hydrodynamic tests.
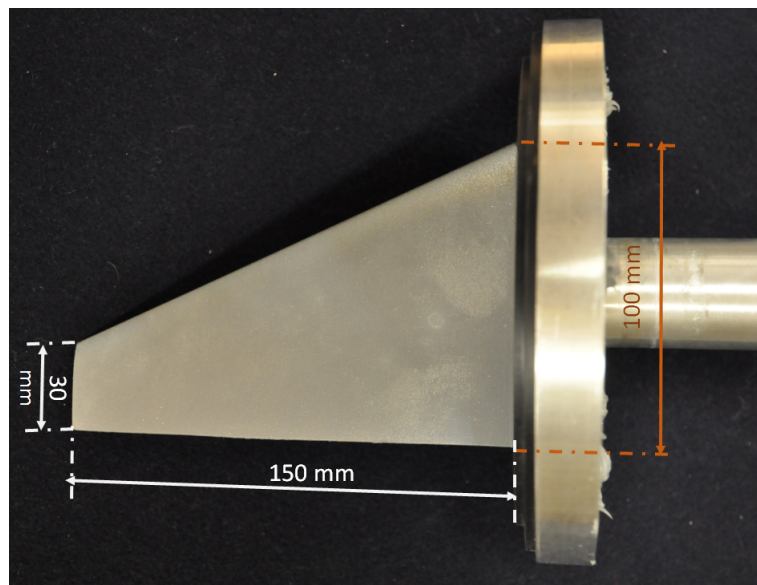
FIGURE 2.6 – POM hydrofoil

2.1.2 Mechanical characterization

For the sake of numerical comparisons, the mechanical properties of the materials were obtained from well-controlled experiments based on the static response of the structure itself undergoing static loading. We are particularly interested in the Young modulus of elasticity and we perform bending tests. The structure is loaded in simple bending and, a measurement of the loading force and displacement of the structure is recorded. The analysis of these data leads to the modulus of elasticity of the hydrofoils.

2.1.2.1 Experimental setup

Figure 2.7a shows a tensile test bench dedicated for tensile and compression tests but can also perform bending tests with an adjusted mounting of the structure.
Figure 2.7b from the IRDL laboratory shows the tensile bench adapted for bending tests : a sliding rail is added to the machine to allow the hydrofoil installation. The hydrofoil is cantilevered to its base by bolted clamping on the rail and its tip is subjected to a vertical loading applied by the excitation cell of the test bench.
The maximum load that can be provided on this machine is $300k$N. The excitation cell available for the study can create a loading up to 250N with an accuracy of ±0.01N.
The test bench is connected to a computer by wiring and is controlled through a dedicated software.
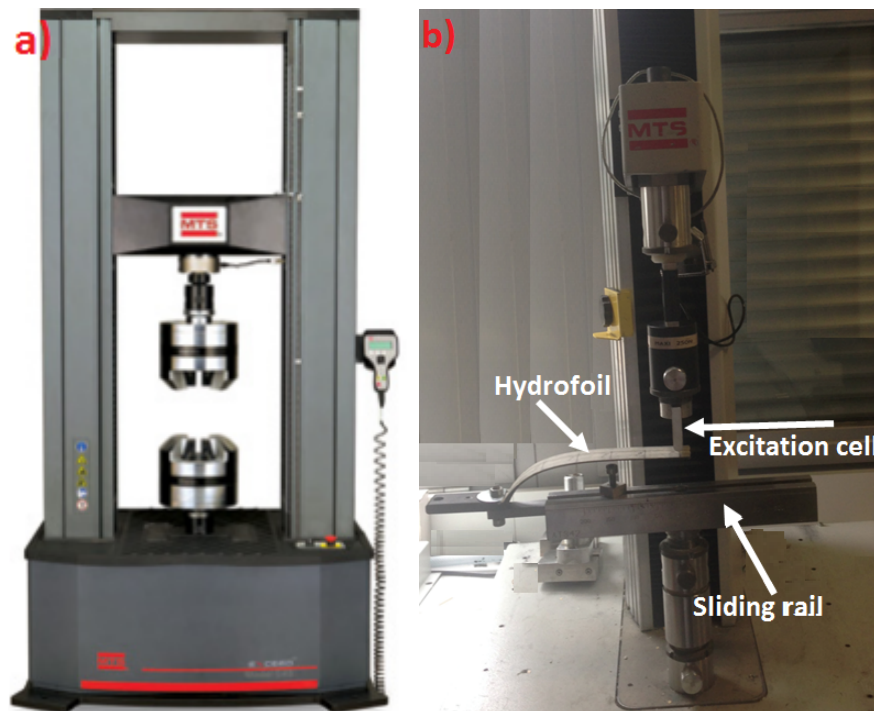
FIGURE 2.7 – a)Tensile test bench. b) Adaption of the bench for bending tests.

To perform a simple bending test, the hydrofoil is firstly mounted on the bench and the expected value of its vertical displacement after the bending is set on the computer. The motion speed of the excitation cell is fixed and the test is triggered on the computer. The excitation cell moves down vertically with a constant velocity and starts loading the hydrofoil as soon as contact is made, it continues to move down until the displacement set is reached, and then stops and rises.
The computer records the displacement of the cell and the load applied on the hydrofoil. At the end of an experiment the load applied on a section and the displacement of that section are measured.
This setup is only for the kevlar and carbon hydrofoils. The disk at the root of the POM hydrofoil is not compatible with the system described above, its experimental setup will be described in a section below. The configurations investigated for each foil are also given below.

Kevlar hydrofoil

The structure is considered as two parts : a high curvature part close to the root and a low

curvature part. To allow the assumptions of straight beam experiencing elastic deforma-
tions, the loading is applied on 4 points chosen along the span on the low curvature part.
The stroke of the test bench is set to $10mm$ with a velocity $50mm/min$ and, the force is
recorded with the displacements for each point.
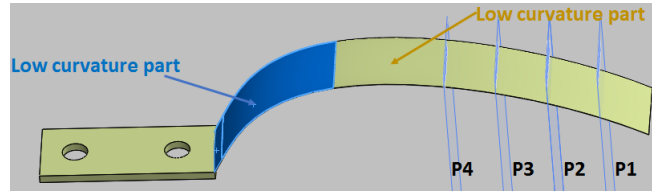
FIGURE 2.8 – Position of the points

Points	P_1	P_2	P_3	P_4
L [mm]	147	127	97	77

TABLE 2.4 – Distance of the points from root

Figure 2.8 shows the positions of the measurement points on the foil, showing the
highly curvature (blue) and the slightly bend, their distances from the hydrofoil base are
given in table 2.4.

Carbon hydrofoil

Four sections located on the span of the hydrofoil are investigated, their location from
the hydrofoil base is given in table 2.5. The tests are setup to perform the three loading
cases given in table 2.6.

Points	P_1	P_2	P_3	P_4
L [mm]	75	110	145	177

TABLE 2.5 – Distance of the points from root, Carbon foil

Loading	F_1	F_2	F_3
F [N]	4	7.6	11.5

TABLE 2.6 – Forces applied to the carbon foil

POM hydrofoil

The POM hydrofoil is assembled at its root with a flush disk attached to a cylindrical
rod as shown in figure 2.9a, making it impossible to use a conventional bending bench.
Bending tests are carried out in the hydrodynamic test configuration, using the back wall
of the tunnel of IRENAV as support. The disk connected to the POM hydrofoil is indeed
designed to be fixed on the back wall of the tunnel. The setup of the tests is presented in
the images of figure 2.9, the boundary conditions are fixed free.
The loading is applied by a rod that presses against the structure with its one end and the
other end has a tray on which calibrated masses are placed (figure 2.9e).
The rod is fixed to the frame by means of a articulated arm that uses the tunnel back wall
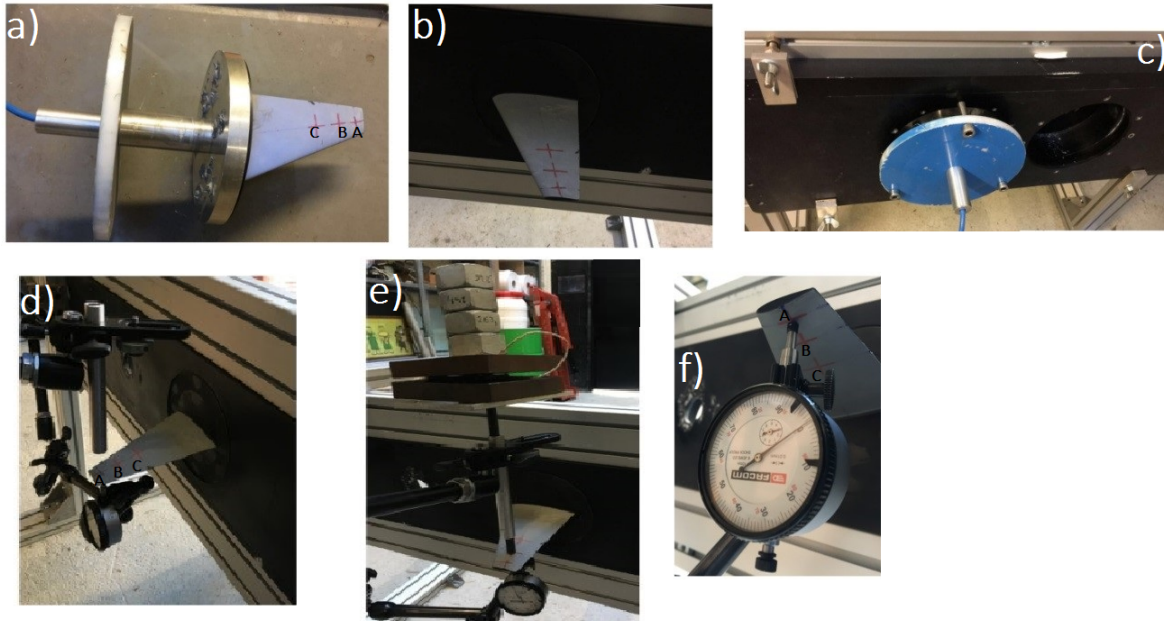
FIGURE 2.9 – Experimental setup of the bending tests on POM hydrofoil.

as support (figure 2.9d). The accuracy of the load calibration is $\pm 0.001 g$.
An needle comparator with an accuracy of $\pm 0.001 mm$, attached to articulated arms, measures the displacements of the structure (see figure 2.9f).
Three loading cases are performed for 5N, 7N, 10N. The hydrofoil is loaded on two points A and B located from the root at $140 mm$ and $120 mm$ on the span, at the middle of the corresponding section.
For each loading case, the comparator measures the displacement of the points : A $(140 mm)$, B $(120 mm)$ and C $(90 mm)$.

2.1.2.2   Data post processing : determination of the Young modulus

To analyze the bending tests, the hydrofoils are considered as a beam under the following assumptions :

— the material is homogeneous, continuous and works in the linear elastic domain : its behaviour is governed by the Hooke's law.

— Navier-Bernoulli kinematics : only the neutral fiber deforms, the plane sections normal to the neutral fiber before the deformation, remain plane and normal to the neutral fiber during transformation.

The bending tests performed on the hydrofoils are equivalent to the simple bending of a cantilevered beam loaded at its tip, as presented in figure 2.10.
The figure presents a beam in the global reference coordinates (X,Y,Z), the beam is loaded by a vertical force F at a position L from its root.
With Euler Bernoulli's assumptions, and considering the theorem of virtual works and the balance of moments [79], the displacement of the neutral axis along its axis is expressed by 2.1.

$$Z(Y) = \frac{F \times Y^2 \times (3L - Y)}{6EI_x} \quad \rightarrow F = \frac{6Z(Y) \times EI_x}{Y^2 \times (3L-Y)} \tag{2.1}$$
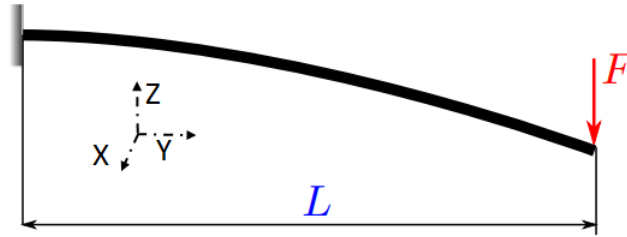
FIGURE 2.10 – Simple bending of a cantilevered beam loaded at its tip

F is the applied force, L is the position along the span where the force is applied. Y is the position of any point along the span and Z(Y) is its vertical displacement. I_x is the moment of inertia in X-axis of the beam cross section.

For Y=L, the relation between the force F and the displacement Z is linear with a slope m (equation 2.2).

$$F = \frac{3EI_x}{L^3} \times Z(L) \quad \rightarrow F = m \times Z(L) \tag{2.2}$$

The determination of m leads to the bending stiffness EI_x where E is the Young modulus and I_x is easily obtained with a CAD tool. The Young modulus is then calculated with equation 2.3.

$$EI_x = \frac{m \times L^3}{3} \quad \rightarrow E = \frac{EI_x}{I_x} \tag{2.3}$$

The measured data are the displacements of a point on the the foil and the applied loading at this point as shown in figure 2.11.

The loading cell stroke and its velocity is imposed and two tests are performed performed two tests for each configuration, the result is the average. The post processing is realized through scripts that we developed on Matlab software.
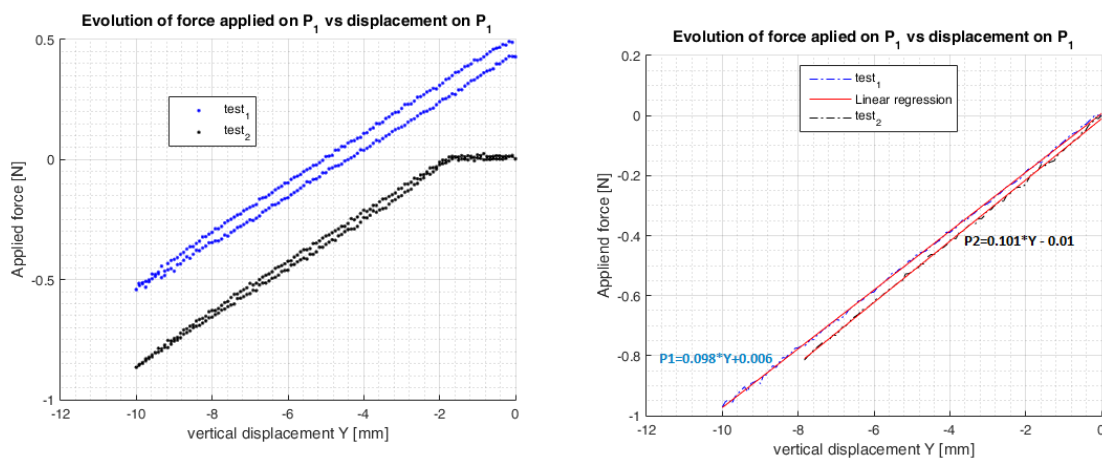
(a) Example of recorded data without post-processing.

(b) Example of recorded data with post-processing

FIGURE 2.11 – Example of data post-processing on kevlar hydrofoil

Figure 2.11 shows an example of data recorded during the bending test on the kevlar hydrofoil. Figure 2.11a shows a plot of the data output without post-processing.

In the first test (blue curve), the loading cell was already on the foil so there is a non zero

force at the beginning of the test (displacement= 0mm). The second test shows no contact between the excitation cell and the structure at the beginning of the test. the horizontal line with 0N corresponds to the displacement of the load cell in air. An hysteresis is observed in the curves according to the upward or downward of the loading cell motion.
Figure 2.11b shows the result after post processing : the horizontal part of test 2 is deleted, the hysteresis is replaced by the average and the curves are translated to the origin. A linear regression gives the slope of the curves.
The bending stiffness is then calculated using an average of the two slopes.

In this example, the load was applied at L = $187mm$ and gave a bending stiffness EI$_x$ = 1.058×10^5MP$a.mm^4$.

2.1.3   Hydrodynamic setup : hydrodynamic tunnel of IRENAV

The aim of hydrodynamic experiments is to investigate the fluid-structure interactions on the hydrofoils. The tests are carried out on the model scale hydrofoils in the cavitation tunnel of IRENAV. The water flows around the structures and creates forces on the hydrofoils that lead structural displacements. These displacements modify the pressure distribution on the structure until it reaches an equilibrium.
The forces applied to the structure and its movements under the effect of this loading are measured and their analysis allow the understanding of the hydrofoils behavior under FSI.
This section describes the cavitation tunnel of the IRENAV and the equipment used to measure the forces and the displacements in the hydrodynamic tests.

2.1.3.1   Description

The hydrodynamic tunnel of IRENAV is presented in figure 2.12, it is used to study the flow around various obstacles in the test section (1) ($192mm$ square cross-section and 1m length). The installation is deployed over a length of approximately $15m$ and a height of $7m$ for a water volume of $35m^3$. The liquid motion is set in the tunnel (in the direction trigonometric in the figure) by a 10-blade propeller pump (2) driven by an electric motor of 21 kW (3).
A convergent (4) is placed before the test section to accelerate the flow for maximum speed at the entry is $15m/s$. Two honeycomb grids (5) are placed upstream of the convergent to make the flow more homogeneous from the turbulence point of view and the turbulence rate in the vein is thus about 2%.
The pressure in the tunnel is adjusted by means of a so-called "downstream" flume (6), which allows to have a free surface. The volume of air contained above the surface can then be connected via two servo valves either to a storage flume held at 6 bar by a compressor, or to another storage flume vacuumed by a pump.
This allows a variation of the pressure in the test section between 0.1 and 3 bar. A third valve connects the air volume to the atmospheric pressure.
A programmable logic controller controls the installation and its regulation by two piezoelectric pressure sensors : the first one takes the pressure average over three measurement points distributed upstream of the convergent and the second one takes the pressure at the inlet of the vein on a measurement point on the lower wall. The PLC thus has the input pressure of the vein and can calculate the flow velocity from the pressure difference between upstream and downstream of the convergent.
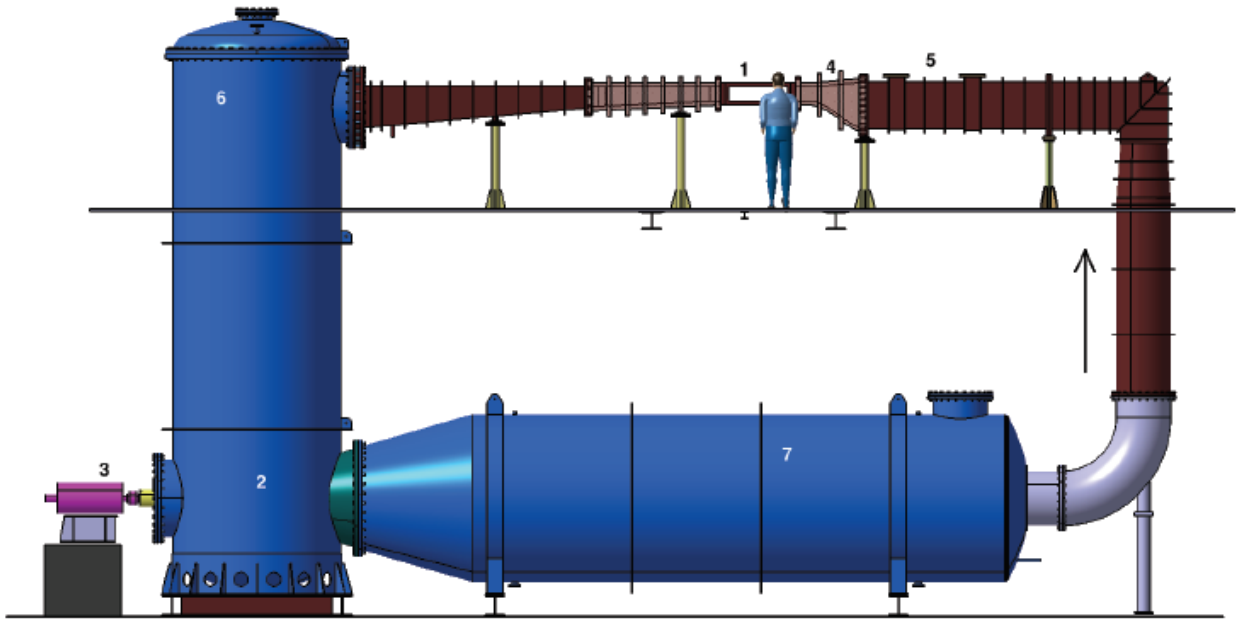
FIGURE 2.12 – Cavitationnal tunnel of IRENAV [55]

A resorber (7) is used to reduce the bubble content in the flow and prevents bubbles caused by the flow from being reintroduced into the vein.

2.1.3.2   Installation of the hydrofoil in the test section

Figure 2.13 shows the kevlar hydrofoil foil mounted in the hydrodynamic tunnel of IRENAV. The boundary condition in the tunnel is fixed free and the span the kevlar hydrofoil is $187mm$ in the $192mm$ square test section. There is therefore a gap of $5mm$ between the vein wall and the tip of the structure. The walls of the vein are 80 mm thick, the back is made of aluminium (coloured in black in the picture) while the front, top and bottom panels are made of Plexiglas.
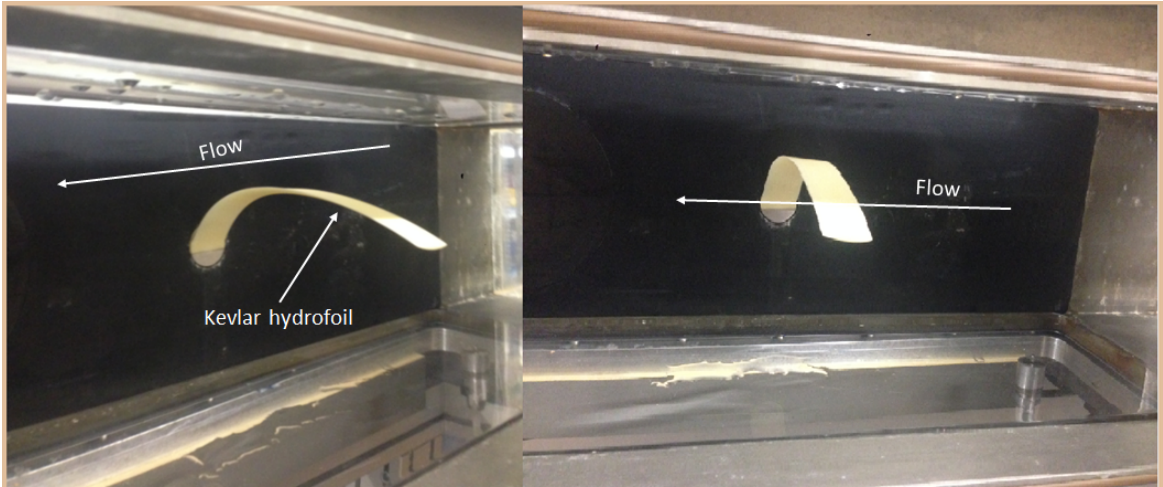
FIGURE 2.13 – Images of the Kevlar hydrofoil mounted in the cavitation tunnel of IRENAV

The carbon hydrofoil mounted in the tunnel is shown in figure 2.14.

When the incidence rises over the zero lift angle, the hydrofoil is lifted upward as shown in figure 2.15. When the incidence decreases under the zero lift angle, the lift force
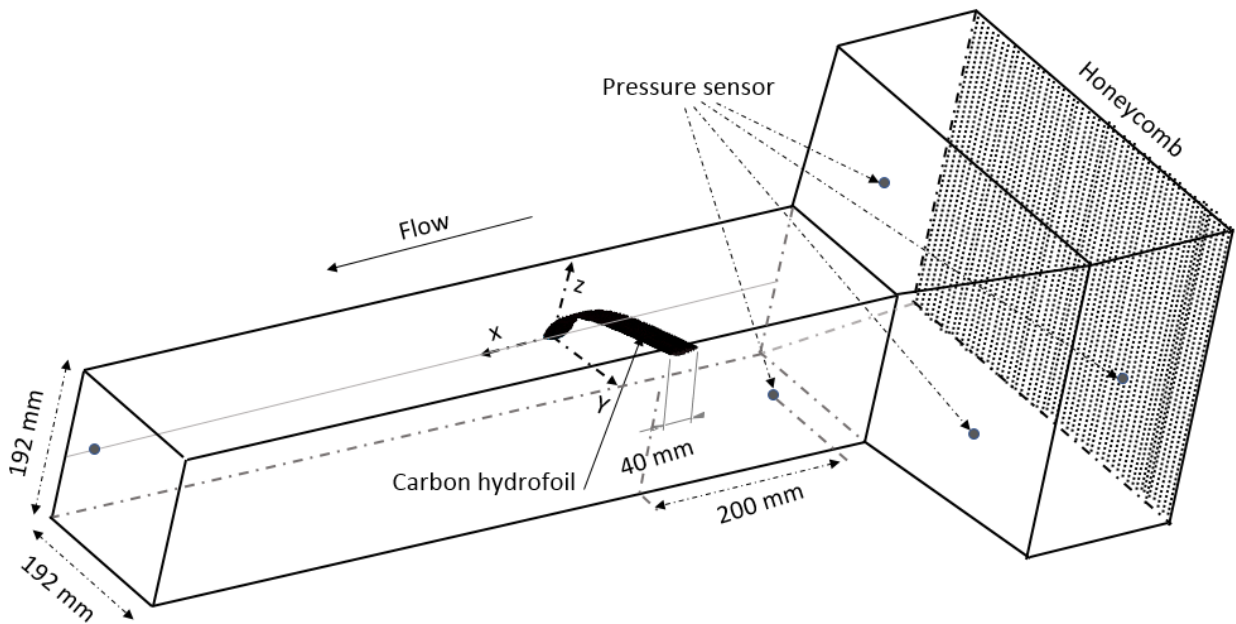
FIGURE 2.14 – Carbon hydrofoil mounted in the cavitation tunnel of IRENAV

goes downward.
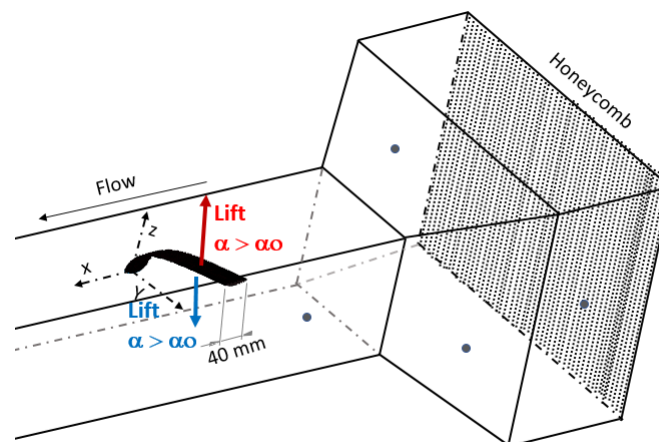
FIGURE 2.15 – Orientation of the lift force in the tunnel.

At the back of the hydrodynamic tunnel, a balance and a stepper motor are mounted, the hydrofoil is directly fixed on the balance by means of a keyway assembly and the block balance-hydrofoil is fastened to the motor. The assembly scheme is presented in figure 2.16.

Figure 2.17 shows a picture of the backside of the tunnel. The balance support is coloured in grey and the gear motor in black. The motor is controlled by software developed within the IRENAV and is use to set the angle of attack of the profile in the flow. The accuracy of this setting is around ±0.01°.

2.1.3.3 Measurement of the hydrodynamic forces

The hydrodynamic drag force, lift force and moment created on the hydrofoil by the fluid motion are measured with the hydrodynamic balance shown in figures 2.16 and 2.17.
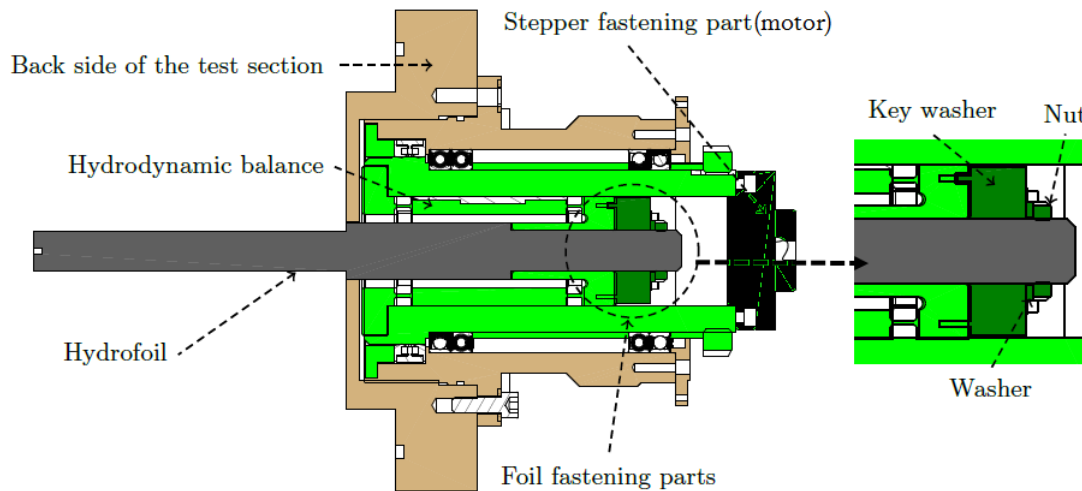
FIGURE 2.16 – Embedding scheme of the hydrofoil and the hydrodynamic balance in the tunnel. [86].
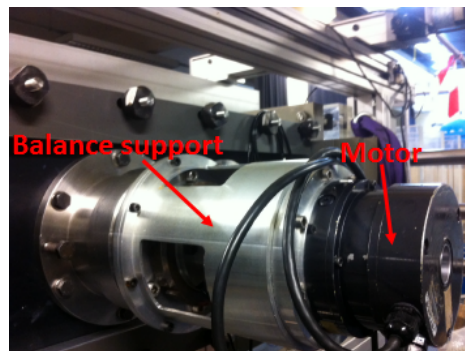
FIGURE 2.17 – Backside of the tunnel showing the gear motor(black) and the balance support (steel).

The hydrofoil is embedded to the balance : the balance rotates with the hydrofoil when the motor changes the angle of attack.

The hydrodynamic balance is made of six gauge bridges which record the voltage signal created by the loading on the structure and transmit it to a computer via a signal amplifier rack Iotech®️ Strainbook 616. A data post processing describing the conversion of the voltage signal (volts) into forces and moments(Newton and Newton.meter) is described in section 2.3.

At the beginning of a campaign, the foil is mounted in the tunnel and a first set of measurements are performed with the balance without flow (velocity of $0m/s$) and then, experiments with flow (velocity $> 0m/s$) are carried out.

To perform a test with flow, the angle of attack is set and when the flow is stable around the profile, the balance records the signal within 10 seconds with an acquisition frequency of 100Hz, the averaged measurement is sent to the post processing to compute the forces. The hydrodynamic forces of a configuration are the data with flow subtracted by the data without flow.

The output of the post processing are the lift, drag and moment for each configuration case (flow velocity and angle of attack).

The precision of these measurements are : ±5N on the lift force, ±1.6N on the drag force and ±1N.m on the moment.

2.1.3.4 Measurements of the displacements

There are several procedures to measure deformations at IRENAV. [40] set up a method to evaluate large deformations in spinnaker sails downwind. It uses six cameras and 54 targets spread over the sail and the position of the targets over time is measured by triangulation. The shape of the sail is then reconstructed in three dimensions.

[45], uses a method to measure the displacements of extruded hydrofoils in the hydrodynamic tunnel. It consists in placing in front of the tunnel a fast camera facing the tip of the profile and measuring its position over time but this method is not adapted to rebuild the bending of the hydrofoil.

For this study, we are using a laser telemeter to measure the displacements of the hydrofoil along the spanwise giving the structure's bending under hydrodynamic loading. That method was previously used at IRENAV by [86] and [63].

The laser is placed on the top of the tunnel on a motorized rail and can move both along the spanwise and the chordwise. It performs continuous measurements at a user-defined acquisition frequency.
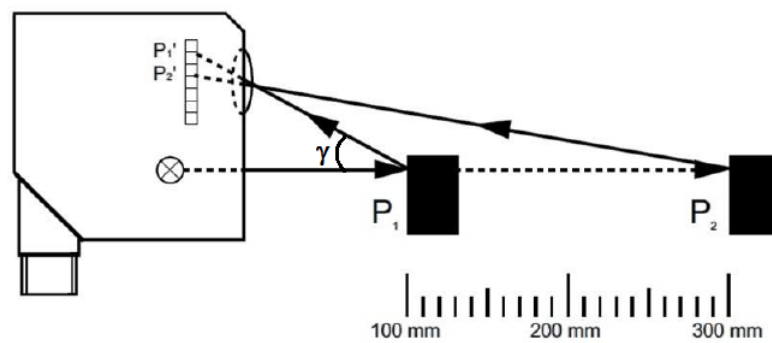
FIGURE 2.18 – Laser principle.

Figure 2.18 shows the principle of a laser rangefinder, made of a transmitter and a receiver. The laser sensor emits a light beam that creates a spot on the object, this spot is detected by the receiver with an inclination angle γ and that angle will be converted into distance.

The laser measures the position of the object through the windows of the tunnel (made in glass material) and its beam light passing through 3 media with different properties (air, glass and water) is deviated after each change.

To consider the refraction of the laser through the different interfaces, its calibration is performed prior to the measurement : the laser measures the dimension of a test pattern in air, and a second measurement is perform in water+the glass of the tunnel window. A comparison of these two measurements gives a correction factor which is applied to all the laser measurements.

Figure 2.19 show the importance of the calibration of the laser through a comparison of three measurements : in air (real dimensions), in water+glass (without calibration) and in water+glass (with calibration). The measurement in water+glass with the calibration overlap perfectly to the real measurements in air when the measurement without calibration has the good trend but the amplitude is different.
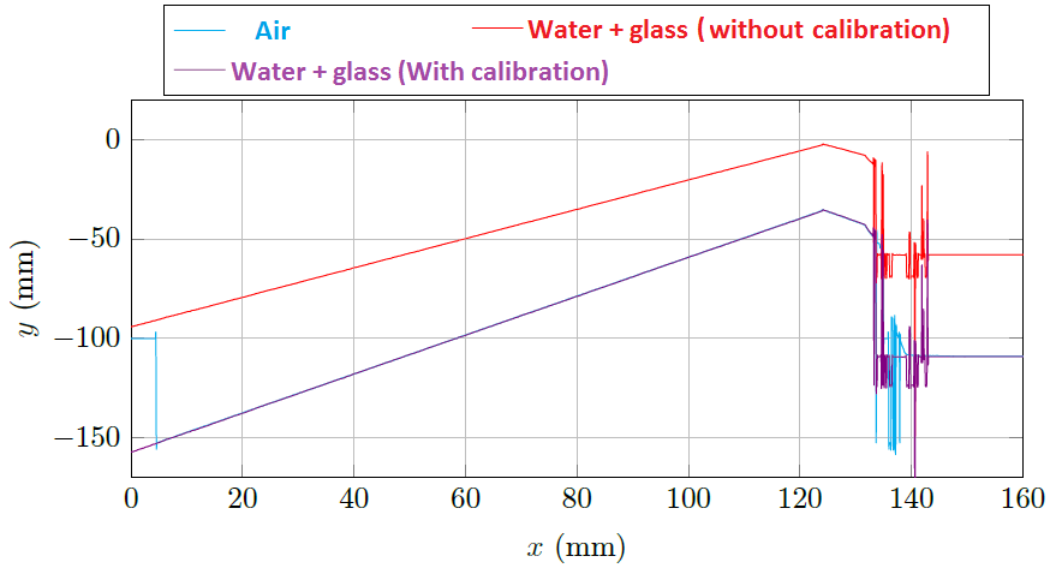
FIGURE 2.19 – Importance of calibrating the laser.

2.1.3.5 Configurations investigated

This section presents the hydrodynamic tests investigated on the three model-scale hydrofoils in the tunnel of IRENAV. It starts with the kevlar hydrofoil, then the configurations of the carbon hydrofoil are presented and the section ends with the POM hydrofoil.

Kevlar hydrofoil
The profile of the hydrofoil is non symmetric, a first test aiming to find the zero lift incidence is performed. A flow velocity is imposed at a chosen value, the angle of attack is modified to find the value that gives a zero lift force. Results comes out with $\alpha_0 = 11.5°$.
During this first test, the foil exhibits a very flexible behavior so that only two small velocities $U_1 = 1.06 m/s$ and $U_2 = 1.6 m/s$, are investigated for angles of attack in a range of [5.5° - 11.5°] in 1° step. To avoid the damage of the foil, the incidence range is reduced to [8.5° - 11.5°] for $U_2 = 1.6 m/s$. The Reynolds number for these velocities are $Re_1 = 31800$ and $Re_2 = 48000$.
The incidences investigated are under the zero lift angle thus, the hydrofoil lifts downward, its deformation amplifies its curvature and the foil moves away from the front glass of the tunnel.
The measurement line is chosen at $X = 13.44 mm$ (x=0 is set at the leading edge of the root 's section). The laser performs a continuous scan of that line and gives the vertical displacements of the entire hydrofoil, and the balance measures the hydrodynamic coefficients.
To ensure the location of the continuous scan on the y-axis, seven points defined in table 2.7 are also measured.

Points	P_1	P_2	P_3	P_4	P_5	P_6	P_7
x [mm]	13.44	13.44	13.44	13.44	13.44	13.44	13.44
y [mm]	0	34.4	68.6	103.1	137.5	171.9	173.8

TABLE 2.7 – Measurement points along the spanwise of kevlar hydrofoil

Carbon hydrofoil
In order to define the experimental configurations, tests are carried out beforehand and

the foil's behaviour is observed.

The flow velocity is set at U = $3m/s$: $\alpha_0 = 0°$ is the zero lift incidence but the hydrofoil experiences small oscillations.

When the incidence decreases, the foil lifts downward and it deforms towards the rear of the tunnel. The curvature of the foil is amplified and it moves away from the font glass of the tunnel but the oscillations are amplified and became hazardous under $\alpha = -4°$.

When the incidence rises, the oscillations decreases. The lift force is positive and the deformation unfolds the hydrofoil that moves towards the front glass of the tunnel. When the incidence α becomes higher than $2°$, the hydrofoil comes into contact with the front window of the tunnel.

The experiments are thus carried out on this hydrofoil for two velocities $U_1 = 2m/s$ and $U_2 = 3m/s$ ($Re_1 = 80.000$ and $Re_2 = 120.000$) and the incidences investigated are : $\alpha = \{-4°, -2°, 0°, 2°\}$.

The measurement line is chosen at X = $20mm$ (x=0 is set at the leading edge of the root 's section) and seven points located in the y-axis as defined in table 2.7 are measured. The laser measures the displacements of the entire hydrofoil, and the balance measures the hydrodynamic coefficients.

POM hydrofoil

The hydrodynamic tests are carried out in the hydrodynamic tunnel of IRENAV for five Reynolds numbers calculated at the mean chord (C = $65mm$) and seven incidences given in table 2.8 are investigated.

$Re \times 10^5$ []	3	4	5	6	7		$\alpha[°]$	-10 , -6, -2 ,0, 2 ,6,10
U[m/s]	4.62	6.15	7.69	9.23	10.77			

TABLE 2.8 – Configurations investigated for hydrodynamic tests on the POM hydrofoil.

The measurement line is chosen at X = $22.5mm$ (the reference is the leading edge of the root section) as shown in figure 2.20. Seven points located on that line are also measured, their position are given in table 2.9. A continuous measurement of the displacement is performed on the line and the curve is set in the y-axis using the measurements of the points, as described in section 2.3.2.

FIGURE 2.20 – Position of the points
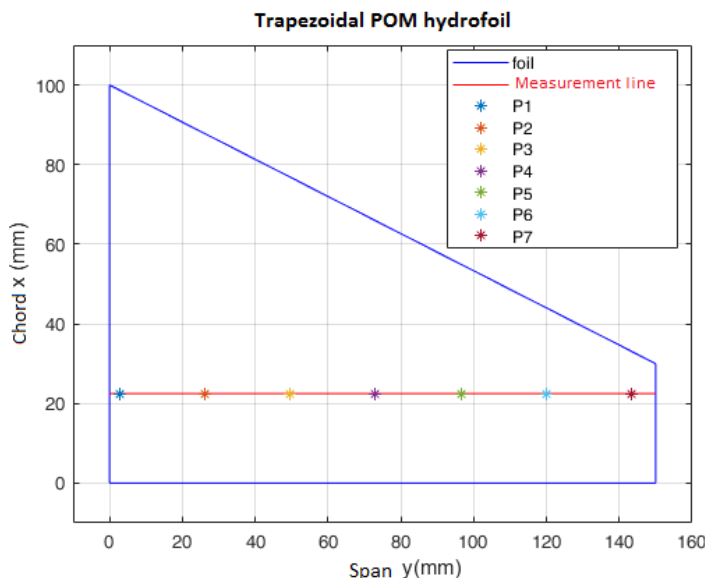
Points	Y [mm]
P_1	2.73
P_2	26.17
P_3	49.61
P_4	73.05
P_5	96.48
P_6	119.92
P_7	143.36

TABLE 2.9 – Points position in spanwise, X = $72.5mm$

2.1.4 Results of Kevlar and carbon hydrofoils

This part shows the preliminary results of the kevlar and carbon hydrofoils.

2.1.4.1 Results of the Kevlar hydrofoil

Mechanical characterization

Bending tests are performed on the test bench to determine the equivalent Young modulus E of the hydrofoil.

Figure 2.4 shows the evolution of the force applied on a point versus its displacement for the 4 points tested. "Reg lin" is the linear regression of the curves. When the distance to the root decreases(P_1 to P_4), the slopes of the curves rises because it is inversely proportional.
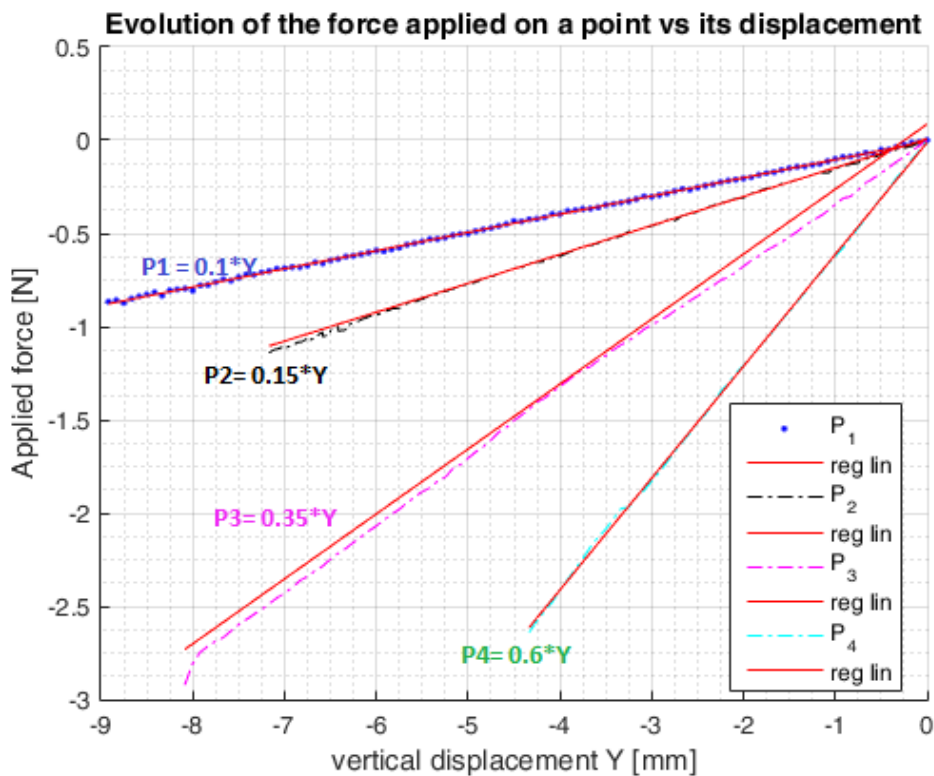
FIGURE 2.21 – Evolution of the force versus the displacement on a point

The bending stiffness EI_x calculated with equation 2.3 are given in table 2.10. The first three points are very close, leading to a mean value of $EI_x = 1.19e^5$ MP$a.mm^4$.

Points	P_1	P_2	P_3	P_4
EI_x [MP$a.mm^4$]	$1.03e^5$	$1.05e^5$	$1.06e^5$	$9.1e^4$
E [MPa]	2625.4	2686.5	2712.9	2317.7

TABLE 2.10 – Young modulus of the kevlar hydrofoil.

The inertia $I_x = 39.4mm^4$ is obtained with a CAD software and the averaged Young modulus of the Kevlar hydrofoil is E = 2585.6 Mpa, 12% higher than the theoretical value. This difference is likely due to the straight beam assumptions.

Hydrodynamic coefficients

Figure 2.22 gives the hydrodynamic coefficients of the kevlar hydrofoil versus the angle of incidence for the two flow speed $U_1 = 1.06 m/s$ and $U_2 = 1.6 m/s$.

The lift coefficients shows values for U_2 lower than U_1 and the two configurations seems
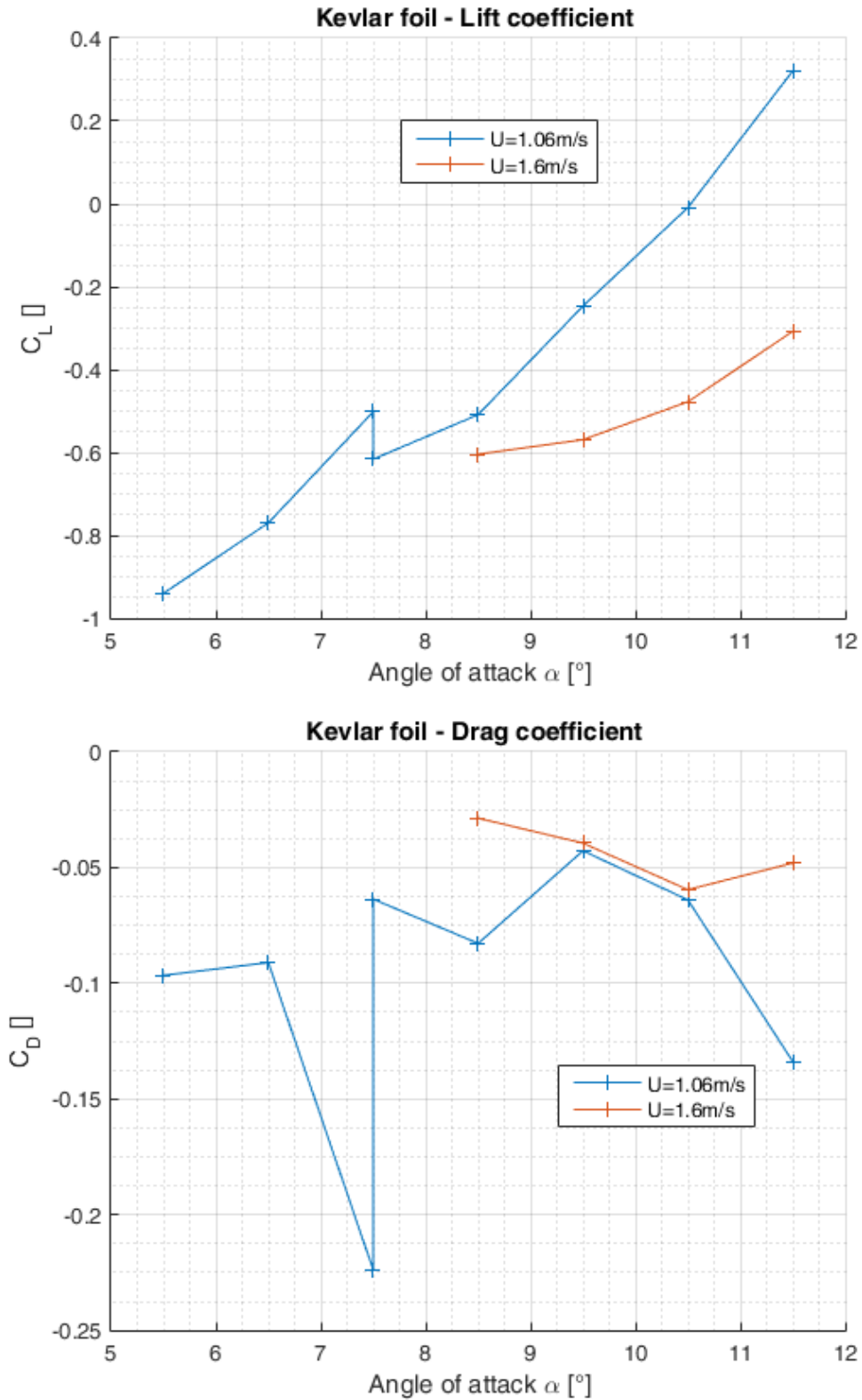
FIGURE 2.22 – Hydrodynamic coefficients of the kevlar hydrofoil

to have different zero lift angle, which is not consistent with the profile behavior (initial

tests shows $\alpha_0 = 11.5°$). U_2 drag coefficient has the same trend as the lift, lower than U_1 values and the curve does not exhibit any particular shape.

During the tests the foil experienced a lot of oscillations mainly due to FSI instabilities, that may influence the measurements, these data are not consistent for a comparison to simulations.

2.1.4.2 Carbon hydrofoil

Mechanical characterization

Figure 2.23 shows the evolution of the force applied to each points with the displacement of that point. The analysis is the same conducted with the 3D printed kevlar foil.
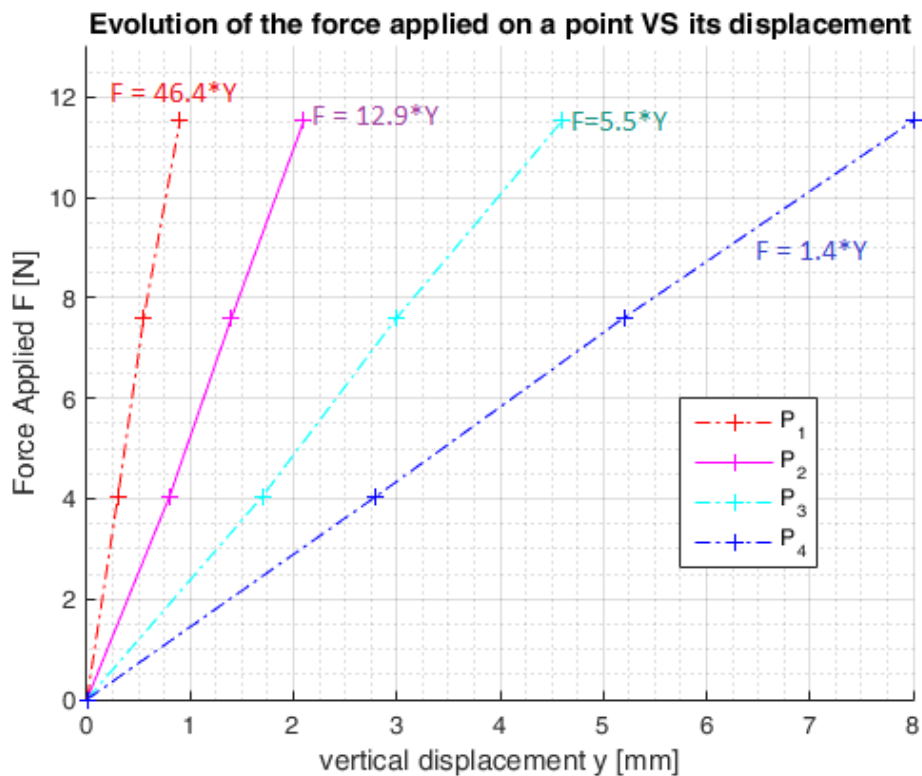
FIGURE 2.23 – Evolution of the force versus the displacement on a point, 3D-printed carbon foil

The bending stiffness EI_x is calculated with equation 2.3 and the results are given in table 2.11. The value are very different from each other excepts P_3 and P_4. The value of P_1 is discarded and the average on the 3 other gives a mean value of $EI = 2.27e^6$ MP$a.mm^4$.

Points	P_1	P_2	P_3	P_4
EI [MP$a.mm^4$]	$1.245e^6$	$1.8e^6$	$2.56e^6$	$2.58e^6$
E [MPa]	$0.8e^4$	$1.07e^4$	$1.12e^4$	$1.13e^4$

TABLE 2.11 – Young modulus of the 3D printed hydrofoil.

The inertia $I_x = 228 mm^4$ is obtained with a CAD software and the average Young modulus is E $= 9.9e^3$ Mpa. This value is 3.6 times higher than the theoretical value. This higher difference likely due to the straight beam assumption and the modulus calculated does not just stand for a material modulus. It should be considered as a whole taking into

account the material stiffness and an added stiffness due to the hydrofoil curvature.

Hydrodynamic tests

Figure 2.24 shows the tip section of the hydrofoil for $-4°$ with the different velocities. We observe a twist in the section, in the clockwise and the white spot corresponding to the hydrofoil stopping, on the tunnel window during the initial tests, is also visible.
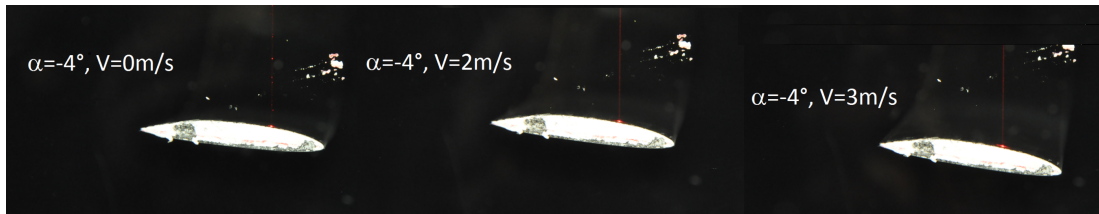
FIGURE 2.24 – Image of tip of the carbon hydrofoil during the hydrodynamic tests.

The displacements of the foil calculated as the difference of the values with flow and without flow is given in figure 2.25 for all the configurations investigated.

The curves don't have any defined trend and exhibit the oscillations observed during the experiments. These data are definitely unusable.

3D printed hydrofoil is a good alternative to manufacture in a reduced model, the complex geometry of the real 747 hydrofoil. It must be pointed out that the resulting geometries achieved in this work are too close to the tunnel limitations and the flexibility of the structures lead to variable oscillations, cancelling them as candidate for these hydrodynamic experiments and numerical validation.

The results of the POM hydrofoil are presented in section 4.1.
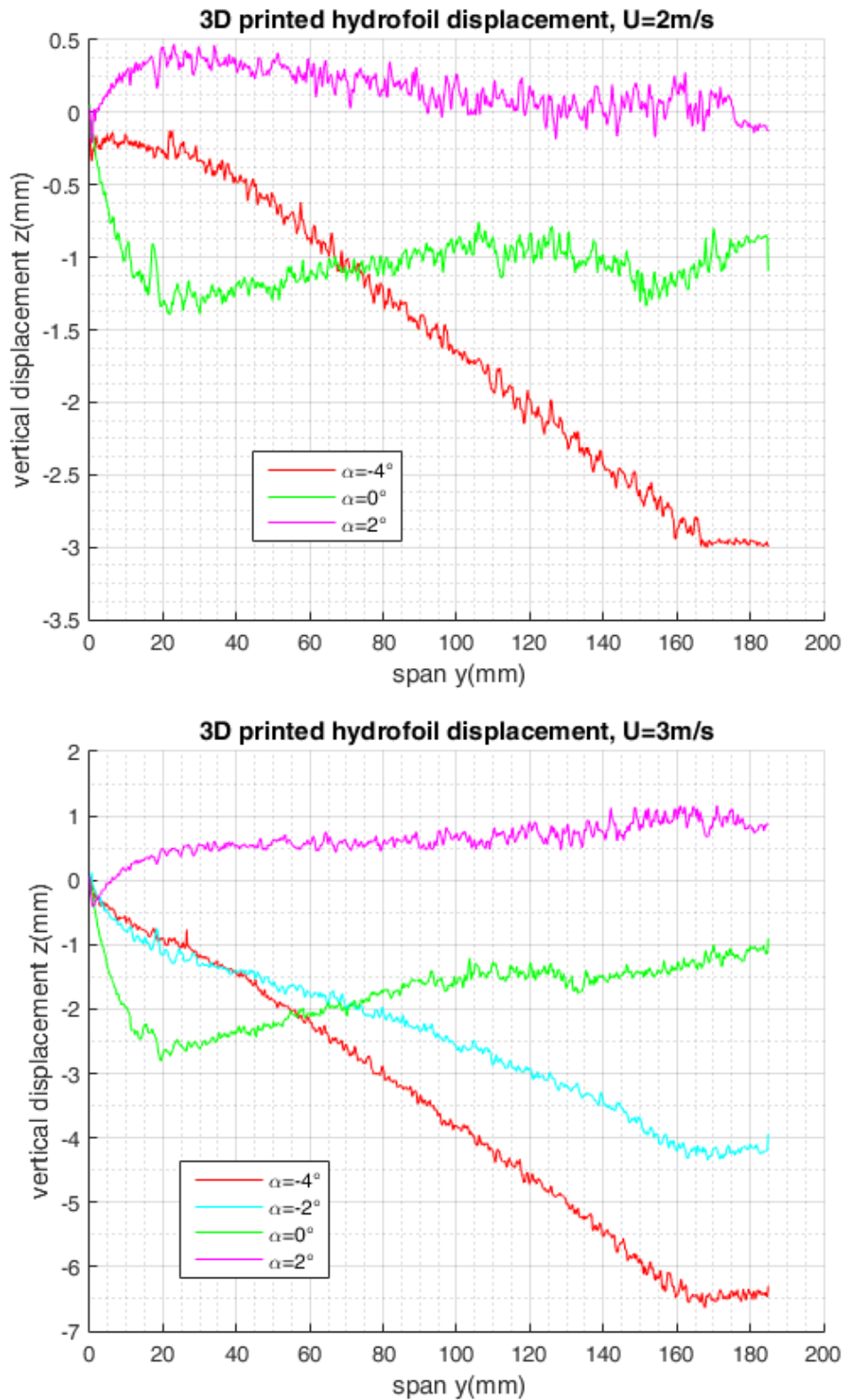
FIGURE 2.25 – Displacements of the carbon hydrofoil under hydrodynamic loading.

2.2 Real scale composite hydrofoils and experimental se-tups

Real scale hydrofoils in composite material are manufactured to :

— Perform a realistic process of fabrication with a representative number of plies.

— To allow the use of a sandwich structure.

— To design structures that experience large deformations.

— To test the hydrofoil in a flume with low speed.

These hydrofoils will allow the investigation of some phenomena not observable with reduced scale hydrofoils in the cavitation tunnel, such as ventilation (free surface inception) or intern structural coupling that may occurs with composite materials (bend twist coupling for instance).

This part describes a complete study process going from the hydrofoil manufacturing to the experiments. The objective is to analyze on one hand the behavior of the hydrofoils, the bend twist coupling and, on the other hand to validate the numerical tools.
The study starts with the sizing and manufacturing of the structures. Then, static tests are perform to assess the mechanical characteristics of the structures. The last section describes the hydrodynamic tests. The experimental setups are presented in this part and the results are discussed in chapter 4.2.

2.2.1 Hydrofoil manufacturing

To capture FSI on the hydrofoils, four hydrofoils are manufactured :

— The four hydrofoils have the same hydrodynamic shape.

— The structures are designed to experience at the tip, displacement of 10% of their length. This will lead to results significantly different from a rigid structure.

— The material are different from one hydrofoil to the other. This will analyse the impact of the composite material on the hydrodynamic performances of the foils.

— The orientation of the layups of each foil are different, to investigate the bend-twist coupling effect.

Regarding these specifications, four hydrofoils are manufactured with the help of SEAir, the industrial partner of this research work.

2.2.1.1 Hydrofoils geometry

The shape of the four hydrofoils are from the same mold. It is imposed by the mold available at SEAir (figure 2.26). This mold is actually used for the manufacturing of the mast of a kitesurf hydrofoil.
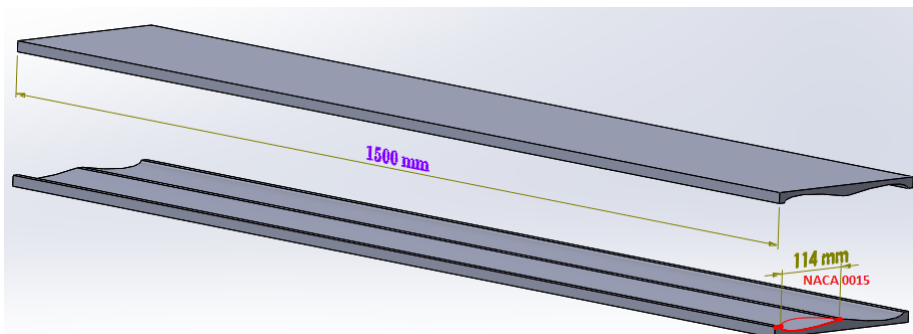
FIGURE 2.26 – Molds used to manufacture the hydrofoils.

The mold is a straight plan form of $1.5m$ span and $0.114m$ constant chord and the section profile is a NACA 0015. It is composed of two parts : suction side and pressure side, its geometry allow the manufacturing of two hydrofoils in at the same time (figure 2.26).

2.2.1.2 Effect of aspect ration on hydrodynamic behavior of the hydrofoils

This section aims to define the span length of the hydrofoils.
The hydrofoils 's section is a NACA 0015 of $0.114m$ chord and the tests are carried out in a flume of $1m/s$ maximum velocity. Thus, theoretical hydrodynamic forces are computed with these parameters.
We are looking for the good compromise between hydrofoil size and aspect ratio influence. Figure 2.27 shows the evolution of the hydrodynamic lift coefficient versus the angle of attack, computed at a flow speed U $= 1m/s$, for several span lengths : {$0.5m$, $0.75m$, $1m$, $1.25m$,$1.5m$}.
The computations are performed with the fluid calculation tool XFLR5 and the 2D coefficient for a hydrofoil with an infinite span is also presented ($C_L = 2 \times \pi \times \alpha$).
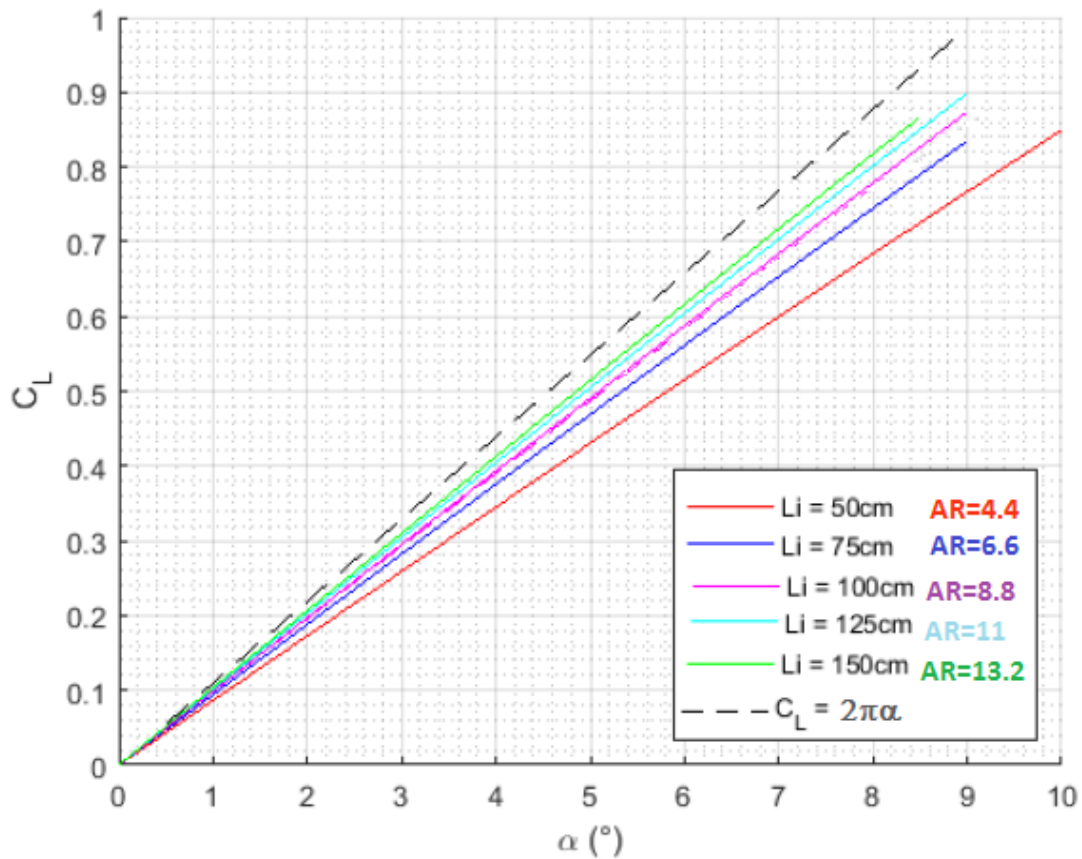
FIGURE 2.27 – Effect of the aspect ratio on the 3D lift coefficient versus the incidence. V=1m/s, the profile is a NACA 0015 and chord=0.114m

In agreement with the theory, when the foil length increases, its behavior gets close to the 2D configuration. The figure also shows that from $Li = 1m$, the lift difference with the maximum length $Li = 1.5m$ gets smaller and stays under 4%. There is no more 3D effects for aspects ratio above 8.8.

The hydrodynamic tests will be carried out in configuration of hydrofoils piercing the free surface and some measurement system are installed on the part of the hydrofoil that stays in air. A minimum length of 0.35m is required for the hydrofoil span in air leading to 1.15m length remaining for the underwater part.

Regarding the figure 2.27, L = 1m is chosen for the submerged length and the material losses during the manufacturing process are consider in the 0.15m remaining.

The total length of the hydrofoils is 1.35m corresponding to a global aspect ratio of 12 and, AR of 8.8 for the underwater part. The geometry stays in the assumptions of lifting line theories and the 3D effects are neglected.

2.2.1.3 Material sizing

This part describes the material layups. The structure follows the assumptions of Euler-Bernoulli beam :

— The material is homogeneous, continuous and works in the linear elastic domain : its behaviour is governed by the Hooke's law. The composite structure is equivalent to a homogeneous structure with an equivalent Young modulus.

— Navier-Bernoulli kinematics : only the neutral fiber deforms, the plane sections normal to the neutral fiber before the deformation, remains plane and normal to the neutral fiber during transformation.

The beam is cantilevered and, under a pressure loading distributed on the submerge surface as shown in the figure 2.28.

The pressure force is applied to the beam as a linear force q distributed along the submerged length η. The resultant force F applies to the middle of the submerged beam is expressed as a function of η and q, given in equation 2.4.

It also corresponds to the hydrodynamic lift force expressed in the equation as a function of the fluid density ρ, the flow velocityU_∞, the submerged surface S, and the lift coefficient C_l. The submerged surface is the product of η and the hydrofoil chord.

$$F = \eta \times q = \frac{1}{2} \times \rho \times U_\infty^2 \times S \times C_l \tag{2.4}$$
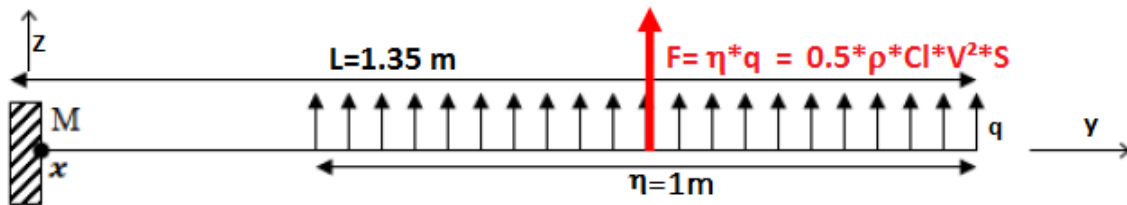
FIGURE 2.28 – Hydrofoil modeled as a cantilevered beam under linear loading q.

With Euler Bernoulli's assumptions, and considering the theorem of virtual works and the balance of moments, the maximum displacement Z computed at the tip of that beam is expressed by 2.5. E is the equivalent Young modulus of the composite beam and I_x is the moment of inertia in x-axis.

$$Z = \frac{F \times L^2}{EI_x} \times \left[\frac{L}{3} - \frac{\eta}{4} \right] \tag{2.5}$$

Figure 2.27 gives the maximum lift coefficient before stall at $\alpha = 9°$ and, for $L_i = 1m$, $C_l = 0.873$. Considering a flow velocity of $1m/s$ and the parameters given in table 2.12, the resultant underwater force applied on the foil in this configuration calculated with equation 2.4 is F = 49.7N.

Z_{max} [m]	η [m]	L [m]	ρ [kg/m^3]	U_∞ [m/s]	C_{lmax} [ ]	S [m^2]
10%L	1	1.35	1000	1	0.873	0.114

TABLE 2.12 – Geometric data and flow parameters

To have a displacement at the tip of 10% of the hydrofoil length, the bending stiffness calculated with equation 2.5 should be EI = 134.4 MP$a.mm^4$.

Material and layups

The composite materials commonly used for hydrofoil manufacturing are made up of glass fibers or carbon fibers. The choice of the orientations in the layup is given by :

— 0° will significantly stiffen the profile in bending.

— 90° will allow a better resistance to buckling on the surface of the skins and keep the shape of the section profiles.

— a mirror symmetry will be imposed in order to avoid overall deformations of the structure such as : warping. Figure 2.29 compares a laminate without mirror symmetry and with that symmetry. In both cases, they are in ambient temperature after heating. The structure without the symmetry deforms when the shape of the structure with the mirror symmetry remain the same.

— Bend twist coupling : an orientation different from 0° and 90° in an unbalanced layup allow to study the bend twist coupling phenomenon.
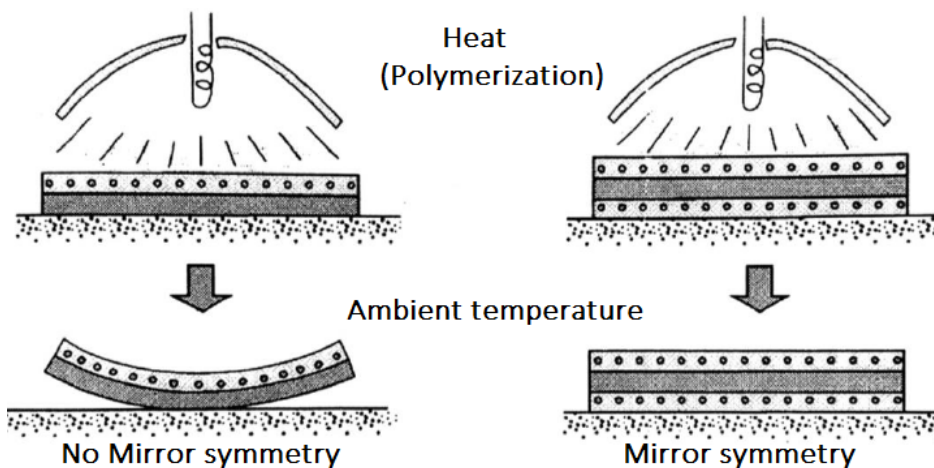
FIGURE 2.29 – The importance of mirror symmetry in the laminate layup [56].

With all these specifications and constraints, the naval architect of SEAIR proposed the four layups defined in the table 2.13. All the composite use the resin epoxy.

P_1 is made up of glass fibers with bi-axial plies oriented at $\pm45°$ and a unidirectional ply at 0°. P_2 is also made up of glass fibers, it only contains unidirectional plies and the orientations are 90°, $-45°$ and 0°. P_3 layup is the same as P_2 and only differ with $+45°$. P_4

Foils	Material	layup
P_1	Epoxy-Glass2	$[(BA_{\pm45})_2/0_{0.5}]_{sym}$
P_2	Epoxy-Glass1	$[(90/-45/0_{0.5}]_{sym}$
P_3	Epoxy-Glass1	$[(90/45/0_{0.5}]_{sym}$
P_4	Epoxy-Carbon	$[(90/0)_{sym}]$

TABLE 2.13 – Hydrofoils layups, BA is a bi-axial ply.

is made up of carbon fibers with 90° and 0° orientations.

The choice of ±45° orientations in the layups P_2 and P_3 is driven by the simplicity (existing plies in the trade with these orientations) and the design process from the engineers. This is an engineering approach from the naval architect. Using unbalanced plies (different from 0° and 90°) in the layup is an approach to cancel the fluttering effect by tailoring the BTC effect to be the twist towards feather.
The difference between P_2 and P_3 aims to investigate the influence of the sign of the ply orientation in the bend twist coupling. Figure 2.30 illustrates the plies in the layup of the hydrofoil P_2.

The hydrofoil P_4 in carbon fibers is designed to be the stiffer and could be reference as a rigid structure. The designed properties of these layup configurations are :

— P_1 : Important bending and no bend twist coupling.

— P_2 : Bend twist coupling with a negative twist.

— P_3 : Bend twist coupling with a positive twist.

— P_4 : Small bending and no bend twist coupling.
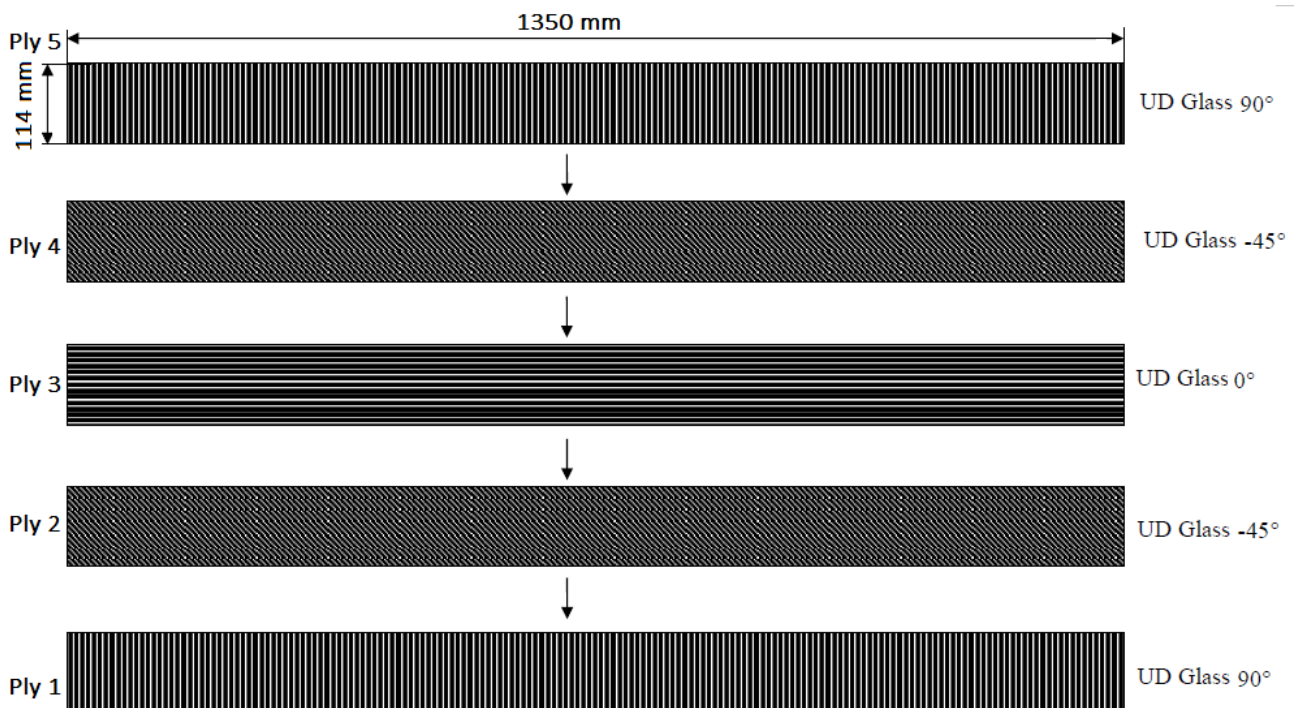
FIGURE 2.30 – Illustration of the plies in the layup P_2.

Mechanical properties of resin and fibers are given by the sellers and homogenization rules exist to obtain the properties of the unidirectional ply (see section 1.2.1).
Depending on the manufacturing of the composite, the ability of the manufacturer, the properties of the manufactured ply are different from calculation with the homogenized laws and more over, some fabrics of fibers are bought without their properties like it was the case in this work.
To determine the properties of the unidirectional ply contained in the hydrofoils, we used the materials database of IFREMER. The database is obtained by experimental tests performed over the years by IFREMER searchers on several specimens to characterize the unidirectional properties of composites plies and for a wide range of materials. It contains the homogenized properties of the resin and fibers and many properties are founded for the same composite material.
For the glass and carbon plies we needed, we calculate the equivalent properties of the laminated skins of the hydrofoils with the laminate theory using the different properties from the database and we compared these values to the bending stiffness obtained experimentally. We kept the values giving results close to the experiments.

Material	Carbon	Glass1	Glass2	Airex
E_l[GPa]	105.4	54	45	0.58
E_t[GPa]	8.6	10.4	10	0.58
G_{lt}[GPa]	3	3.9	5	
ν_{lt}	0.4	0.25	0.25	0.3
e_p [mm]	0.3	0.2	0.2	

TABLE 2.14 – Mechanical properties of the materials. The layup of P_1 uses the Glass2 when the layup of P_2 and P_3 use the Glass1.

Thus the recommended properties for the plies used to manufactured the composite hydrofoils in this work are given in table 2.14.The table gives the longitudinal and transverse modulus of elasticity E_l, E_t, the shear modulus G_{lt}, the Poison coefficient ν_{lt} and the thickness of a ply e_p. The theoretical thickness of the hydrofoils skin are given in table 2.15.

Hydrofoil layups	P_1	P_2	P_3	P_4
t[mm]	1	1	1	1.2

TABLE 2.15 – Theoretical thickness of the laminated skins of the hydrofoils.

Figure 2.31 shows an example of distribution of the pressure coefficient on the NACA 0015, this case is computed at 3° of incidence and the Reynolds number is 3×10^5. Most of the effort is concentrated on the first half of the profile towards the leading edge.

To ensure the shape of profile under the hydrodynamic loads, the section structure is designed in sandwich composite : composed of a skin described by the layups in table 2.13 and a web. The web is a non structural foam only ensuring the profile shape. The material chosen is the "Airex" foam, its properties are given in table 2.14.
The advantages of the sandwich section :

— Avoid the buckling that may be important with large deformations.

— Ensure the shape of the hydrofoil section everywhere

— Transmit the shearing stress between the two skins.
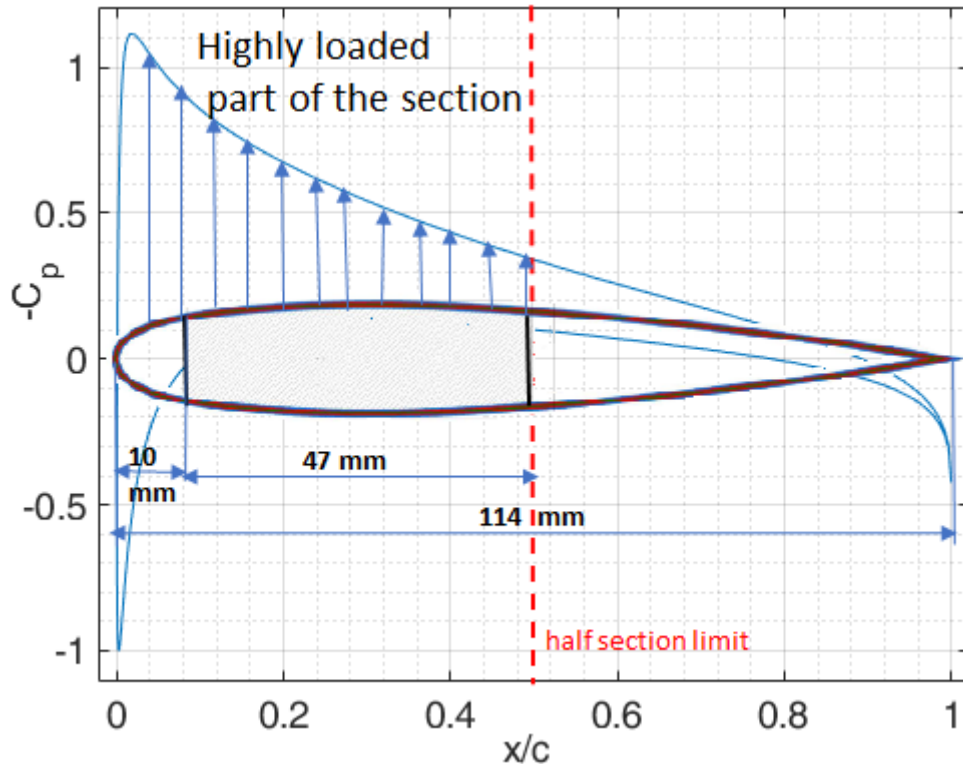
FIGURE 2.31 – Distribution of the pressure coefficient on the section of the hydrofoils. NACA0015, $Re = 3 \times 10^5$, $\alpha = 3°$.

The location of the web on the section is also described in the figure. The web is placed in the first half of the section and a gap of 10 mm is left between the trailing edge and the web to allow the mould to close on that side.
The illustration of the layups for all the hydrofoils is presented in appendix B.

2.2.1.4 Manufacturing process

We made the foils ourselves, in the SEAIR manufacturing workshop by a **contact lamination**, followed by a vacuum application. This process is divided in two main parts : laminating the composite skin in the mold and the vacuum application in the mold.
The process goes through several steps :

— Mold cleaning : a very important step that affects the roughness and the surface quality of the composite skin.

— Layup preparation : the fibers fabrics are cut according to the mold dimensions and the layup orientations.

— Stratification : the fibers are impregnated in the resin and put in contact with the mold. This operation is performed on each side of the mold open.

— 3 fabrics specially dedicated to the stratification process are then applied on top of the fibers in the mold respecting the following order :

  — de-laminating fabrics : it helps to ensure the tightness, makes the surface mat and easier to sand

  — Perforated fabrics : it allows the excess resin to escape from the composite layer

— Drain : it absorbs excess resin during the process

The next step is vacuum application. The vacuum suction process is very simple, after the first stage, the two sides of the open mold are put into a vacuum bag as presented in figure 2.32. The bag is hermetically sealed and connected to a pump by a hose to create depressurization.The vacuum operation lasts 12 hours.
The composite cures by crosslinking the resin at room temperature and the excess resin is vacuumed during the cure.
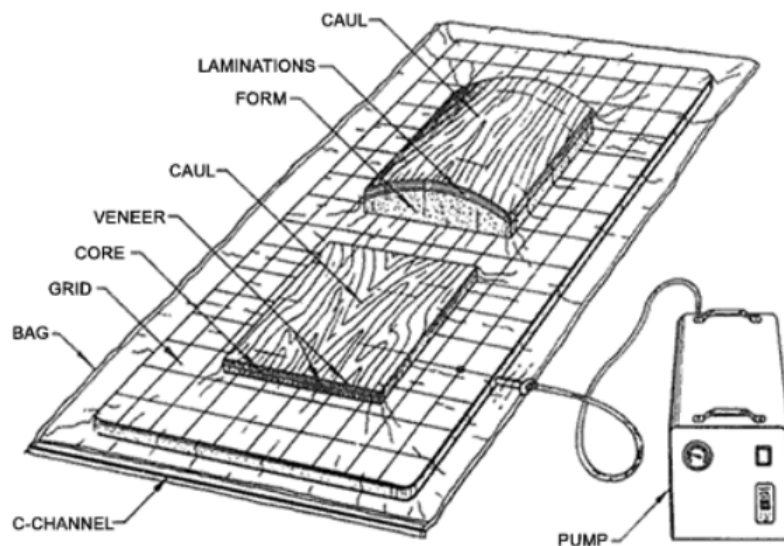
FIGURE 2.32 – Vaacum press.

When the vacuum process is done, the hydrofoils are still in two parts in the open mold. The 3 special fabrics are removed from the internal part of the composite and the composite is sanded from inside to ensure the quality of the next operations.
The next step consist in glueing the web onto the skins with a resin glue. The web is cut into two part in its mid-plane and each part is glued on the two parts of the hydrofoils in the open mold.

The last step of the manufacturing process is to close the mold. The resin glue is added on the leading edge and the trailing edge and the two parts of the mold are bolted. The mold remain closed during 6 hours to ensure the resin curing and the hydrofoils foils are manufactured as shown in figure 2.33.

FIGURE 2.33 – Hydrofoils after demolding
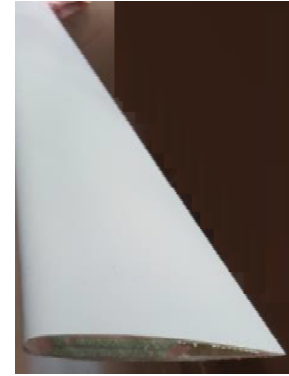
FIGURE 2.34 – Sanded and painted foils

The resin glue used is the Spabond 345. Its used on the trailing edge and leading edge brings bulges and imperfections in the hydrofoils.

Some finishing is required before use :

— Few centimeters are cut at the ends of the structure to remove excess glue and other imperfections and the hydrofoils are $1.35m$ span length.

— The part of the surface going under water is sanded and painted with gel coat to have a good surface finish (figure 2.34)

— Foil base manufacturing : to ensure the connection of the structures with the experimental system, the foils base are directly manufactured on the foils. The equipment used in this operation are presented in figure 2.35 : the black mould of the foil base and a pink 3D-printed piece locating the hydrofoil during the operation.
The process consists in molding the resin directly on the foils as shown in figure 2.36. The foil is put into the black mold, the 3D printed piece is used to locate the foil in the mold and the resin is cast inside.
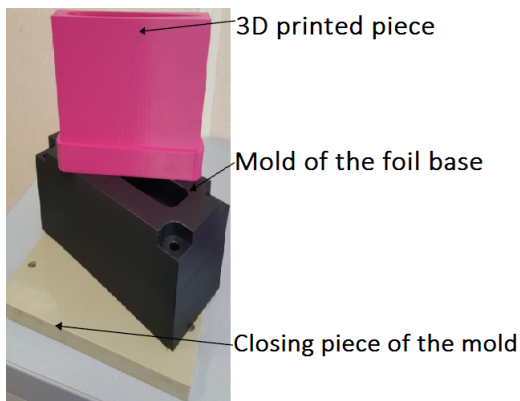
FIGURE 2.35 – Setup of Foil base 's molding

FIGURE 2.36 – Molding process of the foil base

The foil base is thus a resin piece directly molded on one end of the hydrofoil. Its shape presents two parallel faces drilled by two through holes. The parallel faces help to adjust the foil in the clamping system and the holes are used to bolt the base during the tests.

2.2.1.5 Manufactured hydrofoils

As a summary of the manufacturing process, figure 2.37 and 2.38 show the CAD representation of the hydrofoils composition and the manufactured geometry.

The white coat represents the part going under water. A cut-section of the layup P_2 is also presented, the green AIREX is clearly visible, the black part close to the leading edge
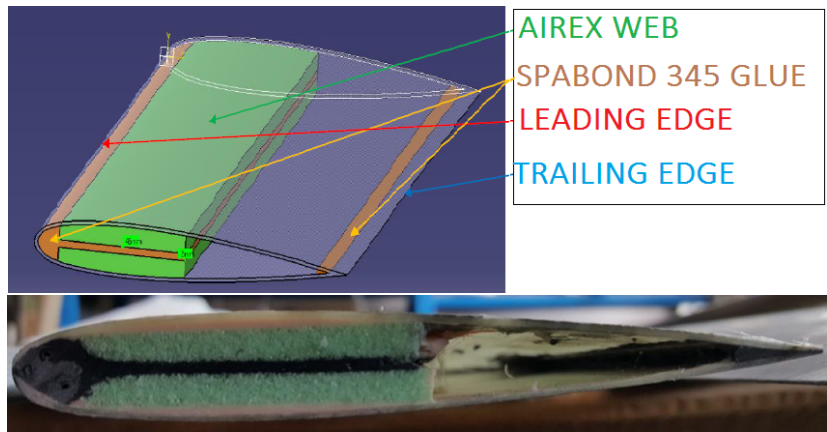
FIGURE 2.37 – Manufactured section of the hydrofoils P_2

is the Spabond 345 glue and the white part is the glass fibers.
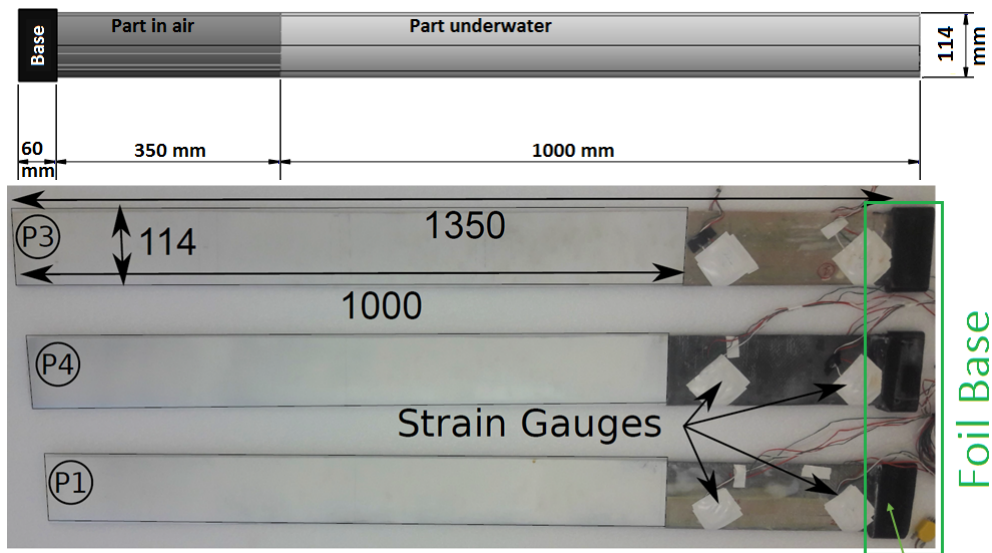
FIGURE 2.38 – PCAD and image of the final hydrofoils showing the strain gauges equipment.

Strains gauges are glued on the part staying in air but their measurements will be unusable.

2.2.2 Mechanical characterization

The straight foils are considered as a beam, with an equivalent bending stiffness EI_x and torsional stiffness GJ, constant along the span (Y-axis). X-axis is tin the chordwise and Z-axis is normal to X, in the section plane. Three different methods are used to experimentally determine the EI_x modulus of the four composite structures :

— Tensile tests on representative specimens.

— Bending tests on the hydrofoils : they are performed on one hand to calculate the bending stiffness of the structures and on the other hand to investigate the bend twist coupling phenomena.

— Vibration tests on the hydrofoils.

The torsional stiffness is obtained by torsion tests. The experiments investigating EI_x are performed at IFREMER Brest and the investigation of the BTC and GJ is performed at IRENAV.

The laminate theory, an analytical method giving the laminate behavior is also used.

This part firstly describe the bending stiffness by the laminate theory and the experimental setup of each test is presented.

2.2.2.1 Laminate theory

The bending stiffness we are looking for is the product E_{yx} (see figure 2.43 for the reference system (X,Y,Z)). E_y is calculated with the laminate theory and I_x is obtained on a CAD tool.
The laminate theory described in section 1.2 allows to computes the equivalent properties E_x, E_y and G_{xy} of a laminate using the properties of each ply contained in the laminate. The theory was coded in an excel tool at IFREMER and we used that tool to compute the equivalent properties of the layups.

The inertia are calculated with the laminate thickness given in table 2.15 and does not consider the AIREX web in the geometry. The AIREX modulus being hundred times lower than the longitudinal modulus of the glass and carbon plies, its influence in the bending stiffness of the hydrofoils is negligible.
Figure 2.39 shows the laminate skin of the layup P_4 modeled on the CAD tool solid works, an analysis of the section in the tool gives the intertia of the section as shown in the figure.
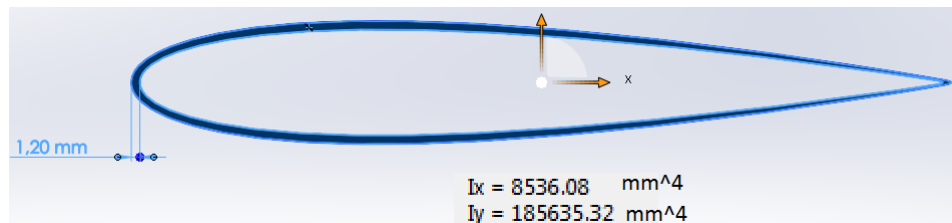
FIGURE 2.39 – Example of inertia calculated with SolidWorks, skin of the layup P_4.

The results of the bending stiffness computed with the laminate theory are given in table 2.16. To simplify the notation we are using EI for the bending stiffness $E_y I_x$.

Hydrofoil layups	P_1	P_2	P_3	P_4
E_y [GPa]	21.2	20.7	20.7	52.7
I_x [mm^4]	7273.4	7273.4	7273.4	8536.08
EI [N.m^2]	153.9	150.3	150.3	449.4

TABLE 2.16 – Bending stiffness of the hydrofoils calculated with the laminate theory.

2.2.2.2 Tensile tests

Tensile tests are performed on specimens, representative of the hydrofoils properties to determine the tensile modulus of the composite. The specimens are thin plates manufactured at during the manufacturing of the hydrofoils with the same layups plan of the skins and the same materials.

2.2.2.2.1 Specimen description

During the hydrofoils manufacturing, three squared plates of $200 \times 200 mm^2$ were simultaneously fabricated according to the layups of P_1, P_2 and P_4.

Specimen name	1A	1B	1C	23A	23B	23C	4A	4B	4C
Lenght L [mm]	21.9	20.8	23	21.9	23.7	21.1	23.1	24	21.5
Width l [mm]	1.5	1.49	1.5	1.11	1.05	1.06	1.33	1.33	1.3
Thickness t [mm]	1.5	1.5	1.5	1.1	1.1	1.1	1.4	1.4	1.4

TABLE 2.17 – Specimen for tensile tests according to ISO 527 standard.

The laminate theory predicts the equivalent Young modulus of P_2 and P_3 to be the same so, only one layup specimen is manufacture for both. For each layup, three specimens (A,B,C) whose dimensions comply with the standard ISO 527 are cut from the plates and their geometries are given in table 2.17.

The specimen were manufactured respecting the same material and layup w*of the composites. The thickness of the specimen given in table 2.17 show a difference between the theoretical values (see table 2.15) and the thickness of manufactured structures.

Specimens 23 stand for both P_2 and P_3, a picture of the specimen 1A is shown in figure 2.40.
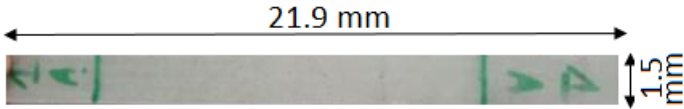
FIGURE 2.40 – Specimen 1A of the layup P_1 and its dimensions.
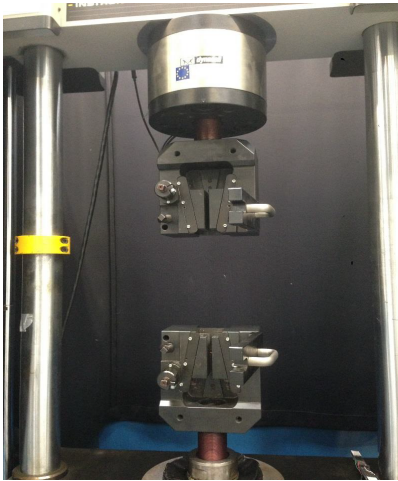
FIGURE 2.41 – Experimental setup for tensile tests.

2.2.2.2.2 Experimental setup

Figure 2.41 shows the tensile machine used for tensile tests. The principle is the same as described in 2.1.2.1, the tests are triggered by a computer which records the measures. A specimen is fixed in the clamping jaws of the machine and the displacement speed is fixed. During a test, the machine pulls on each side creating a tensile stress which deforms the structure. The specimen is gradually elongated and its section is reduced until

it reaches the rupture. The computer records the forces exerted on the specimen and the movement of the jaws, corresponding to the elongation ΔL of the specimen.

2.2.2.2.3 Data post processing

The strain in the structure is the ratio of the specimen elongation ΔL on the length of the specimen as given in equation 2.6. The stress described in equation 2.7 is the ratio between the force to the cross section (the product of the width and the thickness) . L is the initial length of the specimen, l is the width and t the thickness.
The stress is linked to the strain and the elasticity modulus E in the elastic domain by the Hooke 's law given in equation 2.8.

$$\epsilon[\%] = \frac{\Delta L}{L} \tag{2.6}$$

$$\sigma[\mathrm{MP}a] = \frac{F}{l \times t} \tag{2.7}$$

$$\sigma = \mathrm{E} \times \epsilon \tag{2.8}$$

The measures recorded are used to calculate the stress and the strain and, the evolution of σ versus ε is linear in the elastic domain. The Young's modulus E is the slope of the curve in the elastic domain which is theoretically assumed to correspond as a strain of $\epsilon \in [0 - 0.2\%]$.

Figure 2.42 shows the evolution of the stress in the structure with the strain, recorded during the experiments for the specimen 1B and 4B.
In the glass 1B, when the stress increases in the structure, the curve is first linear showing an elastic domain, followed by a small plastic behavior and the stress decreases until the break. This elastic behavior is enhances with the bi-axial plies of ±45° in the layup 1.
The carbon specimen 4B which is a fragile exhibits an elastic behavior but many breaks are observed on the curve. These breaks correspond ruptures that appeared the structure. Only the plies at 5° works against the tensile stress. The graph also shows the linear regression computed in the elastic domain for each specimen and, the elasticity modulus is directly the slope.
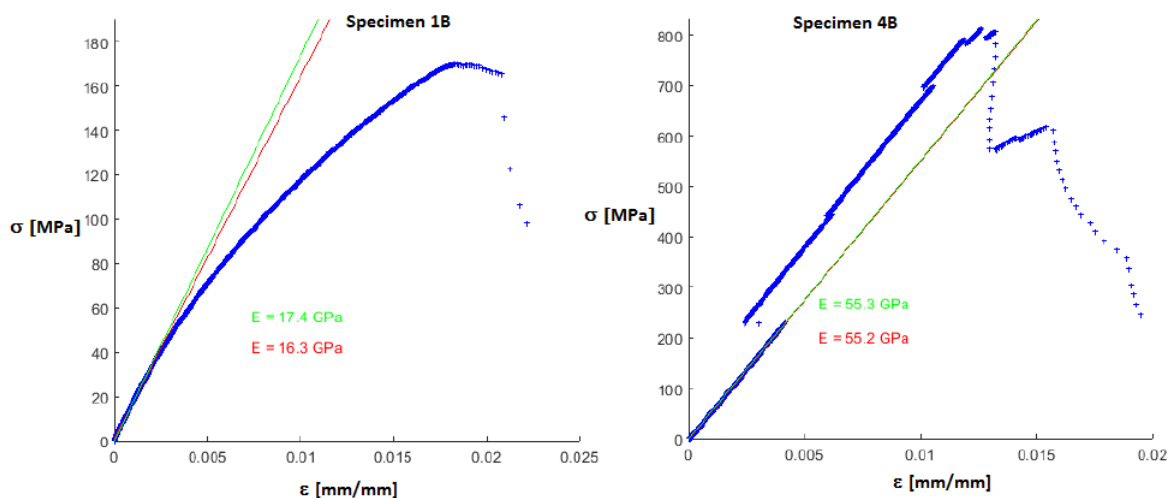
FIGURE 2.42 – Evolution of stress with the strain in the tensile tests on the specimens. 1B is the glass laminate P_1 and 4B is the carbon laminate P_4.

The results of the tensile tests are given in table 2.18. The tensile modulus Ey is average on the different specimens and the inertia are first calculated using the using the theoretical thickness of the laminates (see table 2.16). The elastic modulus obtained with the tensile tests are lower than the results of the laminate theory up to 27%. and a second time using the thickness of the specimens (see table 2.17).

Hydrofoil layups	P_1	P_2	P_3	P_4
E$_y$ [GPa]	15.5	18.93	18.93	42.53
EI [N.m^2]	112.74	137.7	137.7	366.06
I$_x$ modified [mm^4]	10207.55	7977.59	7977.59	9646.69
EI [N.m^2] modified	158.2	151.02	151.02	410.305

TABLE 2.18 – Bending stiffness of the hydrofoils calculated with the tensile tests.

The values obtained with the modified inertia are very close to the laminate theory.

2.2.2.3 Bending tests

Due to the BTC, the bending tests are divided into two parts, each part having a dedicated experimental setup. The bending test are performed for two investigations on two setups. With the hydrofoil geometries, a conventional test bench could not be used, thus experimental setups were installed for the purpose of these tests. The first section describe the bending tests investigating the bending stiffness of the hydrofoils and the second section describe the bend twist coupling investigation.

2.2.2.3.1 Bending stiffness investigation

The bending tests are directly performed on the hydrofoils to determine their bending stiffness. The experimental setup shown in figure 2.43 is mounted at IFREMER Brest.
The foil is clamped and bolted thanks to the foil base at 1m height from the ground to a support. The clamping system is identical to the clamping conditions applied in the hydrodynamic tests.
Four different calibrated masses {M$_1$ = 518g, M$_2$ = 1018g, M$_3$ = 2018g, M$_4$ = 3018g} are applied at a position Y = 850mm from the root (See Figure 2.43).
The load is applied using a foam machined hook system that can slide along the foil. This hook system has an outer groove into which a rope is inserted and the load is suspended at the rope.
The vertical displacement Z of the foil is measured thanks to a laser telemeter. The measurement are performed on only one point, the middle point of the section located at a distance Y = 1250mm from the root.

The laser is connected to a computer and measures during 10 sec with an acquisition frequency of f_{acq} = 100Hz. A first measurement is performed without loading and a second measurement is performed with the loading, the difference gives the bending displacement under the applied load.
The bending tests are performed as follows :

— Installation of a foil on the test bench and tightening of the jaws around the base

— Positioning of the laser above the foil at a distance of 125 0mm from the root

— Laser acquisition on the un-deformed foil
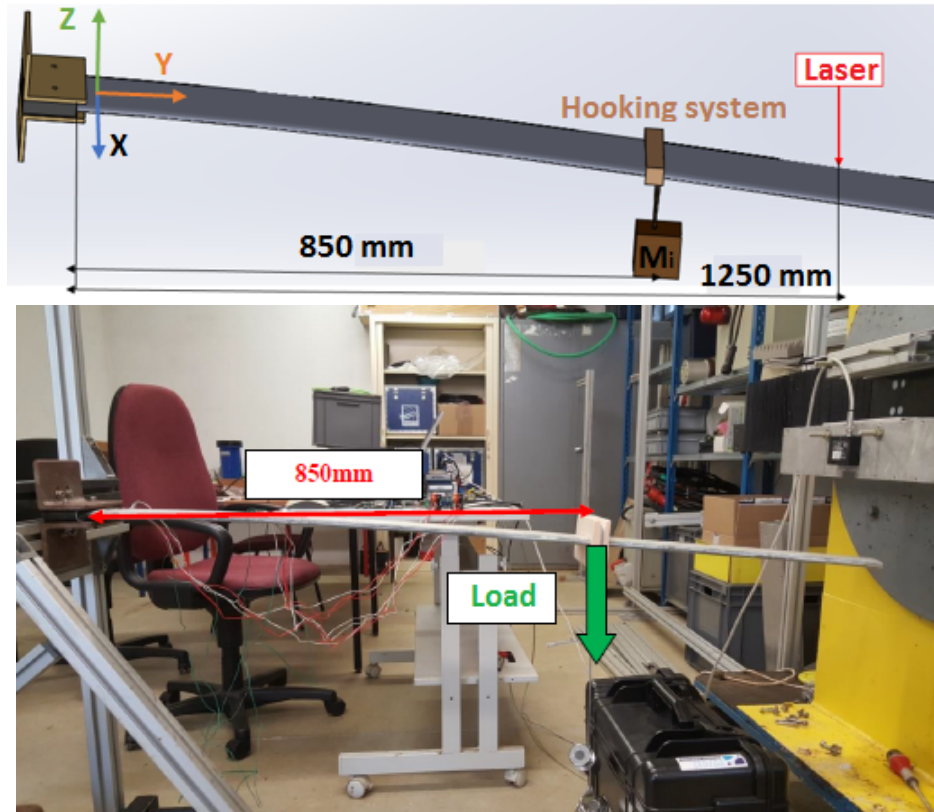
FIGURE 2.43 – Experimental setup of bending tests and vibrations tests.

— Installation of a known mass M on the hooking system at the distance of 850 mm from the root

— New laser acquisition on the loaded foil

— Repetition of the operations for the different masses and processing of the measurements

The output of a test is the vertical displacement of the hydrofoil measured at Y = 1250mm. The test is performed for all the masses and the values are averaged.

The stiffness EI of the structure is calculated with from equation 2.1 as follows :

$$EI = \frac{M \times g \times Y^2(3X - L)}{6Z} \qquad (2.9)$$

2.2.2.3.2 Bend twist coupling investigation

These tests are performed at IRENAV and the experimental setup is the same installed at IFREMER. The clamping and loading system are the same, the only difference with the previous tests is the measurement points of the displacements.

The foil is cantilevered on a marble table with clamp seals and a punctual load is applied at the section S$_1$ located at Y = 1250mm. A laser is mounted above the structure on a rail to measure the vertical position. In that case, the laser moves continuously in the chord direction and measures the entire shape of a section.The laser can also be moved manually along the span to change the measurement section.

Figure 2.44 shows the measurements position on the foils. A load M$_1$ = 2.22kg is applied
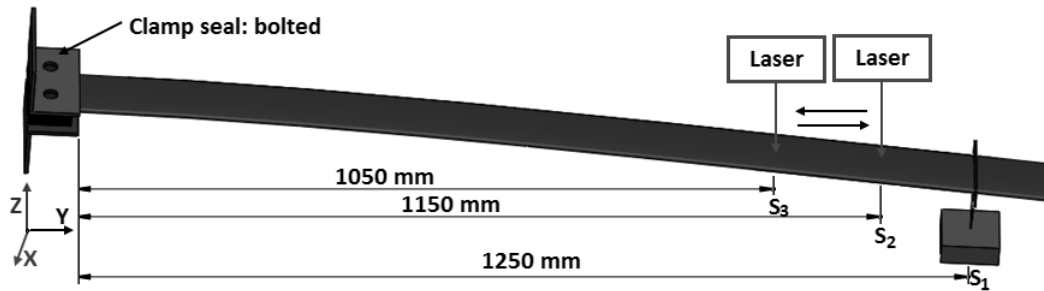
FIGURE 2.44 – Bend twist coupling investigation with bending tests.

on the section S_1 located at $1.25m$ from the root and the laser measures the vertical position of the sections S_2 and S_3, giving their shapes. The distance of these section from the hydrofoil root in the spanwise is given in the figure 2.44.

A continuous measurement of the vertical position of S_2 and S_3 is recorded. A complementary set of measurement is also performed on five points equally located along the chord of the sections. The location of these points in the chordwise is given in table 2.19, the reference $X = 0$ mm is at the leading edge.

Layup	$Point_1$	$Point_2$	$Point_3$	$Point_4$	$Point_5$
X [mm]	20	40	60	80	100

TABLE 2.19 – Position of the measurement points along the chord of S_2 and S_3.
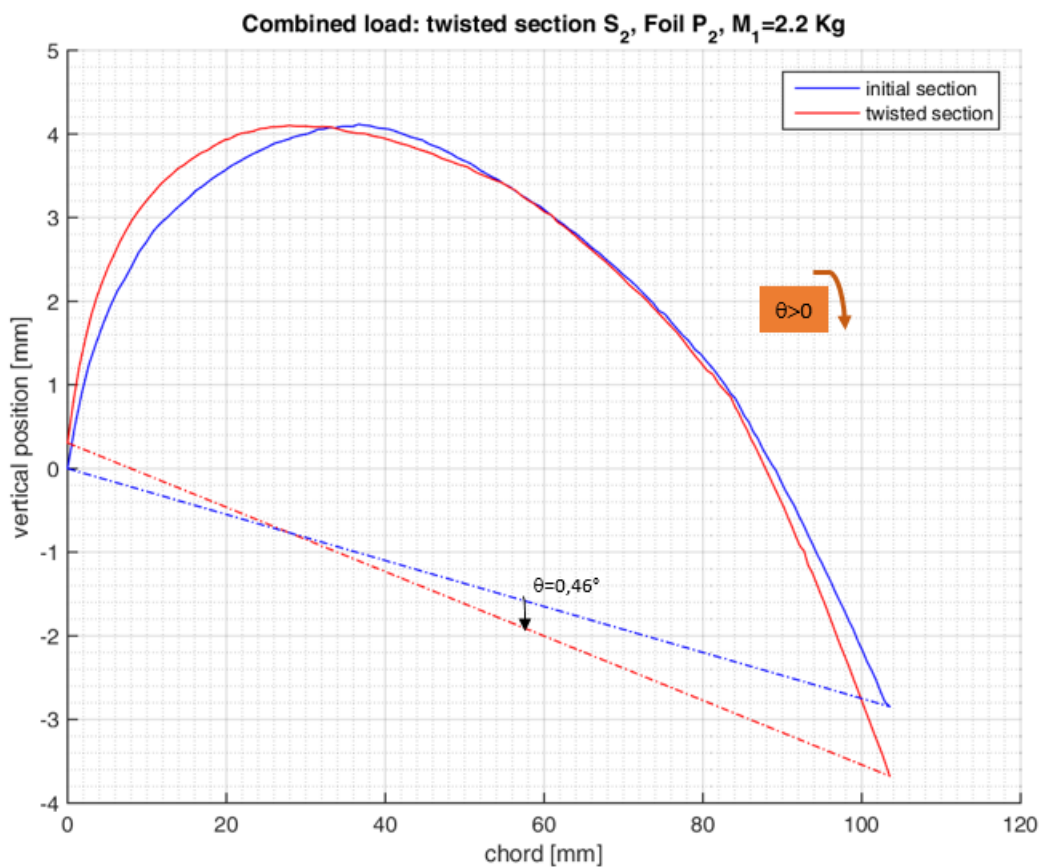
FIGURE 2.45 – Shape of the section S_2 under the bending load M_1 for the layup P_2.

An example of the measurement performed on section S_2 for the layup P_2 is given

in figure 2.45. The curve of the vertical position versus the chord gives the shape of the section. The measurement is performed without and with loading, a comparison of the shape under loading and without loading gives the twist angle induced by that loading.

2.2.2.4 Vibration tests

The vibration tests are also performed directly on the hydrofoils. The structure are cantilevered in the experimental setup described in the bending tests (figure 2.43) and a dynamic bending force is manually applied.
The vibration method consists of determining the natural frequency of the foils from the temporal measurements of the laser using a FFT and, the bending stiffness EI of the structure is calculated by (2.10).

$$\text{EI}_x = \left(\frac{(2\pi \times f_1 \times \text{L}^2)^2}{\lambda_1^4} \right) \times m \tag{2.10}$$

f_1 : the natural frequency of the first bending mode
λ_1 : a number associated to the first proper mode, depending of the boundary conditions
m : the structural weight per unit of length
L : the length of the structure.

The tests are performed as described in the following procedure :

— Installation of a foil on the test bench and tightening of the jaws around the base.

— Positioning of the laser above the foil at a distance L from the root.

— loading by the user (punctual shock) : the structure is manually displaced in the vertical direction and released. Then, natural and damped oscillation starts.

— Laser acquisition during the foil vibration until the foil returns to its quasi-static position : the laser measures the temporal evolution of the vertical displacement.

— Processing of the temporal acquisition : a FFT (Fast Fourier Transformation) is perform to analyse the measurements.

— Extraction of the frequency of the first natural mode and calculation of the bending stiffness EI.

2.2.2.5 Torsional tests

The setup of these tests is the same defined in figure 2.38, the only difference is the loading method. A punctual load, off-center as shown in figure 4.4 is applied on the structure through a plate designed for this purpose. The plate can slide along the hydrofoil and has two slots helping to set the loading. A mass is hanged at a rope and the rope is inserted in the slot of the loading plate.
To allow only the twist motion under this load, the tip of the hydrofoil is placed on a vertical spike locking the bending motion.
The loading is applied on section S_1 and the laser measures the vertical position of the sections S_2 and S_3 (see figure 2.43).
The comparison of the shape of a section without and with loading gives the twist angle θ due to the loading, as shown in figure 2.45.
We calculate the torsional stiffness GJ with the beam theory, using the measured twist
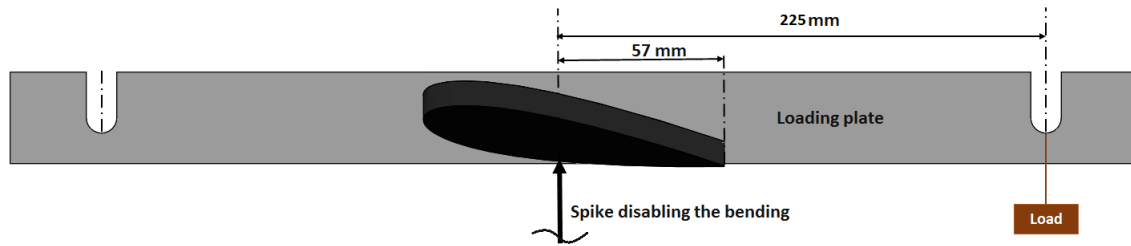
FIGURE 2.46 – Experimental setup of the torsional tests.

angle θ and the geometrical parameters by equation 2.11. l is the distance of the measurement section from the hydrofoil root.

$$GJ = \frac{M_t \times l}{\theta} \tag{2.11}$$

The results expected from these tests are the torsional modulus and the twist angle presented in section 4.2.

2.2.3 Test flume of IFREMER Lorient

To investigate the fluid structure interactions on the composite hydrofoils, hydrodynamic experiments are performed in the test flume of IFREMER Lorient. their drag efficiency but, also serves to carry out other types of experiments such as flow around hydrofoils.
The hydrofoil is immersed in the pool at a fixed position while the water circulates in a flume in a closed loop.
The output of these tests is the hydrodynamic forces and the displacement of the structure under the hydrodynamic loading. The analysis of the results will help to understand the hydrofoil behavior, to investigate the BTC and to validate the numerical tools.
This section describe the experimental setup and the configurations investigated.

2.2.3.1 Description of the experimental setup

Overall dimensions of the test flume are $24.50m$ long, $7.50m$ wide and $3.30m$ high. It is a closed-loop fresh water circulation basin, with a concrete flume of $12m$ long, $2.6m$ wide and $1.5m$ deep as shown in figure 2.47. The working length is $6m$.
The basin consists of two main parts : a flow vein ⑤ in which the experiments take place and a return vein ①. The flow and the return veins are installed on the same horizontal plane. An inspection hatch is used to clean the interior of the walls. In the elbows, fins guide the water flow. The current generating system is installed just upstream of the last bend before the homogenization system ②, located at the beginning of the flow vein.

The current is generated by a propeller with four fixed blades, 1.23 m in diameter, driven by an 88 KW motor rotating at a maximum speed of 1540 rpm. A reducer reduces the propeller's rotational speed to a maximum of 210 rpm. The velocity of the fluid varies from 0.1 to 1m/s, and is controllable by means of the propeller, which reproduces the effects of the sea during the experiment.
The mobile gateway ④ allows the observation of experiments from above and the installation of the instrumentation. The installation has also a $5m^2$ observation window where the tests can be observed from the side way ⑥.
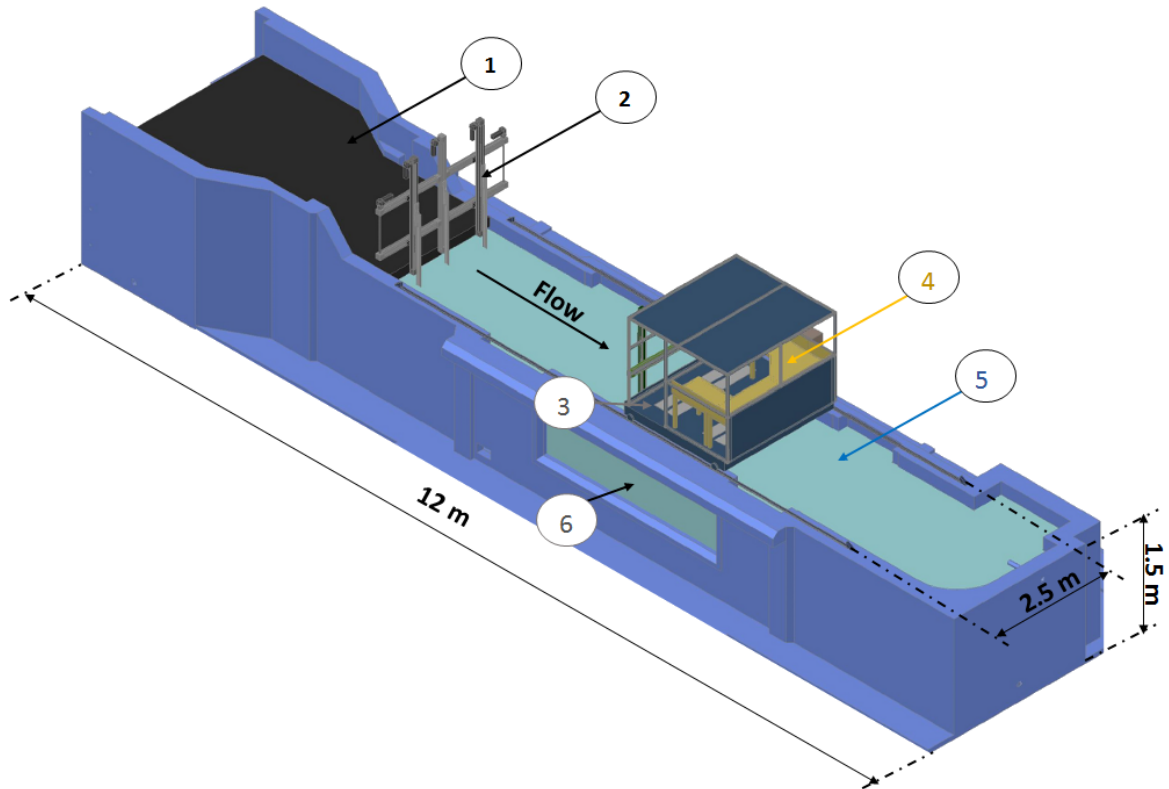
FIGURE 2.47 – Test flume of IFREMER Lorient, [Ref Ifremer].

2.2.3.2 Installation of the hydrofoil and measurement of the forces

The installation of the structure to be tested is realized through the floor of the mobile gateway ③ (figure 2.47). A 6-DOF balance is bolted to the footbridge and the hydrofoil base is bolted on the support of the balance as shown in figures 2.48 and 2.49.
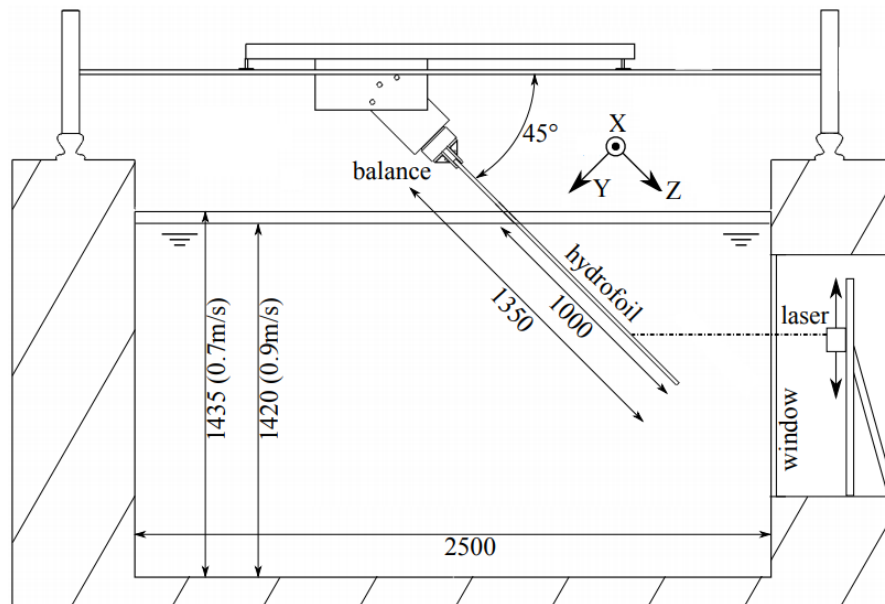
FIGURE 2.48 – Section of IFREMER Lorient flume 's main characteristics and experimental set up with the hydrofoil. Water level changes with flow speed.
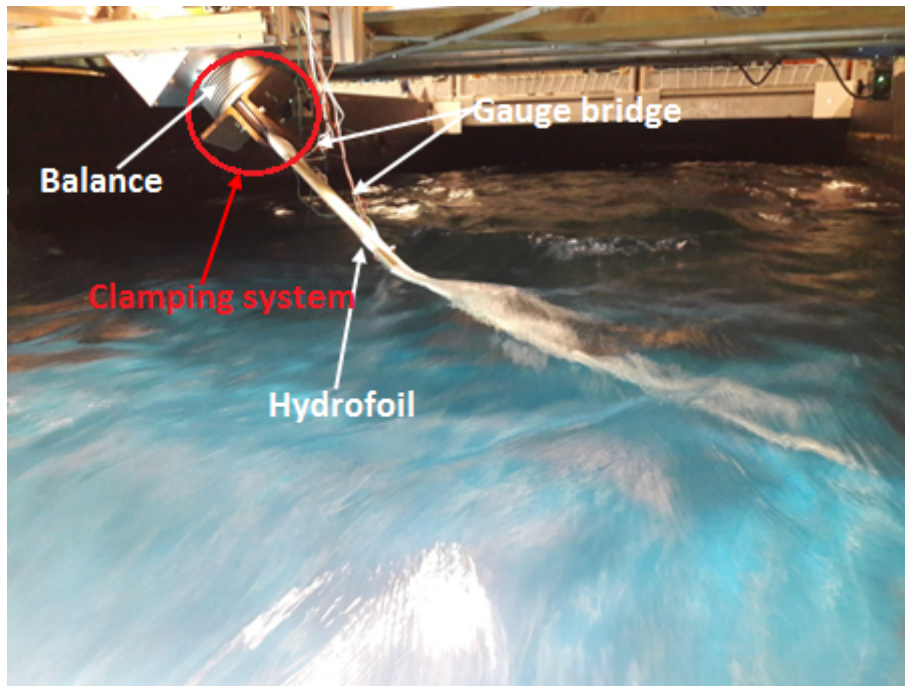
FIGURE 2.49 – Hydrofoil tested in IFREMER Lorient flume at 0.9ms and AoA= $-9°$. The hydrofoil is connected to a 6DoF balance and pierces the free surface at 45°.

As shown on the figures, the foils are piercing the free surface with an angle of 45° and mounted cantilevered on the balance which measures the hydrodynamic forces. The clamping conditions are the same used for the mechanical characterization tests, the flow is aligned with X-axis and the working section is 2.5m width and 1.5m depth.

The 45° tilt angle is chosen for the hydrofoils to experience similar interactions as the MINI 747 hydrofoil with the free surface and to analyze its effects on the hydrodynamic performances of the hydrofoils. It also has the advantage of maximizing the immersed surface with a low ground effect.

The balances rotates with the hydrofoil and records the forces in the hydrofoil reference system (X,Y,Z), (see figure 2.48). The principle of the balance is the same as the one described in section 2.1.3 and the balance outputs are the forces and the moments in the three directions.

A gauge bridge (see figure 2.49) made of two strain gauges is mounted on the hydrofoil as complementary measurement to the balance, to locate the application of the resultant hydrodynamic force. Unfortunately the measurement by gauges will give non-physical and unusable values.

2.2.3.3 Measurement of the displacements

The displacements of the hydrofoils under the hydrodynamic loads are measured with a laser telemeter based on the principle described in section 2.1.3. Figure 2.48 shows the laser placed in front of the observation windows, the laser beam goes through the window and the water.

The lateral displacements of the foils are measured at 3 different heights, located in the spanwise at Z = {1050mm,1150mm,1250mm} from the root. The laser sweeps 10 consecutive times the foil in chord wise at the different height in order to average the distance.

2.2.3.4 Laser calibration

A calibration of the laser is performed prior to the tests to correct the diffraction effect due to the different interfaces that the laser beam encounters.
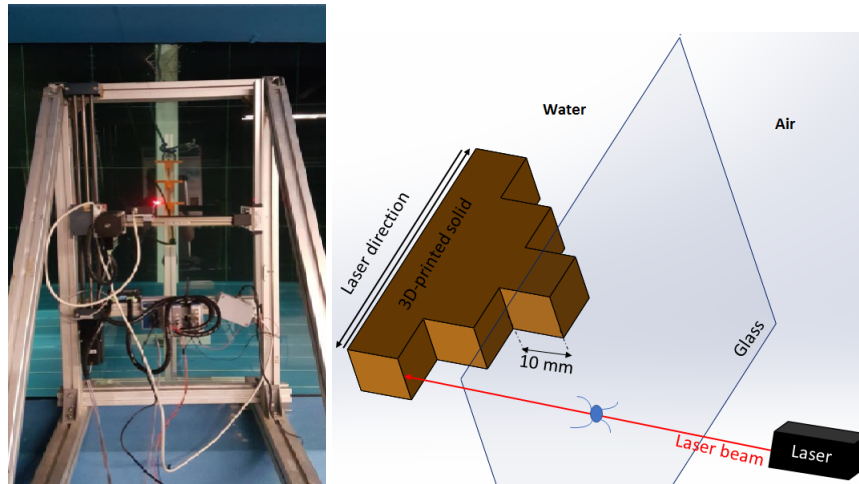
FIGURE 2.50 – Setup for the laser calibration showing in orange the 3D-printed shapes.
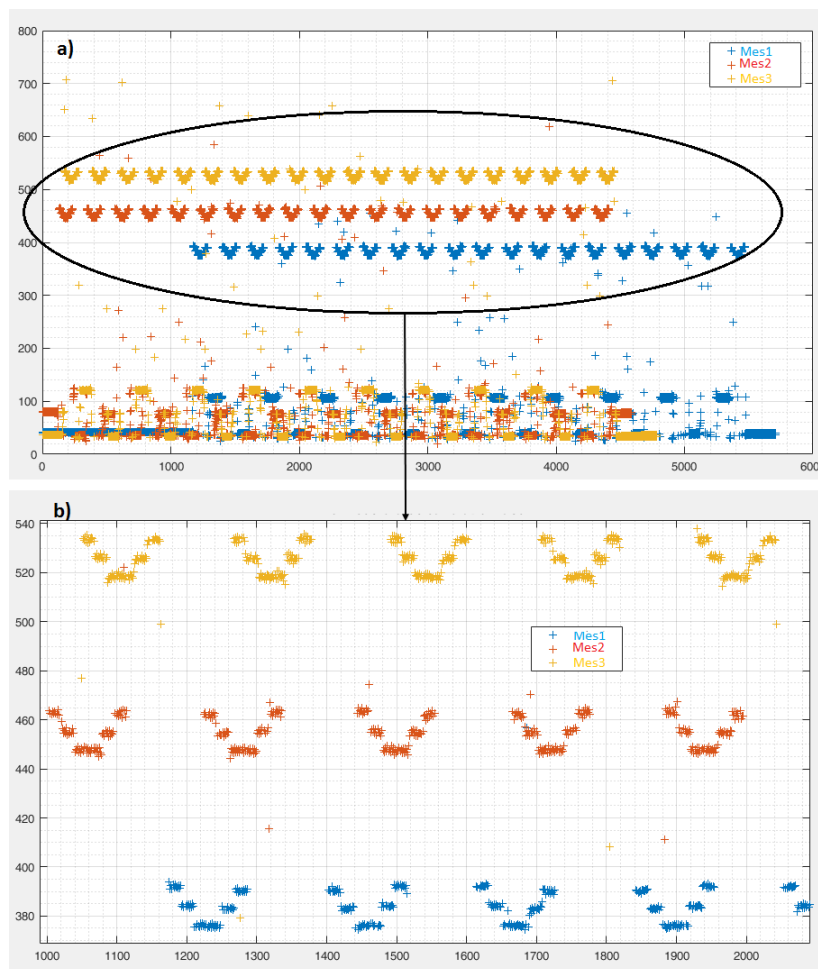
FIGURE 2.51 – Shape of the calibration pieces measured with the laser : a) direct output, b)Measurements filtered.

Three 3D printed pieces shown in orange in figure 2.50 are placed at the three measu-

rement positions. The geometry of the pieces are known. The calibrating pieces are bolted on a ladder and put in the flume with water at the location of the foil. The laser measures their shape and a comparison to the real geometry gives a factor of correction.

Looking a the shape of this calibrating solid, the shape measured will be a two step stair, the real distance between the steps of that stair is $D_O = 10mm$.

Figure 2.51 shows a graph of the recorded measures of the calibration process. On figure 2.51. a, three sets of measurements describing the three objects is clearly observed (Mes1, Mes2, Mes3). The figure also shows noises polluting the measurements.

In order to reduce the noises, a filtering process is perform on the data and figure 2.51. b shows the filtered data. The shape of the objects are clearly visible for each measurement position, the symmetric stair with 2 steps on each side is well defined.

After the filter, a mean value is overloaded on each step and the distance D_L between the steps of each object is measured as shown in figure 2.52.
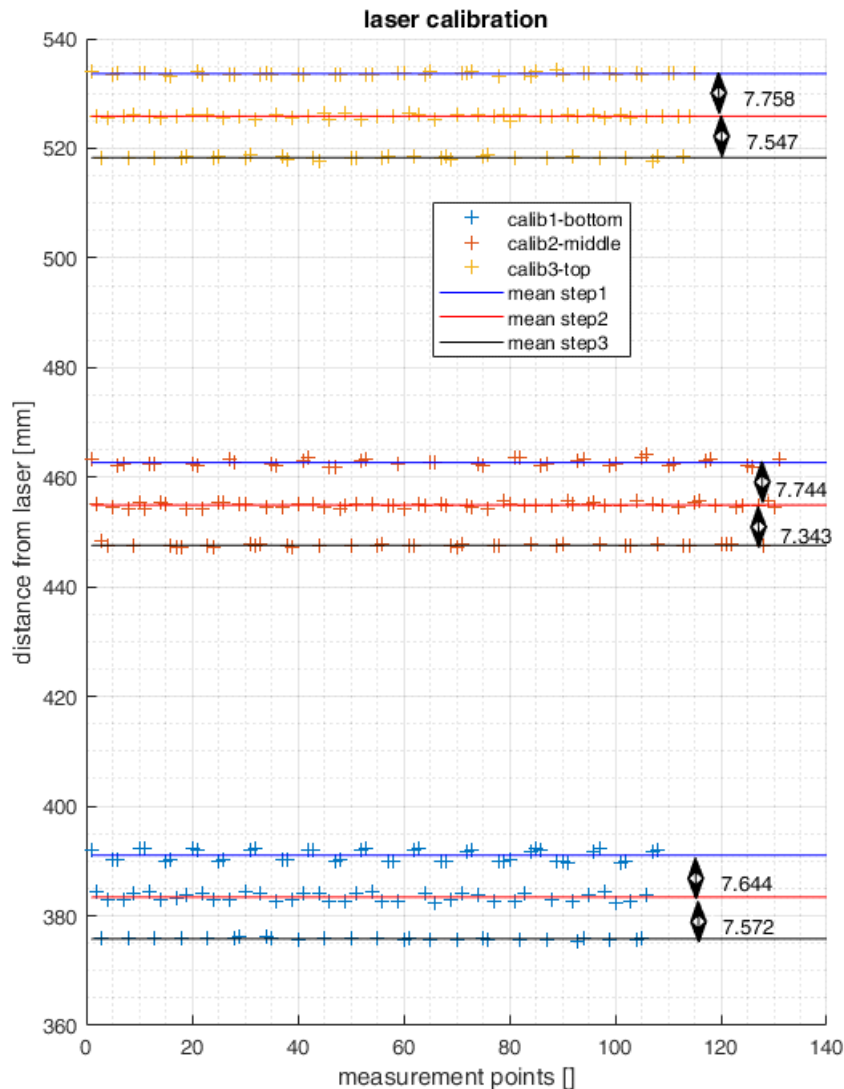
FIGURE 2.52 – Laser calibration

The values are similar, underlying no influence of the water volume crossed by the laser or no influence of the spot where the window is crossed.

The correction factor can thus be calculated as the ratio between the actual measurement D_O of the object and the laser measurement D_L as given in equation 2.12.

$$K = \frac{D_O}{D_L} \tag{2.12}$$

The average of this values gives K = 1.32.

2.2.3.5 Configurations investigated

Figure 2.53 shows a picture of the hydrofoil tested in IFREMER Lorient flume at 0.9ms and $\alpha = -9°$, from the observation window.
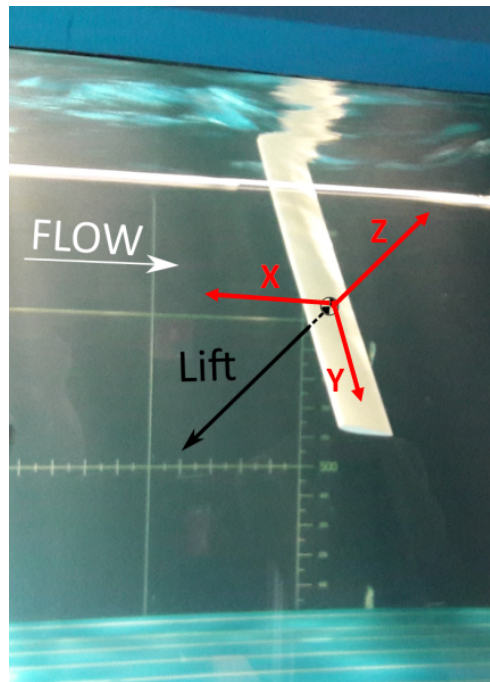
FIGURE 2.53 – Picture of the hydrofoil tested in IFREMER Lorient flume at 0.9ms and AoA= $-9°$, from the observation window.

The configurations investigated are negative angle of attack, to enhance the laser telemeter measurement and to prevent the tip to get to close to the window of the flume. Two speeds $U_1 = 0.7 m/s$, $U_2 = 0.9 m/s$ and several angles of attack ranging from $[-9°, -3°]$ are investigated. As most of flume, the free surface height varies with the velocity : $1.435 m$ for $0.7 m/s$ and $1.42 m$ for $0.9 m/s$ (see figure 2.48).
The output are displacements recorded with the laser and the hydrodynamic loads measured with the 6-DOF balance. The measurements from the gauges are unfortunately not exploitable and should ask much more development to be used.

2.3 Post processing of the balance and laser measurements

The hydrodynamic balance and the laser used to measure the hydrodynamic forces and the displacements of the structures are similar for both model-scale hydrofoils and the composite hydrofoils.
This part describes the post-processing applied on the data recorded during the hydrodynamic tests both in the tunnel of IRENAV and in the flume of IFREMER. It starts by

describing the conversion of the voltage signal recorded by the balance into forces in the first section and, the second section is dedicated to the laser. The laser calibration is presented and the post processing of the post-processing is discussed.

2.3.1 Post-processing of the balance measurements

The aim of the balance is to measure the hydrodynamic forces and moments. Figure 2.54 gives a flowchart of the post processing of a balance measurements. The balance described in the figure has 3-DOF (the lift, drag and the moment around X), typically the balance of IRENAV. The principle is the same for the 6-DOF balance.
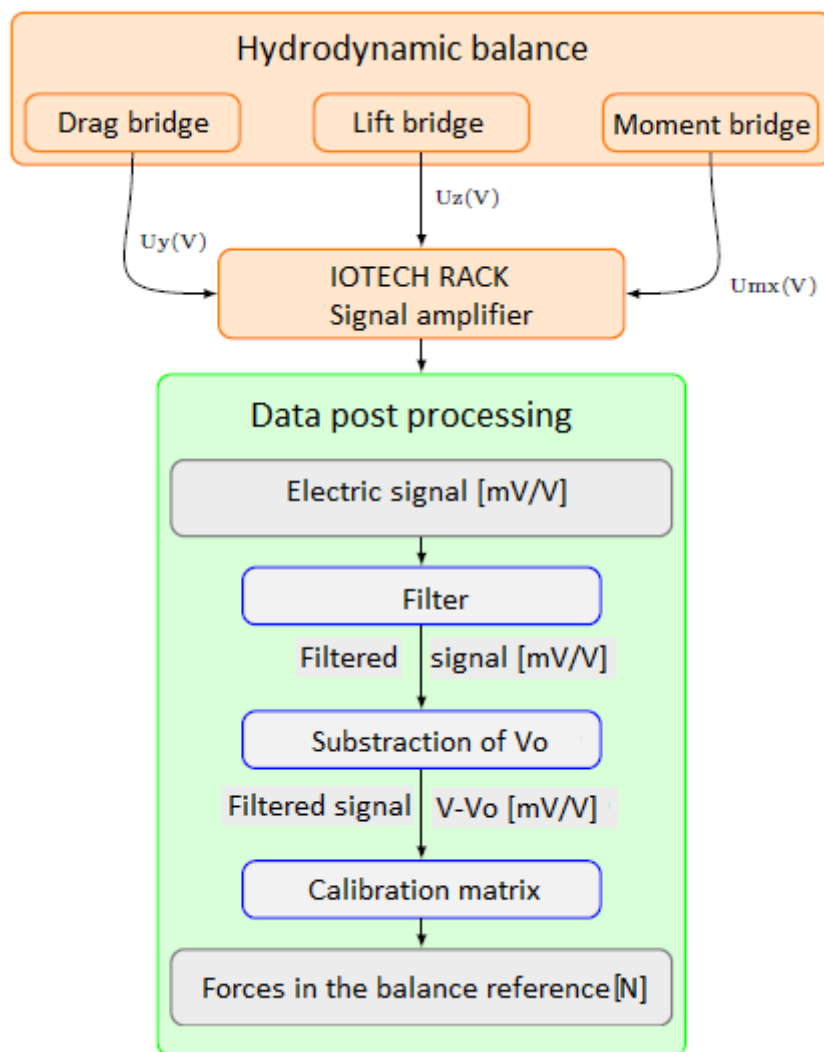
FIGURE 2.54 – Principle of post processing the measures of the balance

Three bridges connected to the degrees of freedom record an electric signal which is first amplified and send into a post processing script.
The signal is filtered to suppress the potential noises. A difference between the signal with flow named V and the signal without flow named Vo is computed. This new signal $V - Vo$ is converted into forces thanks to a calibration matrix.
The calibration matrix is given by the balance constructor and checked by simple tests : The balance measures the signal for a 1 Newton load in each direction, giving the calibration coefficients.

The output at this stage is the lift L and drag D forces and the bending moment M_X, X-axis being the flow direction.

The hydrodynamic coefficients (lift C_l and drag C_d coefficients) are calculated in equation 2.13 using the forces, the upstream flow velocity U_∞, the water density ρ and the section S of the submerged surface.

$$C_l = \frac{L}{2\rho U_\infty^2 S} \qquad C_d = \frac{D}{2\rho U_\infty^2 S} \tag{2.13}$$

2.3.2 Post processing of the laser measurements

The post-processing of the displacement of the hydrofoil is discussed with an example of the kevlar hydrofoil. The same post-processing script is used for all the hydrodynamic tests performed in the study.
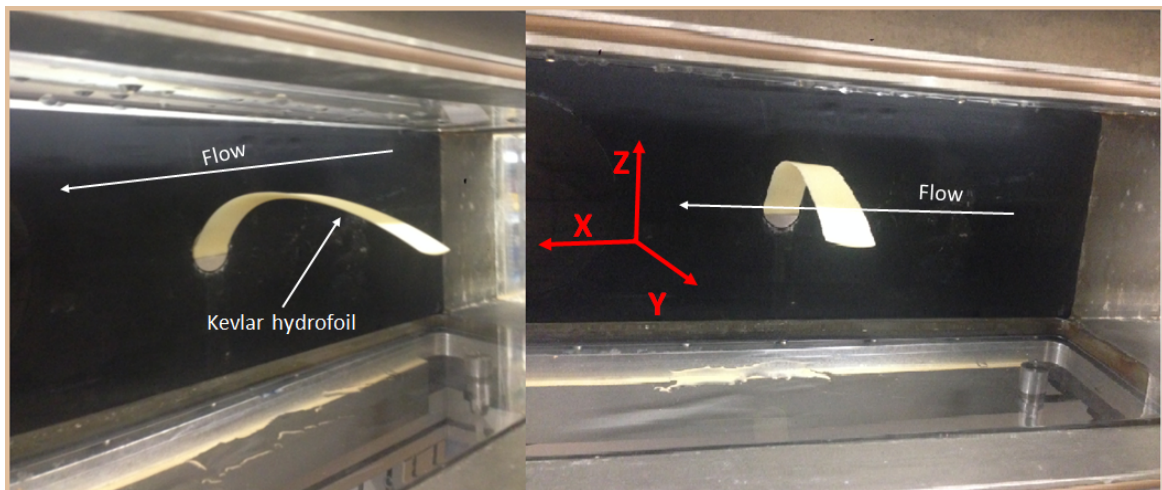
FIGURE 2.55 – Images of the Kevlar hydrofoil mounted in the cavitation tunnel of IRENAV for experiments

The laser can move in the x and y axis corresponding to the chord wise and span wise and, it measures a vertical displacement (z axis) (see figure 2.55). To measure the displacement of a line along the span, the laser is fixed at a position $x = X_{line}$ in x-axis and moves continuously along y-axis. The output is a file containing only the vertical displacement z, the corresponding coordinates (x,y) are not associated.

Figure 2.56 shows an example of the laser measurement for the kevlar hydrofoil at $V = 0\,m/s$ and $\alpha = 5.5°$. The vertical axis is the vertical displacement of the foil and the horizontal axis is the number of the measure recorded. The direct output is shown in figure 2.56a when a filtered curve is shown in figure 2.56b. To make the horizontal axis consistent with the hydrofoil coordinate in span wise, 7 points given in table 2.20 are chosen along the span.

Note that the first measurement point is not really at at 0 in the span wise because the laser assembly comes to a stop a little before and it is impossible to measure at the root. The result is that the span presented in the figures is slightly smaller than that the foil span ($187\,mm$)

The vertical displacements of the seven points is measured and the correction of the curve is performed into two step :

(a) output of laser measurement

(b) cleaned curve
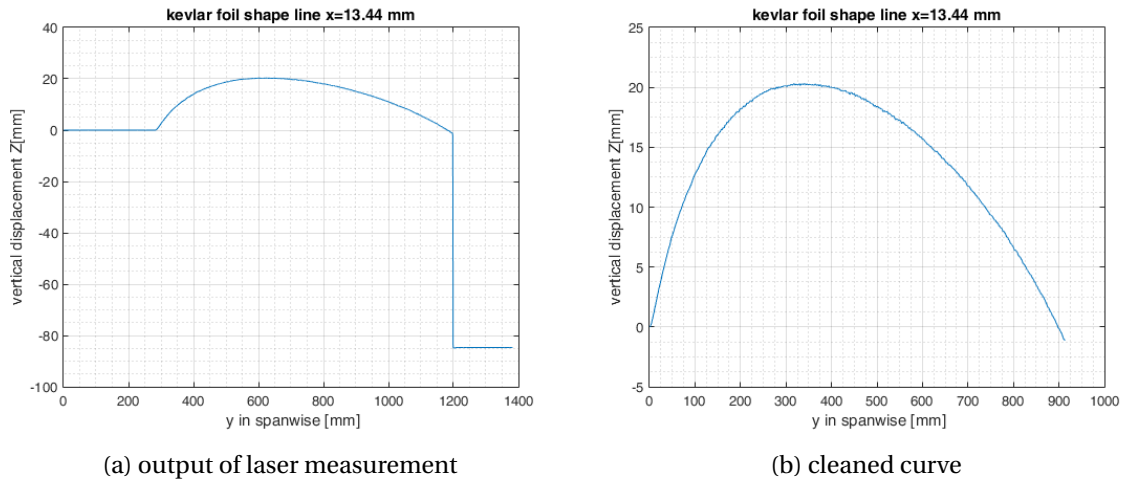
FIGURE 2.56 – kevlar hydrofoil shape for $\alpha = 5.5°$ at $V = 0 m/s$

Points	P_1	P_2	P_3	P_4	P_5	P_6	P_7
x [mm]	13.44	13.44	13.44	13.44	13.44	13.44	13.44
y [mm]	0	34.4	68.6	103.1	137.5	171.9	173.8

TABLE 2.20 – Measurement points along the spanwise of kevlar hydrofoil

— Separate the curve into seven portions
  After finding a correspondence between the curve values and the points measure-
  ments, the seven points are localized one the curve and the curve is divided into
  portions as shown in figure 2.57a.

— Calculate the y coordinate of each measurement
  For a portion of the curve between the points i and j, the span coordinate of each
  measurement is calculated by equation 2.15. $N_{i,j}$ is the number of the measurement
  and $y_{i,j}$ is the span coordinate of the points (table 2.20).

$$y_0 = y_i \tag{2.14}$$

$$y_{k+1} = y_k + \frac{y_j - y_i}{N_j - N_i} \tag{2.15}$$

Figure 2.57b shows the corrected curve, the vertical displacement versus the span. In
this representation, the shape of the foil geometry is altered because the 2 axes do not
have the same scale. the real geometry is presented in figure 2.57c with the same scale
on both axes. For the sake of clarity, the configurations presented in the report will be
identical to figure 2.57b.

The same post-processing is performed for both model-scale and real-scale hydro-
foils, for all the displacements measured in the hydrodynamic tests.

(a) Points localized on the curve.

(b) Data settled with the points positions on span wise

(c) Curve with same scale on both axes
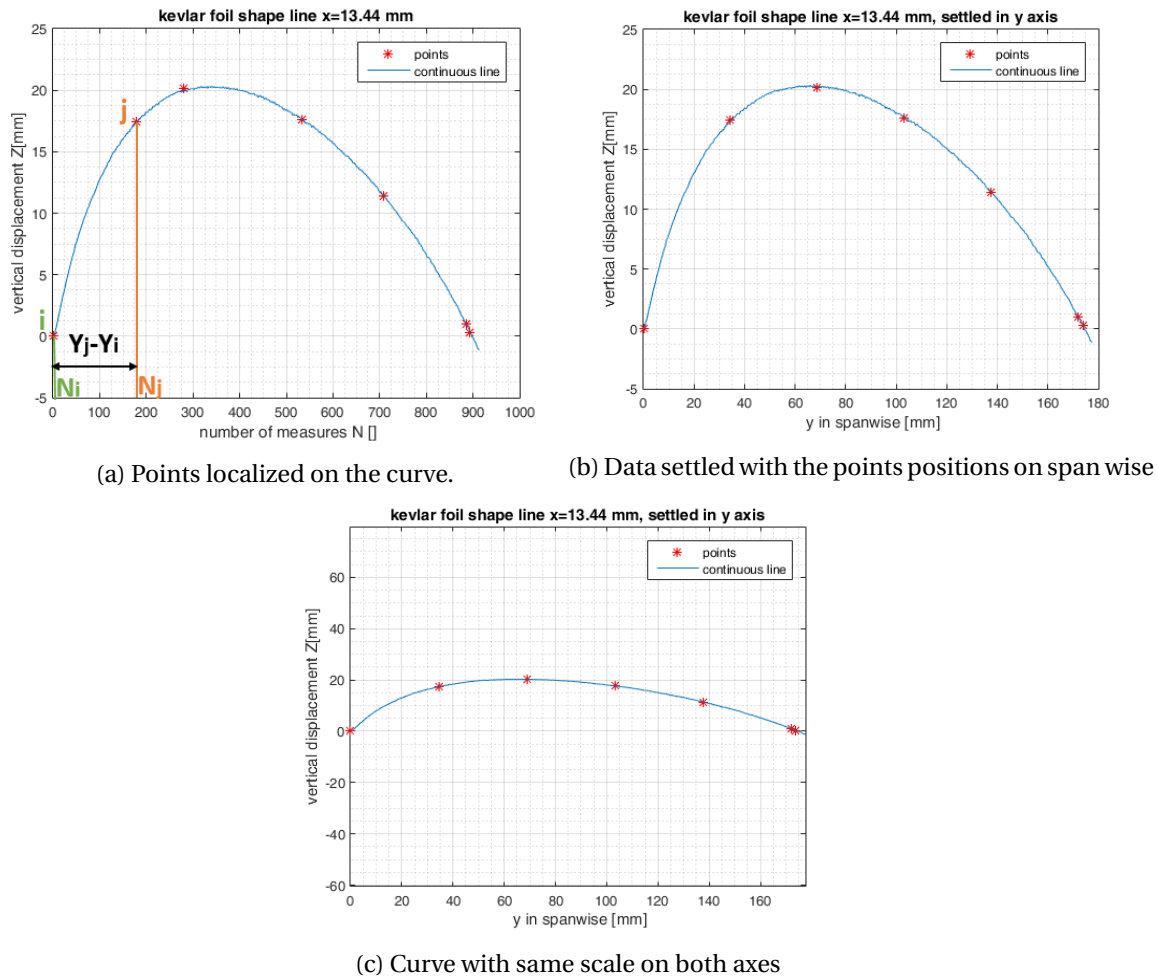
FIGURE 2.57 – Example of post processing of displacement recorded during the hydrodynamic tests : kevlar hydrofoil $\alpha = 5.5°$ at $V = 0 m/s$

2.4 Summary of the chapter

In this chapter, we presented the different hydrofoils investigated in this thesis work and the different tests performed to analyse FSI on the structures. Two groups of hydrofoils are studied : homogeneous model-scale hydrofoils and composite real-scale hydrofoils.

Two model-scale hydrofoils inspired by the hydrofoil of the MINI 747 were manufactured in a 3D printing fabrication process using kevlar and carbon fibers. The shape, the size and the material of these models exhibited unexpected behaviors.

Since then, the study on reduced models has focused on a trapezoidal plan form hydrofoil made in the isotropic POM material. Mechanical tests are carried out to asses the young Modulus of the structure on one hand and hydrodynamic experiments are carried out in the hydrodynamic tunnel of IRENAV to for five Reynolds numbers, to investigate FSI.

The second part of this chapter, we discussed about the real scale hydrofoils made in composite materials. It started by the sizing and manufacturing of the hydrofoils. The specifications aimed to have flexible deformation leading to a tip displacement of 10% of the hydrofoil length and the material layup is designed to allow BTC investigations.

Four hydrofoils have been manufactured : a carbon P_4 to simulate a rigid body, the glass P_2 and P_3 to investigate BTC and the glass P_1 to simulate a flexible structure without BTC.

The equivalent bending stiffness of the structure is assessed through four methods : laminate theory, tensile tests performed on specimen, bending tests and vibration test directly performed on the hydrofoils. The torsional modulus of the structure is asses with torsional tests.
An investigation of the BTC in static test is also perform with bending experiments.
The hydro-elastic response of the hydrofoils in FSI is investigated during hydrodynamic tests performed in the test flume of IFREMER Lorient. Hydrodynamic forces and the displacement of the hydrofoil are measured.

The next chapter presents the numerical method developed to simulate the experiments performed in this chapter. The low fidelity coupling FS6R and the high fidelity Foam-Aster are described.

The results of the experiments are presented in a comparison with the numerical simulations in chapter 4 for the small scale isotropic POM hydrofoil and chapter 5 for the real scale composite hydrofoils.

CHAPTER 3

Numerical couplings implemented to analyse FSI on hydrofoils

« *Anyone who claims to be a judge of truth and knowledge is exposed to the laughter of the gods because we do not know how things really are, but we only know how we represent them.* »

Albert Einstein (1879–1955)

Contents

This chapter is devoted to numerical modelling of the water flow around hydrofoil to predict and optimize the design of foils and validated by experimental data measured during tests. The objective of numerical developments is to create a coupling between a fluid solver and a structural solver. To get rid of commercial licenses, the tools are : either developed on the basis of existing methods in the literature or they belong to the field of open source. Two coupling methods of different level of fidelity are developed to investigate the FSI on the hydrofoils : a low fidelity coupling and a high fidelity coupling.

The first part of this chapter gives the mathematical equations describing the problem together with the boundary conditions.

The second part of this chapter describes the low fidelity tool : methods based on simplifying assumptions for both fluid and solid are investigated. The lifting line theory (LLT) of Prandlt's [5], is certainly the most described and used approach in the literature when we want to solve lifting-body problems in a simplified approaches.

The formulation of this approach firstly published in 1910s, predicts the distribution of lift on a three-dimensional wing based on its geometry. This method is based on hypotheses of potential flow theory.

The wing is modeled as a horseshoe vortex consisting of one bound vortex and two free vortex filaments. The bound vortex is the elongated normal to the hydrofoil section and, the free vortex are aligned with the incident flow and extended to infinity. Hagemeister and al. [66] integrated this method in a VPP (Velocity Prediction Program) for optimization routine and the tool gives encouraging results.

Many studies based on the LLT show great results but some limitations exist : it does not consider compressible flow, viscous flow, low aspect ratio lifting surfaces.

Graf and al. [61] implemented the lifting line with a 2D RANS simulation to consider unsteady flow and show higher accuracy than a 3D RANS simulation.

An extension of the Prandtl 's LLT is the vortex lattice method (VLM) [91] which models the lifting surface as a finite number of horseshoe vortices and allow to study complex geometries. The vortex lattice tool AVL [85] is thus chosen to perform the fluid analysis in the low fidelity tool.

To simplify the structural analysis, the beam theory modeling is chosen. It models the hydrofoil as a beam and the solution is obtained with finite element formulation. To consider the bend-twist coupling behavior of composite material, we propose an approach that modify the terms of the stiffness matrix defined in the beam theory.

The coupling between AVL and the beam theory in this work gives birth to FS6R, the low fidelity coupling.

The last part of the chapter presents the high fidelity coupling. A RANS solver which perform a complete study of the flow with fluid viscosity, turbulence modeling and multiphase flow is used to compute the flow field around the hydrofoils and, a 3D modeling code is used to solve the structural part.

Among the existing tools in the open-souce field, OpenFOAM has proven to be reliable for flow analysis and hydrodynamic forces prediction such as Code_Aster which performs with good accuracy structural analysis. The coupling of OpenFOAM and Code_Aster gives birth to the high fidelity coupling : FOAM-Aster.

Both couplings use the partitioned method, more details on this approach are given in section 1.4.1.1.

For each method (low-fidelity coupling and high-fidelity coupling), the assumptions used to solve the problem are first presented, then coupling algorithms are described. The fluid and structural blocks are described and the influence of the mesh is discussed.

3.1 Modeling of FSI problem

This section describes the equations governing the behaviour of the fluid and the structure. Figure 3.1 shows the fluid-structure problem we are studying.
It corresponds to a deformable solid structure "S", placed in a fluid flow "F".
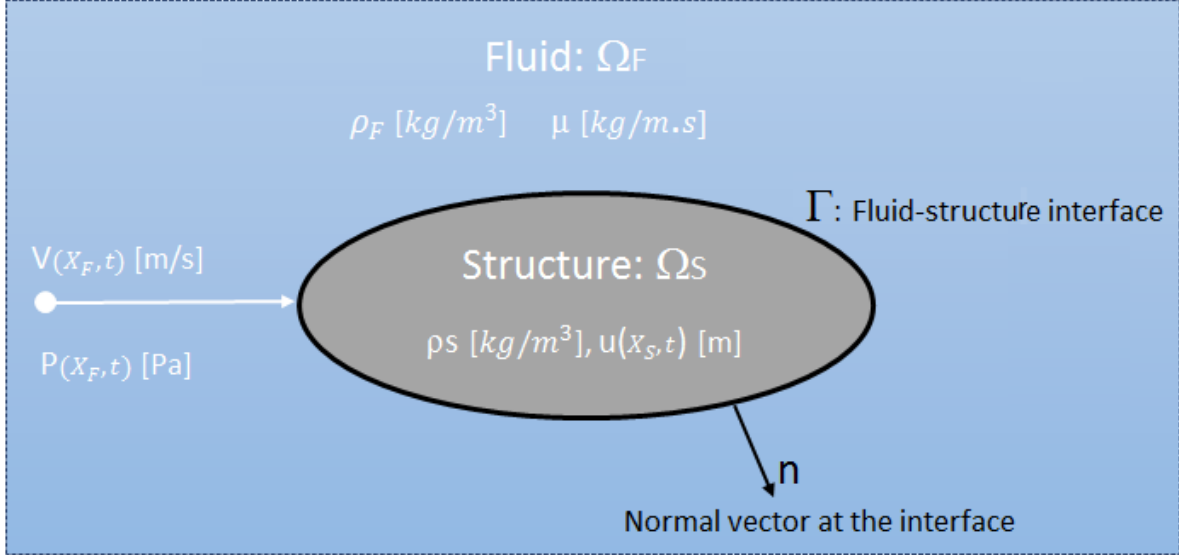
FIGURE 3.1 – Elastic structure "S" submerged in fluid flow "F".

The fluid domain "F" is characterized by its density ρ_F and its dynamic viscosity μ. Each point of the fluid domain has a velocity $U(X_F, t)$ and a pressure field $P(X_F, t)$ which induce a displacement field $u(X_S, t)$ in the solid. ρ_S is the density of the solid.
The interface between the 2 domains is Γ and n is the normal at the interface. X_F represents the points coordinates in the fluid domain Ω_F and X_S, the points coordinates in the solid domain Ω_S.

Fluid equations

The fluid is assumed to be Newtonian : the stress law is linked to deformation rate with a linear expression.
The behavior of an incompressible Newtonian fluid is governed by Navier Stokes equations in the following formulation (mass continuity-equation 3.1, momentum continuity-equation 3.2) :

$$\nabla.(U) = 0 \quad \in \quad \Omega_F \tag{3.1}$$

$$\rho_F(\frac{\partial U}{\partial t} + \nabla.(U \times U)) = -\nabla P + \nabla.\left(\mu(\nabla U + \nabla^t U\right) \quad \in \quad \Omega_F \tag{3.2}$$

The boundary conditions are given in Chapters 4 and 5 in each study case.
For potential flow, the momentum continuity becomes 3.3 where the viscosity included with μ terms are neglected.

$$\frac{\partial \rho_F U}{\partial t} + \nabla.(\rho_F U \times U) = -\nabla P \quad \in \quad \Omega_F \tag{3.3}$$

Solid equations

The formulation of the Navier equation for an elastic and linear solid is defined in equation 3.4 :

$$\rho_S \frac{\partial^2 u}{\partial t^2} - \nabla.\sigma(u) = 0 \quad \in \quad \Omega_S \tag{3.4}$$

σ is the stress field in the solid and u the displacements.

Conditions at the fluid-structure interface Γ
Two conditions ensure the fluid-structure 's balance at the interface :

— The kinematic coupling condition : the flow velocity at the interface is the time derivative of the structural displacement at the interface :

$$U(X_F, t) = \frac{\partial u}{\partial t}(X_S, t) \quad \in \quad \Gamma \tag{3.5}$$

— The dynamic coupling condition : the forces created by the fluids at the interface are balanced by the force tensor in the solid :

$$\sigma_{ij}(u).n_j = \left[-P\delta_{ij} + \left(\mu(\nabla U + \nabla^t U) - \frac{2}{3}\mu I \nabla.V \right) \right].n_j \quad \in \quad \Gamma \tag{3.6}$$

For potential flow, the conditions are given below :

$$\left\{ \begin{array}{ll} V_i.n_i = \frac{\partial u i}{\partial t}.n i & \in \quad \Gamma \\ \sigma_{ij}(u).n_j = P n_i & \in \quad \Gamma \end{array} \right. \tag{3.7}$$

The principal outputs of two numerical couplings are the forces field in the fluid and the displacement field of the structure. The stress field in the structure is not investigated in this work.

3.2 Low fidelity coupling "FS6R"

The acronym FS6R stands for "Fluid Structure interaction for SEAIR". This tool is developed to meet an industrial need of SEAIR : to have a fast tool able to predict the hydroelastic response of an isotropic or composite, flexible hydrofoil in fluid structure interaction : it computes the hydrodynamic loading and the displacements of the structure.
FS6R is dedicated to the early stages of hydrofoils design and the objective is really to optimize the study process by performing calculations in a short period of time where the investigations of the complete flow fields and solid fields, with more robust tools would be very costly in terms of time and resources.
FS6R is based on the coupling of a vortex lattice method AVL corrected with the viscous calculation XFOIL, and an in-house beam theory solved by finite elements.
This section describes the different parts of the low-fidelity coupling.

3.2.1 Coupling algorithm of FS6R

The organizational chart of the coupling is presented in figure 3.2, the process is iterative and works from top to bottom as described below.
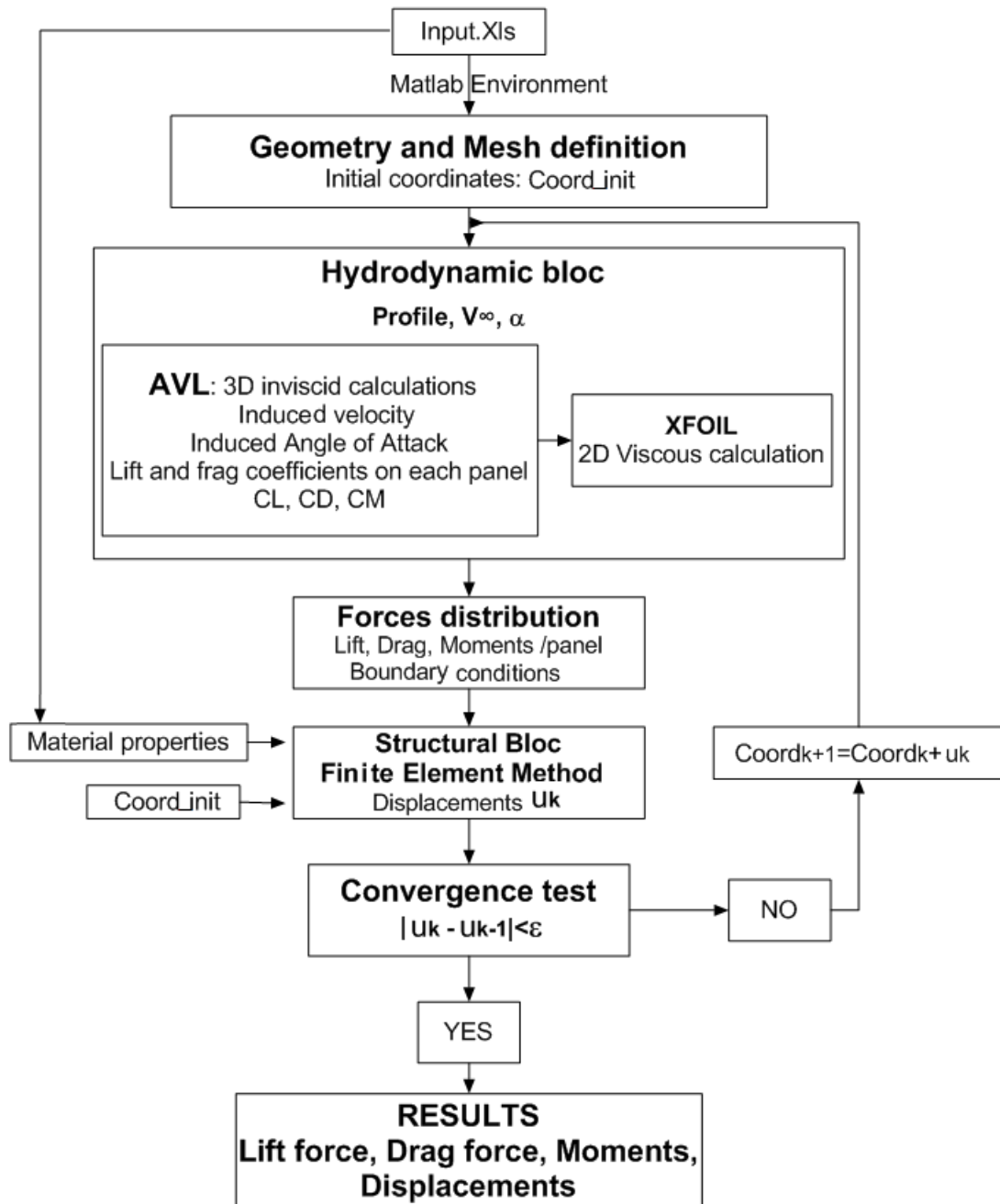
FIGURE 3.2 – FS6R organizational chart.

Inputs : all the parameters needed to perform the analysis are stored in an input file. It contains : the hydrofoil geometry, the fluid parameters (density, viscosity), the solid materials definition (elastic modulus, Poisson modulus, shear modulus) and the configurations to simulate (velocity, angle of attack). Concerning the composite materials, the ply and orientations in the layup can be defined and the equivalent properties will be calculated by the laminate theory or the equivalent mechanical properties of the structure characterized by experiments are directly given as input.

Geometry and mesh definition : This block takes the initial coordinates of the geometry in the input file and prepares the fluid mesh and the structural mesh. Figure 3.3 shows the mesh of the fluid and the structural block. The position the collocation points of AVL is presented in the figure but its mesh is described in section 3.6. In the section, the collocation point P is located at 3/4 of the chord from the leading edge and the discretization

along the span corresponds to the number N of panels of AVL in the spanwise.
The mesh of XFoil is a set of N profiles located at the span nodes of AVL mesh in the span wise.
The structural mesh is a discretization of a beam line into N nodes. That beam line is located at the elastic center of the section Pe which depends on the section geometry and the material. The elastic center is the point at which the moment of the forces generated by the shear stress is zero $M_y = 0$
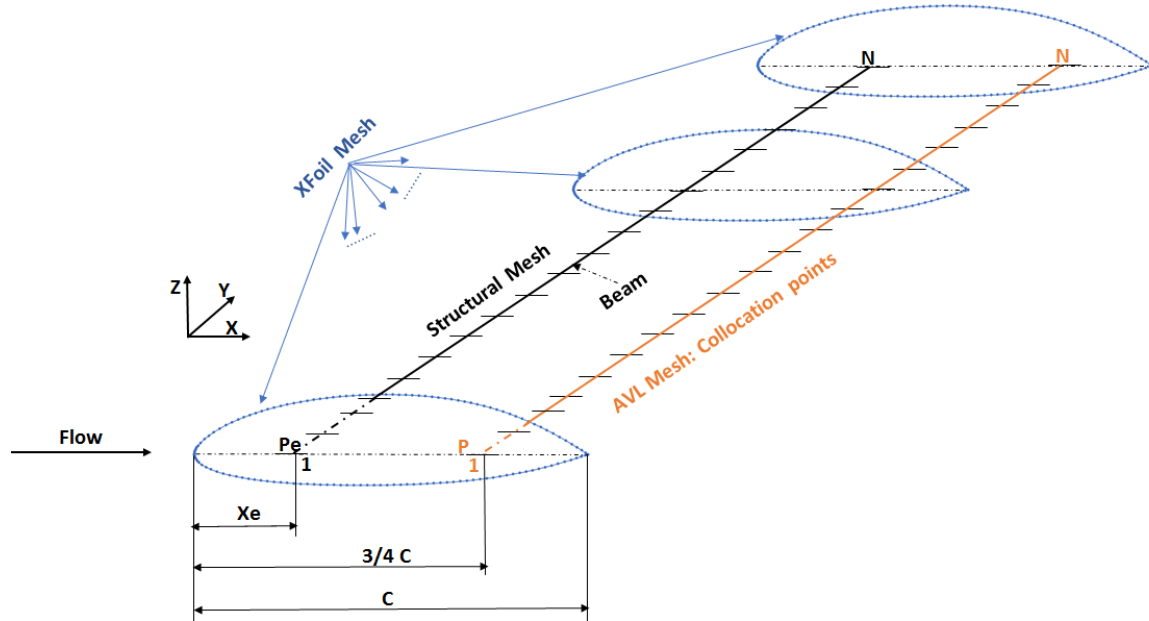
FIGURE 3.3 – Mesh in FS6R showing the elastic points P_e, the AVL collocation point P and the N panels discretized on the beam..

Hydrodynamic block : the Hydrodynamic block includes the two functions : AVL and XFOIL. AVL performs 3D calculations on the whole surface and provides the hydrodynamic coefficients. This calculation of AVL does not consider the viscosity of the fluid. Therefore a correction is applied using XFOIL software, which performs 2D viscous calculations on each section of the fluid mesh to correct the drag.

Forces distribution and relaxation

This block takes as input the hydrodynamic coefficients distributed along the AVL collocation points (see figure 3.3 and computes the forces (lift and drag)). To accelerate the convergence, relaxation is performed on the forces F after each iteration k in this block :

$$F^k = \omega \times F^k + (1 - \omega) \times F^{k-1} \qquad 0 < \omega < 2 \tag{3.8}$$

ω is the relaxation factor, [67] recommends under-relaxation ($0 < \omega < 1$) to accelerate the convergence of iterative process. The influence of the relaxation factor on FS6R results is investigated in section 4.1.3.2.
Then the forces F computed at the AVL collocation point P are transmitted on the structural mesh at the elastic center P_e into forces and moments as follows :

$$\begin{cases} \vec{F_{P_e}} = \vec{F_P} \\ \vec{\mathscr{M}_{P_e}} = \vec{P_eP} \times \vec{F} \end{cases} \tag{3.9}$$

The operation is performed on each panel. $\vec{F}$ stands for the vector of forces and $\vec{\mathscr{M}_{P_e}}$ is the moments of the forces computed at the point P_e.

Structural block

This block performs the structural calculation : the structure is modeled by the beam theory with finite elements calculations. At every iteration k, this block uses the initial mesh, defined on the undeformed geometry (see figure 3.3). It also takes the material definition and the fluid forces as input to compute the structural response. The outputs here are the displacements of the structure.

Convergence block

This block performs a convergence test using the structural displacement u_k as criteria for a prescribed residue ϵ. If convergence is achieved, one get out of the loop with the forces distribution and the displacements. If the convergence is not reached, the loop starts back at the hydrodynamic block with a new fluid mesh defined on the deformed structure from the previous calculation.

3.2.2 Fluid solver

The fluid solver combines AVL and XFoil to computes the induced velocity around a lifting surface and the drag and lift forces on that surface. The theory behind these codes is briefly described below.

3.2.2.1 Vortex Lattice Method in AVL

AVL, Athena Vortex Lattice is a numeric program based on Vortex Lattice Method [90], [85], to analyze arbitrary configurations of rigid aircraft with lifting surfaces and slender body model. It stands on the potential flow theory and assumes that the lifting surfaces are thin and modeled with horseshoe vortices distributed along the span and chord while neglecting the influence of viscosity and thickness. The horshoe vortices are the element that produce the lift force. It calculates lift curve slope, induced drag and lift distribution for the given lifting surface 's configuration. There are four theories describing the behavior of the horshoe vortices and their effect on the lifting surface.

3.2.2.1.1 Basic theories of VLM

Hermann von Helmholtz theory

A vortex filament cannot end in a fluid, it must extend to the boundaries of the fluid or form a closed path. The strength Γ of a vortex filament is constant along its length.

Prandtl lifting-line theory

Following Helmholtz's theorem "a vortex filament cannot end in the fluid". Assuming a bound vortex filament along a wing, Prandlt assumes that each tip of the filament continues as two free vortices trailing downstream from the wing tips to infinity. It forms a vortex made of the bounded vortex plus the two free which form a horseshoe, and is therefore called a horseshoe vortex as shown in figure 3.4. The present description is derived from Anderson [5].

Helmholtz recommends that the vortex must be a closed path. In this modeling, the 4th part closing the horseshoe starts at the infinity. Since this vortex is placed in infinity, its influence can be neglected (Liu, 2007, [87]).
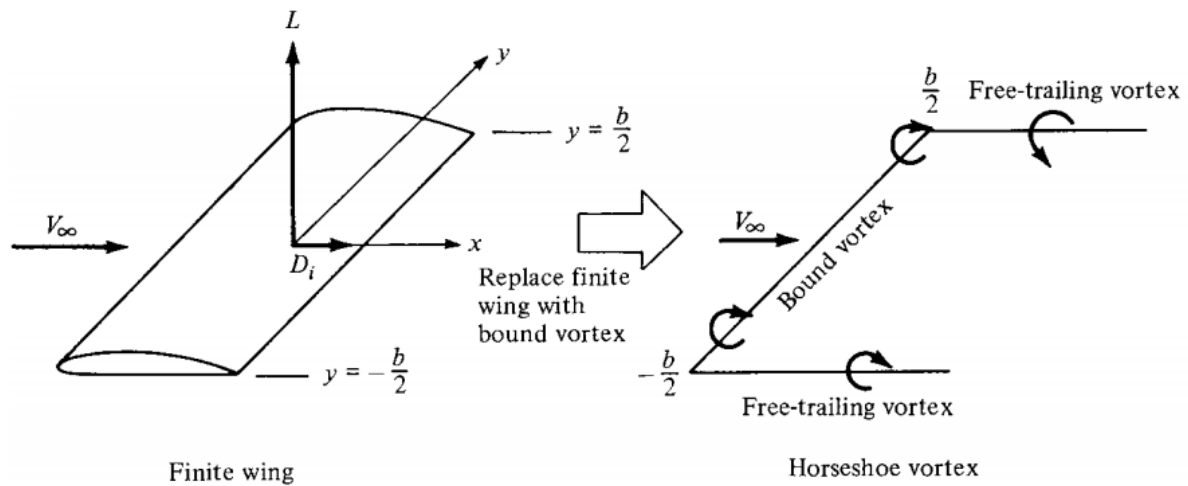
FIGURE 3.4 – *Modeling a finite wing by a horsehoe vortex (Anderson,2001 [5]).*

Biot-Savart Law

Figure 3.5 shows a vortex filament with a strengh Γ and dl is an infinitely small part of the filament.
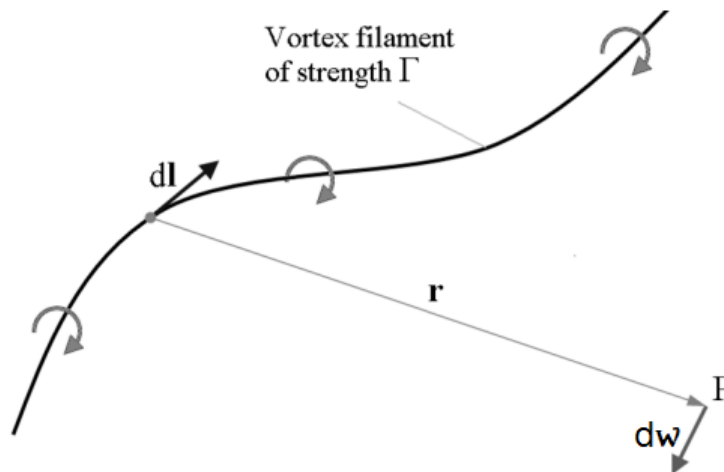
FIGURE 3.5 – *Illustration of the Biot-Savart law for a Vortex filament (Anderson,2001 [5]).*

In agreement with Biot-Savart law : each vortex line of a certain circulation Γ creates an induced velocity field. The induced velocity V_i in an arbitrary point P, placed in a distance of radius r from filament (see figure 3.5) is given in equation 3.10

$$\vec{V}_i \quad = \quad \frac{\Gamma}{4\pi} \frac{\vec{dl}}{\times} \vec{r} r^3 \qquad (3.10)$$

Kutta - Joukovsky theorem

According to this theorem, a vortex of certain circulation Γ moving with velocity V experiences forces. In the case of the horseshoe vortex, the bound vortex fixed within the flow of velocity V_∞ produces the lift force L :

$$L \quad = \quad \rho V_\infty \Gamma \qquad (3.11)$$

V_∞ is the free stream velocity and ρ is the fluid density.

3.2.2.1.2 Horseshoe Vortex distribution on the lifting surface : AVL mesh

The lifting surfaces are represented as single-layer vortex sheets, discretized into horseshoe vortex filaments, whose trailing edges are assumed to be parallel to the x-axis.

Figure 3.6 shows a lifting surface meshed with the VLM : it is composed of N panels along the span-wise and N_c panels in the chord-wise.

A panel "k" of length L in chordwise is modelled by a horseshoe vortex of amplitude Γ_k such as the bound vortex along the span is located at in the chord-wise at $\frac{1}{4}$L from the front of the panel seen by the flow.

For example, on the panels highlighted in orange in the figure, on the first we have the horseshoe vortex abcd. On the panel behind it, we have the horseshoe vortex aefd. On the following, the vortex aghd, etc. The entire surface is covered by a lattice of horseshoe vortices, each of a different unknown strength Γ_i.
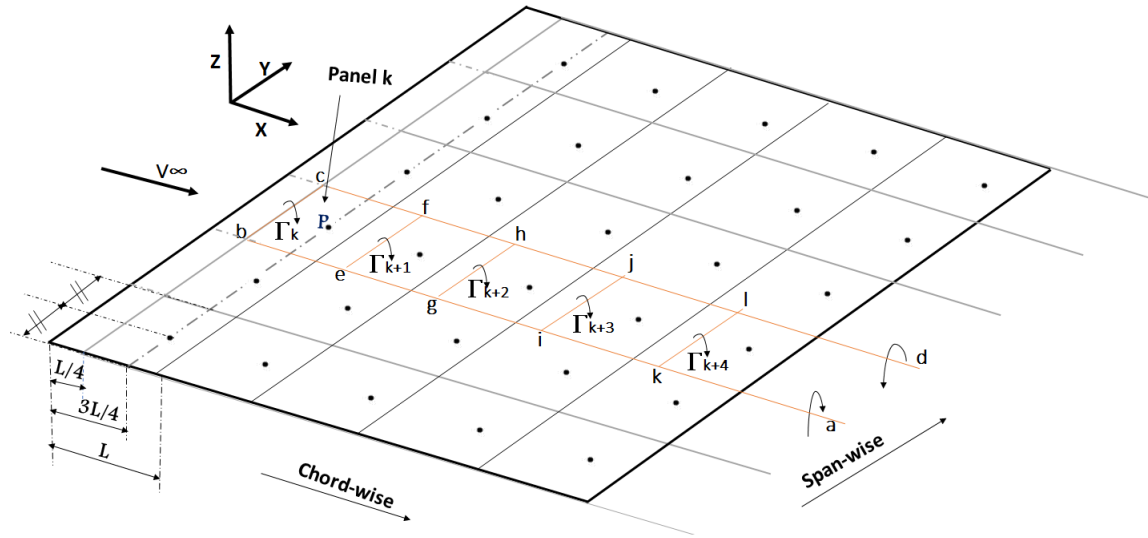
FIGURE 3.6 – *Vortex lattice system on a finite wing.*

On each panel, the calculation of the induced velocity is performed on a collocation point P located in the streamwise at $\frac{3}{4}$L from the front of the panel and placed in the middle of the panel in the span direction.

The velocity induced by the horshoe vortices at any control point P is the sum of the contribution from each vortex. Each contribution is calculated with the Biot-Savart law.

When the flow-tangency condition is applied at all the control points, the problem becomes algebraic equations (3.12) to solve with the unknowns Γ_i.

$$[A_M] \times [\Gamma] \quad = \quad [b_N] \tag{3.12}$$

$[A_M]$ is the influence matrix consisting of geometrical terms and $[b_N]$ are the boundary conditions.

3.2.2.1.3 Lift L and induced drag D_i calculation

The total lift force is calculated with an integration of the Kutta- Joukowsky theorem on the lifting surface (equation 3.13). C is the chord ans b the span.

The vortices create the induced velocity V_i which lead to in induced drag D_i. D_i is calculated in equation 3.14 as the sum of the contribution of each horseshoe.

This induced velocity modifies the effective angle of attack α_e (equation 3.16), creating an induced angle of attack α_i.

$$L \;=\; \rho V_\infty \int_0^C \left(\int_{\frac{-b}{2}}^{\frac{b}{2}} \Gamma(x,y) dy \right).dx \tag{3.13}$$

$$D_i \;=\; -\frac{\rho}{2} \int_0^C \left(\int_{\frac{-b}{2}}^{\frac{b}{2}} \Gamma(x,y) w(y) dy \right).dx \tag{3.14}$$

$$\alpha_i \;=\; tan^{-1}\left(\frac{V_i}{V_\infty} \right) \tag{3.15}$$

$$\alpha_e \;=\; \alpha - \alpha_i \tag{3.16}$$

$$\tag{3.17}$$

The lift and drag coefficients are calculated using the following relations :

$$C_L = \frac{L}{\frac{1}{2}\rho V_\infty^2 S} \qquad C_{D_i} = \frac{D_i}{\frac{1}{2}\rho V_\infty^2 S} \tag{3.18}$$

AVL takes as inputs a geometry file containing the surfaces defining the structure, the meshing parameters and a run file describing the configurations to simulate.
A surface is defined by sections and a section consists of x, y, and z coordinates of the profile's leading edge and the profile type.
If the profile is a NACA then the name will be sufficient and AVL will computes its coordinates (example : NACA 0015) but if the profile is of any shape, you will have to give a file of its coordinates as input.
[90] presents the guidelines for AVL 's utilization. Considering each set of pannel in the chord-wise, the forces are computed and stored in a collocation point located at 3/4 of the chord, resulting a set of N values as shown in figure 3.3.
If the section profile is not provided, AVL computes the case as a thin plate.

3.2.2.2 Xfoil : viscous formulation

The inviscid approach of AVL only computes the induced drag. A drag correction is performed using Xfoil which computes the viscous drag and the profile drag. Xfoil is developed by M. Drela and al. [43] to reduce the computational time and capacity requirements of flow computations and to predict with good accuracy, low Reynolds number flow field with laminar and turbulent viscous formulations. The present description is extracted from Drela and al. [43] and Ramanujam and al. [104].

Xfoil models the viscous layer influence on potential flow, by superimposing source distributions (γ_i) on the airfoil itself and its wake as shown in figure 3.7.
The airfoil is discretized into N panels and its wake into N_w panels. Each panel of the airfoil has a vortex sheet of strength γ and a source sheet of strength σ. Xfoil stands on a panel method with a linear-vorticity stream function.
The steam function of this configuration expressed in equation 3.19.

$$\Psi(x,y) \;=\; u_\infty y - v_\infty x + \frac{1}{2\pi} \int \gamma(s) ln r(s,x,y) ds + \frac{1}{2\pi} \int \sigma(s) \theta(s,sx,y) ds \tag{3.19}$$

s is the coordinate along the vortex and source sheet, r is the magnitude of the vector between the point at s and the field point (x,y), θ is the angle of that vector, u_∞ and v_∞ are
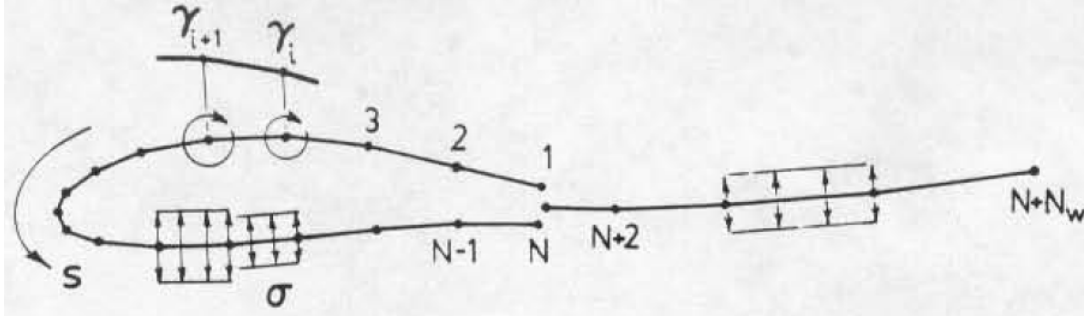
FIGURE 3.7 – section and wake discretization and source's flow distribution [43].

the freesteam velocity components.

After some transformations, and by requiring the steam function to be equal to a constant Ψ_0 at each node of the airfoil, equation 3.19 gives the following linear system.

$$\sum_{j=1}^{j=N} a_{ij}\gamma_j - \Psi_0 = -u_\infty y_i - v_\infty x_i - \sum_{j=1}^{j=N+N_w-1} b_{ij}\sigma_j \quad ; \quad 1 < i < N \tag{3.20}$$

The system is composed of N equations and $2N + N_w$ unknowns : N unknowns γ_j and $N + N_w$ unknowns σ_j.
The unknowns γ_j can be solved in an inviscid approach by assuming σ_j equals to a constant σ on the airfoil and the wake. The system 3.20 becomes a N equation with $N + 1$ unknowns and the last condition to solve it, is the Joukowsky condition on the trailing edge :

$$\gamma_1 + \gamma_N = 0 \tag{3.21}$$

In this formulation (equation 3.20), the source strength σ_j are directly related to the viscous layer quantity.
Xfoil models the boundary layer behavior with the integral two equation boundary layer model : the integral momentum equation and the kinetic energy shape parameter equation.
The main variables chosen to describe the boundary layer are the layer momentum thickness θ and the boundary layer thickness δ.

The momentum thickness is given in terms of stream-wise coordinates ,η and the reference velocity is the velocity at the edge of the boundary layer U_e as defined :

$$\theta_e = \int_0^\delta \frac{u}{U_e}(1 - \frac{u}{U_e})d\eta \tag{3.22}$$

θ_e is the momentum thickness calculated by using U_e as reference velocity and u is the local velocity.
U_e is obtained by coupling the boundary layer equations to the potential flow equations describing inviscid, irrotational flow in the outer region. The stream-wise coordinates ξ and η are shown in figure 3.8 in a flow around a profile.

The drag coefficient is computed by :

$$C_d = \frac{2[\theta_e]_{x=\infty}}{C}$$ (3.23)

C is the chord of the profile.

Xfoil also neglects the viscosity outside of the boundary layer and, this assumption leads to a reduction of the predicted drag.

Studies such as [104],[93], investigate methods to improve the drag prediction of Xfoil but, implementing them in Xfoil 's code is out of the scope of the present study. Hence, Xfoil is used in its standard release and the predicted drag will be expected lower than experiments due to these limits.
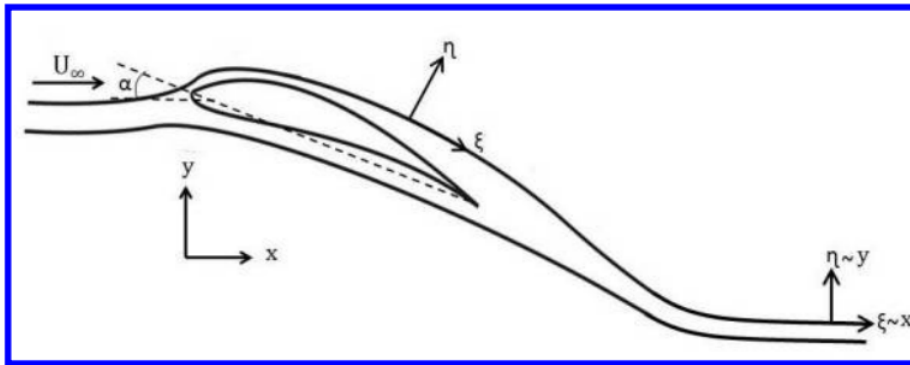
FIGURE 3.8 – Cartesian (x, y) and Streamwise (ξ, η) directions on an airfoil. U_∞ is the stream flow and α is the angle of attack. [104]

Inputs

To correct AVL drag 's calculation, Xfoil takes as an input the corresponding hydrofoil section at each node of AVL mesh in the spanwise (see figure 3.3). Each section is given with the effective angle of attack computed by AVL. Xfoil performs a viscous calculation and the drag force of the fluid block is updated.

3.2.2.3 Free surface modeling

We consider here the case of an hydrofoil piercing the free surface (working in air and water).

The free surface effects investigated in the literature only discuss the case of totally submerged hydrofoils and there are no parallels for the hydrofoils piercing the free surface.

In the case of submerged hydrofoils, Faltinsen [49] describes the free surface effect depending on the immersion depth of the hydrofoil and shows a dependent lift coefficient to the immersion depth h.

It also proposes an analytic calculation of the influence of the immersion dept on the lift coefficient, more details are given in [49].

Figure 1.2 shows the evolution of the lift coefficient with the submerged Froude number $Fn_h = \frac{U}{\sqrt{gh}}$.

The analysis is performed for many immersion ratio h/c where c is the chord of the hydrofoil. The results show a decrease of the lift coefficient when the foil gets close to the free surface (when h/c decreases).

They also observed that when the Froude number is very small, the free surface acts like a rigid wall. The problem is then similar to a lifting wing close to the ground.
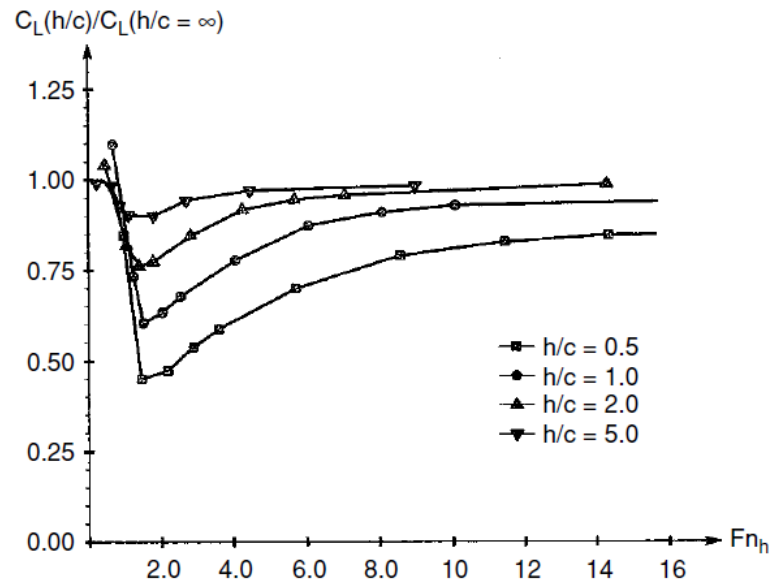
FIGURE 3.9 – Lift coefficient with the submerged Froude numberFn_h [49]

The velocity investigated with the hydrofoil piercing the free surface are $0.7 m/s$ and $0.9 m/s$ giving submerged Froude numbers (computed with the immersion height at the tip of the hyfrofoils h=0.707m) of $Fn_{h1} = 0.28$ and $Fn_{h2} = 0.34$. The Froude number being that small, we propose to model the free surface effect with AVL with a plane is located at the free surface position as shown in figure 3.10.
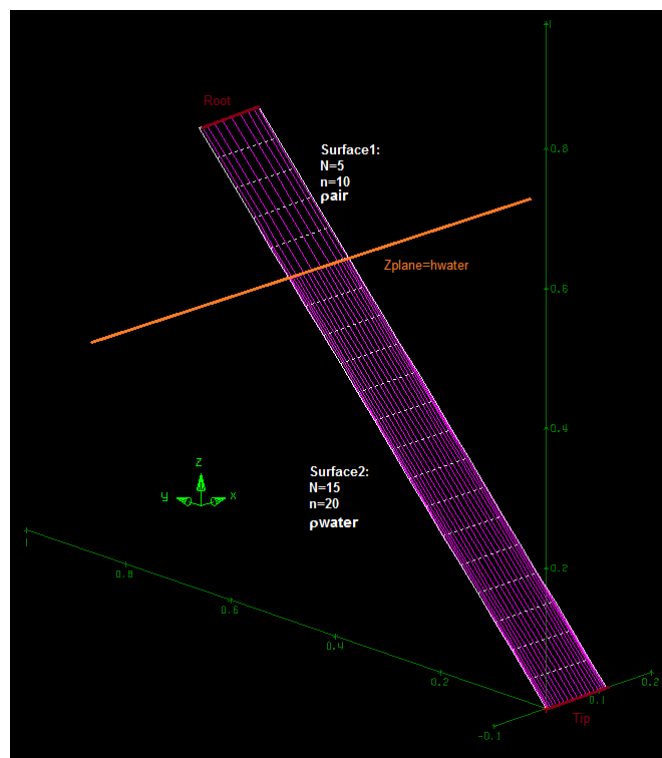
FIGURE 3.10 – Hydrofoil geometry on AVL and free surface modeling.

3.2.3 Structural solver

The structural solver of the low fidelity coupling is an in-house code that stands on beam theory.
We used the CALFEM toolbox which proposes functions to solve the problem with the finite element method. Next section firstly presents the beam theory and its discretization for the finite element modeling. The second part of the section prensents a description of the formulation we proposed to implement the bend twist coupling analysis in that beam theory.
Appendix C presents CALFEM functions to compute the element stiffness matrix for a three dimensional beam element and the internal forces in the beam.

3.2.3.1 Beam theory by finite elements

Beam structures are slender solids with one dimension larger than the other two. The theory is based on simplified assumptions to describe the behaviour of a beam. This section briefly describes the main concepts of this method.

3.2.3.1.1 Description

The hydrofoil is modeled by a 3D Euler-Bernoulli beam with a linear static structural behaviour. This beam is prismatic as shown in figure 3.11 and made of a single isotropic and homogeneous material.
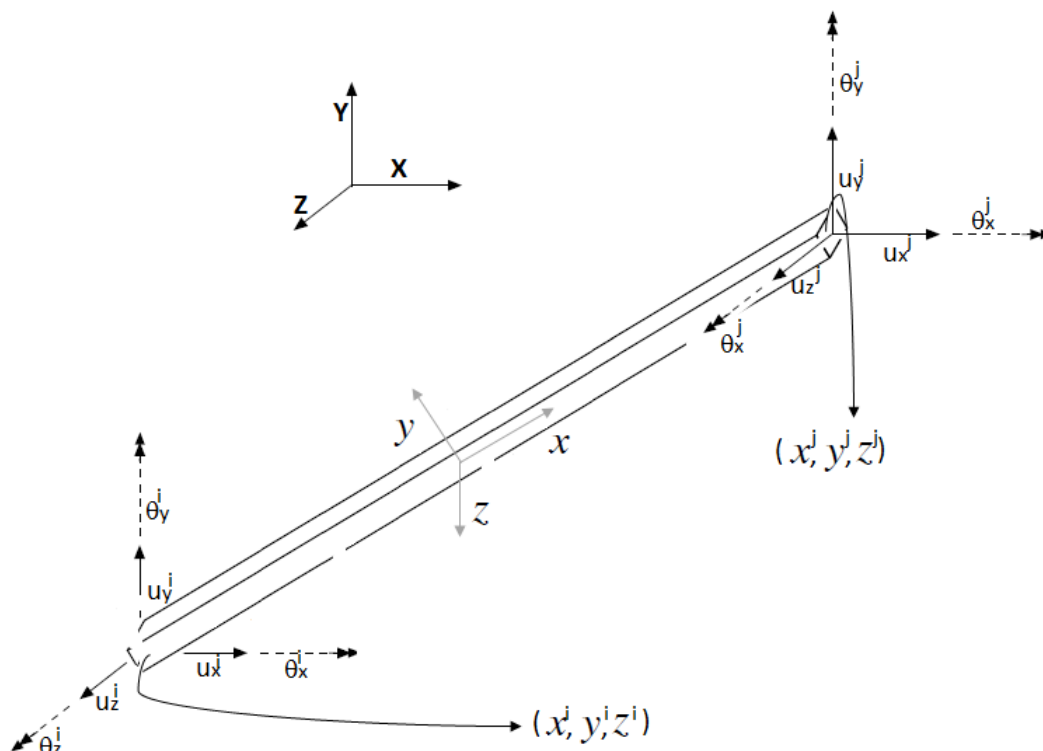
FIGURE 3.11 – Beam element with i and j nodes showing its local references (x,y,z) and its DOF in the global reference (X,Y,Z) [9].

The beam is characterized by its neutral axis (along x) and a straight cross-section within the (y, z) plane.
The section stays straight even after the beam deformation and the analysis of the beam

is performed in the section 's principal inertial coordinate system $\{H; \vec{y}, \vec{z}\}$. H is the intersection between the neutral axis x and the (y, z) plane. The global reference is (X, Y, Z)

This kind of beam has the following displacement field :

$$\vec{u}(x, y, z) = \vec{\tilde{u}}(x) + \vec{\tilde{\theta}}(x) \wedge (y\vec{e}_y + z\vec{e}_z) \tag{3.24}$$

where $(\vec{\tilde{\theta}}, \vec{\tilde{u}})$ is the displacement screw and the moment $\vec{\tilde{u}} = (\tilde{u}_x, \tilde{u}_y, \tilde{u}_z)$. This moment matches the neutral axis displacements, it's resultant $\vec{\tilde{\theta}} = (\tilde{\theta}_x, \tilde{\theta}_y, \tilde{\theta}_z)$ matches the cross-section rotations.
Euler Bernoulli assumptions imply that : $\tilde{\theta}_y = -\frac{d\vec{\tilde{u}}_z}{dx}$ and $\tilde{\theta}_z = -\frac{d\vec{\tilde{u}}_y}{dx}$.
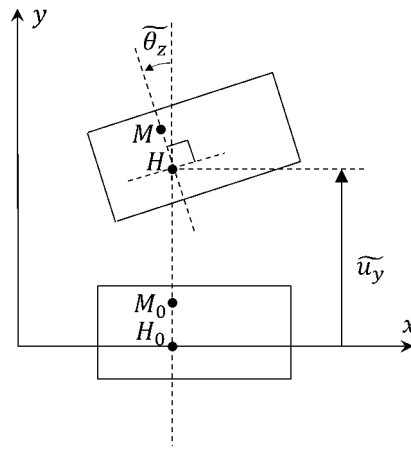
FIGURE 3.12 – *Euler Bernoulli assumptions illustrated for the relation between $\tilde{\theta}_z$ and $\tilde{u}_y$, H_o and M_o are within the same cross section. in initial state and H and M are the same points in deformed configuration.*

Besides the linkage reactions loads, the beam is subjected to external distributed forces $\vec{q} = (q_x, q_y, q_z)$ and torsional torque M_x. The beam internal loads are depicted by the internal screw given at H by : $\{\tau\} = \{N \ T_y \ T_z; M_x \ M_y \ M_z\}$.

Given that the torsion is allowed, the strain tensor has three components ε_{xx}, ε_{xz} and ε_{xz} different from zero. Consequently, σ_{xx}, σ_{xy} and σ_{xz} are the only stress tensor components different from zero.
The beam constitutive laws are described by the Euler Bernoulli theory.

$$N = \quad ES\frac{d\tilde{u}_x}{dx} \tag{3.25}$$

$$M_x = \quad GI_o\frac{d\tilde{\theta}_x}{dx} \tag{3.26}$$

$$M_y = \quad -EI_y\frac{d^2\tilde{u}_z}{dx^2} \tag{3.27}$$

$$M_z = \quad -EI_z\frac{d^2\tilde{u}_y}{dx^2} \tag{3.28}$$

where E and G are the material Young and shear modulus ; I_y and I_z are the two second moments of area of the cross-section and I_0 its polar moment.

Furthermore, the mechanical equilibrium of the beam is given by :

$$\frac{d\mathrm{N}}{dx} + q_x = 0 \quad , \quad \frac{d\mathrm{M}_x}{dx} + q_x = 0 \tag{3.29}$$

$$\frac{d\mathrm{T}y}{dx} + q_y = 0 \quad , \quad \frac{d\mathrm{M}_y}{dx} - \mathrm{T}_z = 0 \tag{3.30}$$

$$\frac{d\mathrm{T}_z}{dx} + q_z = 0 \qquad \frac{d\mathrm{M}_z}{dx} + \mathrm{T}_y = 0 \tag{3.31}$$

Hodges [70] proved that the solution of the problem $(\vec{\theta}, \vec{u})$ matches the displacement field minimizing the elastic potential energy E_p. E_p is a function of the strain energy E_{def} and the work of the external loads W_{ext} as described in equation 3.32.

$$\mathrm{E}_p \quad = \quad \mathrm{E}_{def} - \mathrm{W}_{ext} \tag{3.32}$$

$$\mathrm{E}_{def} \quad = \quad \frac{1}{2} \int_{beam} (\sigma_{xx}\varepsilon_{xx} + 2\sigma_{xy}\varepsilon_{xy} + 2\sigma_{xz}\varepsilon_{xz}) \tag{3.33}$$

$$\mathrm{W}_{ext} \quad = \quad \int_{beam} \vec{q} \cdot \vec{u} + m_x\theta_x + boundary\ terms \tag{3.34}$$

3.2.3.1.2 Finite element formulation : CALFEM toolbox

Many open source tools are available such as FEnics Project, RDM6, Calculix or CALFEM and we chose CALFEM Matlab toolbox as a starting base of our structural development. Its integration in a structural code designed to be coupled with another part is simple and the it's easily customizing for composite foil simulations.
CALFEM "Computer Aided Learning of the Finite Element Method" [9] is being developed since the 70's and the lately updated in 2012.

CALFEM tool box proposes to solve the structural problem using the displacement finite element method. The beam is discretized within N elements, with two nodes each as shown in figure 3.13.
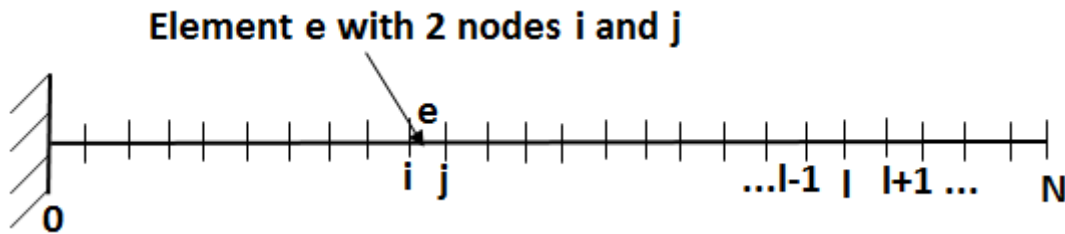
FIGURE 3.13 – *Discretization of the beam into N elements.*

It consists of a line linking the elastic center of the sections (the sections corresponding to the load collocation position in AVL mesh, see figure 3.3).

A node i is characterized by : six degrees of freedom $(u_x^i, u_y^i, u_z^i, \theta_x^i, \theta_y^i, \theta_z^i)$, six nodal loads $(\mathrm{N}^i, \mathrm{T}_y^i, \mathrm{T}_z^i, \mathrm{M}_x^i, \mathrm{M}_y^i, \mathrm{M}_z^i)$ and six shape functions (one per degree of freedom).

Considering an element, the shape functions are the functions used to express the coordinate of any point of that element using the coordinates of its two nodes.

The shape functions corresponding to $\tilde{u}_x$ and $\tilde{\theta}_x$ are chosen linear, the ones corresponding to $\tilde{u}_y$ and $\tilde{u}_z$ are cubic while the function corresponding to $\tilde{\theta}_y$ and $\tilde{\theta}_z$ are deduced from $\tilde{u}_y$ and $\tilde{u}_z$ by using Euler-Bernoulli relations.

For an element e linking two nodes i and j, the strain energy and the work of external loads in finite element formulation are given by :

$$E_{def} = \frac{1}{2} \{U^e\}^{\mathrm{T}} [K_e] \{U^e\} \tag{3.35}$$

$$W_e xt = \{U^e\}^{\mathrm{T}} (\{f^e\}) + \{f^e\}_{nod}) \tag{3.36}$$

Where $\{U^e\} = (u_x^i, u_y^i, u_z^i, \theta_x^i, \theta_y^i, \theta_z^i, u_x^j, u_y^j, u_z^j, \theta_x^j, \theta_y^j, \theta_z^j)$ is the vector of nodal displacement of the element beam and $[\bar{K}_e]$ is the element stiffness matrix. This matrix is expressed using the cross-section properties as explained in CALFEM [9]. $\{f^e\}_{nod}$ stands for the loads which are directly applied to the nodes.

Then, the element matrix $[K_e]$ and $\{f^e\}$ are assembled for all the element discretized in the beam to obtain the global linear system (equation 3.37) we need to solve with boundary conditions.

$$F = [K]U \tag{3.37}$$

K is the stiffness Matrix in the global reference (X,Y,Z), F represents the Forces applied to the structure in the global reference (X,Y,Z) and U, the DOF of the structure in the global reference (X,Y,Z).
The expressions of the stiffness matrix and the different shape functions are given in appendix C.

Equation 3.38 express equation 3.37 for the 1 element beam with two nodes.

$$
\begin{bmatrix} N^1 \\ T_y^1 \\ T_z^1 \\ M_x^1 \\ M_y^1 \\ M_z^1 \\ N^2 \\ T_y^2 \\ T_z^2 \\ M_x^2 \\ M_y^2 \\ M_z^2 \end{bmatrix}
=
\begin{bmatrix}
k_1 & 0 & 0 & 0 & 0 & 0 & -k_1 & 0 & 0 & 0 & 0 & 0 \\
 & \frac{12EI_z}{L^3} & 0 & 0 & 0 & \frac{6EI_z}{L^2} & 0 & -\frac{12EI_z}{L^3} & 0 & 0 & 0 & \frac{6EI_z}{L^2} \\
 & & \frac{12EI_y}{L^3} & 0 & \frac{6EI_y}{L^2} & 0 & 0 & 0 & -\frac{12EI_y}{L^3} & 0 & -\frac{6EI_z}{L^2} & 0 \\
 & & & k_2 & 0 & 0 & 0 & 0 & 0 & k_2 & 0 & 0 \\
 & & & & \frac{4EI_y}{L} & 0 & 0 & 0 & \frac{6EI_y}{L^2} & 0 & \frac{2EI_y}{L} & 0 \\
 & & & & & \frac{4EI_z}{L} & 0 & -\frac{6EI_z}{L^2} & 0 & 0 & 0 & \frac{2EI_z}{L^2} \\
 & & & \mathbf{SYM} & & & k_1 & 0 & 0 & 0 & 0 & 0 \\
 & & & & & & & \frac{12EI_z}{L^3} & 0 & 0 & 0 & -\frac{6EI_z}{L^2} \\
 & & & & & & & & \frac{12EI_y}{L^3} & 0 & \frac{6EI_z}{L^2} & 0 \\
 & & & & & & & & & k_2 & 0 & 0 \\
 & & & & & & & & & & \frac{4EI_{\bar{y}}}{L} & 0 \\
 & & & & & & & & & & & \frac{4EI_{\bar{z}}}{L}
\end{bmatrix}
\begin{bmatrix} u_x^1 \\ u_y^1 \\ u_z^1 \\ \theta_x^1 \\ \theta_y^1 \\ \theta_z^1 \\ u_x^2 \\ u_y^2 \\ u_z^2 \\ \theta_x^2 \\ \theta_y^2 \\ \theta_z^2 \end{bmatrix}
\tag{3.38}
$$

107

In the force vector and DOF, the bending forces, moment and displacement are highlighted in red when the torsional moment and twist are highlighted in blue. The element stiffness matrix is expressed in the cross section beam reference $((x, y, z)$, see figure 3.11). This matrix is expressed using the homogenized cross-section properties : the modulus of elasticity E, the shear modulus G, the cross section area A, the element beam length L, the moment of inertia with respect to the y axis I_y, the moment of inertia with respect to the z axis I_z, and St Venant torsional stiffness K_v. $k_1 = \frac{EA}{L}$, $k_2 = \frac{GK_v}{L}$.
In that expression of the stiffness matrix, the coupling terms linking a bending force to a twist motion (highlighted in blue) and a torsional moment to a bending motion (highlighted in red) are usually neglected and set to zero.
Thus, it is necessary to implement a formulation which consider the bend twist coupling of the composite materials.

3.2.3.2   Bend twist coupling implementation

Lobitz and al. [121] introduced a coupling coefficient **g** in the stiffness matrix to consider BTC.
Equation 3.39 shows a simplified relation between the torsion and bending moments M_t, M_b linked to the bending and torsion response of a cross section k_b, k_t, by **g**. EI is the bending stiffness, GJ is the torsion stiffness.

$$\begin{bmatrix} M_b \\ M_t \end{bmatrix} = \begin{bmatrix} EI & -g \\ -g & GJ \end{bmatrix} \begin{bmatrix} k_b \\ k_t \end{bmatrix} \tag{3.39}$$

The BTC is created with fibers non aligned with the beam axis [51]. [31] defines the coupling percentage $\alpha[\%]$ (see equation 3.40) as a function of **g**, the bending stiffness EI and the torsional stiffness GJ.

$$\alpha[\%] = \frac{g}{\sqrt{EIGJ}} - 1 < \alpha < 1 \tag{3.40}$$

Therefore, to consider bend twist coupling in this structural part of FS6R, coupling terms k_{ij} defined in equation 3.41 are added in the element stiffness matrix (defined in the cross section reference $(\overline{x}, \overline{y}, \overline{z})$).

$$k_{ij} = \sum_\theta A_\theta \times \alpha_\theta \times \sqrt{k_{ii} \times k_{jj}} \quad i = 2, 3, 4, 5, 6, 8, 9, 11, 12, j = 4, 10 \tag{3.41}$$

The expression comes from equation 3.40 where k_{ij} depends on the coupling percentage $\alpha[\%]$, the torsional stiffness k_{jj} and the bending stiffness k_{ii}. θ is the orientation of the plies in the layup.
The proportion of plies at different orientation sθ is weighted by a coefficient A_θ to consider their influence on the laminate.
Capellaro [31] describes the evolution of the coupling coefficient $\alpha[\%]$ with the fiber orientation for carbon and glass fiber as shown in figure 3.14.

The limitation of this approach in the present work is the determination of the coupling percentage $\alpha[\%]$.
This determination need to perform an experimental campaign on structures composed

of only one unidirectional ply. Several ply for several orientations are investigated : a bending loading is applied to the ply and the induced twist angle is measured. A correlation between the applied loading and the induced twist will lead to the coupling percentage $\alpha[\%]$.

This investigation will be performed in future works. For the actual study where the composite hydrofoils are made of glass and carbon fibers, the values needed for the coupling are extracted from figure 3.14.
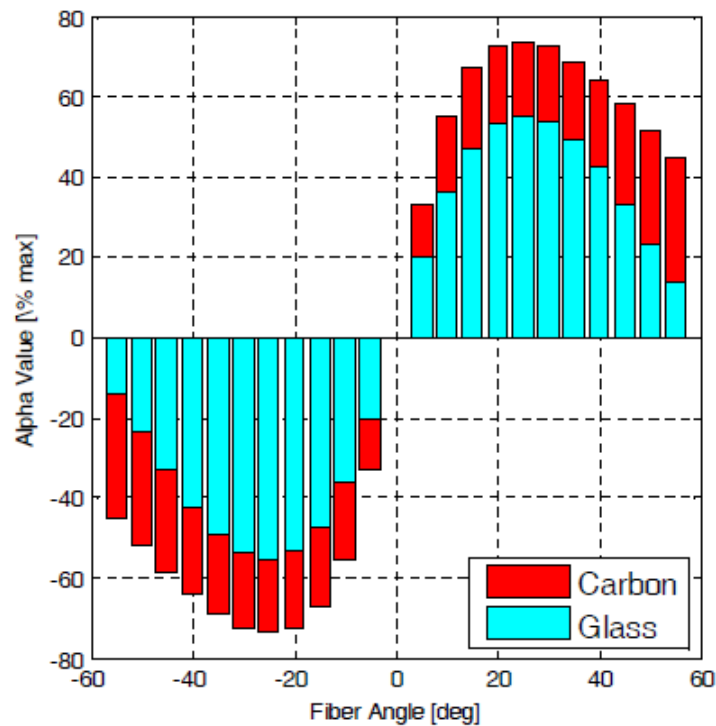
FIGURE 3.14 – Evolution of bend twist coupling percentage with the plies orientation for glass and carbon fibers. [31]

3.3 High fidelity coupling "FOAM ASTER"

This part describes the high fidelity coupling developed in this ph.D. work to analyse FSI on flexible hydrofoils. Unlike the low-fidelity approach FS6R, this high-fidelity coupling aims to couple two existing tools that model the whole physics of each problem : a coupling between CFD simulations and static FEM simulations.

To get rid of commercial licences, the open-source tools OpenFOAM for fluid resolution and Code_Aster for structural analysis are chosen.

A manual coupling was performed between OpenFoam and Code_Aster for propeller applications (M. Eichhorn & al. 2016), [47] : a CFD calculation was performed on OpenFoam and the loads were extracted, then, a second calculation was performed on Code_Aster taking the loads as input.

Yvin,2010) [135] has implemented a partitioned coupling algorithm between OpenFoam and Code_Aster that has been tested on a cavity with a flexible bottom and gave good results. These studies show on the one hand the good individual performances of the two codes calculations, and on the other hand their ability to be coupled together.

The main work of this part is to implement a coupling algorithm enabling the communication of the two codes.

3.3.1 FOAM-Aster coupling 's algorithm
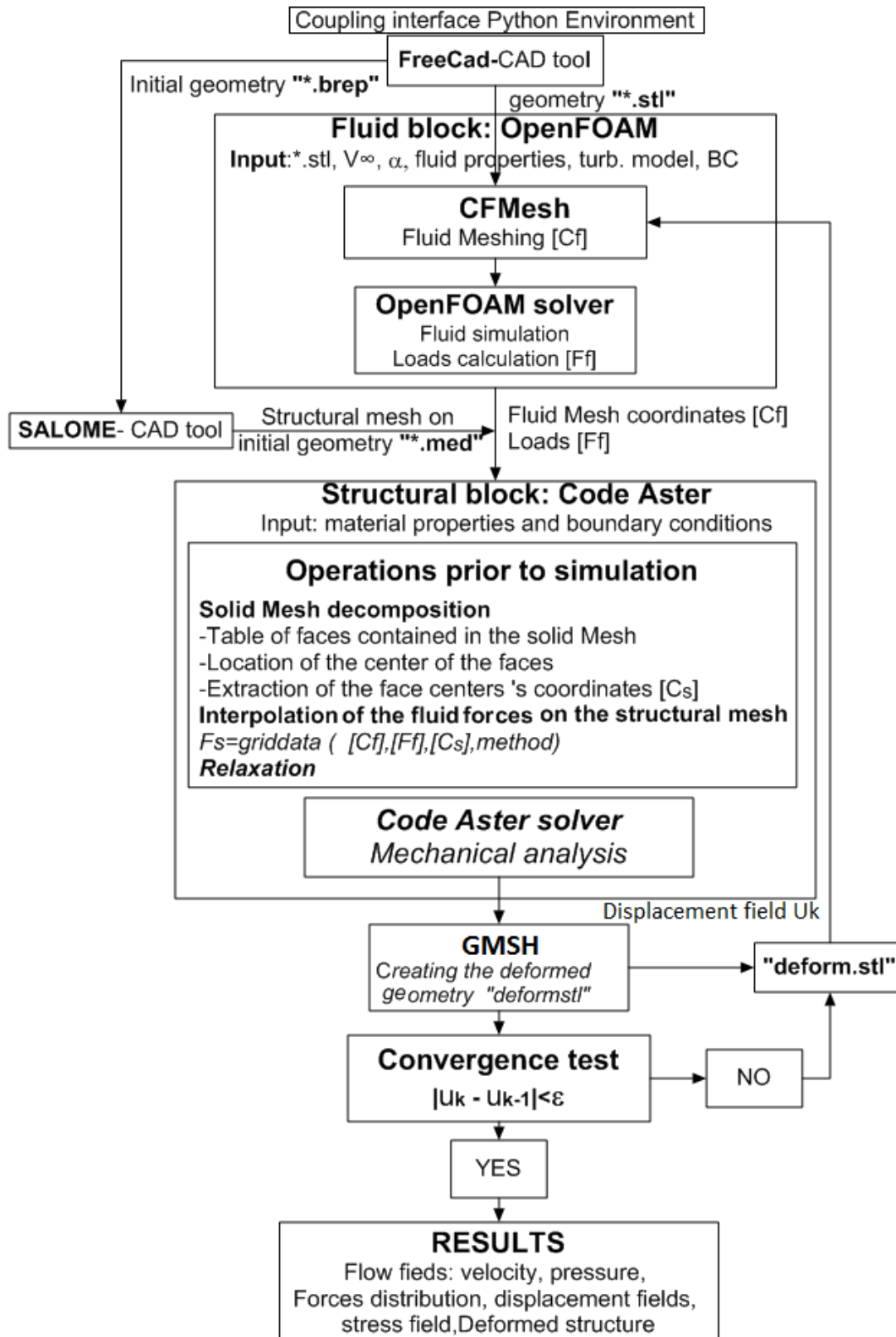
FIGURE 3.15 – Organizational chart of FOAM-Aster coupling.

The coupling is implemented with a partitioned approach and its algorithm is presented in figure 3.15. The coupling is performed through a python interface and it the process is iterative, working from top to bottom as described below.

Geometry preparation

Prior to the coupling interface, the structural geometry is exported with the CAD tool Free-Cad within two extensions : one "*.stl" for the fluid meshing and one "*.brep" for the solid meshing. They both describe only the surface geometry of the three-dimensional object. They are presented as a raw, unstructured and triangulated meshing for the stl, and tetrahedral meshing of the brep.

Fluid block

The first block of the coupling is OpenFOAM code which takes as input : the "*.stl" geometry file, the running case parameters (flow velocity V_∞, angle of attack α, turbulence model and the transport properties (ρ, ν,...)).
The process starts by meshing the fluid domain with CfMesh, a mesh generator tool compatible with OpenFOAM. The fluid mesh coordinates are stored in $[C_f]$. Then, according to the running case, one of the multiple OpenFOAM solvers is chosen to perform the simulation in the domain. The simulation is followed by a post-processing which extracts as outputs of this block : the mesh coordinates $[C_f]$, the pressure and viscous loads distribution $[F_f]$.

Structural mesh

In the first loop prior to the structural analysis, the geometric file "*.brep" goes into the CAD tool Salome and the structural mesh "*.med" is computed on the initial geometry.

Forces projection and relaxation

Before the mechanical analysis, operations are performed to project the fluid loads on the structural mesh : All the faces belonging to the fluid-structure interface are extracted from the structural mesh. Then the center of each face is located and their coordinates are stored in $[C_S]$. The loads $[F_f]$ computed on the fluid mesh $[C_f]$ are projected on the structural mesh using the scipy interpolation "$griddata$" [108].
It takes as inputs $[F_f]$, $[C_f]$, $[C_S]$, a method type and performs an interpolation $[F_S]$ giving the loads on the structural mesh : $F_S = griddata([C_f], [F_f], [C_S], method)$.
The interpolation method used is "nearest", it returns the value at the data point closest to the point of interpolation.
To accelerate the convergence, the relaxation of the the forces F is proposed after each iteration $k-1$ for the following iteration k :

$$F^k = \omega \times F_i^k + (1 - \omega_i) \times F_i^{k-1} \quad 0 < \omega_i < 2 \quad i = x, y, z \tag{3.42}$$

The relaxation factor ω_i is a value chosen between 0 and 2 or the following expression can be used :

$$\omega_i = \frac{|d_i^k - d_i^{k-1}|}{Max(|d_i^k|, |d_i^{k-1}|)} \tag{3.43}$$

i is the direction (x,y,z), F_i is the force in the direction i, d_i is the displacement in the direction i and ω_i is the relaxation factor applied to the force F_i.
The simulations performed with relaxation shows some divergence between the iterations thus the results presented in chapter 5 are the simulations without relaxation. A

tailored relaxation factor will be investigate in further works.

Structural block

The structural block of the coupling uses Code_Aster which always takes as input the structural mesh "*.med" performed on the initial geometry, the material properties, the boundary conditions, the fluid mesh coordinates and the forces distribution on the structure from OpenFOAM calculation.

According to the running case, the mechanical analysis is performed and the outputs of this block are : The displacement field and the stress field of the structure. For the present study, a static mechanical analysis is performed.

After the mechanical analysis, the mesh generator tool "Gmsh" takes the structural displacements as input and generates the deformed geometry "deform.stl".

Convergence

A convergence test is performed based on a displacement criteria. If the convergence is not reached, a new iteration starts with "CfMesh" using "deform.stl" as input and the process loops until convergence.

The outputs of the FOAM-ASTER coupling are : The flow field (velocity, pressure, ...), the loads distribution on the structure, the displacements, the stress field and the deformed structure.

3.3.2 Fluid block : OpenFOAM

OpenFOAM is an open code based on a development framework principle for CFD solvers (Computational Fluid Dynamics). The code is either available via the commercial company OpenCFD Ltd. ("OpenFOAM.com") or via the OpenFOAM Foundation ("OpenFOAM.org"), and is released open source under under the GNU-GPL. This coupling is developed with the version v6.

OpenFOAM has a wide range of features to solve the Navier Stokes equations, describing all complex fluid flows involving incompressible, compressible, multiphase and free surface such as chemical reactions, turbulence and heat transfers to solid dynamics and electromagnetics.

The code is parallelizable and has the characteristics of standard CFD codes : modeling by finite volumes, viscosity, turbulence models, ALE (Arbitrary Lagrangian-Eulerian) formulation, multiphase including the VOF (Volume Of Fluid) method, second order, spatial and temporal discretization, etc.

Laminar to turbulent flows calculations are performed with the code and a lot of turbulence models are available such RANS, LES, DES, etc.

The code has two principal mesh generators "blockMesh", "snappyHexMesh" and is compatible with many other mesh generators such as CfMesh used in this coupling for its ease of producing a good quality mesh on complex geometries.

To analyse the V-shape of T-shape hydrofoils, two solver are chosen :

— SimpleFoam for fully submerged hydrofoils (T-shape) : Steady-state solver for incompressible flows with turbulence modelling

— InterFoam for hydrofoils piercing the free surface (V-shape) : Solver for 2 incompressible, isothermal immiscible fluids using a VOF (volume of fluid) phase-fraction based interface capturing approach, with optional mesh motion and mesh topology changes including adaptive re-meshing.

Other solver exist to consider phenomena with changing phase flow such as cavitation. Readers should refer to the user guide [98] that presents the solver features and how to execute them in a complete way.

Shaoshi and al. [35] evaluate OpenFOAM for use in the field of Ocean engineering. Simulations of the flow field around a full-scale Tension-Leg Platform (TLP) in steady current at high Reynolds number were performed and OpenFOAMs ability to accurately predict the unsteady hydrodynamic loads was assess. The results validate suitability of this open-source tool, when used with the appropriate turbulence closure.
[64] describes the principles behind the computational approach of OpenFOAM.
This section presents the finite volume method (FVM) implemented in OpenFOAM to solve the Navier-Stokes equations.

3.3.2.1 Discretization of the transport equation : finite volume method (FVM)

OpenFOAM allows to solve Navier Stokes' equations by the finite volume method which consists in integrating on a volume of control, the equations 3.1 and 3.2. This section describes the discretization of the transport equation in its general formulation with the finite volume method. This description is strongly inspired from JASAK [77].

The fluid domain is divided into a finite number of arbitrary control volumes CV such as the one illustrated in figure 3.16.
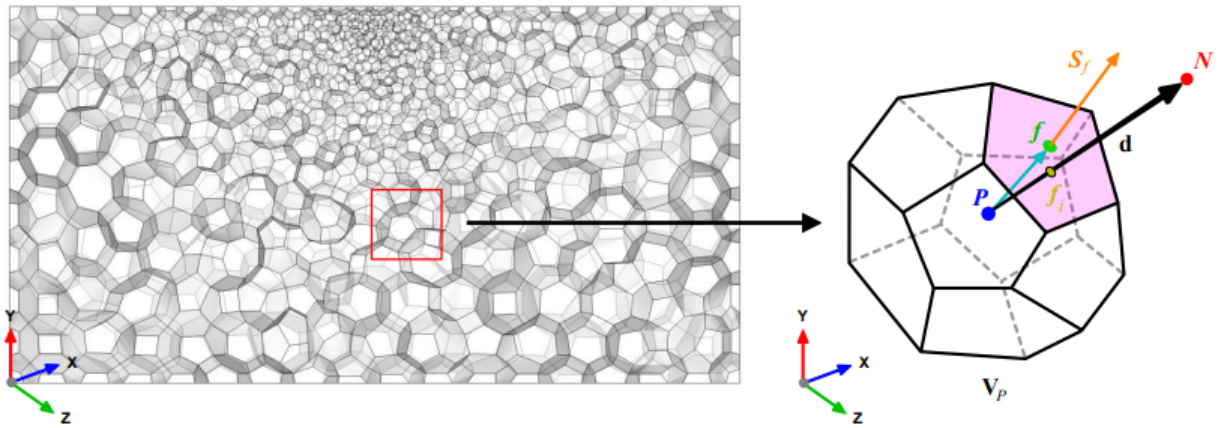
FIGURE 3.16 – Example of volume of control (CV) showing the centroid of the volume P and the center of a face f. N is the centroid of the neighbour of CV and S_f is the normal of the face f. [77].

The control volumes can be of any shape (tetrahedrons, hexes, prisms, pyramids,...), the only requirement specifies that the elements must be convex and the faces that made up the control volume need to be planar.

The control volume (CV) has a volume V and is constructed around point P, which is the centroid of the control volume. All the variables are computed and stored at P. The control volume faces are labeled f, which also denotes the face center. P is the centroid of the volume and f the centroid of the face defined as follow :

$$\begin{cases} \int_{V_P}(X - X_P)dV = 0 \\ \int_{S_f}(X - X_P)dS = 0 \end{cases}$$

(3.44)

N "as neighbour" is the centroid of the CV neighbour to the actual volume. S_f computed for each face is a vector normal the face and has a magnitude equals to the area of that face. The vector from the centroid P of to the centroid N is named d. f_i is the location where the vector d intersects a face.

The transport equation in its general formulation for the fluid domain is 3.46.

$$\int_{V_P} \frac{\partial \rho \phi}{\partial t} dV + \int_{V_P} \nabla.(\rho u \phi) dV - \int_{V_P} \nabla.(\rho \Gamma_\phi \nabla \phi) dV = \int_{V_P} S_\phi(\phi) dV \tag{3.45}$$

Using the Gauss theorem $\int_V \nabla.a dV = \oint_{\partial V} dS.a$ (∂V is a closed surface bounding the control volume V and dS represents an infinitesimal surface element), the equation becomes :

$$\underbrace{\frac{\partial}{\partial t} \int_{V_P} (\rho \phi) dV}_{temporal} + \underbrace{\oint_{\partial V_P} dS.(\rho u \phi)}_{convective} - \underbrace{\oint_{\partial V_P} dS.(\rho \Gamma_\phi \nabla \phi)}_{diffusion} = \underbrace{\int_{V_P} S_\phi(\phi) dV}_{Source} \tag{3.46}$$

Discretization of the convective term

$$\oint_{\partial V_P} dS.(\rho u \phi) = \sum_f \int_f dS.(\rho u \phi)_f \approx \sum_f S_f.(\rho u \phi)_f \tag{3.47}$$

$S(\rho u \phi) = F^C$ is the convective flux

Discretization of the diffusive flux

$$\oint_{\partial V_P} dS.(\rho \Gamma_\phi \nabla \phi) = \sum_f \int_f dS.(\rho \Gamma_\phi \nabla \phi)_f \approx \sum_f S_f.(\rho \Gamma_\phi \nabla \phi)_f \tag{3.48}$$

$S(\rho \Gamma_\phi \nabla \phi) = F^D$ is the diffusive flux
The convective and diffusive fluxes computed on both sides of a face f are interpolated from the values computed at the centroid P of the control volume. [76] and [77] discuss several interpolation schemes.

Discretization of the source term

$$\int_{V_P} S_\phi(\phi) dV = S_c V_P + S_P V_P \phi_P \tag{3.49}$$

S_c is the constant part of the source term and S_P is the non linear part.

Discretization of the gradient

$$(\nabla \phi)_P = \frac{1}{V_p} \sum_f (S_f \phi_f) \tag{3.50}$$

Temporal discretization

After spatial discretization, the transport equation is :

$$\int_{V_P} \frac{\partial(\rho\phi)d}{\partial t}V + \sum_f S_f.(\rho u\phi)_f - \sum_f S_f.(\rho\Gamma_\phi\nabla\phi)_f = (S_c V_P + S_P V_P \phi_P) \tag{3.51}$$

The temporal discretization (equation 3.52) is performed using the method of lines(MOL) that allows to select numerical approximations of different accuracy for the spatial and temporal terms.

$$\int_t^{t+\delta t}\left[\left(\frac{\partial\rho\phi}{\partial t}\right)_P.V_P + \sum_f S_f.(\rho u\phi)_f - \sum_f S_f.(\rho\Gamma_\phi\nabla\phi)_f\right]dt = \int_t^{t+\delta t}(S_c V_P + S_P V_P \phi_P)dt \tag{3.52}$$

The available time discretization schemes in OpenFOAM are : Crank-Nicolson, Euler implicit, backward differencing,...

The informations on the discretization schemes for the different terms appearing in the governing equations are stored in OpenFOAM in the fvSchemes dictionary.
Figure 3.17 shows the fvSchemes dictionary that we used for the simulations in the present study. This file contains the discretization type chosen for each terms of equation 3.52 :

— **ddtSchemes** refers to the time discretization. backward is chosen here, its is a time dependent second order (implicit), bounded/unbounded

— **gradSchemes** refers to the gradient term discretization

— **divSchemes** refers to the convective terms discretization

— **laplacianSchemes** refers to the Laplacian terms discretization

— **InterpolationSchemes** refers to the method used to interpolate values from cell centers to face centers. It is unlikely that you will need to use something different from linear

— **snGradSchemes** refers to the discretization of the surface normal gradients evaluated at the faces

3.3.2.2 Resolution of the discretized system

After spatial and temporal discretization, equation 3.52 in every control volume of the domain, a system of linear algebraic equations (equation 3.53) for the transported quantity ϕ assembled.

$$[A] \times [\phi] = [b] \tag{3.53}$$

This system can be solved by using any iterative or direct method. SimpleFoam uses the SIMPLE algotithm [100] and interFoam uses the PIMPLE [16], they are both described in [76].

$$
\begin{pmatrix}
a_{11} & a_{12} & & & \ddots & & \\
a_{21} & a_{22} & a_{23} & & & \ddots & \\
& \ddots & \ddots & \ddots & & & \ddots \\
\ddots & & \ddots & \ddots & \ddots & & & \ddots \\
& a_S & & a_W & a_P & a_E & & a_N \\
& & \ddots & & \ddots & \ddots & \ddots \\
& & & \ddots & & \ddots & \ddots & \ddots \\
& & & & \ddots & & \ddots & a_{PP}
\end{pmatrix}
\times
\begin{pmatrix}
\\
\phi_S \\
\phi_W \\
\phi_P \\
\phi_E \\
\\
\phi_N \\
\end{pmatrix}
=
\begin{pmatrix}
\\
b_S \\
b_W \\
b_P \\
b_E \\
\\
b_N \\
\end{pmatrix}
$$

ddtSchemes $\longleftarrow \dfrac{\partial \phi}{\partial t}$
{
    default   backward;
}

gradSchemes $\longleftarrow \nabla \phi_P$
{
    default   Gauss linear;
    grad(p)   Gauss linear;
}

divSchemes $\longleftarrow \nabla \cdot (\mathbf{U}\phi)$
{
    default   none;
    div(phi,U)   Gauss linear;
}

laplacianSchemes $\longleftarrow \nabla \cdot \Gamma \nabla \phi$
{
    default   Gauss linear orthogonal;
}

interpolationSchemes $\longleftarrow \begin{cases} \phi_f = f_x \phi_P + (1 - f_x)\phi_N \\ f_x = \dfrac{fN}{PN} = \dfrac{|\mathbf{x}_f - \mathbf{x}_N|}{|\mathbf{d}|} \end{cases}$
{
    default   linear;
}

snGradSchemes
{
    default   orthogonal; $\longleftarrow \mathbf{n}_f \cdot \nabla \phi_f$
}

FIGURE 3.17 – Discretization schemes chosen for the simulations of OpenFOAM in the present work.

3.3.2.3 Turbulence modeling

The turbulence is modeled to avoid too large calculation requirements for the direct resolution of Navier-Stokes equations.

The modelling method used in this study is RANS (Reynolds Avergered Navier-Stokes), based on the Navier-Stokes equations averaged using Reynolds decomposition which shares any flow variable such as the velocity in an average part $\overline{U}$ and a fluctuating part U' :

$$U = \overline{U} + U'$$

The averaged equations are thus :

$$\begin{cases} \nabla.\overline{U} = 0 \\ \frac{\partial}{\partial t}\overline{U} + \nabla.(\overline{UU}) = g - \nabla\overline{P} + \nabla(\nu\nabla\overline{U}) + \overline{U'U'} \end{cases} \tag{3.54}$$

The Reynolds averaged turbulence modelling expresses the Reynolds stress tensor $\overline{U'U'}$ in terms of the known quantities. It uses the Boussinesq approximation [27] which prescribes a linear relation of the form :

$$\overline{U'U'} = \nu_t \nabla(U + (\nabla U)^t) + \frac{1}{3}\overline{U'U'}I \tag{3.55}$$

The turbulence model $k - \omega$ SST of Menter [92] is chosen among the turbulence models to evaluate the kinematic viscosity ν_t. It appears for the users of openFoam as the one to give the more stable computations with less crash.

3.3.2.4 Boundary layer

The determination of the flow in the boundary layer is important for the accuracy of the results and in particular for the prediction of the parietal pressures at the origin of the forces on the structure. The $k - \omega$SST turbulence model used, allows a low-Reynolds resolution that requires a fine mesh size close to the walls or a resolution of the boundary layer by wall laws. The transition from one formulation to another is automatic and make possible to have in the same problem a low-Reynolds formulation and a formulation of wall laws. To have a good prediction of the forces on the hydrofoil, a low-Reynolds resolution is performed on the hydrofoil surface and a wall function is used on the other walls of the domain.

The value of parameter y^+ (equation 3.56) on the wall is an important criteria : on the foil must be less than 5 and as close as possible to 1. On the other walls, a value between 30 and 300 is recommended [55].

$$y^+ = \frac{\rho_f \Delta y U_t}{\mu} \tag{3.56}$$

y is the distance to the wall and U_t the speed of friction to the wall as a function of the wall shear stress τ_ω :

$$U_t = \left(\frac{\tau_\omega}{\rho_f}\right)^{\frac{1}{2}} \tag{3.57}$$

The wall law used introduces additional flow terms into the equations of the problem and these terms allow to model the boundary layer more or less finely.

3.3.2.5 Criteria for a good mesh

To avoid losses in accuracy or discrepancies in the calculation, the quality of the meshes is checked on the basis of three criteria :

— **Orthogonality** : Orthogonality is a criterion defined by the angle between the faces of adjacent elements and the theoretical angle of the perfect element (60° for triangles, 90° for quadrilaterals). A value greater than 20 is considered acceptable and the closer the value is to 90, the better the orthogonality of the element. Compliance with this criterion makes it possible to avoid highly deformed elements.

— **Aspect ratio** : The aspect ratio is the ratio between the largest area defined by the segments of the integration points and the smallest area. Its value must be less than 100 and compliance with this criterion avoids highly elongated elements that can introduce errors.

— **Expansion factor** : The expansion factor indicates how the mesh size changes. It is calculated for a control volume and is defined by the ratio between the largest area of the control volume sector and the smallest one. A value lower than 20 is acceptable to limit jump phenomena of mesh. These jumps can cause significant discontinuities and loss of accuracy.

3.3.2.6 Fluid properties

The fluid used in the tests is fresh water with the following properties :

Density ρ_f $[kg/m^3]$	998
kinematic viscosity ν_f $[m^2.s^{-1}]$	1.09×10^{-6}

TABLE 3.1 – Properties of water.

As a brief conclusion of this section, RANS simulations are performed with Open-FOAM, using the $k - \omega$SST as viscosity model and the discretization schemes applied are given in figure 3.17. The outputs are the flow fields, all the variable U,P, etc, can be accessed. The boundary conditions and the meshes are presented in chapter 5 for each simulation case.

3.3.3 Structural block : Code_Aster

The structural Code_Aster [37] is a mechanical open source code based on finite element analysis. It is developed by EDF Research Development since 1989 and released under the GNU-GPL (GNU General Public License) since October 2001. The code is programmed in Fortran and many additional modules are made in Python languages.
Their solvers are based on the theory of the mechanics of continuous media, its uses the Method of the balanced residues of Gallerkin and discretizes the structural domain with the finite element method. It solves different types of analysis such as : mechanical, thermal, acoustic, seismic and other problems.
1D, 2D and 3D structures such as beam, shell and 3D solid are analyzed with a wide range of finite elements types. Contacts between different type of models can also be investigated.
Code_Aster allows various type of material behaviors (elastic, viscous, etc) through elastic, orthotropic materials such as polymers, metals and composites, etc. The code considers

the geometric or material non-linearities and performs static studies or non-linear dynamics, modal studies and etc.

This code has an important level of validation similar to the commercial structural code Abaqus. J.-P. Aubry [7] presents a simple use of Code_Aster in a wide range of applications. This section starts by a presentation of the method of the balanced residues, then the isoparametric finite element is described with the process to solve the problem.

This description of Code_Aster equations is inspired from [2].

3.3.3.1 Method of the balanced residues of Gallerkin

The problem consists of solving equation 3.4 in the solid domain Ω_S. For our application, we consider that the problem is stationary and does not depend on time.

Equation 3.4 can be rewritten in a general way as :

$$\begin{cases} L(u) + f = 0 & with \quad L(u) = L\left(u, \frac{\partial u}{\partial x_1}, ..., \frac{\partial^2 u}{\partial x_1.\partial x_2}, ..., \frac{\partial^m u}{\partial x_\alpha^m}\right) \\ C(u) = h & on \qquad\qquad \Gamma = \partial\Omega_S \end{cases} \qquad (3.58)$$

$C(u)$ gives the boundary conditions on the border of the domain. L is a differential operator acting on the vector of the unknown solid field u, according to its partial space derivative. f and h are constants.

The residue $R(u)$ is the quantity cancelling itself when u is the solution of the physical problem :

$$R(u) = L(u) - f = 0 \quad in \quad \Omega_S \qquad (3.59)$$

The method of the balanced residues consists in two steps :

— To build an approximate solution u by the linear combination of judiciously selected functions :

$$u(x) = \sum_{i=1}^{N} c_i.\phi_i(x) \qquad (3.60)$$

$\phi_i(x)$ are the functions of forms and c_i are coefficients that will be determined.

— To solve the system in integral form :

$$\exists u \in E_u \ / \quad \forall P \in E_p \quad W = \int_{\Omega_S} R(u).P(u).d\Omega_S + \int_\Gamma [C(u) - h].P(u).d\Omega = 0 \,(3.61)$$

$P(u)$ are the weight functions belonging to a set of functions E_P and the solution of the problem u belongs to the solution space E_u. u must be derivable until the order m. The choice of the weight functions $P(u)$ leads to several methods.

In the method of Gallerkin, the weight functions $P(u)$ are the same functions of form $\phi_i(x)$.

Thus the problem consists in finding the functions of form $\phi_i(x)$ and solve equation 3.61.

3.3.3.2 Isoparametric finite element in Code_Aster

The finite element method reduces the complexity in analyzing geometries of an unspecified forms and facilitates the determination of the functions of form.
To build the approximation of the solution u (equation 3.60), the finite element method goes into two steps :

— Meshing : Ω_S is discretized into a number N_e of geometrically simple sub-domains Ω_e :

$$\Omega_S = \sum_{e=1}^{N_e} \Omega_e \tag{3.62}$$

— Define shape function $\overline{N}^e$ on each sub-domain to approximate the coordinates of the mesh 's nodes :

$$x^e = \sum_{i=1}^{N_{nd}} x_i^e . \overline{N}_i^e \tag{3.63}$$

e is an element, N_{nd} are the node contained in e and x^e express the coordinates in the global reference of a point belonging to the element e. x_i^e are coefficients to determine.

Depending on the geometry and especially in a 3D domain, the meshing process can be a complex operation. Code_Aster has algorithms able to perform Triangles (free grid) or quadrangles (regulated grid) for 2D and tetrahedrons (free grid) or hexahedrons (regulated grid) for 3D domains.

To ensure a conform mesh, two rules are mandatory :

— Each element must be defined in a single way starting from the coordinates of its geometrical nodes (and not those of its neighbors)

— The border of an element must be defined in a single way starting from the nodes of these borders,these nodes being common between the elements dividing this border

3.3.3.2.1 Elements of reference

To calculate the shape functions $\overline{N}^e$ on any element (x_1, x_2), we use a reference element (ξ_1, ξ_2) from which all the elements of a same family can be generated by a geometric transformation τ (figure 3.18).
The approximation of the solution u (equation 3.60) in the base of the reference element is written for a finite element e as :

$$u^e(\xi) = \sum_{i=1}^{N} a_i . N_i^e(\xi) \quad with \quad a_i = u_i \tag{3.64}$$

The finite element method proposes to construct a nodal approximation where the coefficients a_i correspond to the solution in u_i in these nodes. Equation 3.64 is a nodal approximation of the solution where $N_i^e(\xi)$ are the functions of form on the element ξ.
The method is isoparametric when $\overline{N}_i^e = N_i^e$, the interpolation of the solution u is identical the interpolation of the geometrical coordinates.
The literature [38] offers writings of nodal functions of form for the most common elements, depending on the choice of the polynomial base.
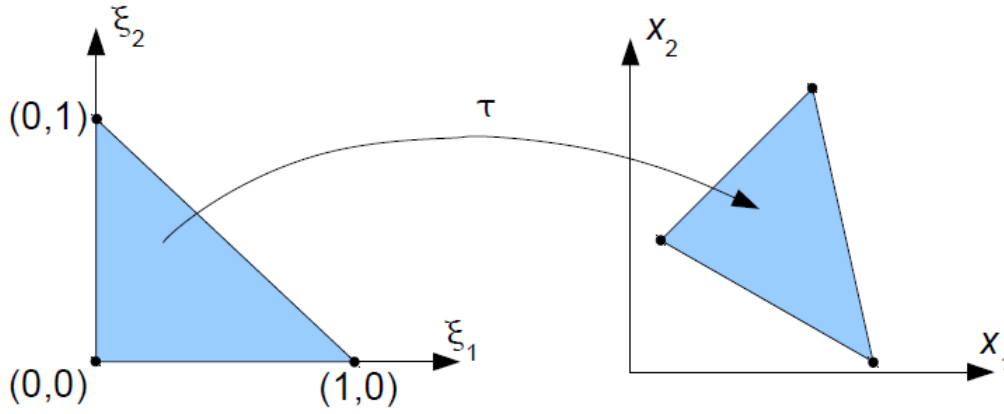
FIGURE 3.18 – From reference space to real space(x_1, x_2)

3.3.3.2.2 Discretized system

In a mechanical problem W defined in equation 3.61 is the potential energy of the system and the solution of the problem is the value of the unknown that minimizes the potential energy. Introducing the principle of virtual work, the system to solve take the following form :

$$\exists u \in E^h \ / \quad \forall \tilde{u} \in E^h \quad a(u, \tilde{u}) + b(\tilde{u}) = 0 \tag{3.65}$$

$\tilde{u}$ is the virtual displacement and E^h is the space virtual solutions h.
a is a bilinear, symmetrical form which represents the potential energy of the structure and b is the potential of volume and surface forces defined as :

$$a(u, \tilde{u}) = \int_{\Omega^h} \epsilon(\tilde{u}) : \sigma(u).d\Omega^h \tag{3.66}$$

$$b(\tilde{u}) = \int_{\Omega^h} f.\tilde{u}.d\Omega^h + \int_{\Gamma^h_N} g.\tilde{u}.d\Gamma^h \tag{3.67}$$

ϵ is the strain tensor, σ is the stress tensor. f and g are coefficients.
Discretizing this system consists in defining the function of form of the space Ω^h and computes the resulting matrix A and B (equations 3.66, 3.67).

After transformations, the system to solve is :

$$< \tilde{u} > .[A].\{u\} + < \tilde{u} > .\{B\} = 0 \quad \forall \tilde{u} \ \rightarrow [A].\{u\} + \{B\} = 0 \tag{3.68}$$

Code_Aster uses a method of factorisation matrix LDL^t to solve the system. The matrix [A] is generally hollow, thus Code_Aster rewrites it as [A] = [L][D][L]^t. [D] is a diagonal matrix, [L] is lower triangular and [L]^t is uper triangular. This factorization is possible when [A] is symmetric.

3.3.3.3 Some modeling in Code_Aster

This section briefly describes the models we used for the calculations of the two studied cases : the trapezoidal hydrofoil and the composite hydrofoils (see chapter 2).

3.3.3.3.1 3D elements

We use 3D elements to model th trapezoidal hydrofoil. This modeling is adapted for geometries with full volume
. These elements only allows 3 degrees of freedom on their nodes : the linear displacements in X,Y and Z.
Their mesh supports can be tetrahedrons, pyramids, prisms or hexahedrons. Depending of the mesh support, the interpolation recommended for the shape functions is given in figure 3.19.

Modeling	Mesh	Interpolation
3D	TRIA3	Linear or Bilinear
	TRIA6	Quadratic or Serendip
	QUAD4	Bilinear
	QUAD8	Serendip
	QUAD9	Quadratic

FIGURE 3.19 – Types of mesh allowed with the volume 3D elements and interpolation types for the shape functions.

3.3.3.3.2 Shells elements

The shell models are intended for computations in small strains and small displacements of thin structures where the ratio between the dimensions (thickness/characteristic length) is less than 1/10.
Code_Aster recommends to use DST elements when the thickness/characteristic length is between 1/20 and 1/10 and use DKT elements in the other cases.
In the case of the composite hydrofoils investigated, the theoretical thickness is $1mm$, and the shell length is $1350mm$ then, the thickness/characteristic length gives $7.4e-4$, less than 1/20. DKT models are used to model the skin of these laminates but simulations performed with the both models give the same results for this application case.
Two types of finite elements are possible with DKT model : triangular elements (DKT) or quadrangles (DKQ). This modeling is based on the Love-Kirchhoff model [119], dedicated to linear and non-linear behavioral relationships with integration sub-point fields in the thickness. .
The shape functions or function of form of the DKT elements are given in the figure 3.20.
The functions N are used as shape funcions for the coordinates as described above and function of form for the linear displacements. P are the functions of form used for the bending angles.
A complete description of these elements is given in [119]
For the composite hydrofoils, the sandwich section is model with DKT shell elements for the laminate skin and a 3D volume element for the web.

3.3.3.4 Definition of composite materials

The shell elements allow the analysis of thin structures made of elastic multi-layer composite material. The calculation of composite material in Code_Aster is performed using the operator **DEFI_COMPOSITE** which allows to define a multi-layer composite
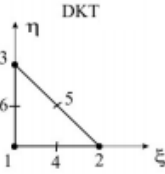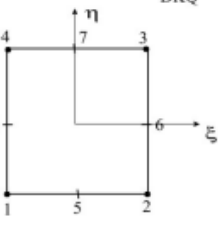
	$N_i \; (i=1,n)$	$P_i \; (i=n+1,2n)$
DKT	$i=1$ with 3 $$N_1(x,\eta)=\lambda=1-\xi-\eta$$ $$N_2(x,\eta)=\xi$$ $$N_3(x,\eta)=\eta$$	$i=4 \quad 6$ $$P_4(\xi,\eta)=4\xi\lambda$$ $$P_5(\xi,\eta)=4\xi\eta$$ $$P_6(\xi,\eta)=4\eta\lambda$$
DKQ	$i=1$ with 4 $$N_1(\xi,\eta)=\frac{1}{4}(1-\xi)(1-\eta)$$ $$N_2(\xi,\eta)=\frac{1}{4}(1+\xi)(1-\eta)$$ $$N_3(\xi,\eta)=\frac{1}{4}(1+\xi)(1+\eta)$$ $$N_4(\xi,\eta)=\frac{1}{4}(1-\xi)(1+\eta)$$	$i=5 \quad 8$ $$P_5(\xi,\eta)=\frac{1}{2}(1-\xi^2)(1-\eta)$$ $$P_6(\xi,\eta)=\frac{1}{2}(1-\eta^2)(1+\xi)$$ $$P_7(\xi,\eta)=\frac{1}{2}(1-\xi^2)(1+\eta)$$ $$P_8(\xi,\eta)=\frac{1}{2}(1-\eta^2)(1+\xi)$$

FIGURE 3.20 – Shape functions N and P of DKT and DKQ elements [119].

shell starting from from the bottom layer to the top layer.

It takes as input the layer-by-layer characteristics of the laminate layup : thickness of each layer, type of constituent material and orientation of the fibers relative to a reference axis. The orientation of the fibers is set in default θ = 0°, otherwise it must be provided in degrees and must be between −90° and and 90°.

The type of the constituent material of each layer is set by the operator **DEFI_MATERIAL** and we use the keyword **ELAS_ORTH** for orthotropic materials.

ELAS_ORTH defines the orthotropic behavior of a ply and takes as input the elastic modulus in longitudinal E_l and transverse direction E_t, the Poisson coefficient ν_{lt} and the shear modulus G_{lt}.

[130] shows how to use the operator **DEFI_COMPOSITE** and [10] presents the pre and post processing of composite in Code_Aster.

3.4 Summary of the chapter

This chapter describes the numerical couplings developed in this thesis to study FSI on hydrofoils. Two coupling with different level of fidelity are implemented.

The first part of the chapter presents the problem to solve, the Navier-stokes equations describing the fluid behavior and the structural behavior are presented and the kinematic and dynamic coupling conditions at the border are described.

In the second part, FS6R the low-fidelity coupling is discussed. It is a coupling between AVL plus Xfoil for the fluid analysis with an in-house beam theory. AVL stands on the vortex lattice method and allow 3D flows around a lifting surface. It computes non viscous calculation and a correction of the viscosity on the drag is performed using Xfoil which performs a 2D viscous calculation. The assumptions made in the standard version of Xfoil lead to an underestimation of the drag force, thus the drag force is expected lower than in the experiments.

Free surface effect is implemented in AVL calculation by adding a plane surface at the wa-

ter/air interface, the aim is to produce a ground effect which is observable in the case of submerged hydrofoils with small Froude numbers F_{nh}.

The structural calculation of FS6R is performed using the Euler-Bernoulli beam theory which is resolved by finite elements based on CALFEM functions. Bend-twist coupling is implemented in the model by modifying the stiffness matrix of the structure.

New terms are added for this structural coupling. These terms are calculated in a combination of the bending stiffness, the torsional stiffness, the percentage of composite layer inducing the twist and the percentage $\alpha[\%]$ of a ply orientation to induce the bend-twist coupling. The actual limitation of this coupling is the determination of $\alpha[\%]$ when computing composite materials. In our study, we used empirical values from the literature.

The outputs of the low-fidelity coupling is the distribution of the hydrodynamic loads on the structure and the displacement of the structure.

In the last part of this chapter, the high-fidelity coupling FOAM-Aster is presented. The coupling is performed between OpenFOAM which computes RANS simulation to describe the complete behavior of the flow and Code_Aster which performs mechanical analysis to describe the behavior of the solid structure.

The finite volume method is used in OpenFOAM uses to perform the computations. The discretization of the fluid domain is presented and the discretization of all the terms of the governing equation is discussed. The discretization schemes used for the calculations in this study is also presented and $k - \omega$ SST is used as viscosity model. The mesh is computed with the mesh generator CfMesh and the V6 of OpenFOAM is used.

Code_Aster stands on the balanced residue method of Gallerkin solved using finite element method. The balanced residues method is presented and discretized. The isoparametric finite element is formulated and the function of form/shape functions are presented. A brief overview of the 3D volume element, shell element and modeling of composite material is discussed.

The outputs of this high fidelity coupling is the complete flow field and structural field of the fluid+solid domain when the equilibrium is reached.

Relaxation factor is introduced in both coupling to accelerate their convergence.

The validation of these coupling is presented in chapter 4 for FS6R and chapter 5 for Foam-Aster. The meshes and boundary conditions will be discussed for each case.

CHAPTER 4

Experimental results and low-fidelity coupling FS6R : Numerical and experimental comparison

« *Et c'est là que jadis, à quinze ans révolus*
A l'âge où s'amuser tout seul ne suffit plus
Je connus la prime amourette
Auprès d'une sirène, une femme-poisson
Je reçus de l'amour la première leçon
Avalai la première arête »

Georges Brassens

Contents

This chapter aims in one hand to analyse the FSI behavior of the different hydrofoils studied in this ph.D. thesis and on the other hand, to validate the simulations of the low-fidelity coupling FS6R.

The chapter is divided into two parts corresponding to the model-scale and real-scale hydrofoils : the the trapezoidal POM hydrofoil and the composite hydrofoils. Each part has two sections : the experimental results are presented and analyzed in the first section and a comparison of FS6R simulations to the experiments is performed in the second section. For each case, the sensitivity to the mesh is analyzed.

4.1 POM hydrofoil

Figure 4.1 shows the geometry and dimensions of the POM hydrofoil. The location along the span of the points A, B and C used in the mechanical characterization are given.
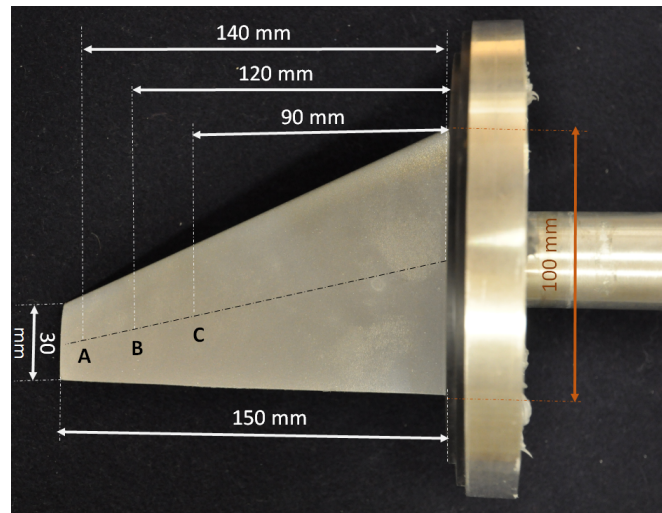
FIGURE 4.1 – Geometry and dimensions of the trapezoidal POM hydrofoil.

4.1.1 Mechanical characterization

The POM characteristics found in the literature are ranging from 2.9 MPa to 3.2 MPa. The aim of this mechanical characterization is to determine the young modulus of the manufactured hydrofoil.

Bending tests are performed for three loading cases applied on points A and B sown in figure 4.1 and the vertical displacement of the three points A, B and C are measured. The results are given in table 4.1 for the loading applied on point A.

Force [N]	$Point_A$ [mm]	$Point_B$ [mm]	$Point_C$ [mm]
5	0.25	0.18	0.12
7	0.52	0.36	0.26
10	0.78	0.55	0.38

TABLE 4.1 – Vertical displacements measured at points A, B, C. The load is applied on A.

The recorded values are very low, under 1mm. To analyse these data and assess the Young modulus of the foil, a numerical simulations are performed with Code_Aster for three

Young modulus starting with the theoretical value 2.9 GPa : $E_1 = 2.9$ GPa, $E_2 = 3$ GPa, $E_3 = 3.1$ GPa.

The comparison between the experimental measurements and the simulations with Code_-Aster are shown in figures 4.2 and 4.3.
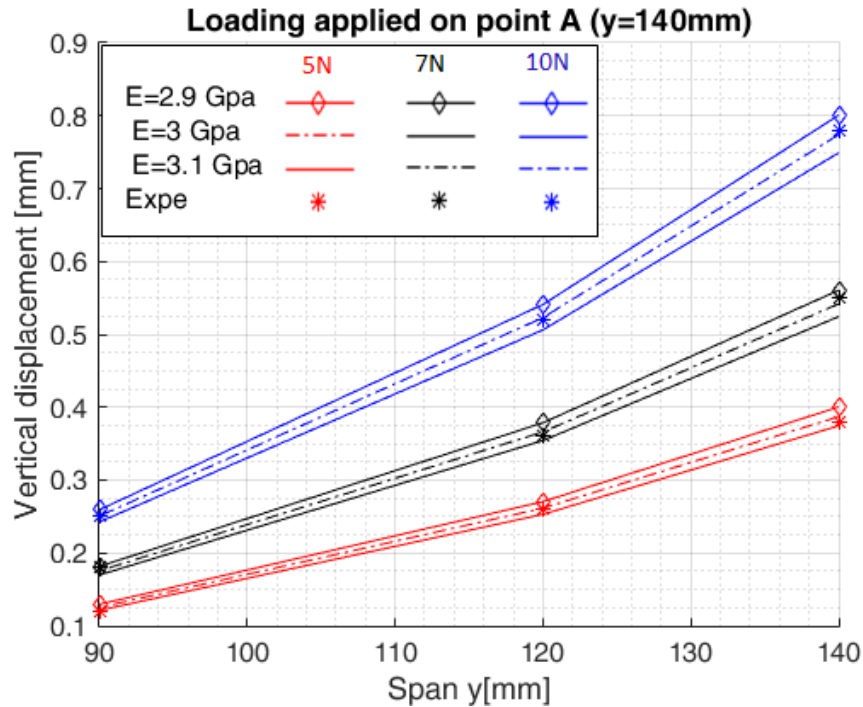
FIGURE 4.2 – Displacement of POM hydrofoil under bending loading on point A for several Young modulus.
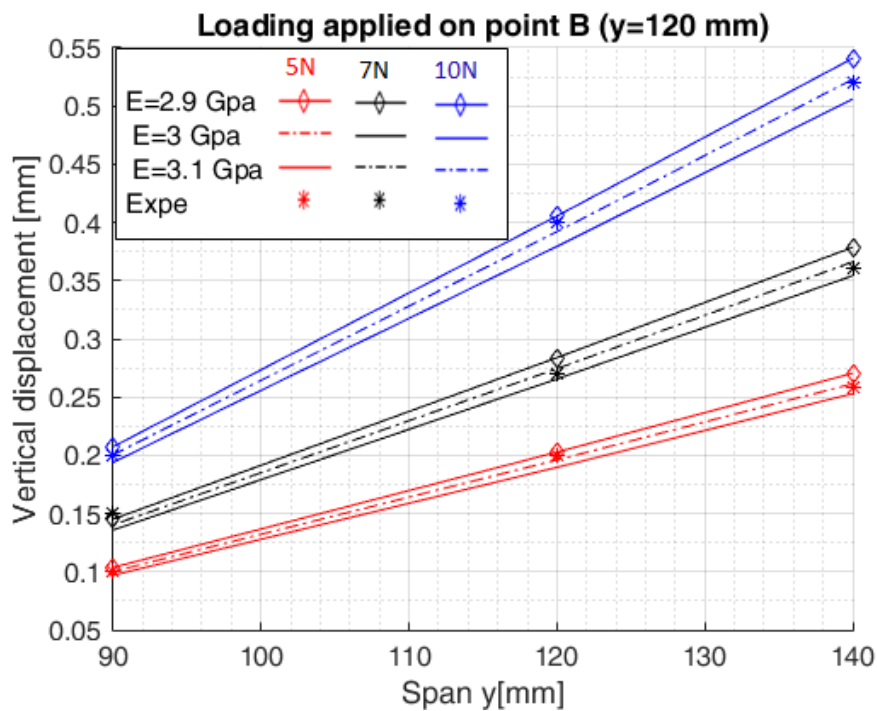
FIGURE 4.3 – Displacement of POM hydrofoil under bending loading on point B for several Young modulus.

The numerical simulations have the same trend with the experiments. The displacement increases when the load increases.

When the load is applied on point A, the displacement curves exhibit a small bending, when the behavior is linear for the loading applied on point B. For both numerical and experimental approaches and for each measurement point, E = 3 GPa appears as the best match.

Thus the Young modulus of the POM hydrofoil that will be used in numerical simulations is E = 3 GPa.

4.1.2 Hydro-elastic behavior of the POM hydrofoil : Experimental results

FSI on the hydrofoil are investigated in hydrodynamic tests carried out in the hydrodynamic tunnel of IRENAV for several angles of attack and five Reynolds numbers : 3×10^5, 4×10^5, 5×10^5, 6×10^5, 7×10^5 .

Due to the disk at the root of the hydrofoil (see figure 4.1), it was not possible to connect the hydrodynamic balance and thus, only the displacement are measured in these experiments.

The displacement of the hydrofoil along the span is measured on a continuous line and seven points along this line presented in figure 4.4.
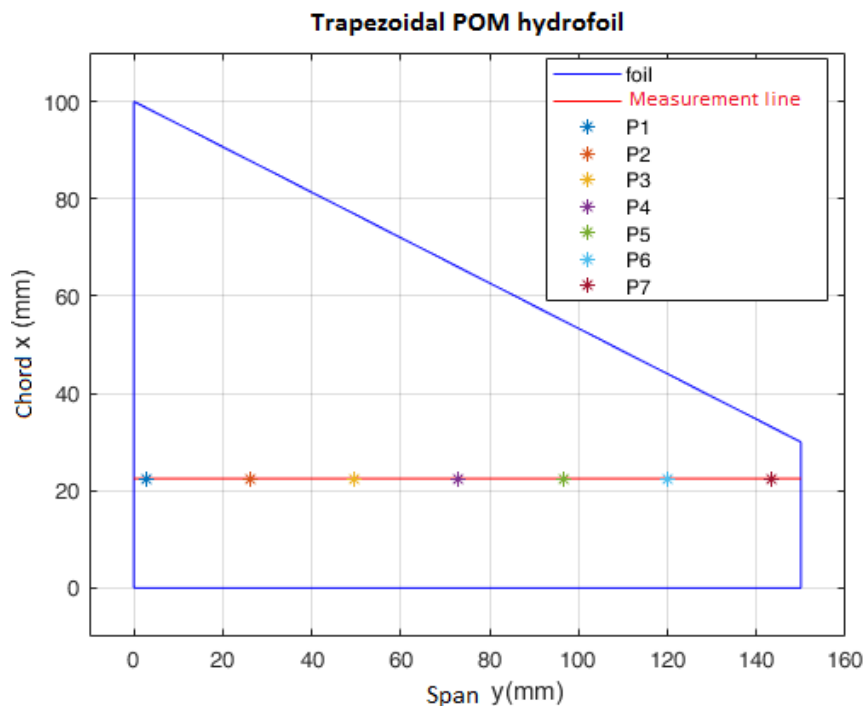
FIGURE 4.4 – Measurement line and measurement points of the POM hydrofoil used the hydrodynamic tests.

Figure 4.5 shows the deformed shapes of the hydrofoil along the span measured at $\alpha = 6°$ for all the Reynolds numbers.

The first graph shows the shape of the hydrofoil obtained with the continuous measurement on the line along the span and the second graph is obtained from the measurement on the seven points along the span. The measurements on the points are smoother than the continuous line thus, the experimental results presented in this chapter will be extracted from the data measured on the points.
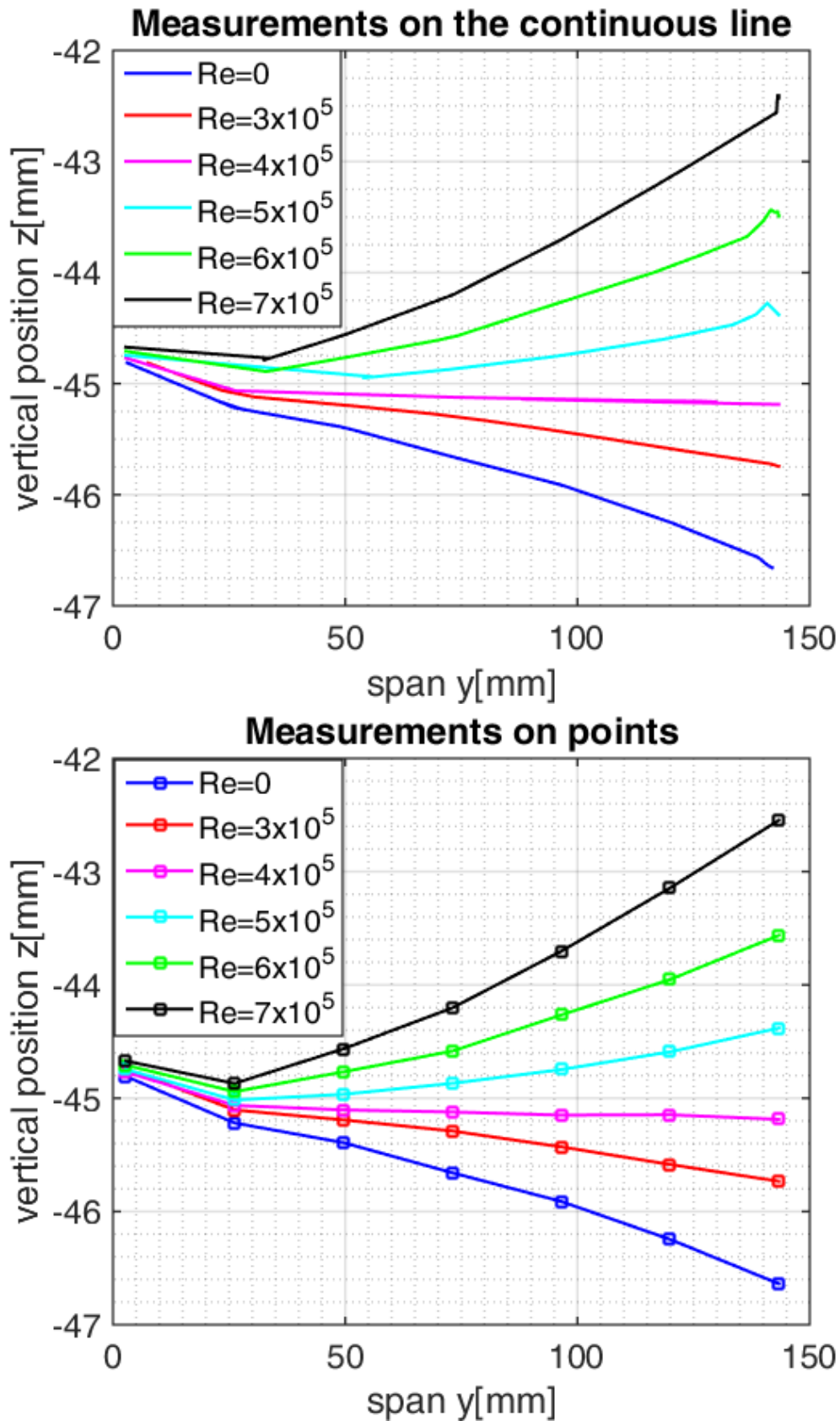
FIGURE 4.5 – Shape of the hydrofoil at α = 6° : continuous and discontinuous measurements

Figure 4.6 shows the images of the hydrofoil recorded at α = 10° for all the velocities investigated.

FIGURE 4.6 – Hydro-elastic response of the POM hydrofoil, $\alpha = 10°$

The images exhibit a bending behavior as hydro-elastic response of the hydrofoil. The incidence is positive thus, the hydrofoil bends upward and that bending increases with the velocity, in agreement with the lift increase.

In the following, figures 4.7, 4.8 and 4.9 give the vertical displacements of the POM hydrofoil under the hydrodynamic loads for all the configurations.

The displacement is calculated as the difference between the measurements of the hydrofoil deformed (with flow) and the measure of its reference position (without flow at $0 m/s$). Example of measurements are shown in figure 4.5.

For all the figures 4.7-4.9, the results highlight the behavior of a classical symmetric profile as expected for a NACA0015 section.

The symmetry is not well respected for $\alpha = \pm 2°$, that difference might come from the data post-processing or a small error in the incidence setup.

The measurements were mistakenly not recorded for $\alpha = -10°$ at $Re = 7 \times 10^5$.

For lower Reynolds number, the curves show some jumps modifying the bending trend of the foil, it can be related to a post-processing of the small of the displacement field.

As the speed increases, the forces on the structure increase and the displacement values become significant up to 4.7% of the hydrofoil span at the tip for $\alpha = 10°$ at $Re = 7 \times 10^5$.
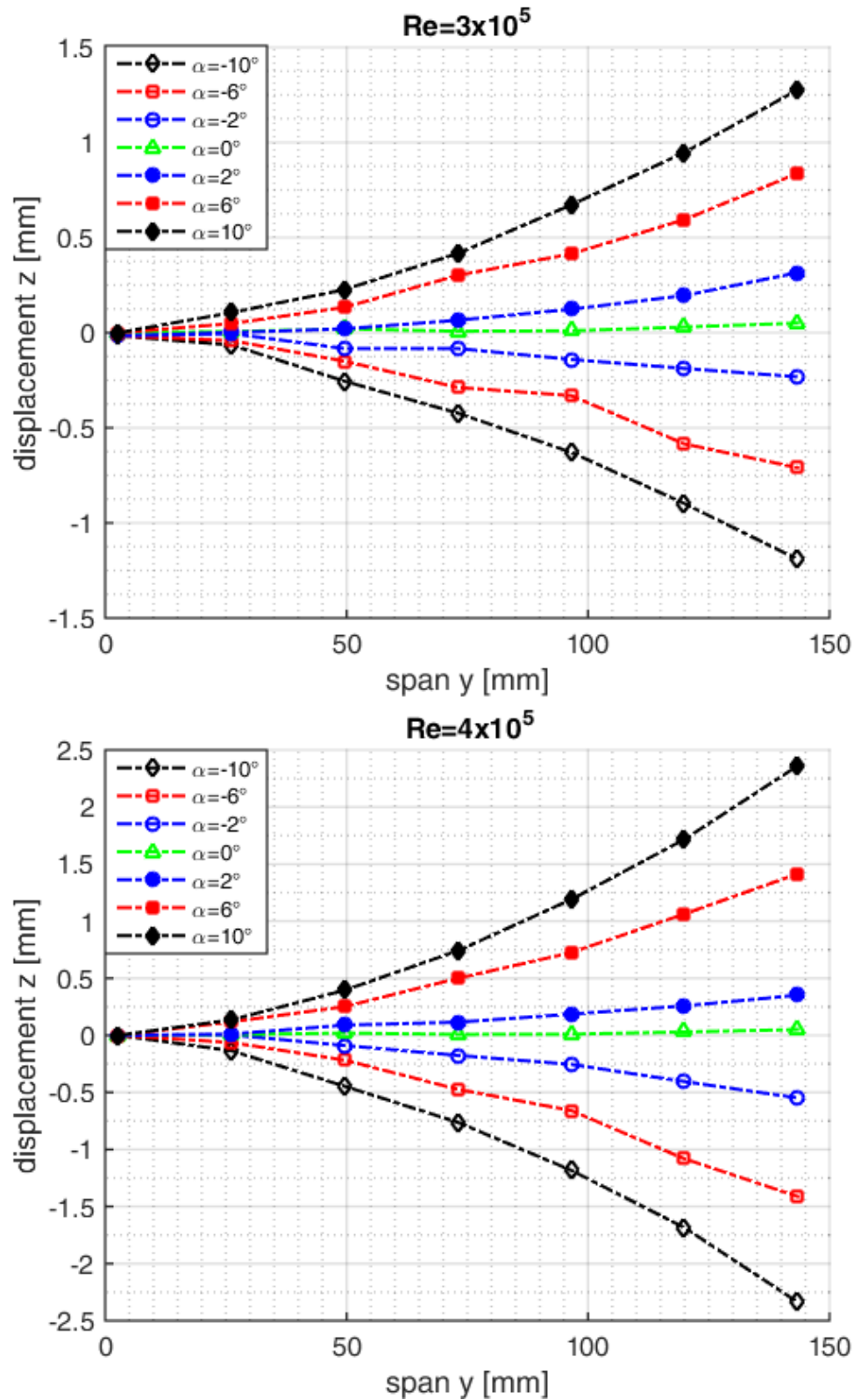
FIGURE 4.7 – Experimental displacement of the POM hydrofoil Re = 3×10^5 and 4×10^5.

The displacement curves show a well defined bending.
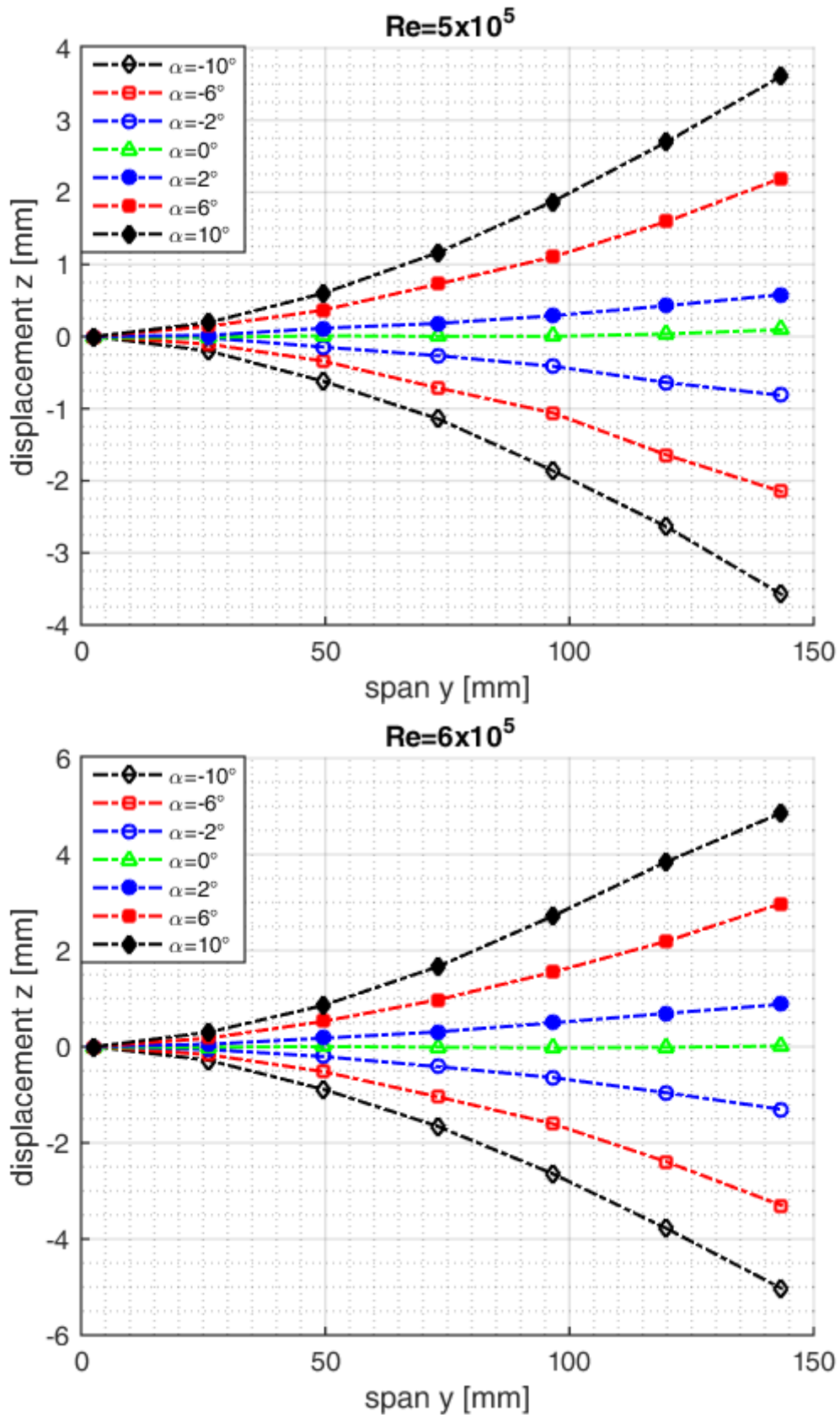
FIGURE 4.8 – Experimental displacement of the POM hydrofoil R$e = 5 \times 10^5$ and 6×10^5.
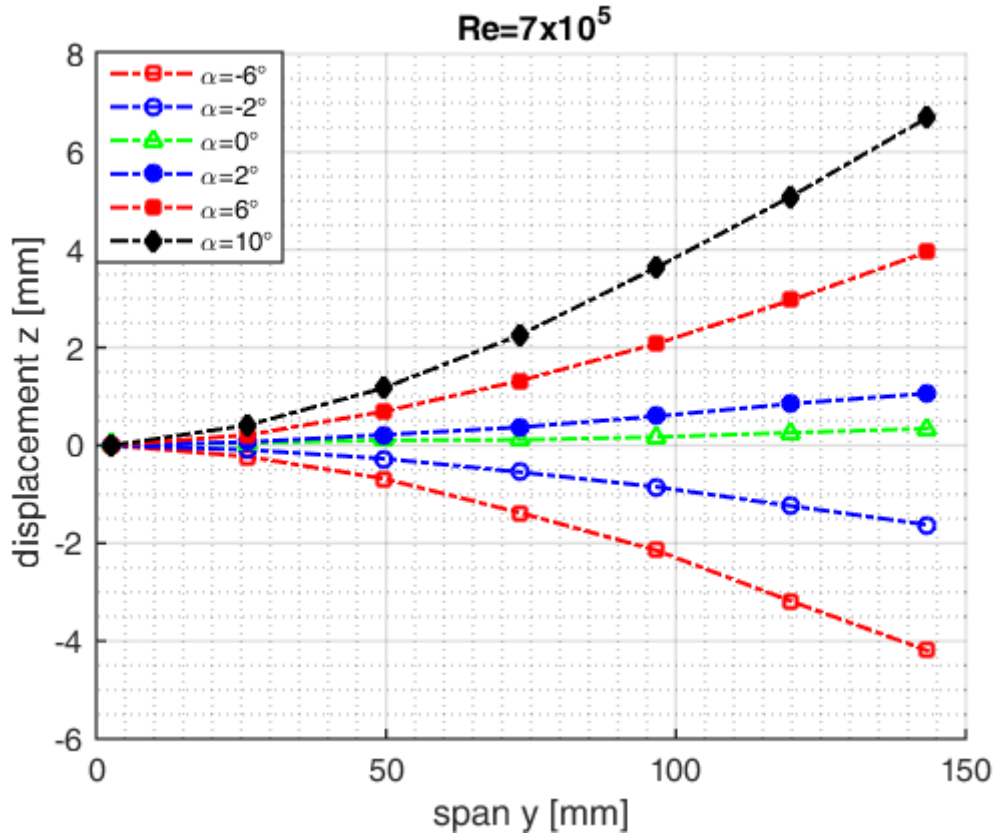
FIGURE 4.9 – Experimental displacement of the POM hydrofoil R$e = 7 \times 10^5$.

4.1.3 Hydro-elastic behavior of the POM hydrofoil : comparison with FS6R

The validation of FS6R on the model-scale hydrofoil in isotropic POM material is performed in this section. The simulations on the hydrofoil are performed with FS6R in the same configurations as the experiments and the numerical-experimental comparison is presented.

4.1.3.1 Mesh sensitivity

The purpose of this section is to investigate the influence of the mesh on the numerical results. We vary the panel discretization along the chord and along the span and we analyze the convergence on the lift coefficient and displacement at the tip for three simulation cases : $\alpha = 2°$, $\alpha = 6°$, $\alpha = 10°$ at R$e = 7 \times 10^5$.
The convergence criteria is set at $\epsilon = 10^{-3}$ on the displacement. These simulations are performed without relaxation on the forces.

4.1.3.1.1 Mesh variation along the span

The number of panel is set at 100 along the chord and simulations are performed on FS6R for several panels along the span.
FS6R takes 66 seconds CPU time : 50 seconds to read the input file and takes 16 more seconds to compute the simulation with 20 panel along the span. The simulation time evolves with the number of panel along the span and each case converges after 3 iterations for the tolerance ϵ.

Figure 4.10 shows the influence of the number of panel on the lift coefficient and the vertical displacement of the tip of the hydrofoil.
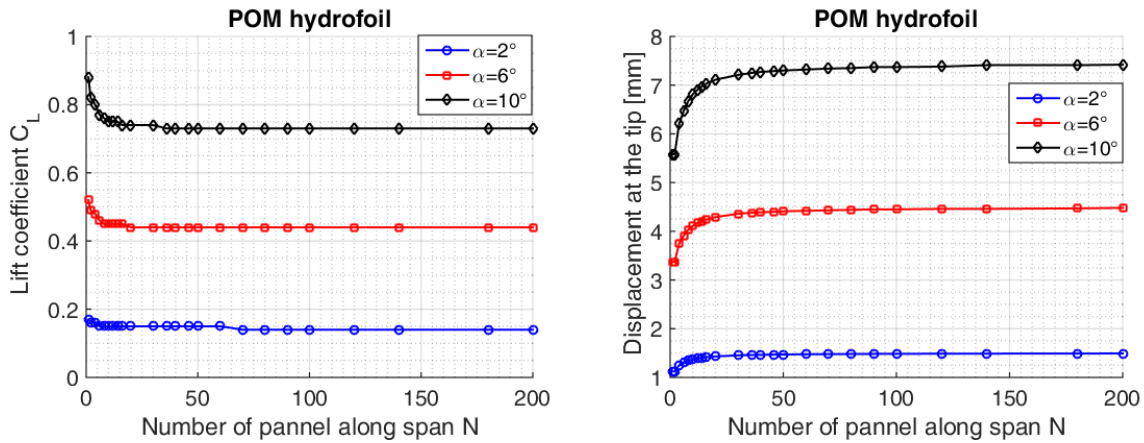
FIGURE 4.10 – Influence of the span discretization on the lift and displacements of the POM hydrofoil (100 panels along the chord), Re=7×10^5.

The trend of the lift coefficient is the same for the three configurations and for a number of panel above 50, the variation on the lift coefficient become negligible.
The displacement increases when the mesh gets refined and the trend is the same for the three configurations. For a number of panels above 80, the displacement at the tip of the hydrofoil becomes constant.

4.1.3.1.2   Mesh variation along the chord

The number of panels along the span is set at 120 and the simulations are performed for several number of panels along the chord.
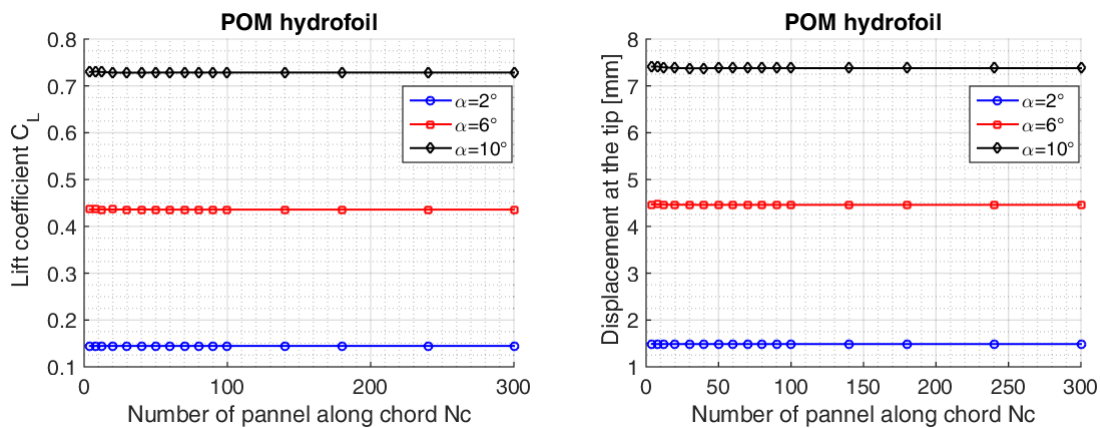
FIGURE 4.11 – Influence of the chord discretization on the lift and displacements of the POM hydrofoil (120 panels along the span), Re=7×10^5.

FS6R also takes 146 seconds CPU time : 50 seconds to read the input file and 96 seconds to perform a simulation. The simulation time does not varies with the number of panel along the chord and the convergence is also reached after 3 iterations.

The influence of the number of panels along the chord on the lift coefficient and the displacement of the tip of the hydrofoil is shown in figure 4.11 .
The displacement and the lift decrease when the number of panel increases and the convergence is reached in both cases for a number of panel above 50 along the chord.

4.1.3.1.3 Mesh

The mesh chosen for the POM hydrofoil contains an equal distribution of 80 panels along the span and 50 panels along the chord as shown in figure 4.12.
For this mesh, a simulation without relaxation takes 94 seconds CPU time (50 seconds to read the input file and 44 seconds to run the case).
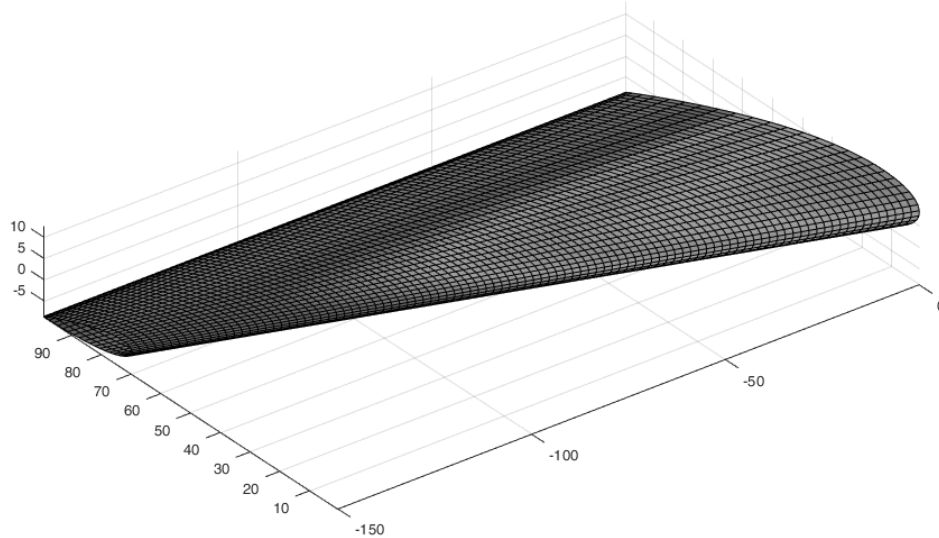
FIGURE 4.12 – Mesh of the POM hydrofoil

4.1.3.2 Relaxation factor

This parts investigates the influence of the relaxation factor on the convergence of the simulation. The mesh is presented in figure 4.12 and the simulations are performed for several values of the relaxation factor ω.
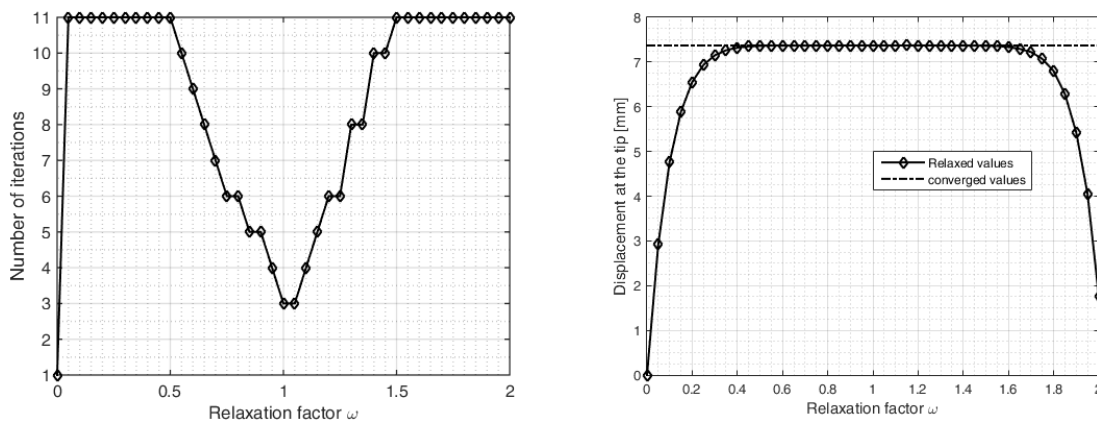
FIGURE 4.13 – Influence of the relaxation on the convergence, α = 10° Re=7×10^5,ε = 10^{-3}.

The reading time of the input file remains the same but the simulation time varies with the relaxation factor ω.
Figure 4.13 shows the evolution of the number of iteration before a convergence with the relaxation factor ω and the convergence on the displacement at the tip of the hydrofoil.
For ω = 1, the number of iteration is the same without and with the relaxation and this number increases when ω become slower or higher than 1 and as a consequence, the

simulation time increases too.

The displacement does not converges to the same value when ω varies and it reaches the experimental value for $0.5 < ω < 1.5$. With these observations, the following simulations are performed without relaxation.

4.1.3.3 Hydrodynamic coefficients

This section compares the lift and drag coefficients computed with FS6R for the POM hydrofoil experiencing FSI with a simulation performed on XFLR5 in a rigid configuration (only a fluid simulation).

The simulations are performed for the positive angles at $Re = 7 \times 10^5$ and the method chosen on XFLR5 is the VLM with viscous effect.

Figure 4.14 compares the evolution of the total drag coefficient along the span with FSI and without FSI in a rigid case for three angles of incidence.
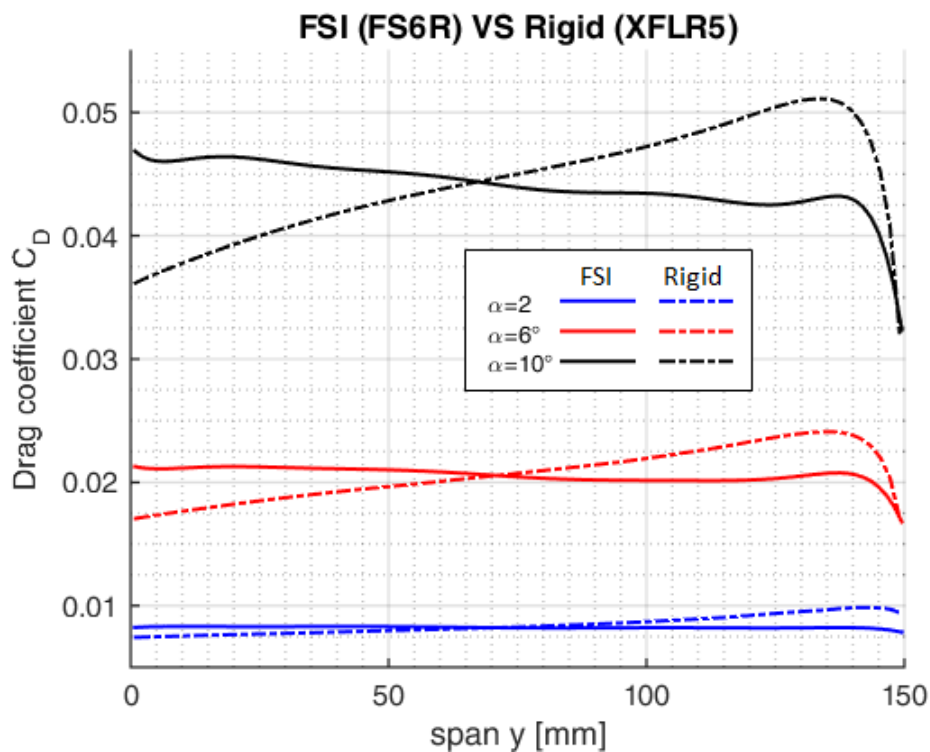
FIGURE 4.14 – Comparison of the drag coefficient with and without FSI on POM hydrofoil, $Re = 7x10^5$.

In the rigid case, the drag coefficient increases from the root to the tip and we observe a sudden decrease at the tip when for the flexible case, the drag starts with a higher value at the root and slightly decreases from the root to the tip. Flexible and rigid cases both decrease to similar values at the tip.

Table 4.2 gives the integrals of the distribution over the span and we observed that the distribution of the drag along the span is different in the flexible and the rigid case but the integral which is the image of the drag force is the same in both case. Thus the FSI does not modify the value of the total drag force but impacts its distribution on the hydrofoil.

Figure 4.15 compares the lift coefficient in the rigid case and the deformable cases for $α = 2°, 6°, 10°$. The trends of the curves are the same in both case for all the incidences : the lift increases slowly from root to tip and decreases around the tip. The rigid and the deformable cases do not overlap and the conclusions are the same with the drag.

Incidence $\alpha[°]$	C_D FSI	C_D Rigid	C_L FSI	C_L Rigid
2	0.0012	0.0012	0.0216	0.0208
6	0.0031	0.029	0.0650	0.0621
10	0.0066	0.0060	0.1085	0.1027

TABLE 4.2 – Integral of the lift and drag coefficients along the span
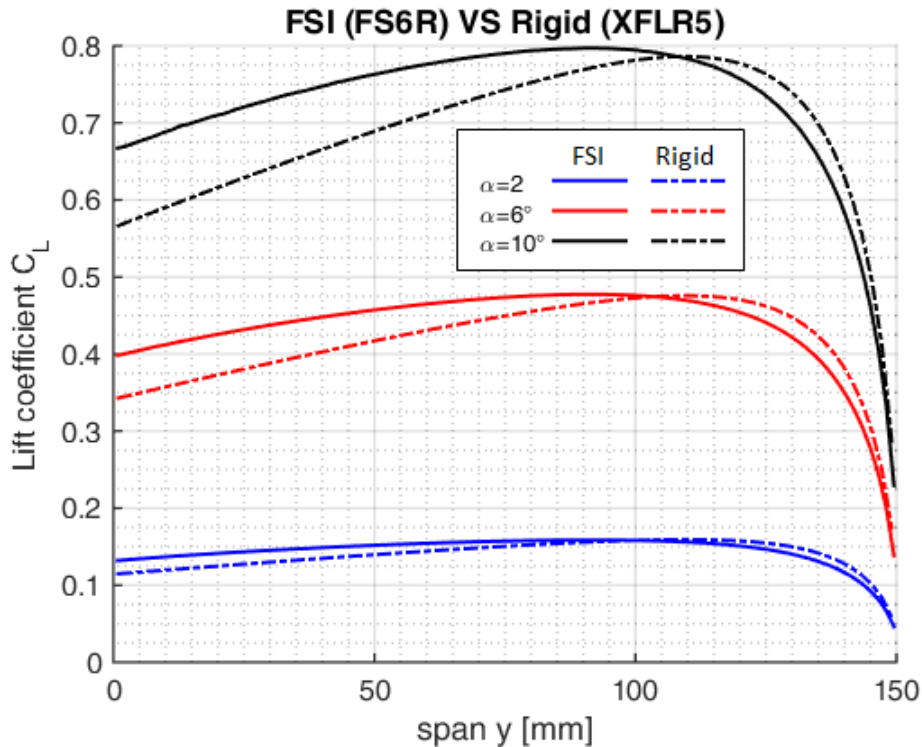
FIGURE 4.15 – Comparison of the lift coefficient with and without FSI on POM hydrofoil, $Re = 7x10^5$.

The integrals of the distributions given in table 4.2 are the same in both cases : the bending motion induced by the FSI does not modify the lift amplitude but its distribution along the span of the hydrofoil.

4.1.3.4 Displacements under hydrodynamic loads

Figure 4.16 shows the experimental shape of the foil recorded during the hydrodynamic tests and the calculated numerical shape of the deformed POM hydrofoil at $Re = 7 \times 10^5$ and $\alpha = 10°$.
During the tests, a camera is fixed on a tripod placed in front of the tunnel and pictures of the hydrofoil are taken without and with flow for several incidences.
The red lines drawn on the chord in the experimental image without and with flow are parallels, there is no twist induced on the deformed shape.
The images are very similar, FS6R computes the displacements of a foil in isotropic material with good accuracy.

Figure 4.17 compares the displacement of the hydrofoil computed with FS6R with the experiments for all the incidences at $Re = 6 \times 10^5$.
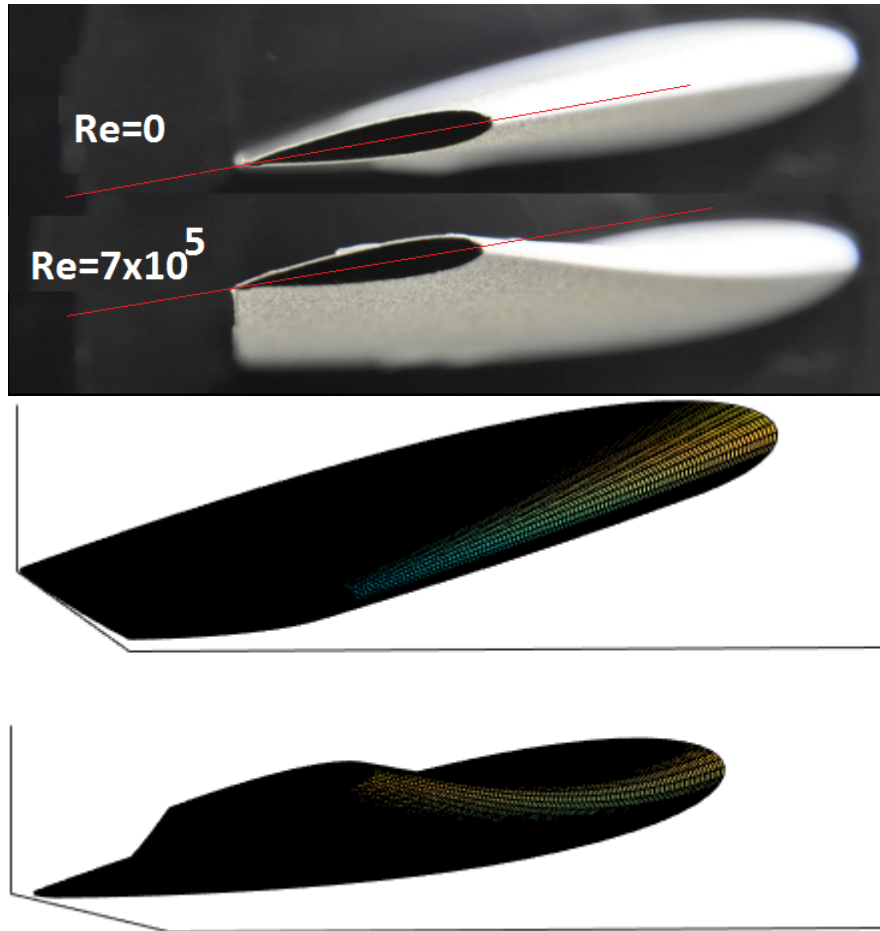
FIGURE 4.16 – FS6R VS experiments : deformed shape of the hydrofoil, $\alpha = 10°$ and R$e = 7 \times 10^5$.

The vertical bars are 5 times the standard deviation computed on the measurements recorded with the laser on each experimental point. The vertical axis corresponds to the vertical displacement of the foil and the horizontal axis is the span.

The structure moves vertically as a consequence of the lift effect, the displacements simulated have the same trend than the experiments and the symmetry with the angles of attack is respected.
The same observations are repeated with R$e = 7 \times 10^5$ and the other Reynolds numbers, FS6R values are within the experimental error bars.

The graphs for R$e = 3 \times 10^5$ and 4×10^5 are shown in figures 4.19 and 4.20.
Both numerical and experimental results match very well along the span and the displacement is numerically lower than the experiments. The Young modulus is suspected to be the origin of that difference.
To assess the difference between the two approaches, the relative discrepancies are calculated for each experimental measure i as :

$$error[\%] = \frac{(\text{FS6R}(i) - expe(i)) * 100}{expe(i)} \tag{4.1}$$

For all the experimental cases, the error is less than 7%, FS6R computes the behavior of the isotropic POM material in good agreement with experiments.
Now we are looking at the composite materials.

FIGURE 4.17 – FS6R VS experiments on POM hydrofoil, R$e = 6 \times 10^5$: displacements, the vertical bars represent 5 times the standard deviation.
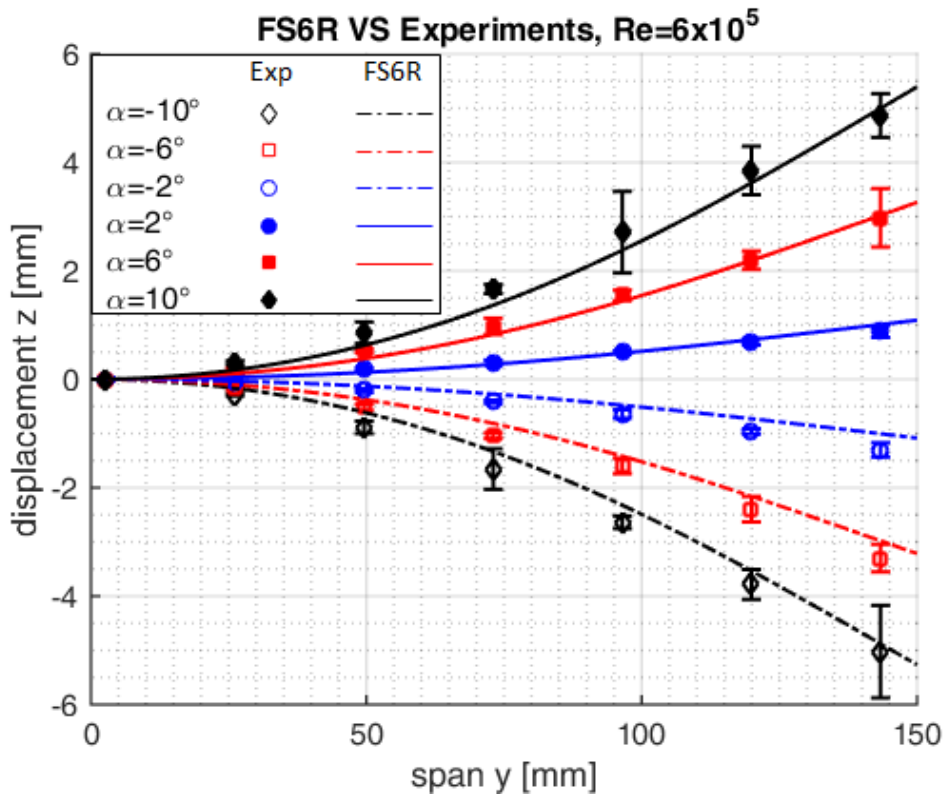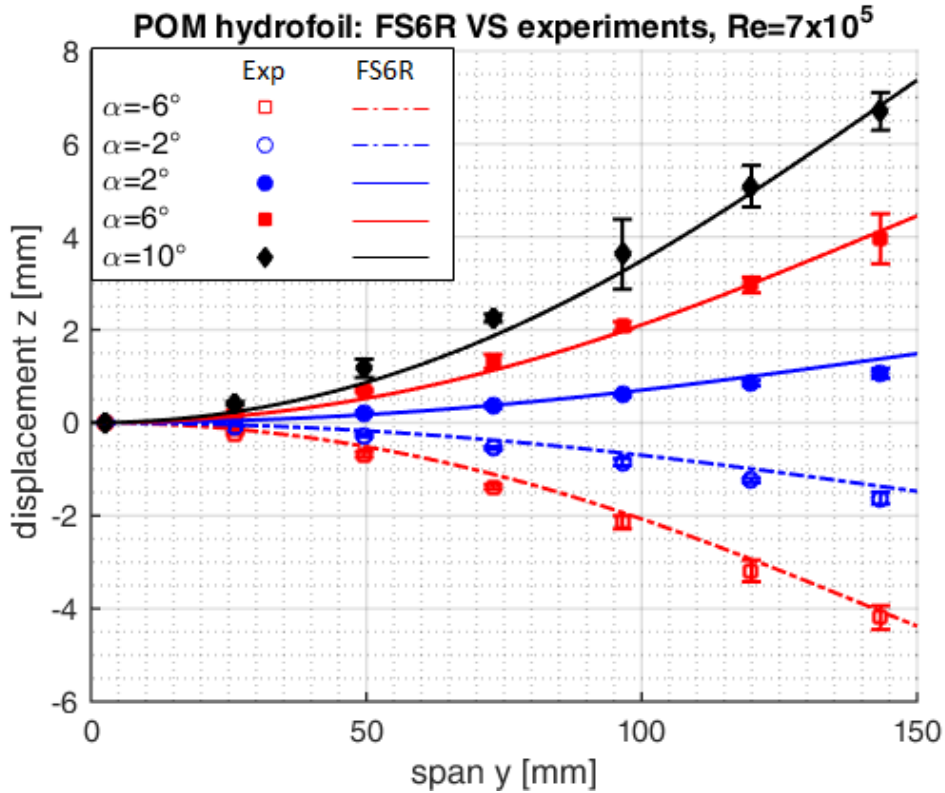

FIGURE 4.18 – FS6R VS experiments on POM hydrofoil, R$e = 7 \times 10^5$: displacements, the vertical bars represent 5 times the standard deviation.
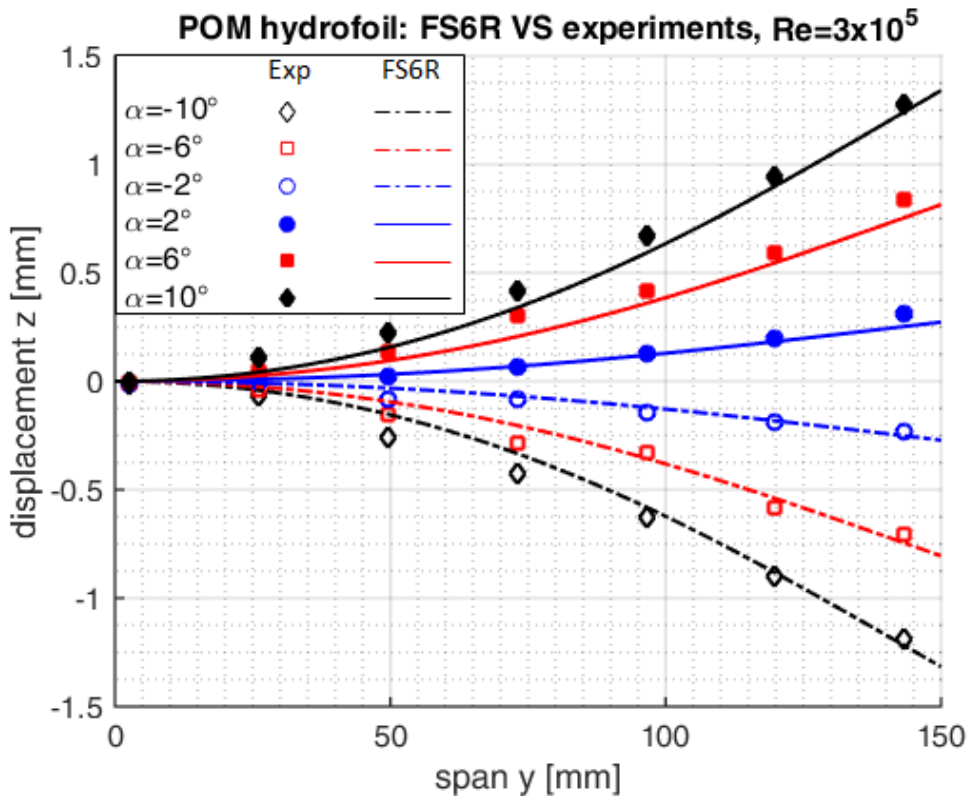
FIGURE 4.19 – FS6R VS experiments on POM hydrofoil : displacements for $Re = 3 \times 10^5$.
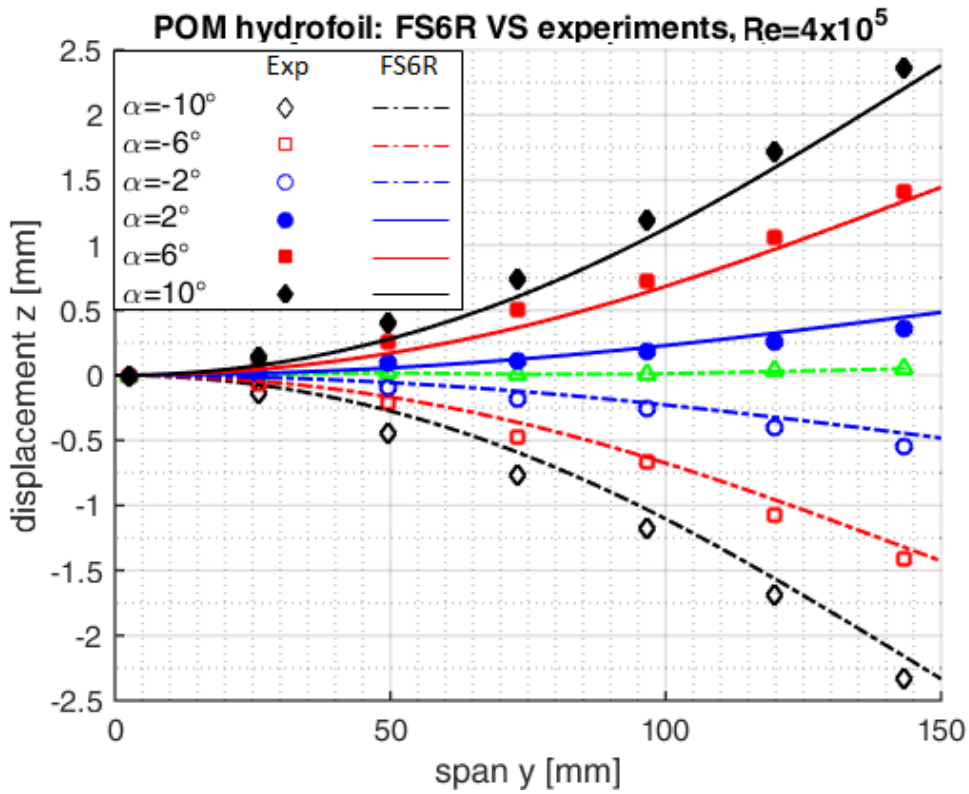
FIGURE 4.20 – FS6R VS experiments on POM hydrofoil : displacements for $Re = 4 \times 10^5$.

4.2 Composites hydrofoils

This section presents the experimental results of the composite hydrofoils which are compared with FS6R. It starts with the mechanical characterization of the hydrofoils to determine the bending and torsional modulus, then the investigations of the BTC is presented and the last part shows the numeric-experimental comparison.

4.2.1 Mechanical characterization

4.2.1.1 Bending stiffness

We are comparing four methods in the determination of the bending stiffness of the hydrofoils (see section 2.2.2) :

— Bending tests performed with five masses M_i, $i = 1,..5$

— Vibration tests noted vib

— Tensile tests performed on specimens with the same layups than the hydrofoils. The bending stiffness is the product of the experimental tensile modules with the inertia of the laminate skin of the hydrofoils.
In the results "tens1", the inertia are calculated using the theoretical the thickness of the hydrofoils skins when in "tens2", the thickness of the specimen are used to compute the inertia of the layups.

— The laminate theory, noted LT. The bending stiffness is the product of the elastic modulus calculated with the inertia calculated using the theoretical thickness of the hydrofoils skins.

The experimental setup of the bending and vibration tests is presented in figure 4.21.
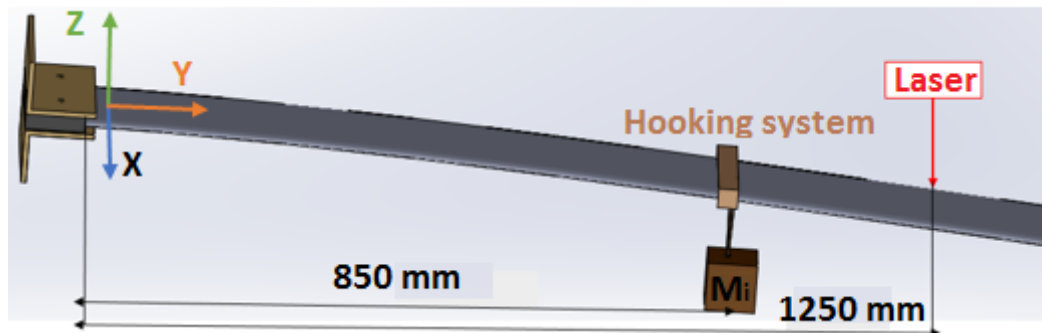
FIGURE 4.21 – Experimental setup of bending tests and vibrations tests.

In the reference system defined in this figure, the stiffness investigated is $E_y I_x$. To simplify the notation we are using EI in the following results.

Figures 4.22 and 4.23 show the bending stiffness EI of the 4 composite hydrofoils obtained with experiments and the laminate theory.

The horizontal axis represents the type of test performed and the vertical axis is the bending stiffness. "vib" stands for vibration tests, M_i with $i = 1,2,...5$ are the bending tests using the masses M_i, "tens1" and "tens2" are the tensile tests and LT is the laminate theory.

The results of the tensile test using the theoretical thickness of the hydrofoils skins "tens2" are lower than the other methods, up to 30% compared to the laminate the vibration test
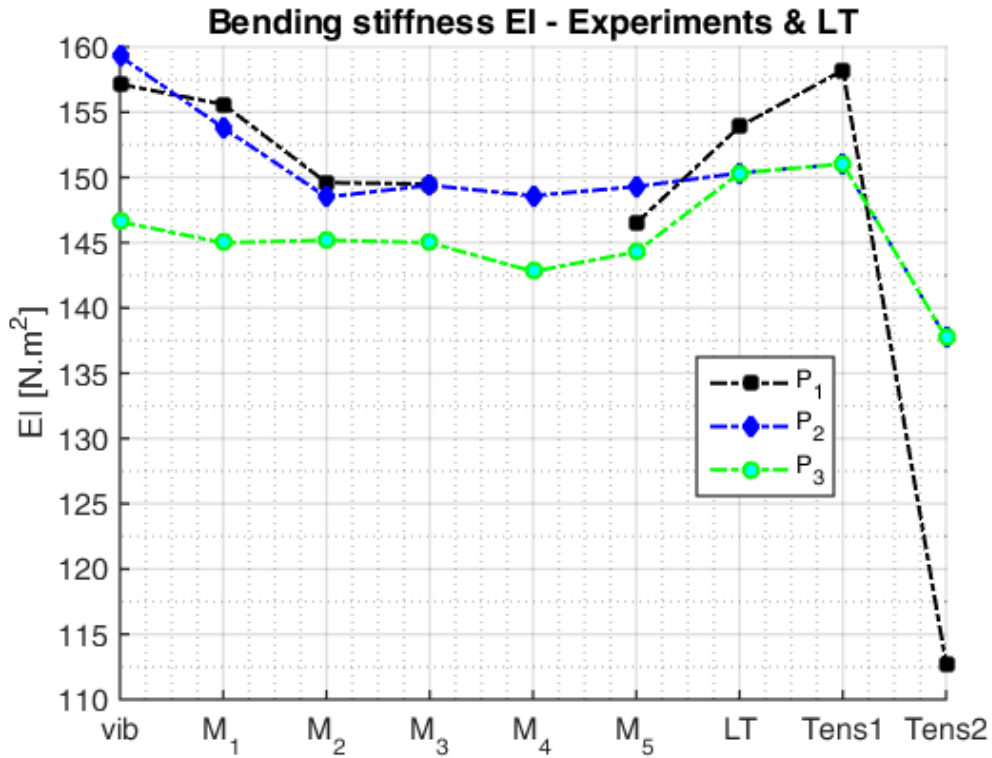
FIGURE 4.22 – Bending stiffness EI of the the composite hydrofoils P_1, P_2 and P_3.
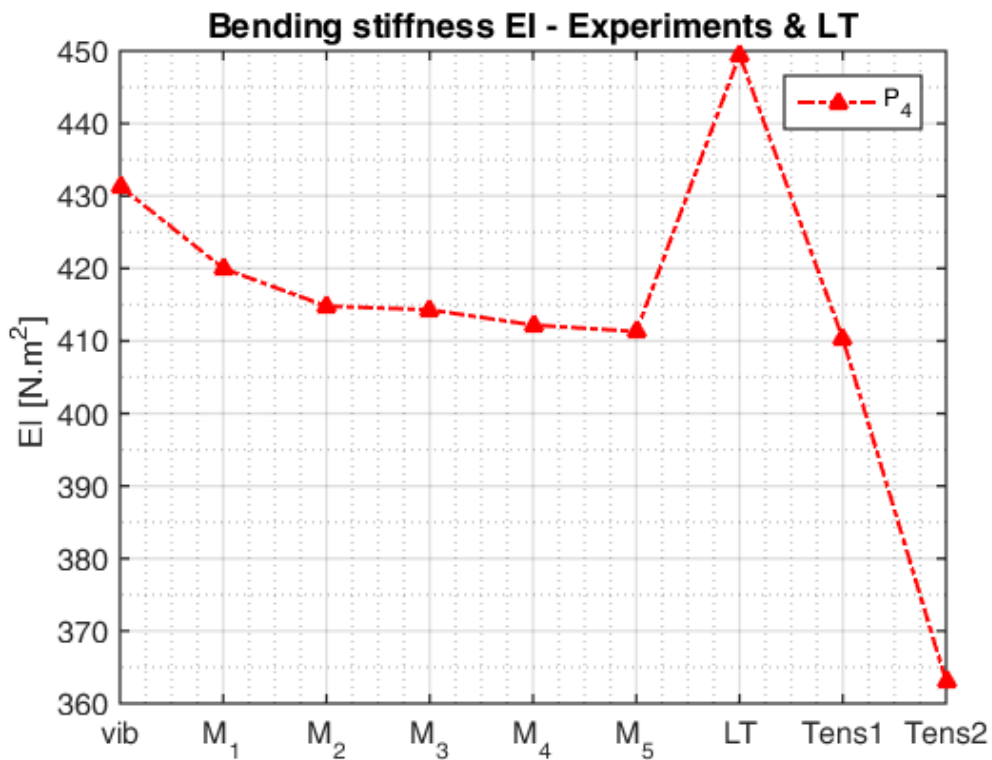
FIGURE 4.23 – Bending stiffness EI of the the composite hydrofoils P_4.

on P_1. That difference may results in difference between the hydrofoil skin and the specimen manufacture. The real thickness of the specimen are higher than the thickness of the

hydrofoil skin, the volume of resin must be higher in the specimen and other errors may have occur in the fabrication leading to such discrepancies.

When using the real thickness of the specimen to compute the inertia of the hydrofoil skin, the results of the bending tests are very close to the other methods. The lower modulus is compensate with the higher inertia giving a bending stiffness in the same amplitude with the bending tests.

All the methods are very close to each other for all the hydrofoils excepts the laminate theory on the carbon hydrofoil that gives the highest results. This could highlight a problem in the embedding of the carbon hydrofoil during the bending tests. An embedding system not well fixed can lead to higher bending deformations and then lower calculated stiffness.

The structure of the composite hydrofoils could be non-homogeneous along the span (from a macroscopic point of view) creating a variation in the inertia, different from the constant value used in the laminate theory. Another explanation of that difference could be the mechanical properties used for the carbon ply that are higher than the composite ply manufactured indeed.

The experimental stiffness of the hydrofoils are given in table 4.3. They are calculated as the average of the results of the vibration tests and the bending tests.

Layus	P_1	P_2	P_3	P_4
EI[N.m^2]	151.67	151.48	144.82	417.32

TABLE 4.3 – Bending stiffness EI of the composite hydrofoils

Equation 4.2 gives the expression to compute the discrepancies of the different methods, the reference values are the bending stiffness of the table 4.3.

$$error[\%] = 100 \times \frac{test - reference}{reference} \tag{4.2}$$

Figure 4.24 compares with the relative difference of each test to the mean value of the experiments. For all the tests the difference is less than 6%, showing a good confidence in the different approaches.

Excepts for P_4, the laminate theory is thus able to compute the bending stiffness of the hydrofoils with a relative difference less than 4%, that will lead to a difference of 4% on the displacements.

Figure 4.25 shows the displacement of the 4 hydrofoils under the bending loading M1 = 2.2 kg.

The figure shows the simulation with FS6R and the experimental measurements on two points along the span. The mesh used in these simulations is shown in figure 4.43 and the computations uses the experimental bending stiffness given in table 4.3.

The numeric displacement of the hydrofoil shows a well defined bend for all the layups. The stiffness of P_4 is the highest thus, its displacement is the smallest. The stiffness of P_1 is very close to P_2 and slightly higher leading to very close displacements and P_2 slightly higher. The stiffness of P_3 is the smallest leading to the highest bend.

The numeric results overlap very well with the experiments, that validates the calculation of the bending stiffness and illustrates the ability of the low-fidelity coupling FS6R to compute the different structural behavior of the different layups.
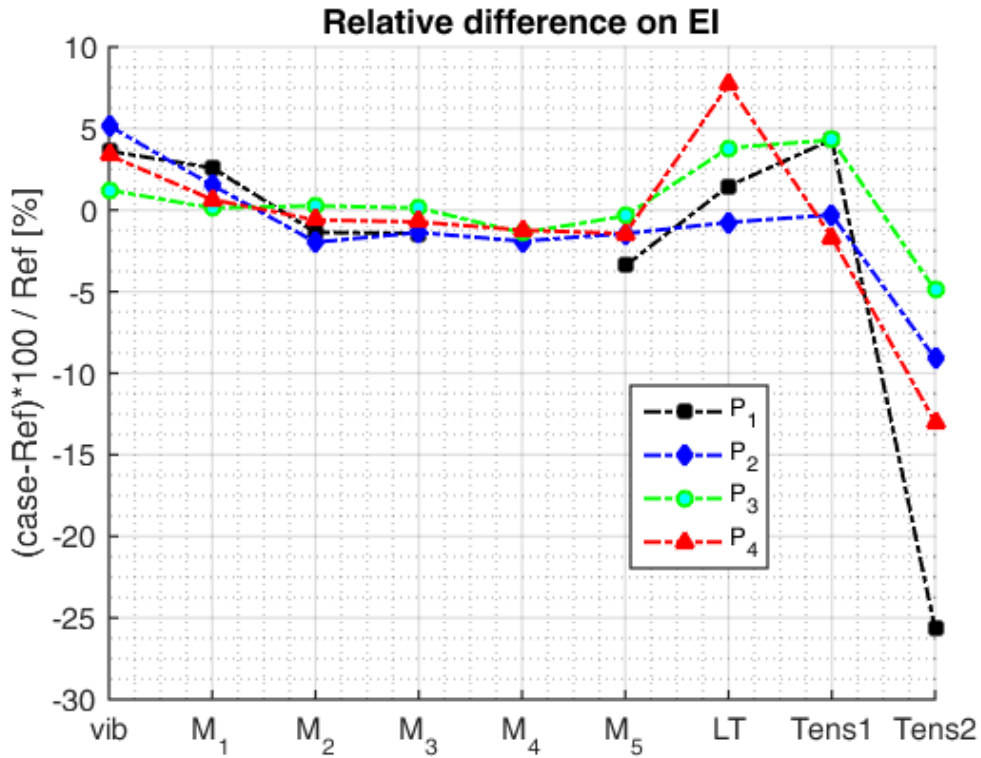
FIGURE 4.24 – Discrepancies computed on the bending stiffness for all the approaches.
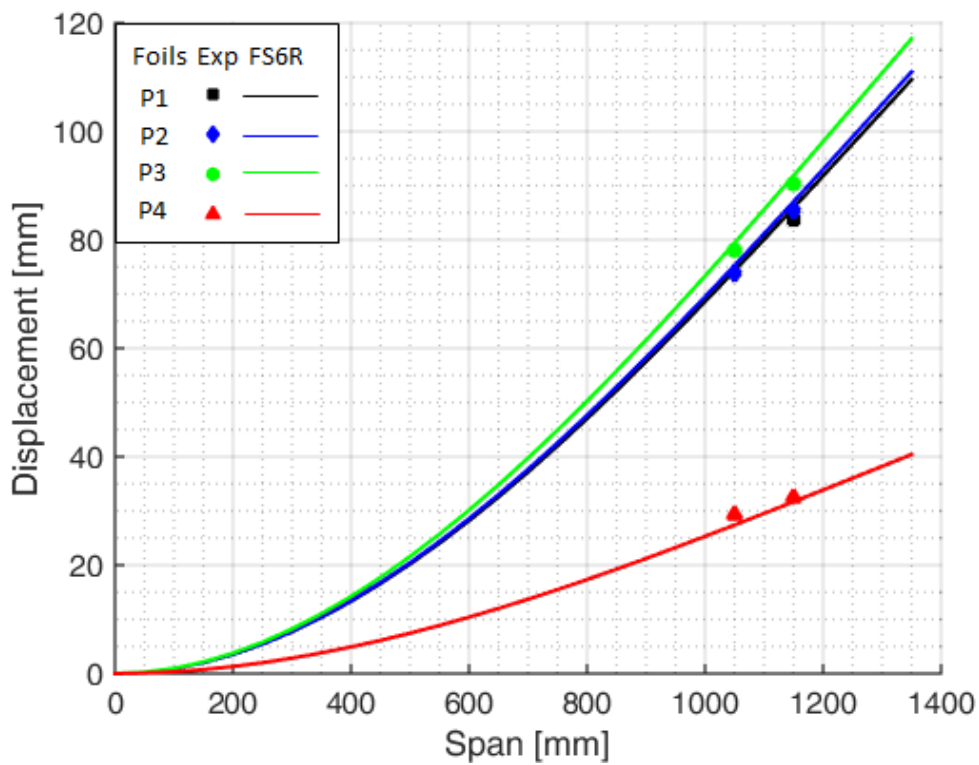
FIGURE 4.25 – Displacements of the composite hydrofoils under static bending loading M1.

4.2.1.2 Torsional stiffness

The experimental setup of the torsional tests is presented in figure 4.26. A moment of torsion is applied at the tip of the hydrofoil with different loading and the twist angle is measured at two sections along the span. The bending displacement is locked in this setup, only the twisting motion is allowed.
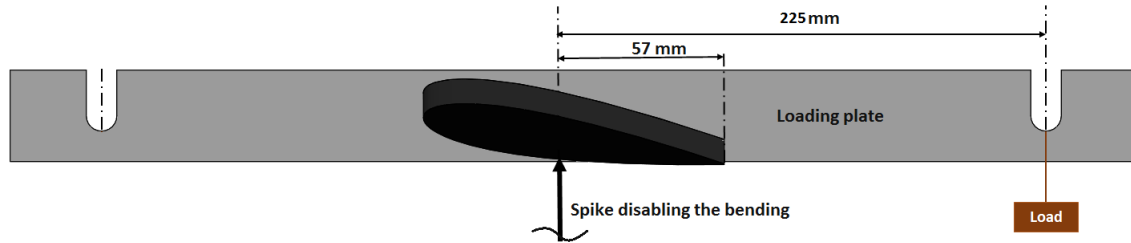
FIGURE 4.26 – Experimental setup of the torsional tests.
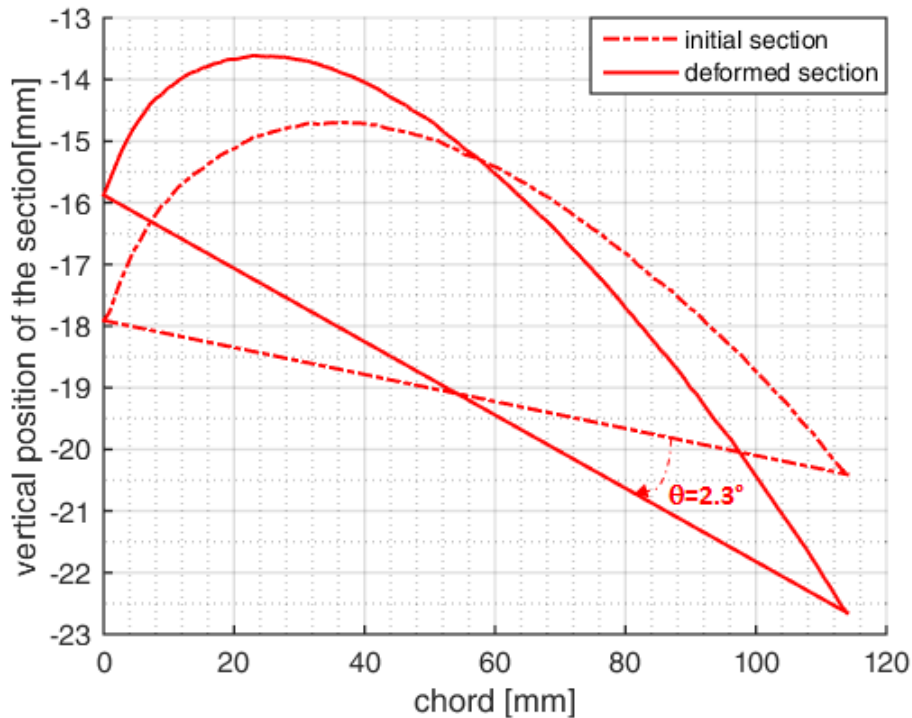
FIGURE 4.27 – Twisted Section S_2 for P_4 loading M1.

Figure 4.27 shows the shape of the section S_2 (y=1150mm in spanwise) measured with the laser along the chord without loading and with the torsion moment applied with in the loading case $M_1 = 2.2$ kg. The loading is applied on the right side of the section so we observe a well defined rotation of $\theta = 2.3°$ in the clockwise.

For all the hydrofoils and all the loading cases, the twist angle is calculated. The torsional modulus calculated with equation 2.11, using the twist angles are presented in Table 4.4. According to the material properties and the layup definition (table 2.13), P_1 has the highest modulus. We expected P_2 and P_3 's modulus to be close and P_4 slightly higher than them but the results show $P_4 < P_3 < P_2$.

Figure 4.28 shows a comparison between the experimental twist angles measured on S_1 (y=1050mm in spanwise) for all the layups and the simulation with FS6R, using the tor-

Foil Layup	P_1	P_2	P_3	P_4
GJ [N.m^2]	290.39	216.3	203.3	186.95

TABLE 4.4 – Torsional stiffness GJ of the different foils

sional modulus of table 4.4.

In agreement with the torsional modulus, for the same loading, the twist angle is highest for P_4, followed by P_3, P_2 and P_1 is the smallest. The results computed with FS6R are higher than the experimental values. This observation indicates an underestimation of the torsional modulus that may be due to the experimental implementation or the data processing method.
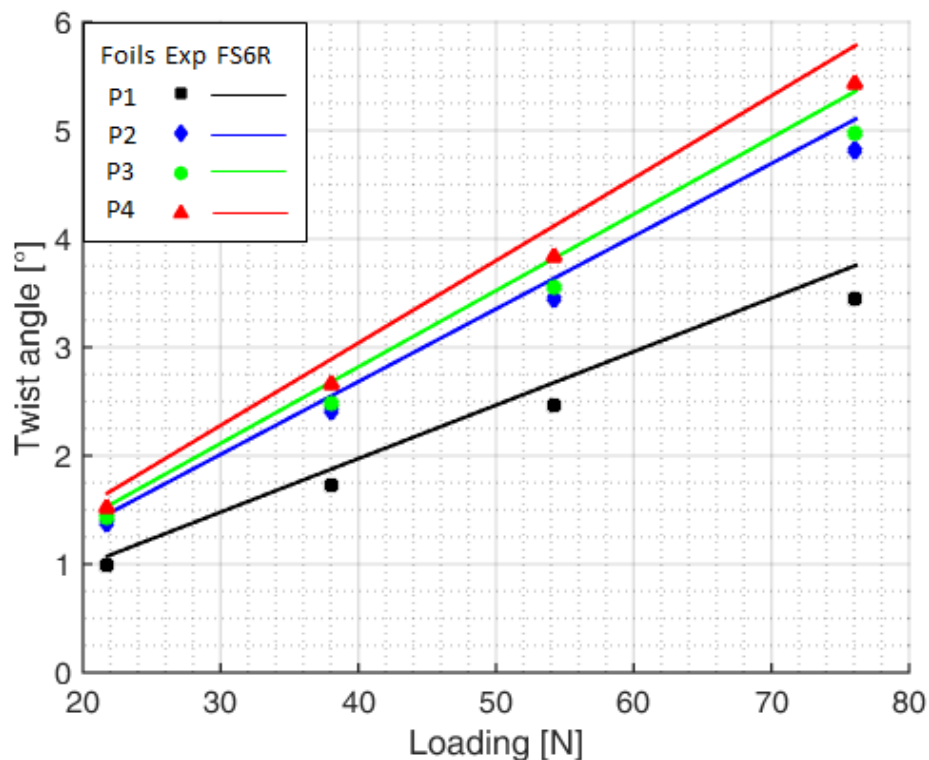
FIGURE 4.28 – Twist angles of the hydrofoils in torsion loading, section S_1.

Figure 4.29 shows the difference between FS6R simulations and the experiments on the estimation of the twist angle in the torsion loading.

The difference is relatively low and we should expect FS6R to compute twist angles with a relative error less than 9%.

4.2.2 Bend-twist coupling investigation in static tests

The bend-twit coupling is investigated in the bending tests performed with the loading case M_1. The designed properties expected with the layup configurations are :

— P_1 : Important bending and no bend twist coupling.

— P_2 : Bend twist coupling with a negative twist.

— P_3 : Bend twist coupling with a positive twist.

146
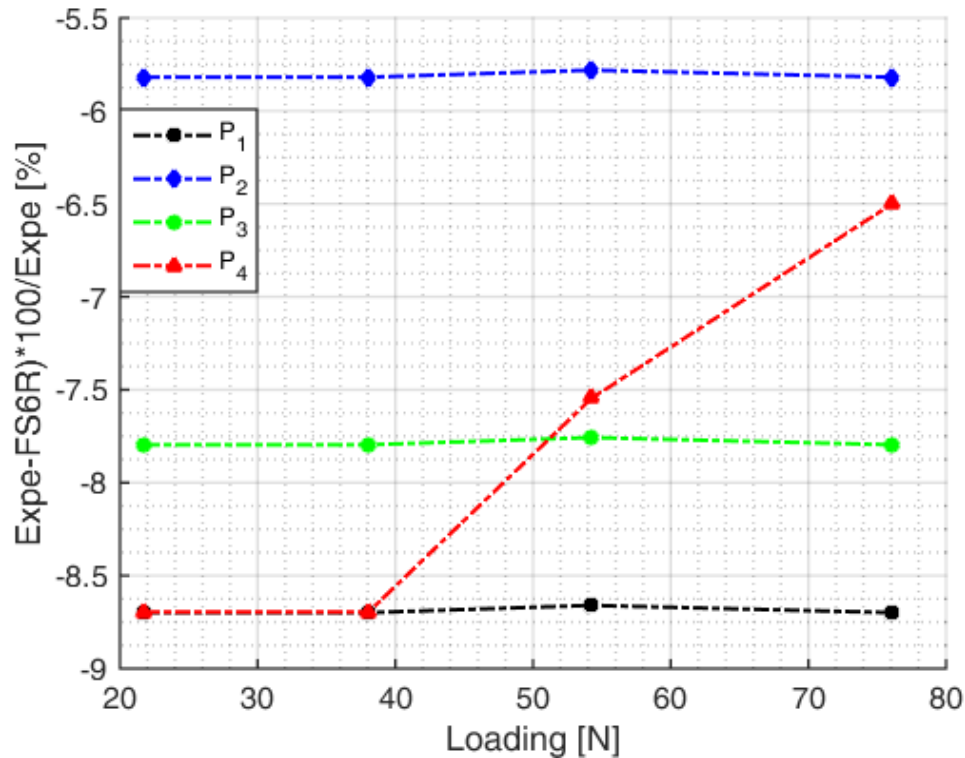
FIGURE 4.29 – Relative error of FS6R on the twist estimation in torsion loading M1, section S_1.

— P_4 : Small bending and no bend twist coupling.

Figure 4.25 shows the bending motion displacement of the hydrofoils in that loading case and the twist angles induced for each hydrofoil are calculated.
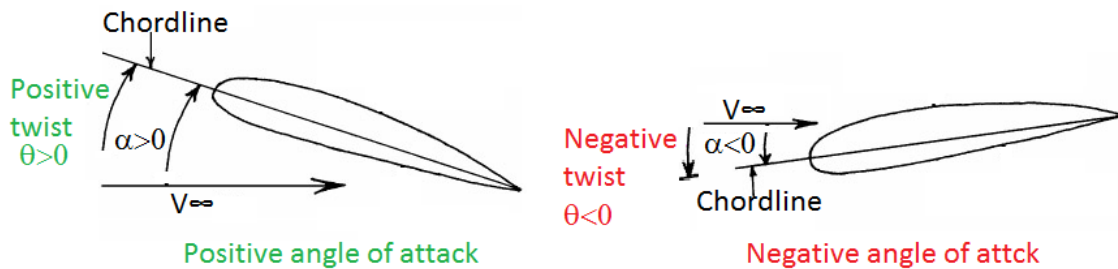
FIGURE 4.30 – sign convention for the angle of attack on a profile

To link the bend twist angle to the flow's angle of attack in a hydrodynamic loading, figure 4.30 shows the sign convention of the angle of attack with the profile orientation. A clockwise rotation is positive and the counter clockwise is negative.

Figure 4.31 and 4.32 show the experimental twist induced by the bending loading of the hydrofoils measured on the section S_2 excepts for P_3 which is the measure on section S_1.

The difference observed on the initial shape of the sections in the different layups, highlight a difference on the natural bending of the hydrofoils and therefore in their bending stiffness, in agreement with table 4.3.

The twist angles induced on P_1 and P_4 are very small, and their initial sections overlap on the the deformed sections when different results are observed on P_2 and P_3.

According to the sign convention of the angle of attacks, P_2 with the plies oriented at $-45°$
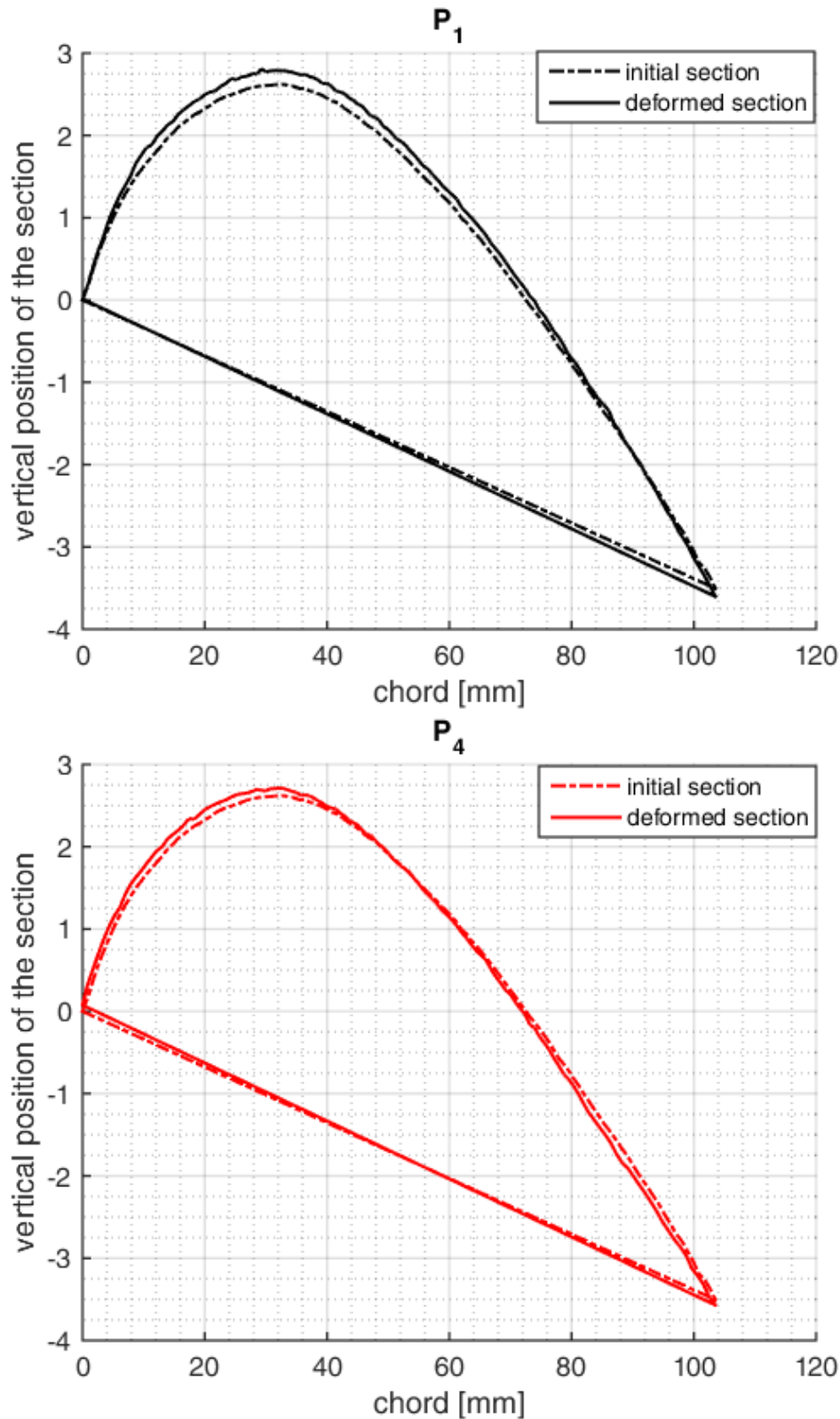
FIGURE 4.31 – Bend twist angle measured for P_1 and P_4 on the section S_2, with M_1 loading

in its layup depicts a negative twist when P_3 with the plies oriented at $+45°$ in its layup experiences a positive twist as expected.

Figure 4.33 compares the bend-twist angles measured with the simulations of FS6R. FS6R computes a zero twist angle for P_1 and P_4, accordingly to the balanced layup of both

composites.
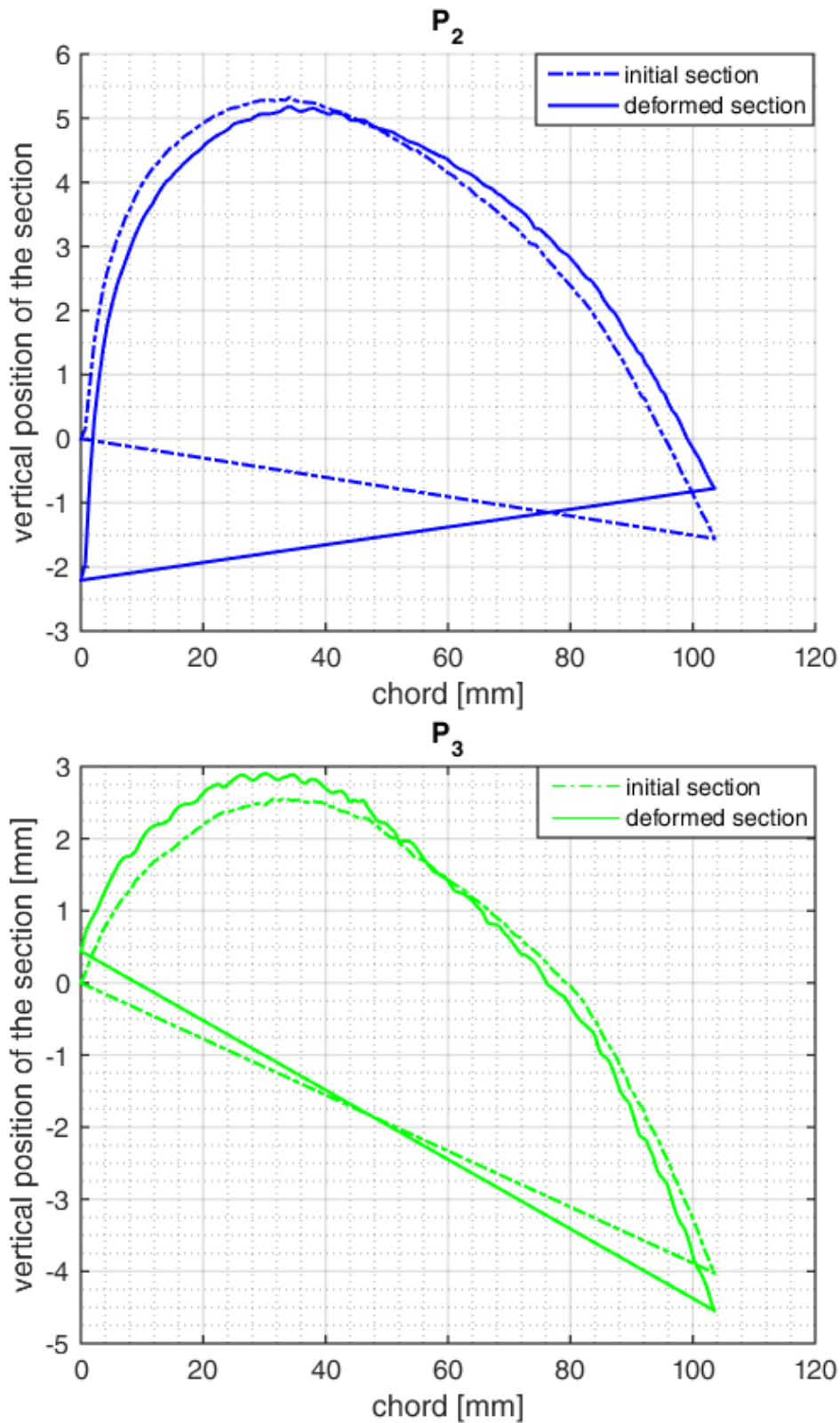
FIGURE 4.32 – Bend twist angle measured for P_2 on the section S_2 and P_3 on the section S_1, with M_1 loading

A small experimental twist of $0.1°$ is measured for P_1 and P_4, which indicates the magnitude of the measurement precision.
As expected, a twist angle is linked to the bending load for the layup P_2 and P_3. The twist
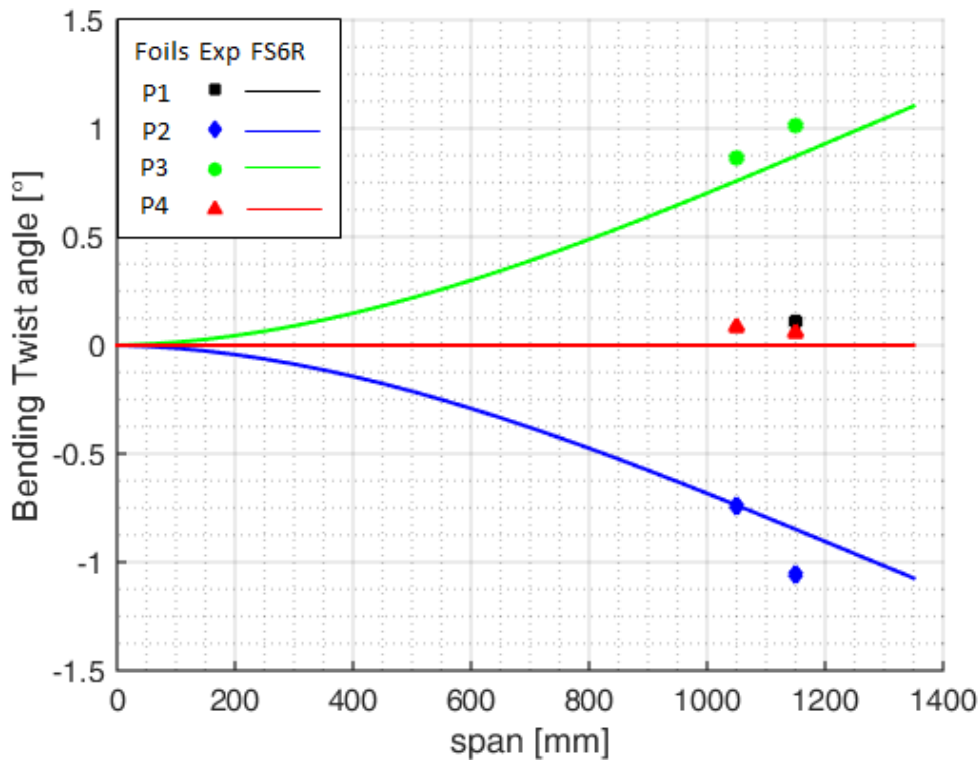
FIGURE 4.33 – Twist angles induced in the hydrofoils in the bending loading.

angle reaches 1°, rather positive or negative, depending on the orientation of the 45° plies. FS6R simulates well the observed tendencies.

The main part of the discrepancies are most likely due to the experimental set up, where the clamping system was not totally rigid.

As a conclusion of this part, the bend twist coupling phenomenon is highlighted with a significant amplitude for P_2 and P_3 layups : P_2 experiences a negative twist when P_3 has a positive twist angle and FS6R is able to simulate the BTC due to the different layup configurations with a great accuracy.

4.2.3   Experimental results : hydrodynamic tests

Hydrodynamic tests where performed for $V_1 = 0.7 m/s$ and $V_2 = 0.9 m/s$. Two test campaigns were carried out on these hydrofoils in July 2018 and January 2019.

The first campaign allowed to measure the displacements of the hydrofoils for both speeds but the calibration of the balance was defective. During the second test campaign, only the force at 9m/s were measured.

Experiments performed in air show a BTC behavior in the layups P_2 and P_3, t hydrodynamic tests being performed for negative angles of attack of the hydrofoils, the expected results are :

— P_1 and P_4 experience the same lift magnitude and different projections on the axis in agreement with their different bending motions

— P_2 experiences the highest lift force : its BTC behavior will lead to a negative bend-twist angle that will increase its angle of attack and therefore its lift force

— P_3 experiences the lowest lift force : its BTC behavior will lead to a positive bend-twist angle that will decrease its angle of attack and therefore its lift force

Figure 4.34 shows the experimental setup of the hydrodynamic flume of IFREMER Lorient. The hydrofoil is mounted piercing the free surface with an tilt angle of 45° with the horizontal. The completed description of the hydrodynamic tests is presented in chapter 2.

The results of this part are the hydrodynamic forces (F_X, F_Y, F_Z) measured with the 6-DOF balance and the displacements of the hydrofoils. The reference system (X,Y,Z) is attached to the hydrofoil and presented in figure 4.34. X is the flow direction, Z is along the span of the hydrofoil and Y is perpendicular to both so that (X,Y,Z) is direct.
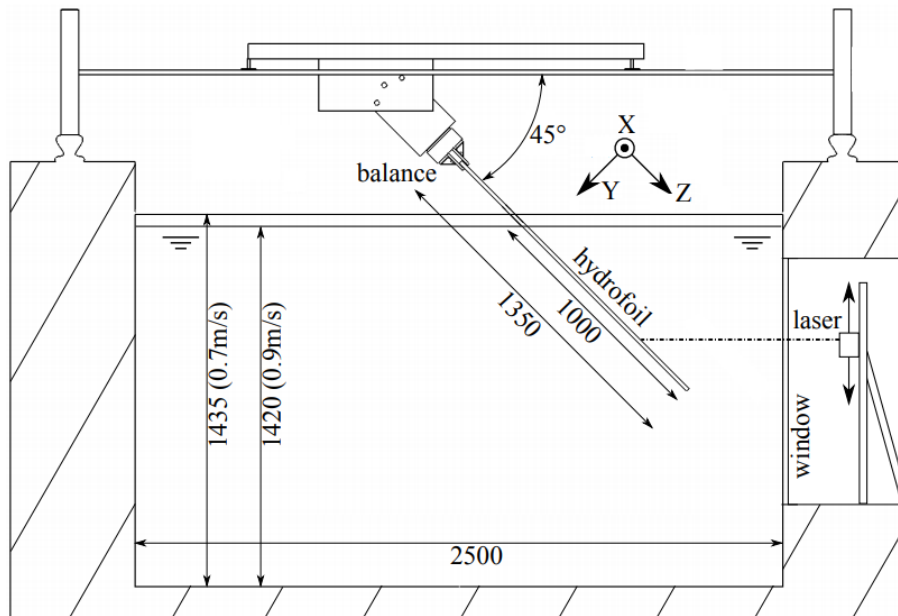
FIGURE 4.34 – Section of IFREMER Lorient flume 's main characteristics and experimental set up with the hydrofoil. Water level changes with flow speed.

The results presented are the displacements for the 2 speeds and the hydrodynamic forces at $V_2 = 0.9 m/s$. The calibration matrix of the balance was erroneous on the drag output. A new matrix will soon be available and the drag results will eventually be presented during the oral presentation of this work. Only the lift force and its projections will be processed in the following results.

4.2.3.1 Hydrodynamic forces

The lift force is calculated as the module of its projections on Y and Z axes as given in equation 4.3 :

$$L = \sqrt{F_Y^2 + F_Z^2} \tag{4.3}$$

Figure 4.35 shows the lift forces calculated for the 4 composite hydrofoils at $U = 0.9 m/s$ and the four incidences investigated. The horizontal axis is the incidence and the vertical axis is the lift.

The lift force clearly exhibits the different behaviors of the layups : P_1 and P_4 overlap as expected from the experiments in air, highlighting no bend twist effect.
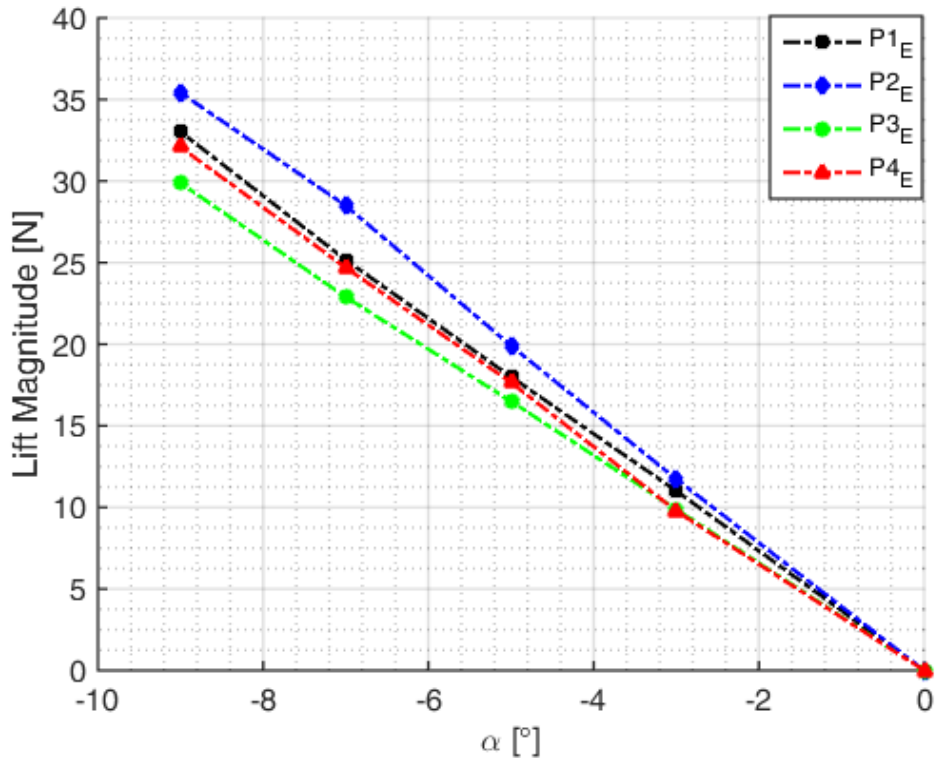
FIGURE 4.35 – Lift force measured on the composite hydrofoils, $U = 0.9 m/s$.
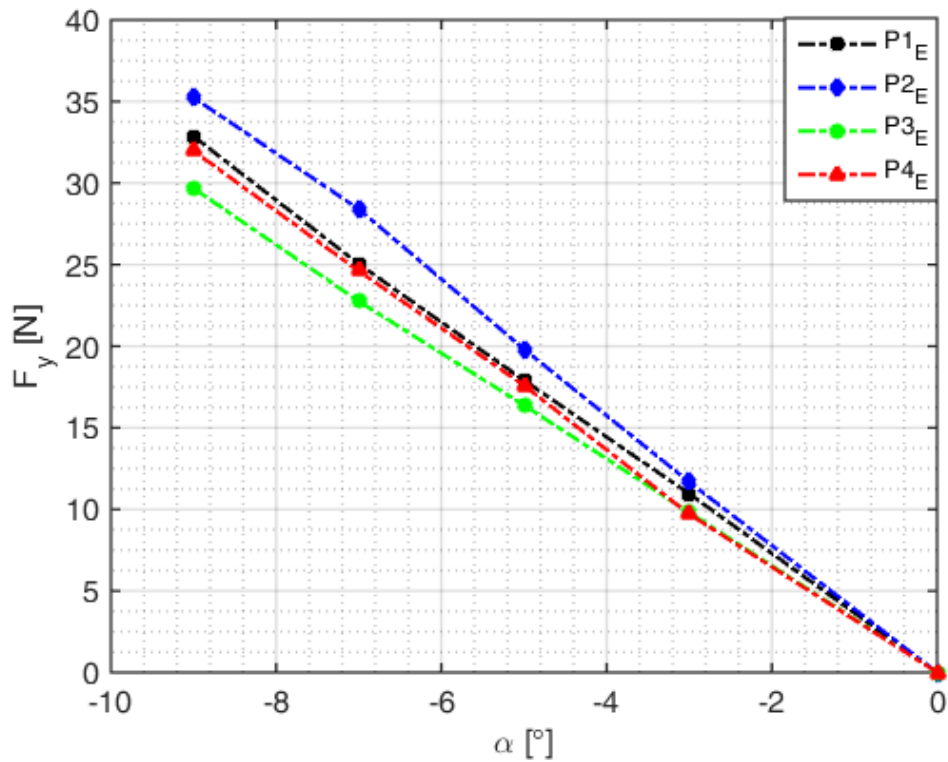
FIGURE 4.36 – Projection on Y axis of the lift force measured on the composite hydrofoils, $U = 0.9 m/s$.

Their results are only linked to their hydrodynamic shape and having the same geometry,

their hydrodynamic signature are the same.

P_3 is smaller than the P_1, P_4 and P_2 is the highest. This behavior is exactly what we expected according to the results of the BTC investigation performed in air (see section 4.2.2). Because negative incidences are investigated, P_2 with the negative twist becomes the most loaded when P_3 with the positive twist become the less loaded.

Figures 4.36 and 4.36 give the projections of the lift force on the axis Y and Z. The projection on Y which is normal to the flow direction is a very good image to the lift when the projection on the span direction Z is directly linked to the bending motion of the hydrofoil.

P_1 and P_4 which had the same amplitude exhibit different projections on Z, in agreement with their different bending stiffness. F_Y of P_1 is slightly higher than FY of P_4 as observed with the lift forces. Being the stiffer one, P_4 has the lowest projection on Z axis.
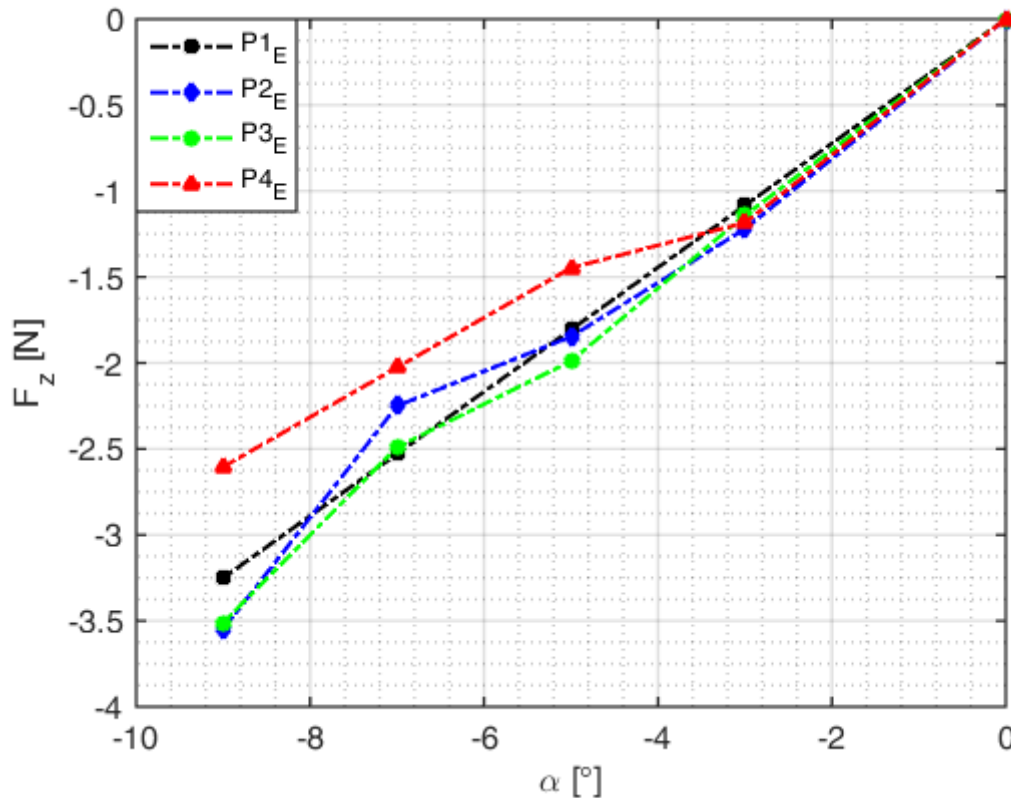
FIGURE 4.37 – Projection on Z axis of the lift force measured on the composite hydrofoils, U = $0.9 m/s$.

4.2.3.2 Displacements of the composite hydrofoils with FSI

This section presents the hydro-elastic behavior of the hydrofoils observed through the displacements. The laser telemeter performed the measurements on three points along the span of the hydrofoils (see figure 2.50).

The laser measure the position of the hydrofoil at these points without and with the flow, the difference between the two measurements give the displacements.

The displacement presented is the displacement normal to the span, in the Y direction.

Figures 4.38 and 4.41 give the displacements of the hydrofoils for α = −5° and α = −7° at velocity $V_1 = 0.7\ m/s$ and $V_2 = 0.9\ m/s$. The hydrofoils bend under the hydrodynamic loading.
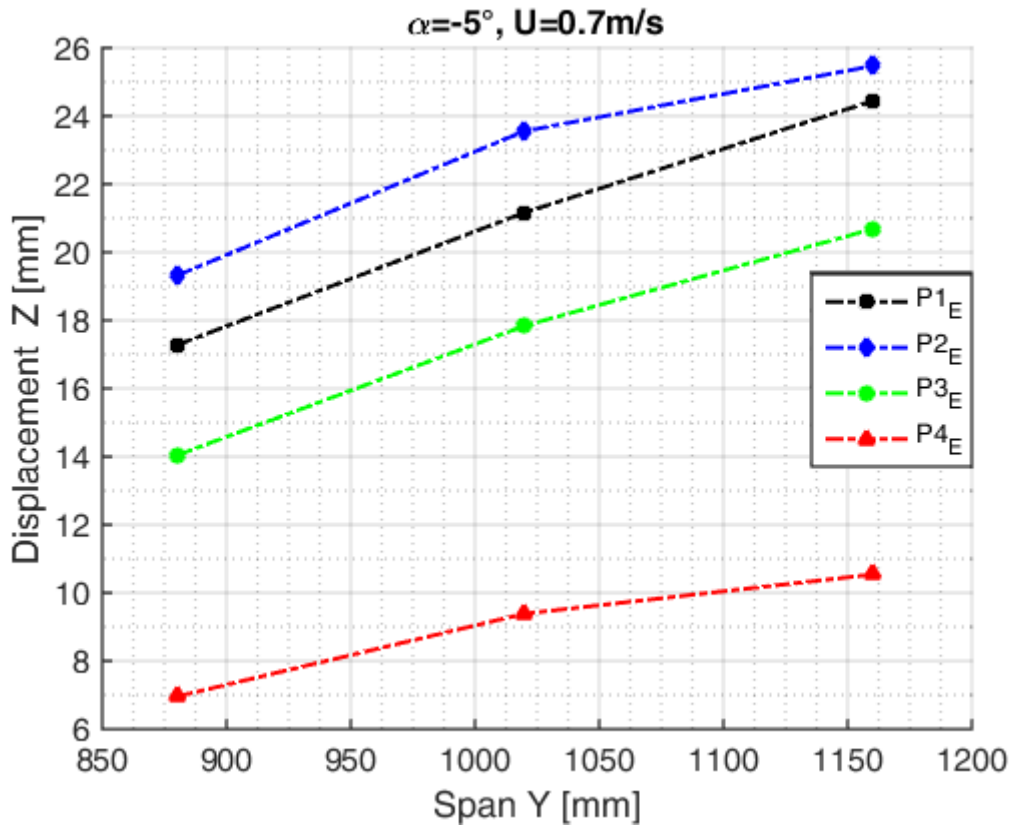
FIGURE 4.38 – Displacement normal to the span of the hydrofoils, α = −5° and U = 0.7m/s.

For all the configurations (incidence, velocity), the displacements highlight different behaviors that are linked both to the materials composing the hydrofoils (stiffness) and the composite layup (BTC).
These results are in agreement with the experimental tests performed in air and the hydrodynamic forces measured.
The carbon hydrofoil P_4 is significantly more rigid than the glass fiber hydrofoils (bending stiffness of 417 N.m^2 for the carbon hydrofoil and ≈ 150 N.m^2 for the glass hydrofoils).
It experiences the lowest displacement when the layup P_2 with its highest lift force due to its BTC behavior experiences the higher displacements.
The displacements of P_1 are smaller than P_2 and P_3 is such as $P_3 < P_1 < P_2$. Moreover, the stiffness of P_3 being the same with P_1 and the stiffness of P_2 being lower, P_2 and P_3 are not symmetrical to P_1, P_2 is further away.

These observations are in agreement with BTC effect observed on the forces. P_2 and P_3 only differ by the plies orientation contained in their layups : −45° for P_2 and +45° for P_3.
As a conclusion on this part, the behaviors of the composite hydrofoils in static (air) and dynamic (in the water) are in agreement with the expectations of their design.
The carbon hydrofoil is the stiffer one and bend the less. Its hydrodynamic forces are close to P_1 results and only differ on the lift projection on the span axis. P_1 does not experience BTC when P_2 twists with a negative angle and P_3 with a positive twist angle.
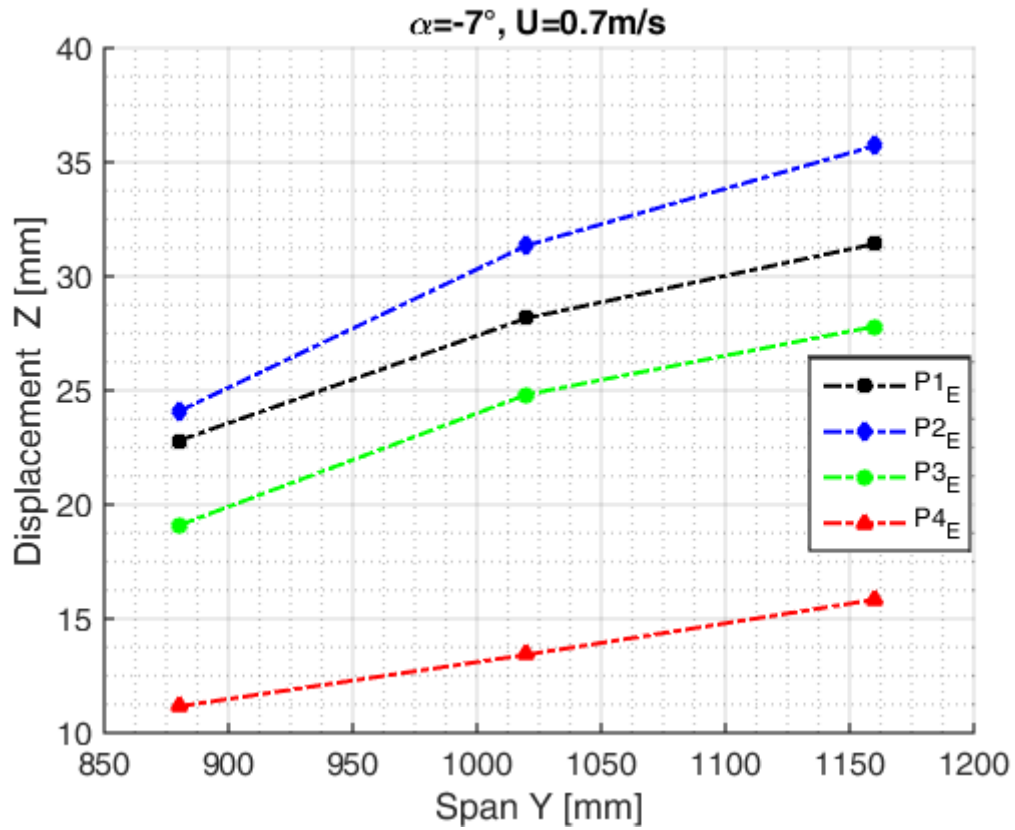
FIGURE 4.39 – Displacement normal to the span of the hydrofoils, $\alpha = -7°$, $U = 0.7 m/s$.
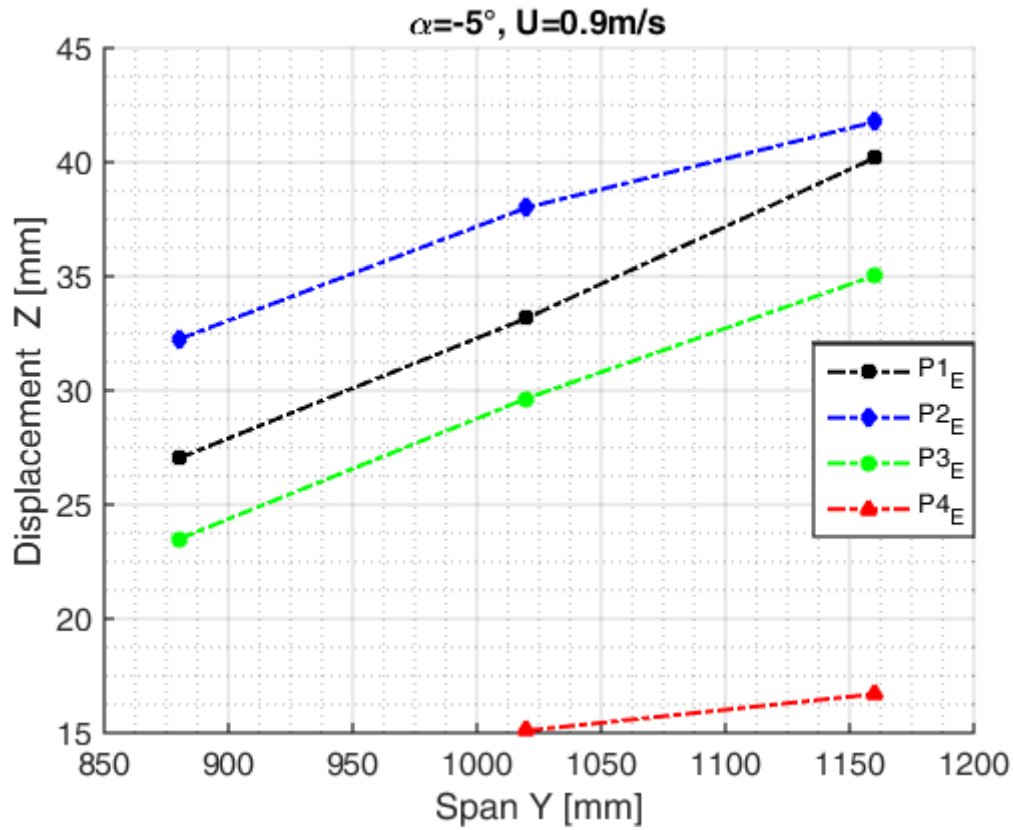
FIGURE 4.40 – Displacement normal to the span of the hydrofoils, $\alpha = -5°$ and $U = 0.9 m/s$.
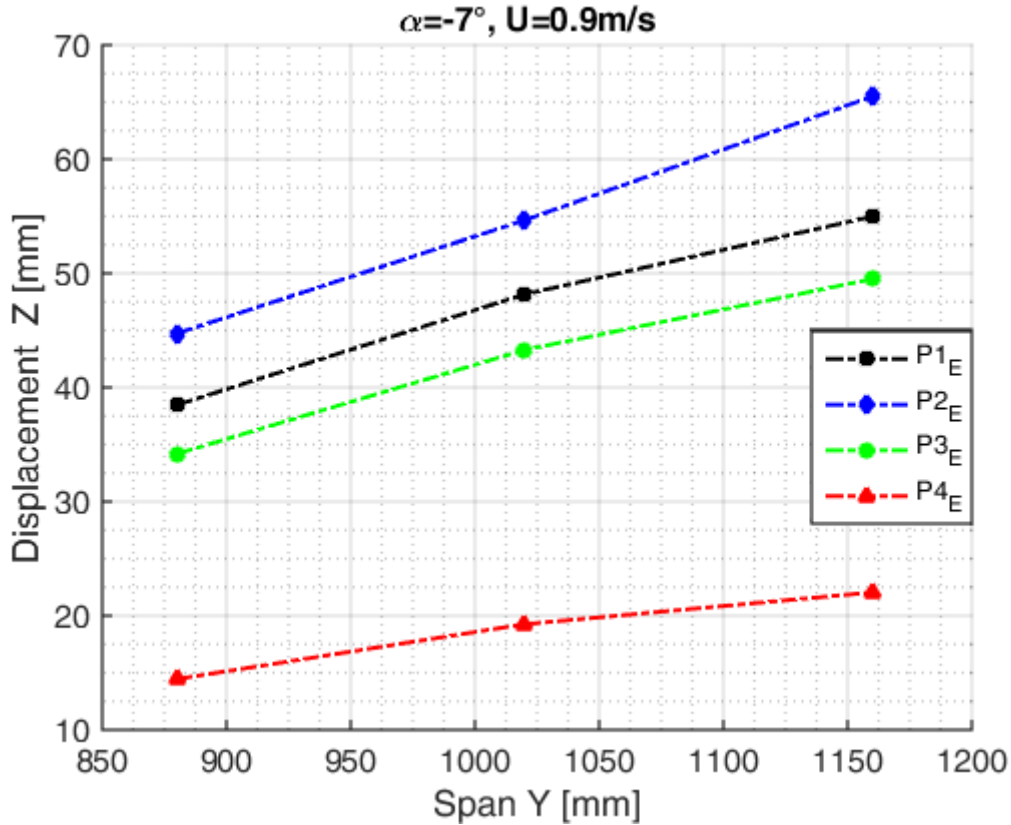
FIGURE 4.41 – Displacement normal to the span of the hydrofoils, $\alpha = -7°$, $U = 0.9 m/s$.

The bending motion does not influences the lift amplitude but its projections on the axes when the BTC modifies the lift amplitude through the variation of the angle of attack. FS6R is able to compute the bend-twist coupling in static test with good accuracy, the next sections presents a comparison of FS6R simulations to the experimental results of the composite hydrofoils.

4.2.4 FS6R VS experiments : hydro-elastic response of the hydrofoils

This section compares the experimental results with the simulations of FS6. The first parts discuss the mesh and the second and third parts presents the comparisons.

4.2.4.1 Mesh sensitivity

Figure 4.42 shows the influence of the number of panels along the span on the convergence of the simulations.

The number of panel along the chord is chosen to $N_c = 50$ (see figure 4.11 showing that the influence of N_c is very small, the hydrofoils profile being the same with the POM (NACA 0015) and the chords length being of same amplitude, this choice is legitimated). The figure shows the evolution for the layups P_1 and P_4 calculated for $\alpha = -7°$ at $U = 0.9 m/s$, the convergence tolerance on the displacement is set at $\epsilon = 1e^{-3}$.

For both the lift and the displacements, the values decreases slowly and converge above 200 panels along the span.

The mesh chosen for the simulations is 200 panels along the span and 50 panels along the chord. It is presented in figure 4.43 and shows a cantilevered hydrofoil piercing the free surface with a tilt of $\alpha = 45°$ as the configuration of the experiments.
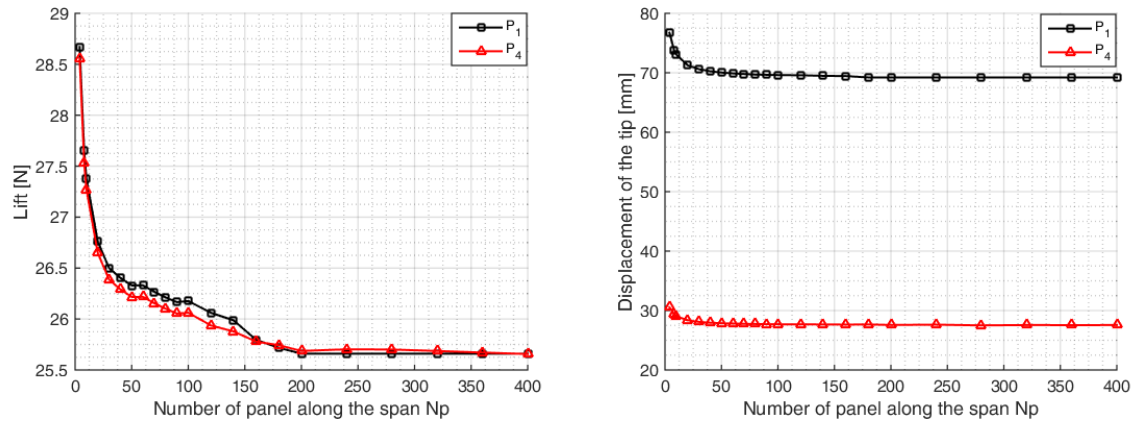
FIGURE 4.42 – Influence of the number of panel along the span on the lift and displacements, (50 panels along the chord and $\epsilon = 1e^{-3}$).
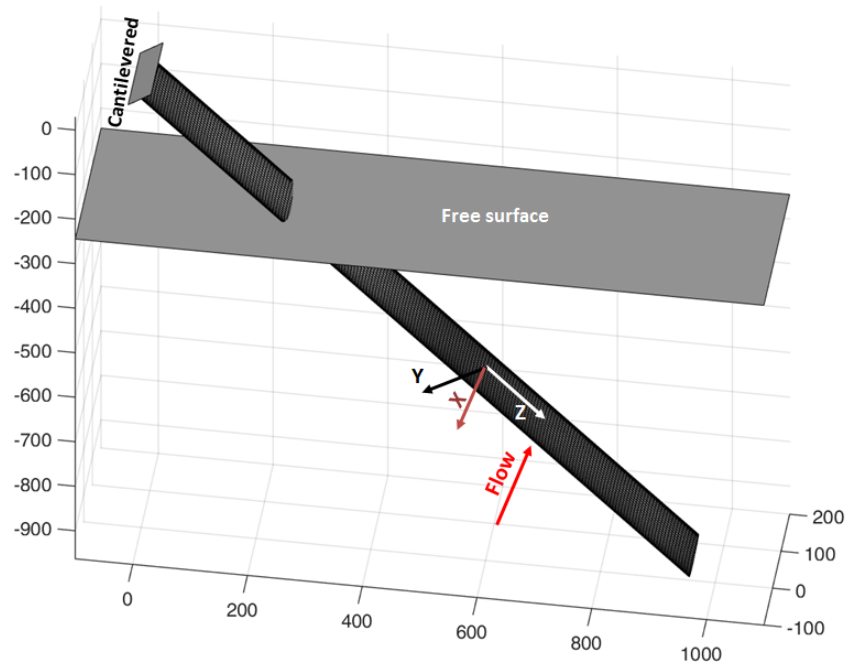
FIGURE 4.43 – Mesh of the composite hydrofoils for FS6R simulations, $N_p = 200$ and $N_c = 50$.

The implementation of the BTC in FS6R calculations is described in section 3.2.3.2. it takes as input the percentage of bend-twist coupling $\alpha[\%]$ that each ply of the layup can create.

The investigation on the determination of this percentage is out of the scope of this work and the values used in these simulations come from the literature.
Figure 4.44 shows the evolution of the coupling percentage with the orientation of the ply in the layup for ply of glass and carbon fibers.
The values used are : -0.3 for the plies oriented at $-45°$, 0.3 for the plies oriented at $45°$ and 0 for the others orientations.

In these configuration a simulation takes 80 seconds CPU time : 70 seconds to read the input file and 10 seconds to run the case. The convergence tolerance on the displacements is set at $\epsilon = 1e^{-3}$ and it is reached within 3 iterations, the results are thus performed without relaxation.
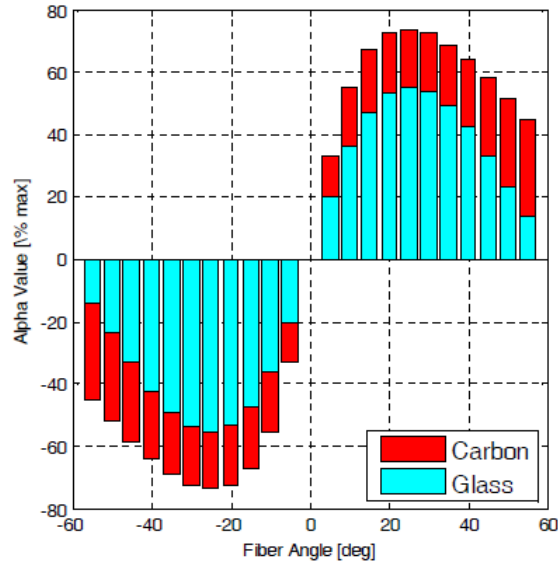
FIGURE 4.44 – Evolution of bend twist coupling percentage with the plies orientation for glass and carbon fibers. [31]

4.2.4.2 Hydrodynamic forces

Figure 4.45 shows the drag force computed with FS6R and the trend of the curves exhibits the parabolic shape of the drag with the angle of attack, predicted in the theories.
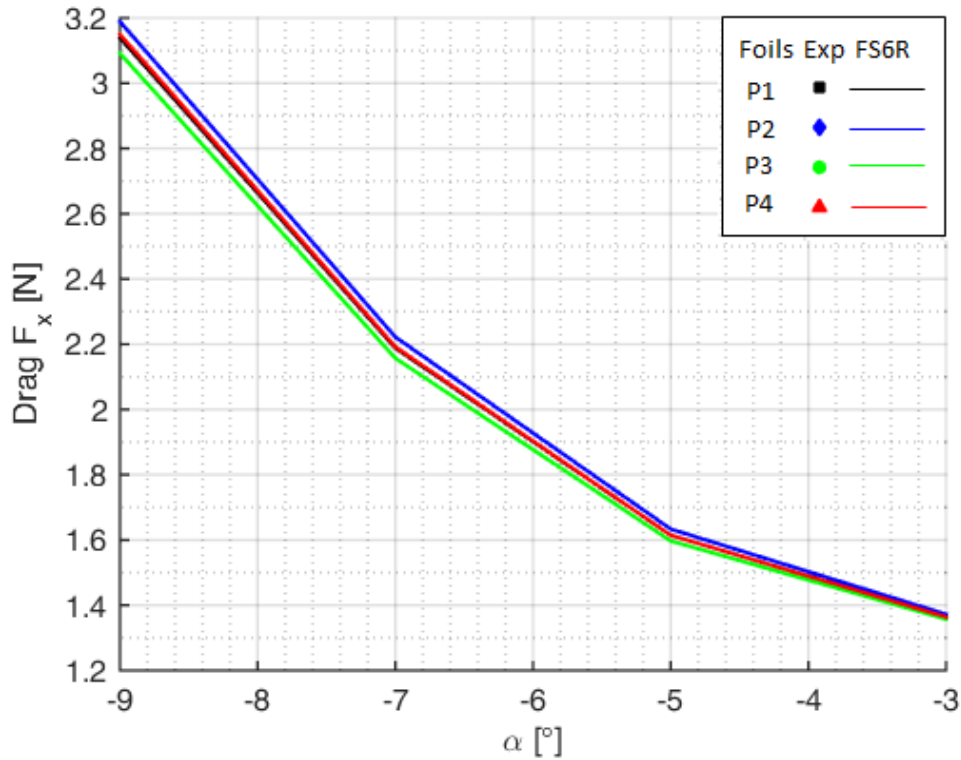
FIGURE 4.45 – FS6R simulations :Drag force on the hydrofoils at $U = 0.9 m/s$.

The drag force of the four hydrofoils overlap well for small incidences but when the incidences rises from $-7°$, a small difference is observed : the drag of P_2 is the highest, the

158

drag of P_3 is the smallest when the drag of P_1 and P_4 overlap. That difference may be linked to the twist angle, the gap between P_2 and P_3 is 3%.

These results will be compared in chapter 5 to the simulation of Foam-Aster that includes turbulence and free surface effects.

The numerical-experimental comparison of the lift projections on Y and Z axis is presented in figures 4.46 and 4.47. The amplitude of the lift is presented in figure 4.48.
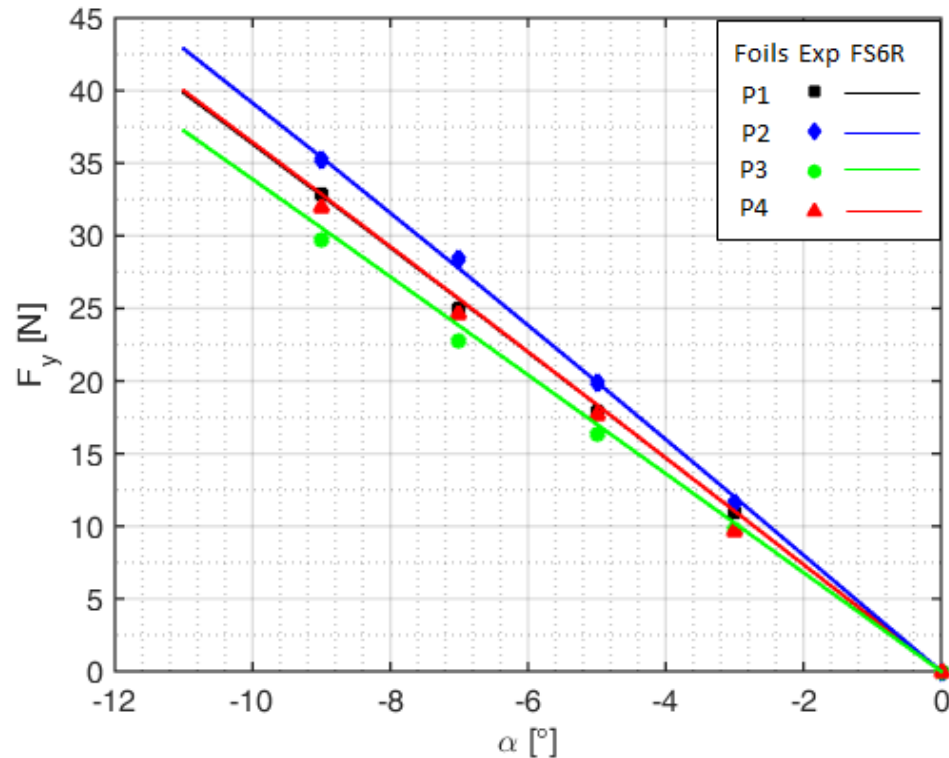
FIGURE 4.46 – FS6R VS experiments on composite hydrofoils : projection on Y axis of the lift force, $U = 0.9 m/s$.

Experimental results and FS6R results have the same trend and the values fits perfectly excepts for Z projection of the lift force. The Z value is very small and does not affect the lift force nor the moment leading to a good agreement of both approaches. The maximum discrepancy observed is around 5% on the lift force for P_3, with the simulation higher.

The lift force simulated with FS6R clearly differentiate the behaviors of the different hydrofoils and the BTC effect is well estimated. We also observe that when P_1 and P_4 lift magnitude are the same, their projections F_y and F_z are different due to their different bending deformation.

F_z from FS6R computations has the same trend as the displacements, the force is transferred to the span wise direction due to the foil deflection, modifying the hydrodynamic behavior.

We observe that F_y match very well with the experiments and the experimental values are slightly higher.
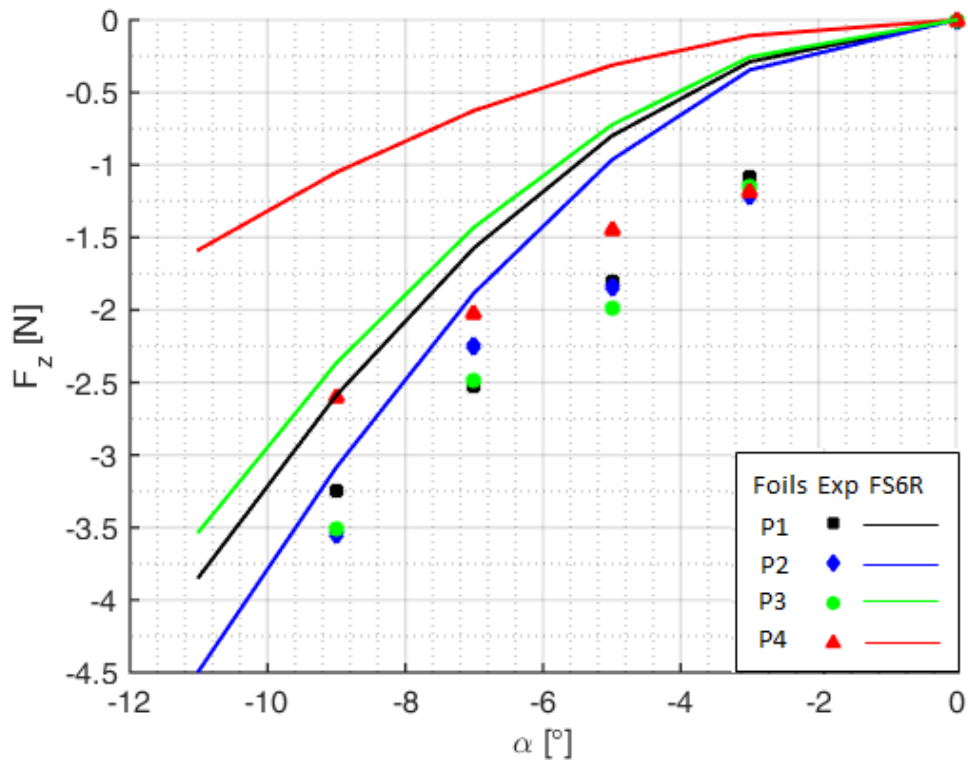
FIGURE 4.47 – FS6R VS experiments on composite hydrofoils : projection on Z axis of the lift force, $U = 0.9 m/s$.
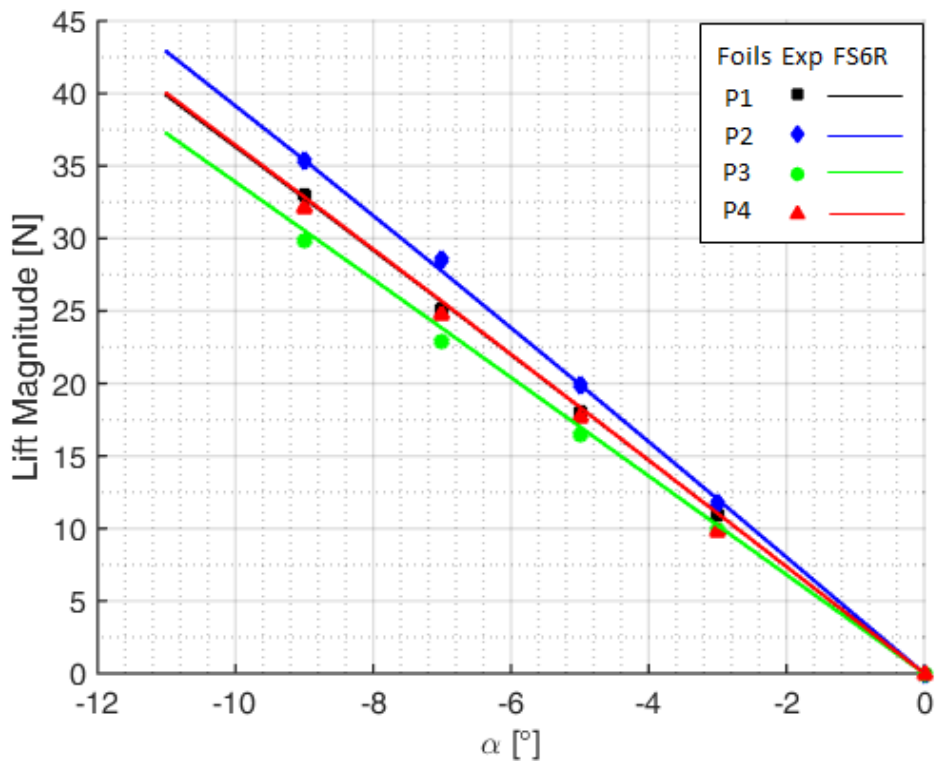
FIGURE 4.48 – FS6R VS experiments on composite hydrofoils : Lift magnitude $U = 0.9 m/s$.

4.2.4.3 Displacements of the hydrofoils subjected to hydrodynamic loads

Figures 4.49- 4.52 compare the displacements of the four composite hydrofoils computed with FS6R with the experiments.
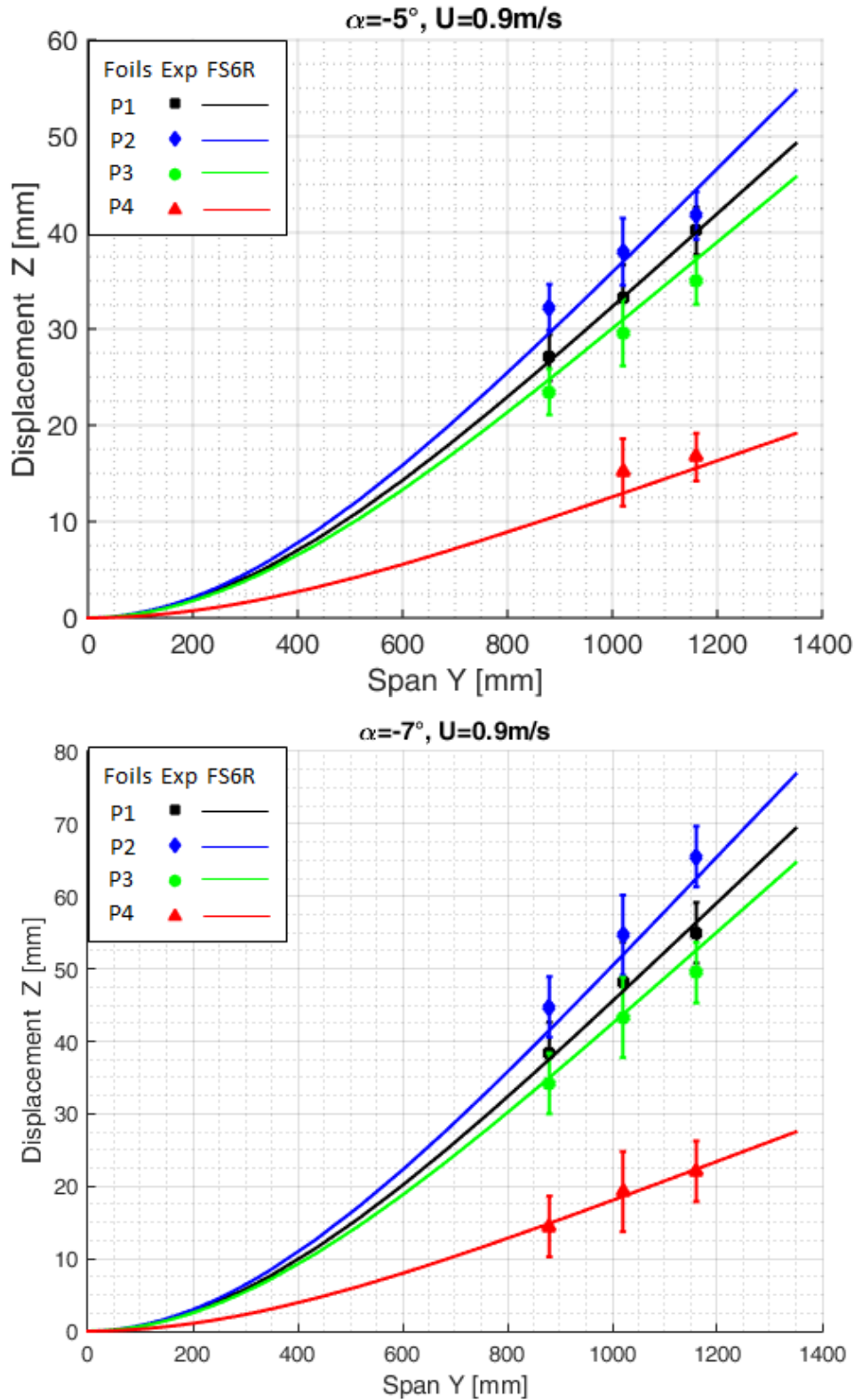
FIGURE 4.49 – FS6R VS experiments : displacements of the composite hydrofoils, $\alpha = -5°$ and $\alpha = -7°$, U = 0.9 m/s. The vertical bars are the standard deviation of the measurements

The vertical bar are the standard deviation of the measurements. These deviations are quite important due to the oscillations of the hydrofoils in the water.
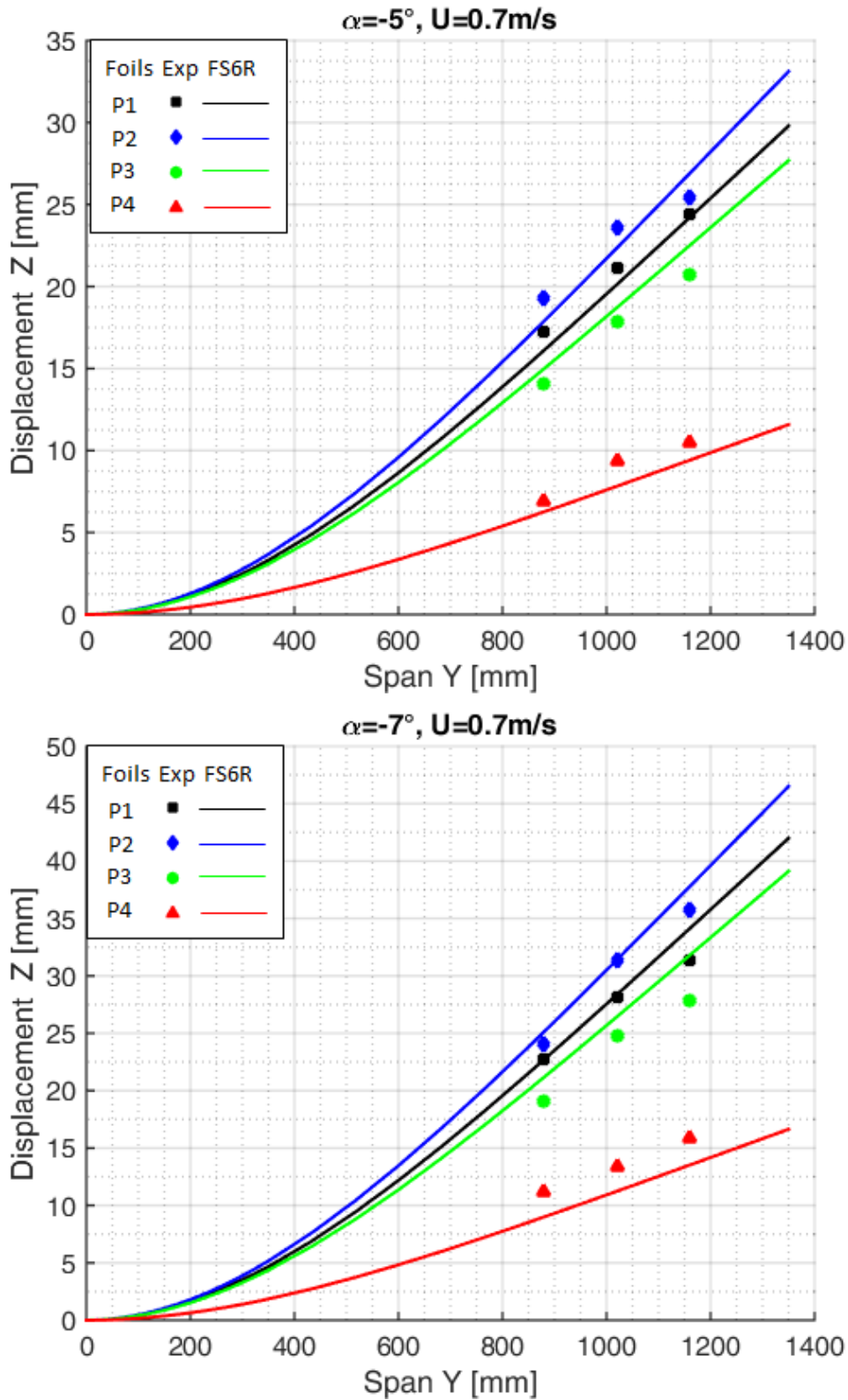
FIGURE 4.50 – FS6R VS experiments : displacements of the composite hydrofoils, $\alpha = -5°$ and $\alpha = -7°$, U $= 0.7 m/s$.

The hydro-elastic response of the entire hydrofoils computed with FS6R leads to a bending motion which fits very well with the experiments. The difference between the

numerical results to the experiments are below the error ranges.

Some experimental data with non-physical values are suppressed, giving some graphs without the four hydrofoils. In a general analysis, FS6R fits well with the experiments and the discrepancies are under 10% in average.
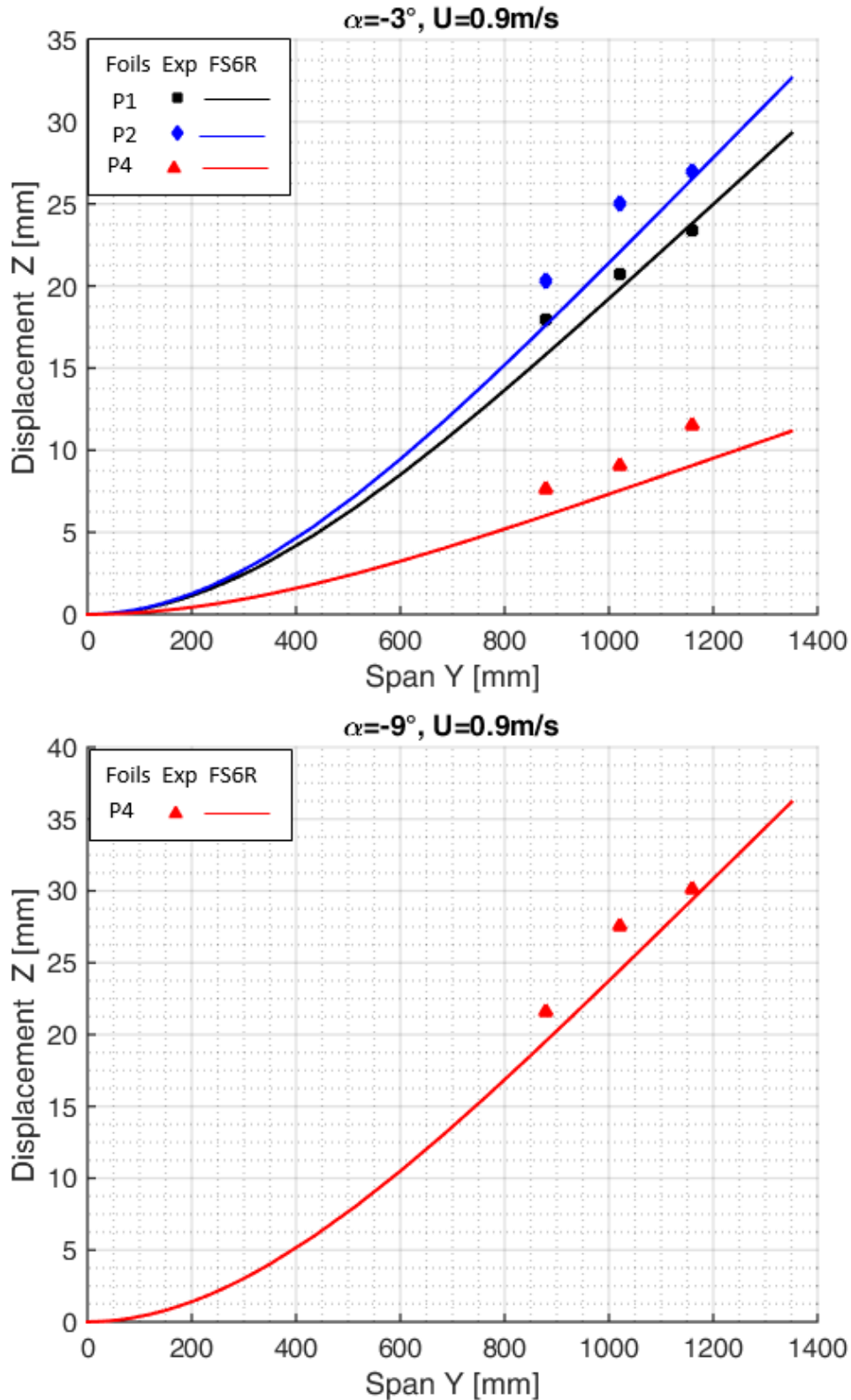
FIGURE 4.51 – FS6R VS experiments : displacements of the composite hydrofoils, $\alpha = -3°$ and $\alpha = -9°$, $U = 0.9 m/s$.
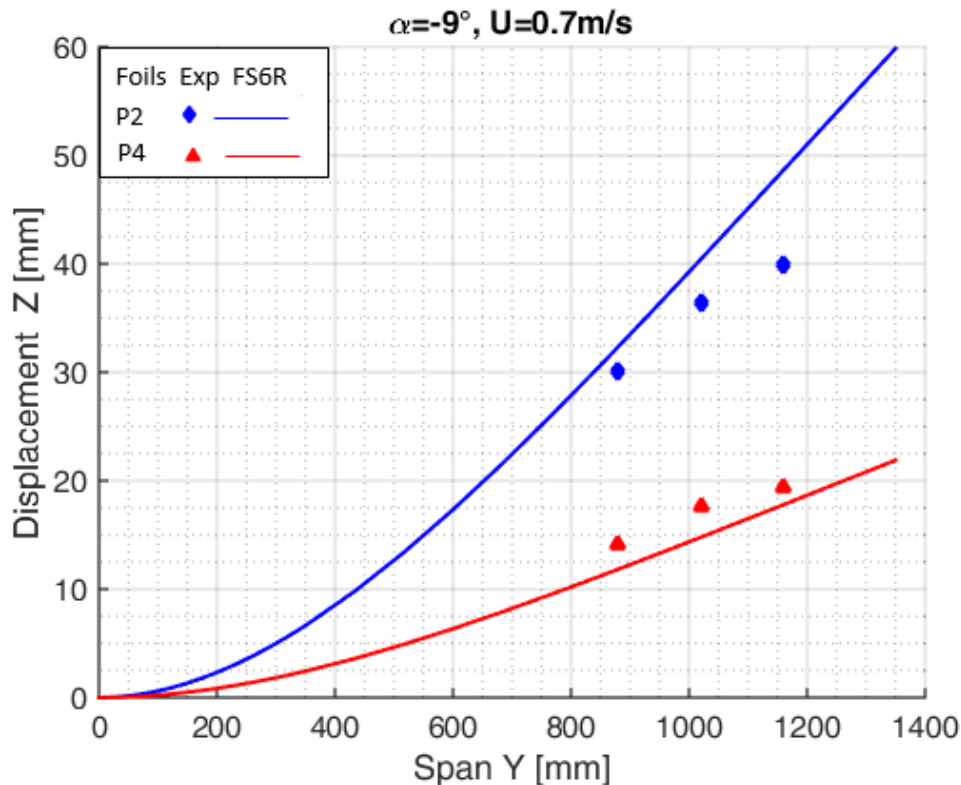
FIGURE 4.52 – FS6R VS experiments : displacements of the composite hydrofoils α = −9°, U = 0.7m/s.

As a conclusion to this part, FS6R uses the mechanical properties of the different composite materials and simulate correctly the behavior of the composite structures including the BTC. The lift force distribution is simulated with good accuracy and therefore the hydro-elastic response of the hydrofoils.
FS6R is then a reliable tool to compute the hydro-elastic response of composite hydrofoils and the impact of the hydrofoil on the balance of a sailing boat.

4.3   Summary of the chapter

This chapter presents the experimental results of the model-scale POM hydrofoil and the real-scale composite hydrofoils on one hand and on a other hand the numerical-experimental comparison of the low fidelity tool **"FS6R"** based on that experimental results.

The first section discussed the POM hydrofoil and it started with the results of the mechanical characterization that gives a Young modulus of E = 3Gpa. The analysis of the hydrodynamic experiments performed in the hydrodynamic tunnel of IRENAV exhibit a bending motion as the hydro-elastic response of the hydrofoil. Using the symmetric profile NACA 0015, the symmetric angles of attack tested clearly show a symmetric behavior. The last part of that section compares FS6R simulations to the experiments. The sensitivity to the mesh variation was investigated and shows that for a number of panel above 50 along the chord and above 80 along the span, the variation of the lift coefficient and the displacement was negligible. Thus, the mesh chosen for these simulations consist of 50 panels along the chord and 80 along the span.
To simulate a configuration (one angle of attack at one velocity) using that mesh FS6R

takes 44 seconds on one processor and converges after 3 iterations with a tolerance criteria of $\epsilon = 1e^{-3}$ on the displacement.

An investigation of the relaxation factor shows an increase of the number of iteration before convergence and the minimum iteration are reached without relaxation. The simulation are thus performed without relaxation and converges quickly, after three iterations. The implementation of the relaxation factor will be more investigated in further work to prevent the case of complex simulations that may need more resources.

The simulations investigate the effect of the FSI on the forces distribution on the POM hydrofoil. A comparison of the lift and drag coefficient with FSI, with a simulation without FSI shows that the both amplitude remained the same but the distribution along the span is modified due to the bending of the hydrofoil.

The comparison of the displacements simulated to the displacements measured are in good agreements. The simulated results describe perfectly the trends observed experimentally. For all the configurations investigated the relative discrepancies between the numeric an experiments are less than 7%. FS6R is able to compute with very good accuracy the hydro- elastic response of a isotropic hydrofoil experiencing FSI in water.

The second section of this chapter concerns the real-scale composite hydrofoils. The mechanical characterization aimed to determine the bending stiffness EI and the torsional stiffness GJ of the four composite hydrofoils. The determination of the bending stiffness compares bending, vibration and tensile tests to the laminate theory and shows that the laminate theory had the same order of amplitude with the experiments and is able to compute the results with a precision of 4%. As expected, the hydrofoil P_4 in carbon is the stiffer than the other hydrofoils in glass. It was determined that P_1 and P_3 had barely the same bending stiffness and P_2 is 4.4% lighter. That difference between P_2 and P_3 is likely due to the manufacturing process.

The torsional modulus was different for the 4 hydrofoils : $P_4 < P_3 < P_2 < P_1$ and the use of that modulus in FS6R to compute the twist of the torsional tests gave good trends in the results with relative discrepancies of around 9%.

The second part of that section investigates the BTC on the hydrofoils and shows that when P_1 and P_4 don't experience a twist angle induced by a bending loading, the bend twist coupling phenomenon is highlighted with a significant amplitude for P_2 and P_3 layups : P_2 experiences a negative twist when P_3 is influenced with a positive twist angle.

The hydrodynamic experiments were in good agreement with the BTC investigations. The angle of incidences investigated being negative, P_2 with its negative bend-twist angle becomes the most loaded and P_3 with its positive bend-twist angle becomes the less loaded. In agreement with the bending stiffness of the hydrofoils, For all the configurations, the displacements of P_4 are the smallest when P_2 has the highest displacement. The difference between P_2 and P_3 is clearly observable.

For a hydrofoil experiencing FSI, if the orientation of the ply inducing the BTC is positive, the bend-twist angle induced is positive and if the orientation of the ply is negative, the induced angle is negative. The analysis of the forces also shows that when the BTC modifies the angle of attack of the hydrofoils and therefore the amplitude of the forces, the bending motion keeps the amplitude of the lift constant and only modifies its projection on the axis and therefore the bending motion modifies the boat stability.

The simulations with FS6R use a mesh consisting in 200 panels along the span and 50 panels along the chord, the tolerance criteria on the displacement is set at $\epsilon = 1e^{-3}$ and a simulation converges after 3 iterations and lasts 10 seconds on one processor.

The simulations are run with the BTC implemented in FS6R and using the experimental stiffness. The results of the forces and the displacements fit perfectly with the experi-

ments. FS6R computes very well the behavior of the hydrofoils and the global differences are less than 10%.

FS6R is a quick tool that demonstrates good ability to estimate the hydro-elastic response of a composite or isotropic and deformable hydrofoil experiencing FSI. The limitations we have at this stage is the determination of the bend-twist coupling percentage and the calculation of the torsional modulus for complex composite layups. The tool FS6R has not yet been tested on swept or complex geometries.

CHAPTER 5

Comparison of experiments to simulations : high-fidelity coupling Foam-Aster

« *The belief in a supernatural source of evil is not necessary ; men alone are quite capable of every wickedness.* »

Joseph Conrad, Under Western Eyes-1911

Contents

This chapter aims to validate the simulations of the high fidelity coupling **Foam-Aster** based on the experimental results of the model-scale POM hydrofoil and the real-scale composite hydrofoils. The experimental results are presented in chapter 4.

The present chapter is divided into two main parts. The first part discusses the POM hydrofoil (described in section 2.1.1.3) and starts with the the fluid and solid modeling. The influence of the mesh variation is analyzed and the dynamic simulation performed with Foam-Aster is compared to the experiments. The last section of this part compares the results of Foam-Aster to FS6R simulations.

The second part of this chapter concerns the real-scale hydrofoils in composite materials. Having mechanical properties more complex than the model scale hydrofoil, due to its sandwich composite structure made of a volume web and a thin laminated skin, the structural modeling of the composite hydrofoil requires more attention.

This part starts with the structural modeling of the real-scale hydrofoils with Code_Aster and the validation is based on the results of the static bending tests performed in air on the composite hydrofoils with the loading M_1 (see figure 4.25).

To check the ability of Code_Aster of computing bend-twist coupling, an analysis of a thin plate in composite material loaded with a punctual loading and a surface loading is investigated in the second section. The third section of this part presents the fluid modeling and the meshes. The following sections present the Foam-Aster simulations compared to the experiments on one hand and the comparison to the low-fidelity coupling FS6R on the other hand.

5.1 POM hydrofoil

5.1.1 Modeling of the hydrofoil and the fluid domain

This part describes the fluid modeling of the hydrodynamic tunnel and the solid modeling of the POM hydrofoil. The boundary conditions used for the simulation are also presented.

5.1.1.1 Solid modeling

The solid modeling concerns only the hydrofoil. The POM hydrofoil is modeled with a 3D volume elements. The mesh is performed with the Code_Aster's Algorithm Netgen3D which needs the specification of the element length as main parameter and performed a meshing composed of tetrahedrons elements in the volume and quadrangles on the external surface as shown in figure 5.1.

To choose the structural mesh size, an analysis of the mesh sensitivity is performed with static simulations : a number of element is imposed on the section of the hydrofoil at the tip, giving the element 's length and a mesh is computed.

The amplitude of the pressure imposed is chosen close to the lift force computed with FS6R for $\alpha = 10°$ and $Re = 7 \times 10^5$.

A pressure of 44×10^4 Pa is imposed on the upper surface of the hydrofoil (see figure 5.1) and the degrees of freedom of the nodes of the root section are fixed to zero to impose a cantilevered condition.

A static mechanical analysis is performed for the different meshes and the displacement of the hydrofoil is measured on the tip section. The displacements presented in the following results are averaged at the tip section.
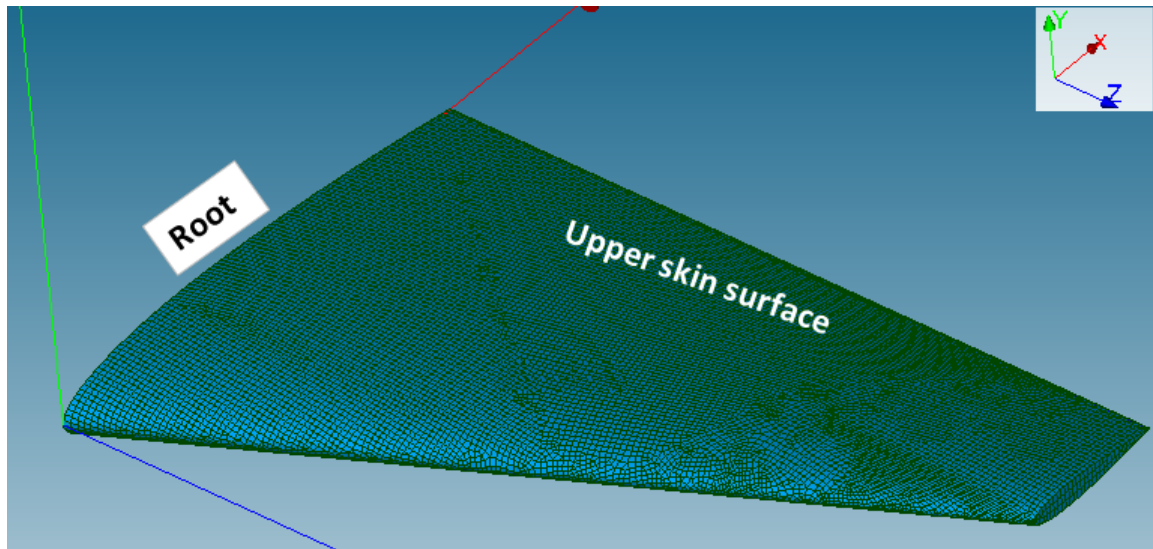
FIGURE 5.1 – Structural mesh of the POM hydrofoil using tetrahedrons elements.

Figure 5.2 shows the evolution of the displacement at the tip section of the hydrofoil (y-axis) with the number of elements imposed on the tip section (x-axis).
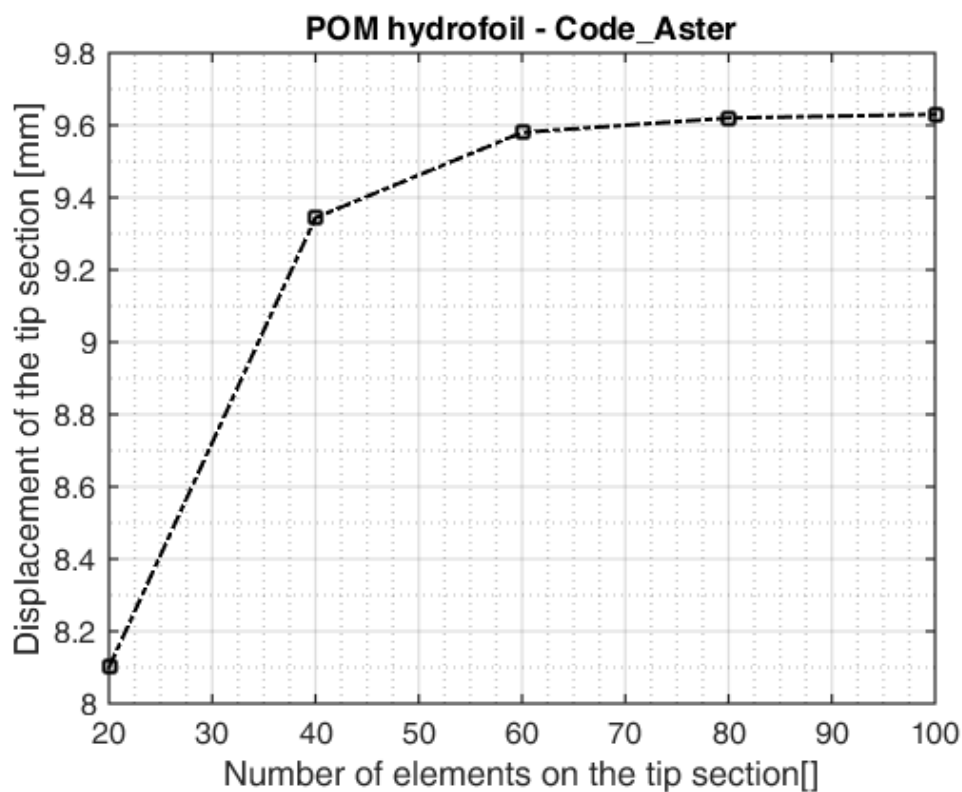
FIGURE 5.2 – Evolution of the displacement at the tip with the mesh size of the solid domain.

The displacement increases when the refinement level increases and converges from 60 elements : the evolution becomes negligible.

We chose to have 80 elements on the tip section giving an element length of $0.75mm$ and the resultant mesh shown in figure 5.1 contains 1.616.401 tetrahedrons.

5.1.1.2 Fluid modeling

This part presents how the hydrodynamic tunnel is modeled in OpenFoam and the boundary conditions are imposed. The tunnel is as a rectangular box with a square cross-section of $192mm \times 192mm$ as shown in figure 5.3.
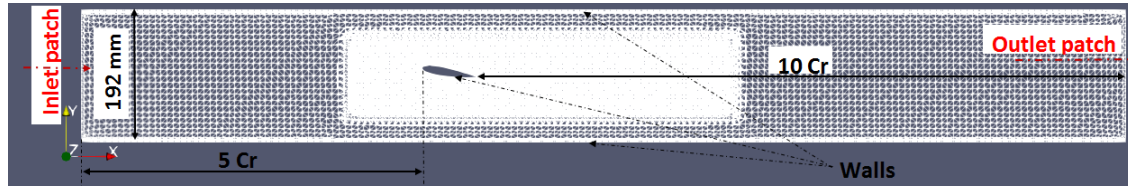
FIGURE 5.3 – Hydrodynamic tunnel of IRENAV modeled in OpenFoam, plane Z=140 mm.

The boundaries are four sides representing the tunnel windows and two patches : the inlet flow and the outlet flow.
The length in the flow stream is chosen to be five times the chord stream and, ten times the chord in the wake (the chord value used is measured at the root of the hydrofoil, $100mm$). The fluid domain is thus a box of $1.6m \times 0.192 \times 0.192m$.

The fluid mesh is performed with the the mesher SnappyHexmesh integrated in Open-Foam. A refinement box with a length of five times the chord is defined around the foil (see figure 5.3) with a refinement level k and the size of the coarse element of the domain is set to $L_s \times 2^k$ where L_s is the length of an element in the structural mesh.
The refinement level k is modified and the FSI simulation using the structural mesh defined in figure 5.1 is performed for the different meshes.

The steady-state solver for incompressible and turbulent flows **simpleFoam** is used to perform the simulations on the POM hydofoil and the model $kOmega - $ SST is used as turbulence model.
The initial conditions set zero pressure in the domain and fix the velocity at the inlet. no-slip conditions and Wall functions are imposed on the four sides and on the hydrofoil for the turbulent fields as shown in table 5.1.

Fields Patches	Inlet	Outlet	Foil and sides
Velocity U	fixedValue	inletOutlet	noSlip
Pressure P	zeroGradient	fixedValue	zeroGradient
k	fixedValue	inletOutlet	kqRWallFunction
omega	fixedValue	inletOutlet	omegaWallFunction
nut	fixedValue	inletOutlet	nutkWallFunction

TABLE 5.1 – Initial conditions of the flow fields on the patches of the fluid domain.

The simulation runs to compute the pressure force on the hydrofoil. After the FSI simulation, the averaged displacement computed at the section at the tip of the hydrofoil is analyzed for the different meshes.

Figure 5.4 presents the evolution of the displacement at the tip simulated with the coupling Foam-Aster. The x axis is the refinement level around the foil in the fluid domain. The displacement that varies with lift force magnitude increases slowly when the
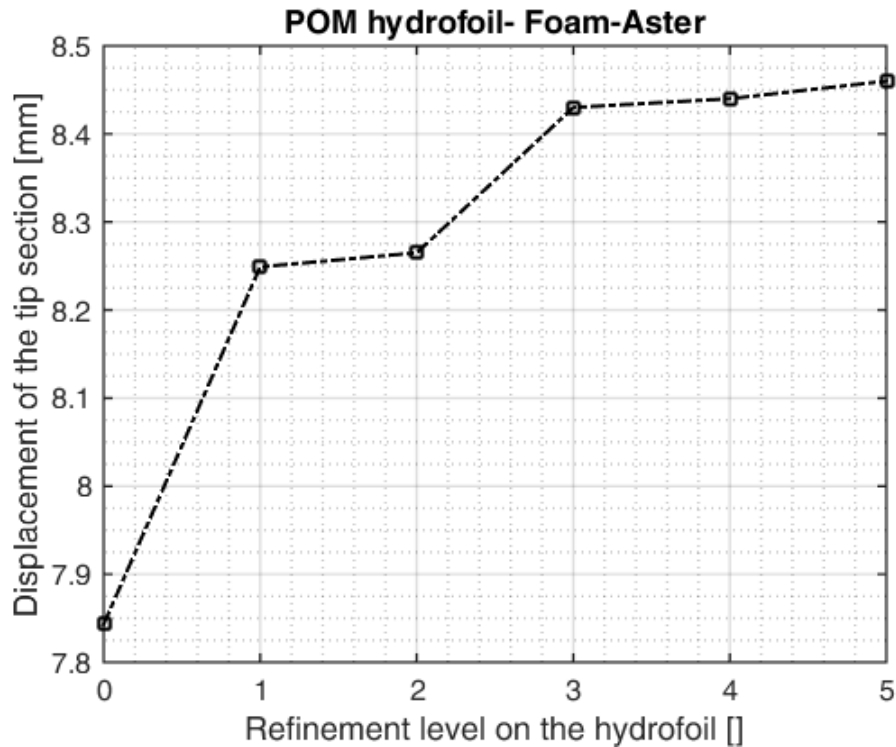
FIGURE 5.4 – Evolution of the displacement at the tip of the hydrofoil with the refinement around the foil in the fluid domain. R$e = 7 \times 10^5$ and $\alpha = 10$ř.

refinement around the foil increases and converges from a refinement level of 3.

The refinement level used for the fluid meshing around the hydrofoils is set to 4, giving a mesh of 1.665.499 hexahedra. The average y^+ is less than one on all the no-slip.

5.1.1.3 Fluid mesh quality

The final mesh of the fluid domain is presented in figure 5.3, the cutting plane is closed to the root at Z = 5mm. The figure 5.5 shows four levels of refinement around the hydrofoil and a zoom on the hydrofoil section are shown in figures 5.6 and 5.7.

The boundary layer around the hydrofoil composed of twelve layers, is visible and well defined on the leading edge.

The checkMesh tool that analyses the errors in the mesh in term of non-orthogonality, skewness, cells aspect ratio, cell volume, outputs no errors for this defined mesh.
The tolerance for the FSI simulation is set at $\epsilon = 1e^{-4}$ on the displacement convergence, a simulation runs during 6 hours and the results converges after 9 iterations.
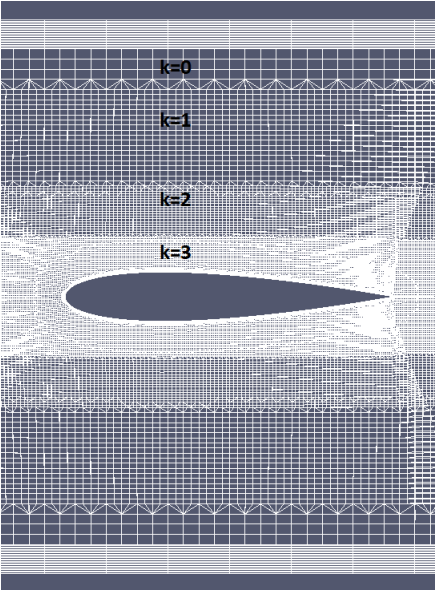
FIGURE 5.5 – Foam-Aster : Zoom of the fluid mesh of the POM hydrofoil in the refinement box showing the four level of refinements.
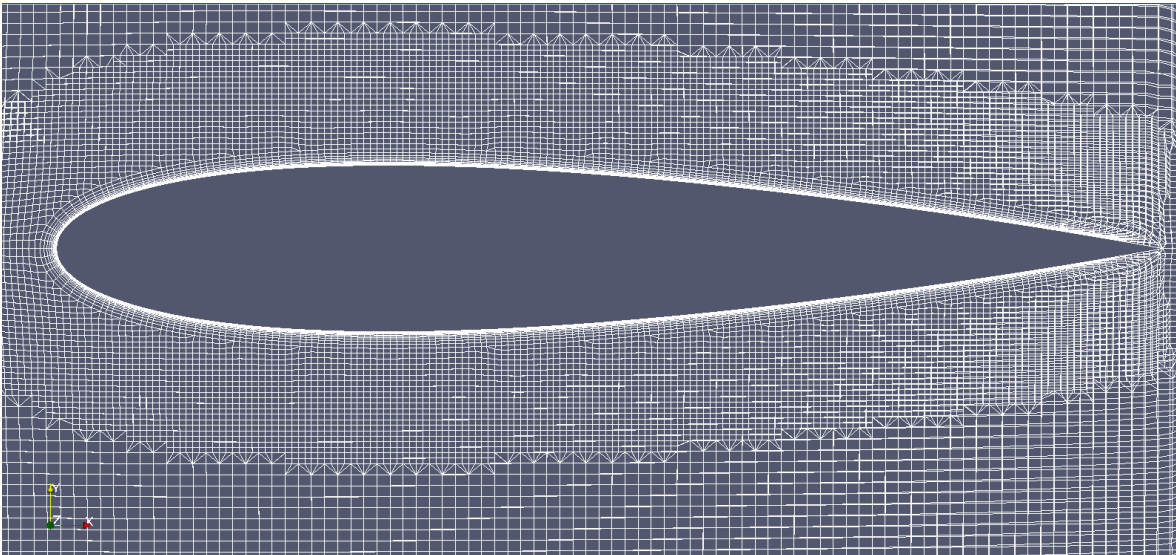
FIGURE 5.6 – Cutting plane close to the root of the hydrofoil showing the boundary layer with 12 layers.
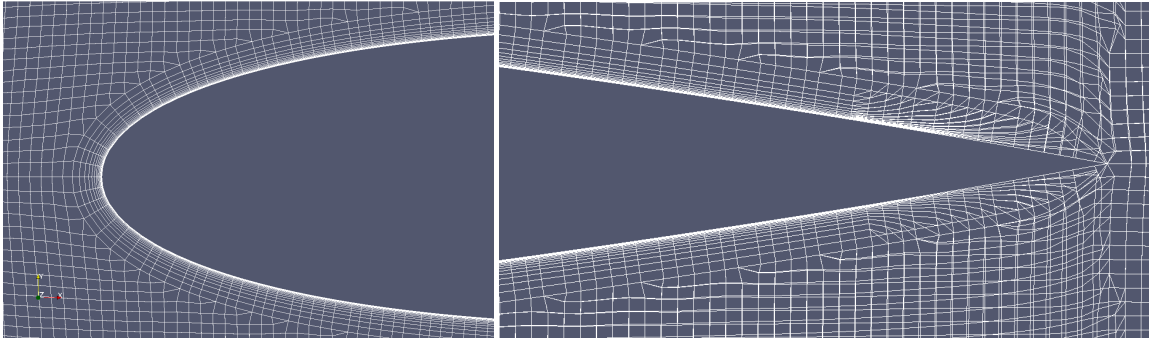
FIGURE 5.7 – Zoom of the mesh on the leading edge and on the trailing edge.

5.1.2 Results : displacement of the POM hydrofoil under hydrodynamic loading

Figure 5.8 shows the picture of the deformed hydrofoils during the experiments VS the simulations of Foam-Aster for $\alpha = 10°$ and all the Reynolds numbers.
The trend and the shape of the simulations are similar with the experiments.
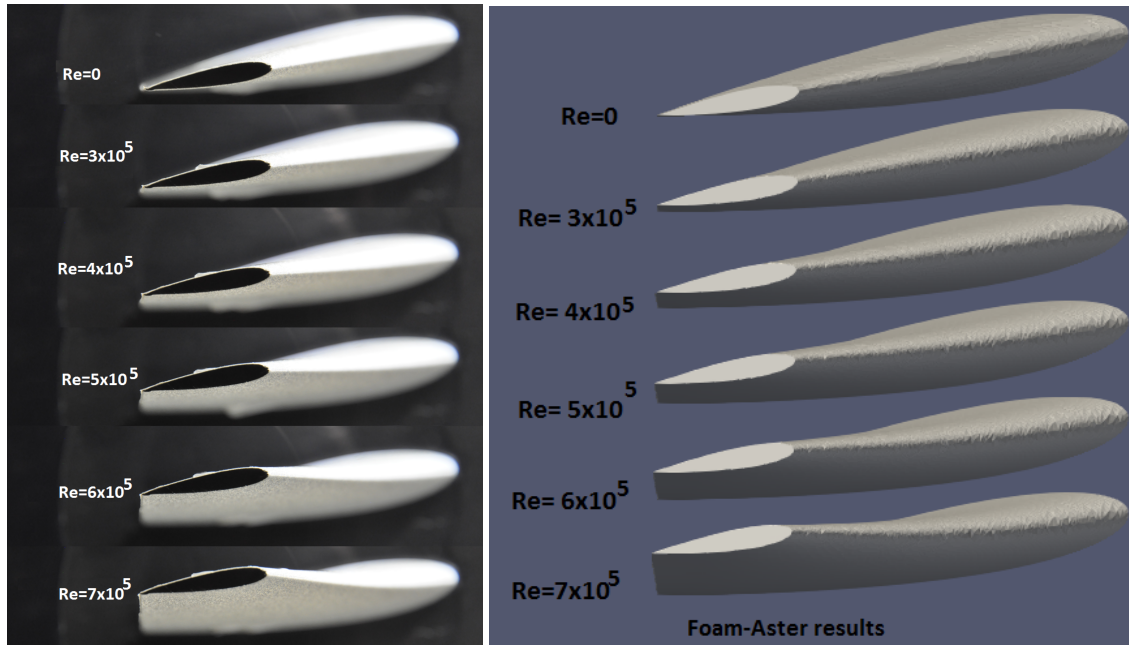
FIGURE 5.8 – Hydro-elastic response of the POM hydrofoil simulated with Foam-Aster VS experiments, $\alpha = 10°$

The following results compares the experimental displacements to the displacement simulated with Foam-Aster coupling. The hydrodynamic forces were not measured during the experiments. The experimental results of the negative and positive incidences being symmetric, only the positive incidences are discussed.
Both numerical and experimental results exhibit no twist motion on the structure during the interaction, thus the following displacements are computed on the trailing edge line. The trailing edge is chosen for its easy extraction on the structural mesh and in the results database.

Figure 5.9 compares the displacements of the POM hydrofoil for three incidences and Reynolds numbers $Re = 3 \times 10^5$ and $Re = 4 \times 10^5$. The vertical bars on the curves are the standard deviation of each experimental data.

Figures 5.10 and 5.11 present the results for $Re = 5 \times 10^5$, $Re = 6 \times 10^5$ and figure 5.11 presents the results for $Re = 7 \times 10^5$.
The numerical simulations predicts well the trend observed in the experiments : the bending shape of the hydrofoil is well computed for all the incidences.
For the lower velocities, the simulations lays in the standard deviation of the experimental measurements and the relative discrepancies are less than 4% up to $Re = 5 \times 10^5$.
When the velocity rises, the simulated shape fit well with the experiments close to the root but near the tip, the difference gets bigger and goes up to 13% for $\alpha = 10°$ and $Re = 7 \times 10^5$.
Excepts $Re = 7 \times 10^5$, the relative difference between Foam-Aster simulations and the experiments are less than 5% and the simulations are highest.

These observations point out an over-estimation of the hydrodynamic forces in the simulations.
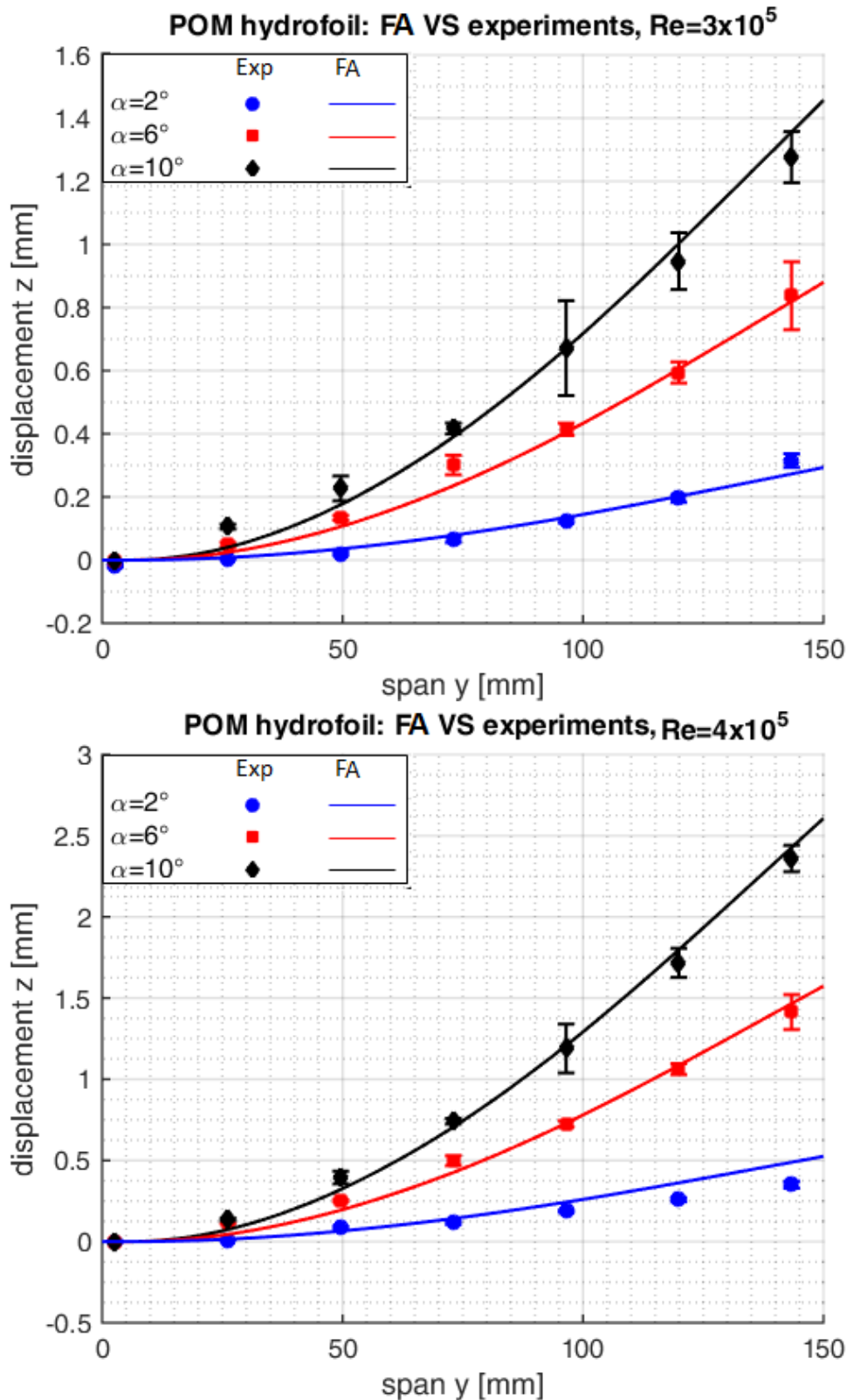
FIGURE 5.9 – Foam-Aster VS experiments : displacements of the POM hydrofoil $Re = 3 \times 10^5$ and $Re = 4 \times 10^5$. The vertical bars are the standard deviation of the experiments.

This may potentially be confinement effects induced by the the no slip modelling that increases the lift force and becomes amplified for high Reynolds number and high incidences.

Figure 5.12 shows the deformed hydrofoil after an FSI simulation for $\alpha = 10°$ and $Re =$
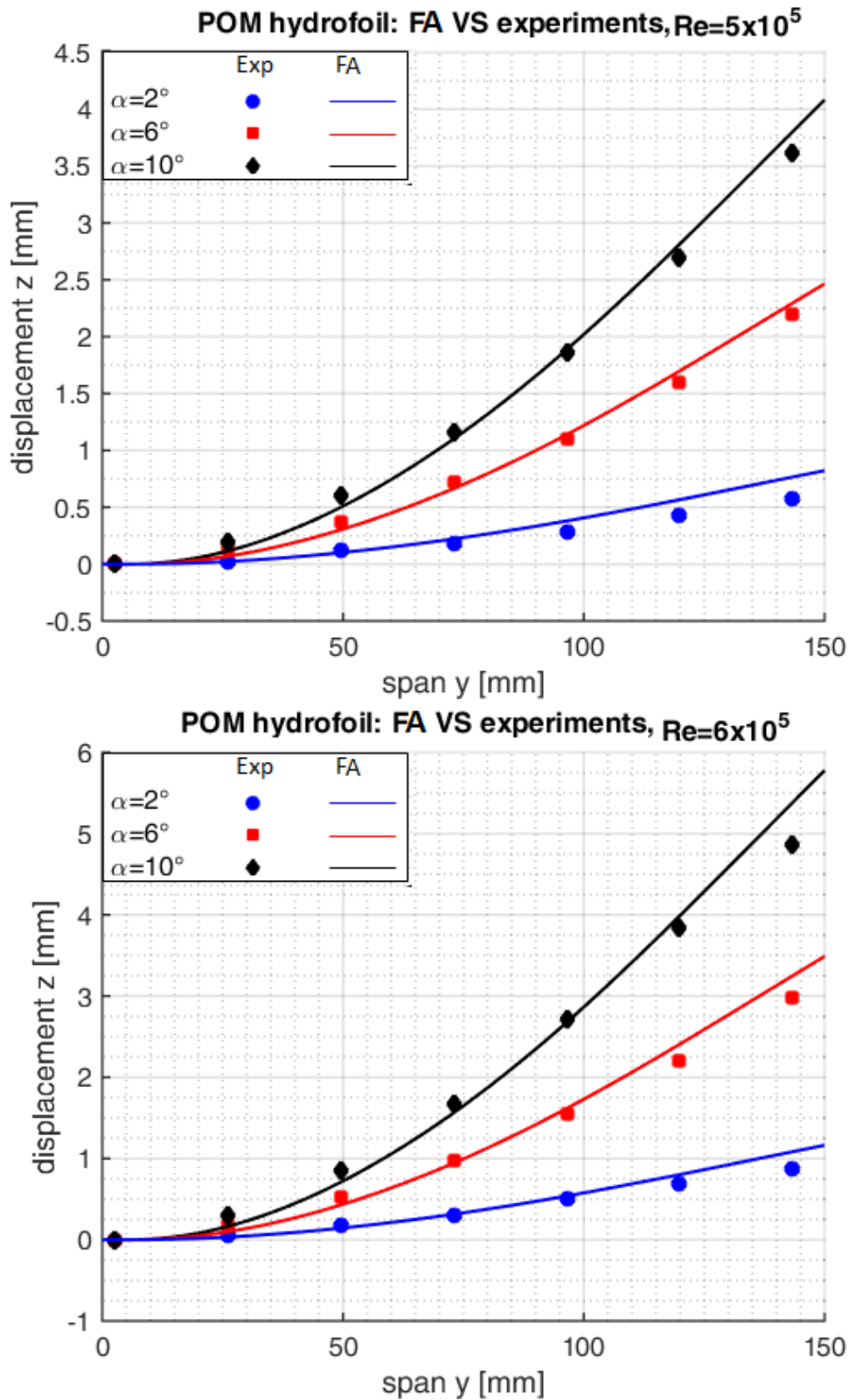
FIGURE 5.10 – Foam-Aster VS experiments : displacements of the POM hydrofoil $Re = 5 \times 10^5$ and $Re = 6 \times 10^5$.

7×10^5. The scale factor on the displacement is 2.5.
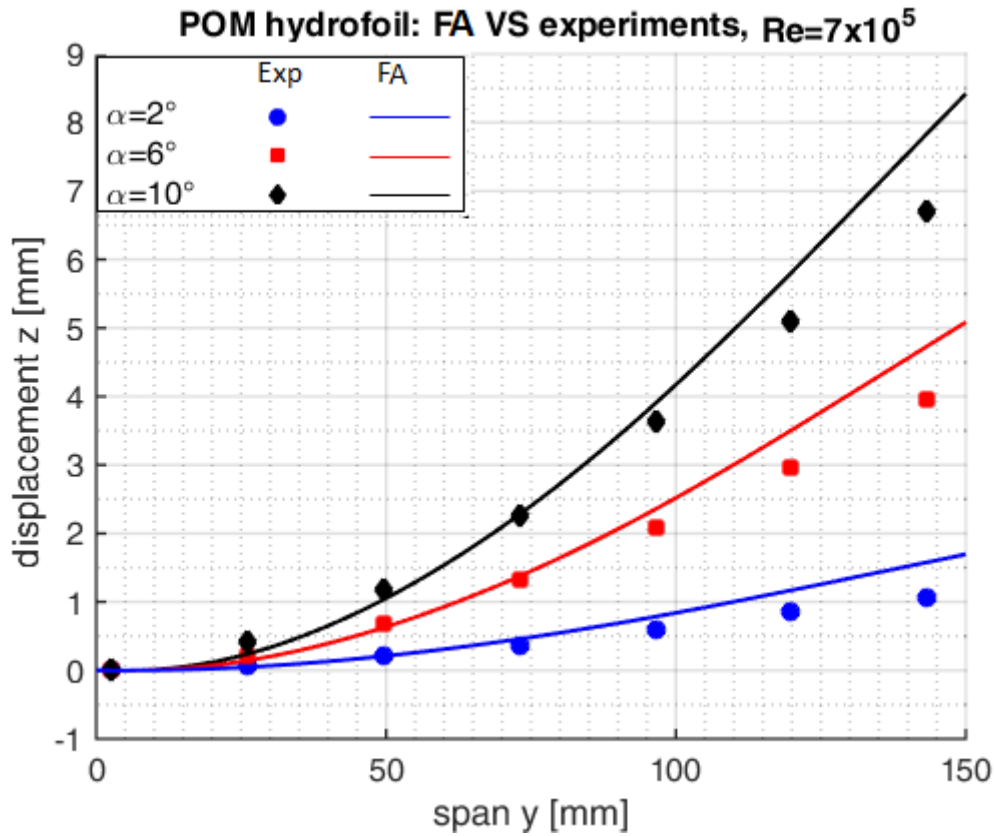
FIGURE 5.11 – Foam-Aster VS experiments : displacements of the POM hydrofoil $Re = 7 \times 10^5$.
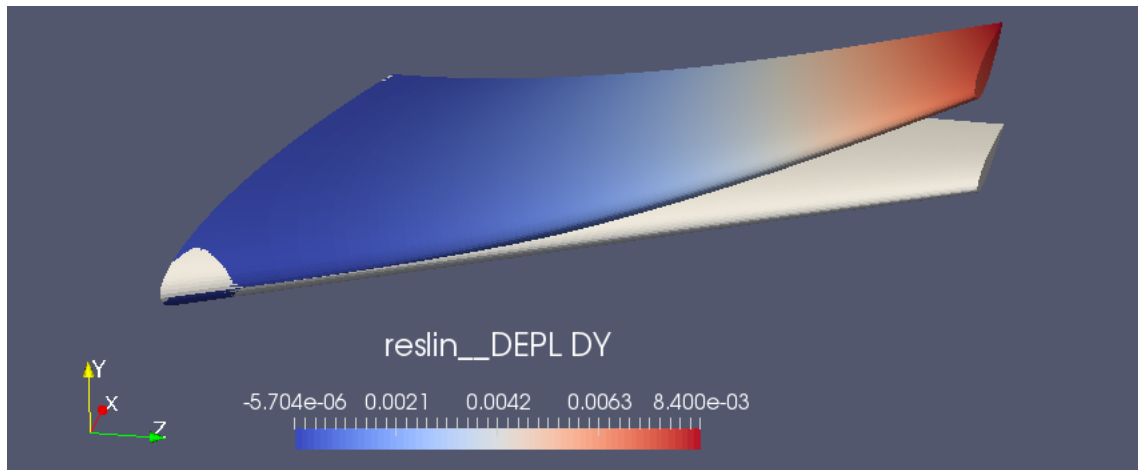
FIGURE 5.12 – Displacement of the POM hydrofoil after a FSI simulation for for $\alpha = 10°$.

5.1.3 Comparison of FS6R and Foam-Aster

This section compares the results of the low fidelity coupling **FS6R** to the results of high-fidelity coupling **Foam-Aster**.

5.1.3.1 Lift force

The lift force on the POM hydrofoil computed with FS6R is compared to the simulation of Foam-Aster in figure 5.13.
The simulations are performed for all the velocities investigated and for $\alpha = -2°, 3°, 10°$.

176
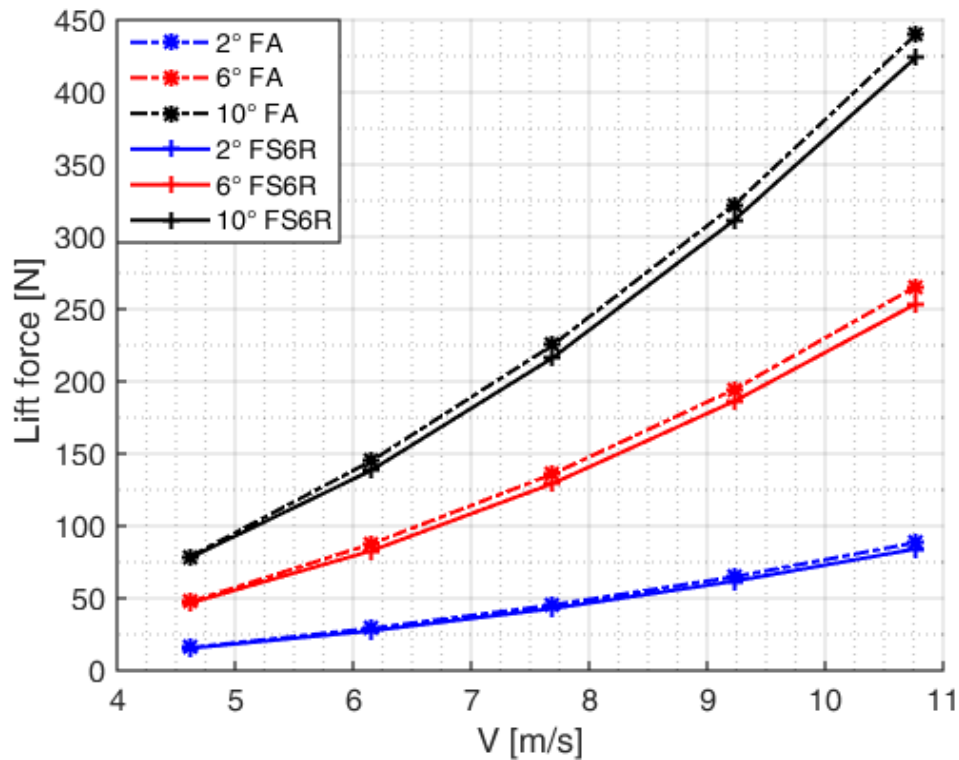
FIGURE 5.13 – Foam-Aster VS experiments VS FS6R : lift force on the POM hydrofoil

The trend of both numeric approaches are the same and Foam-Aster is higher than FS6R up to 4% for $\alpha = 10°$ and R$e = 7 \times 10^5$.
That difference is linked to confinement effects that does not appears in FS6R calculations. Looking at the numerical-experimental comparison of the displacements on Foam-Aster simulations, it can be assumed that Foam-Aster overestimate the confinement effects on this modeling. That effect is amplified when the incidence or the velocity rise.

5.1.3.2 Displacements under the hydrodynamic forces

The displacements simulated with FS6R and Foam-Aster are compared in figures 5.14 to 5.16. The both approaches describe with a good accuracy the trend hydro-elastic response of the POM hydrofoil under hydrodynamic loading. Both cases simulate a bending motion in agreement with the experiments.
For $\alpha = 2°$, where the lift force is the lowest for all the velocities investigated, FS6R results overlaps very well with the simulations of Foam-Aster.

When the incidence increases, the simulations of Foam-Aster gets bigger than FS6R : FS6R is slightly lower than the experiments and Foam-Aster is slightly higher.
Globally, Foam-Aster fit the experiments better than FS6R and, FS6R is lower than Foam-Aster in an average of 10%.
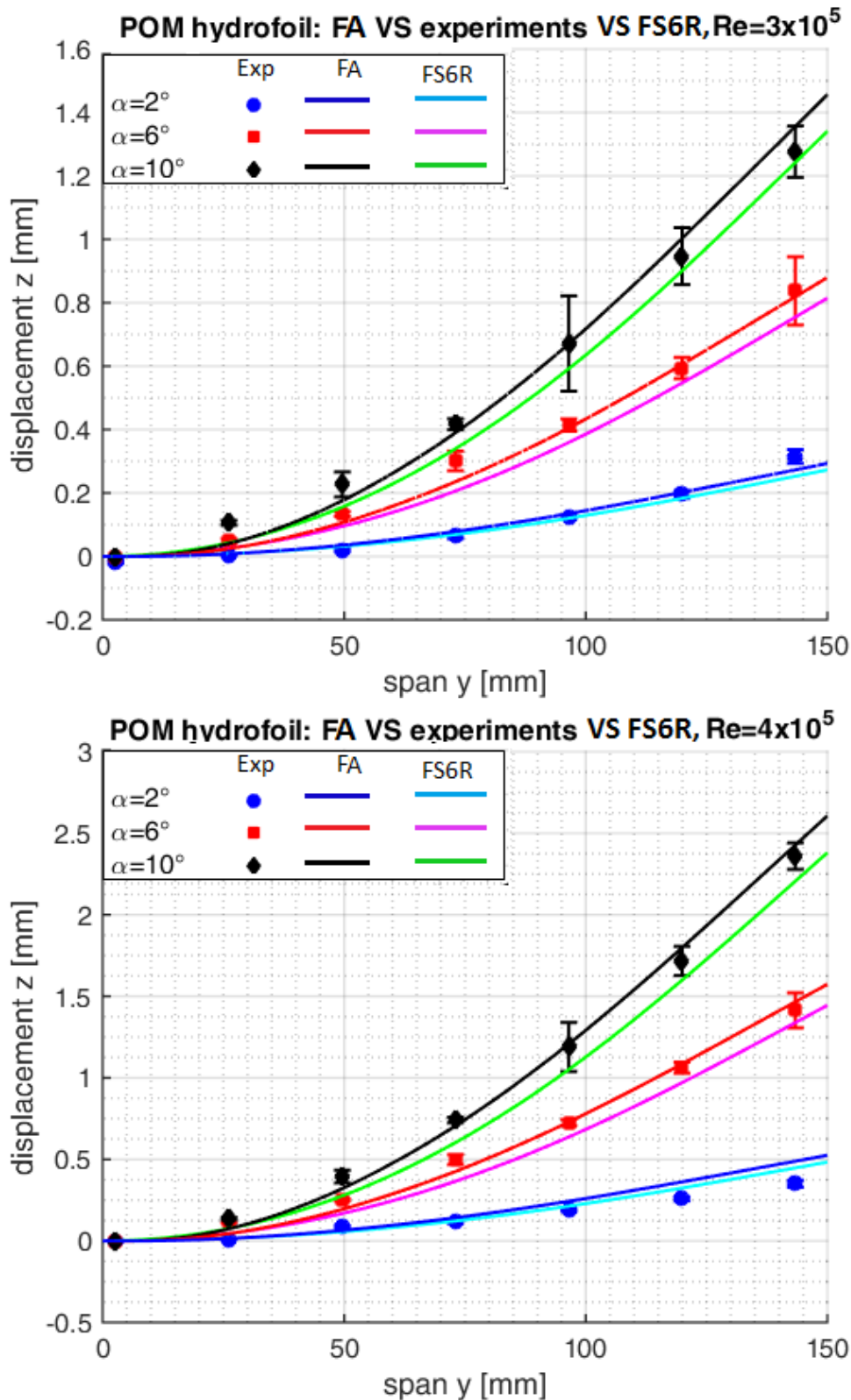
FIGURE 5.14 – Foam-Aster VS experiments VS FS6R : displacements of the POM hydrofoil, Re = 3×10^5 and Re = 4×10^5

We have shown the ability of Foam-Aster to simulate FSI on structural homogeneous Hydrofoil. In the next section we will look at the simulation of FSI on composite structure in a two-phase flow. To reach such a complex problem, we divided the problem and resolved the difficulties step by step. The first section will described the modeling of composite
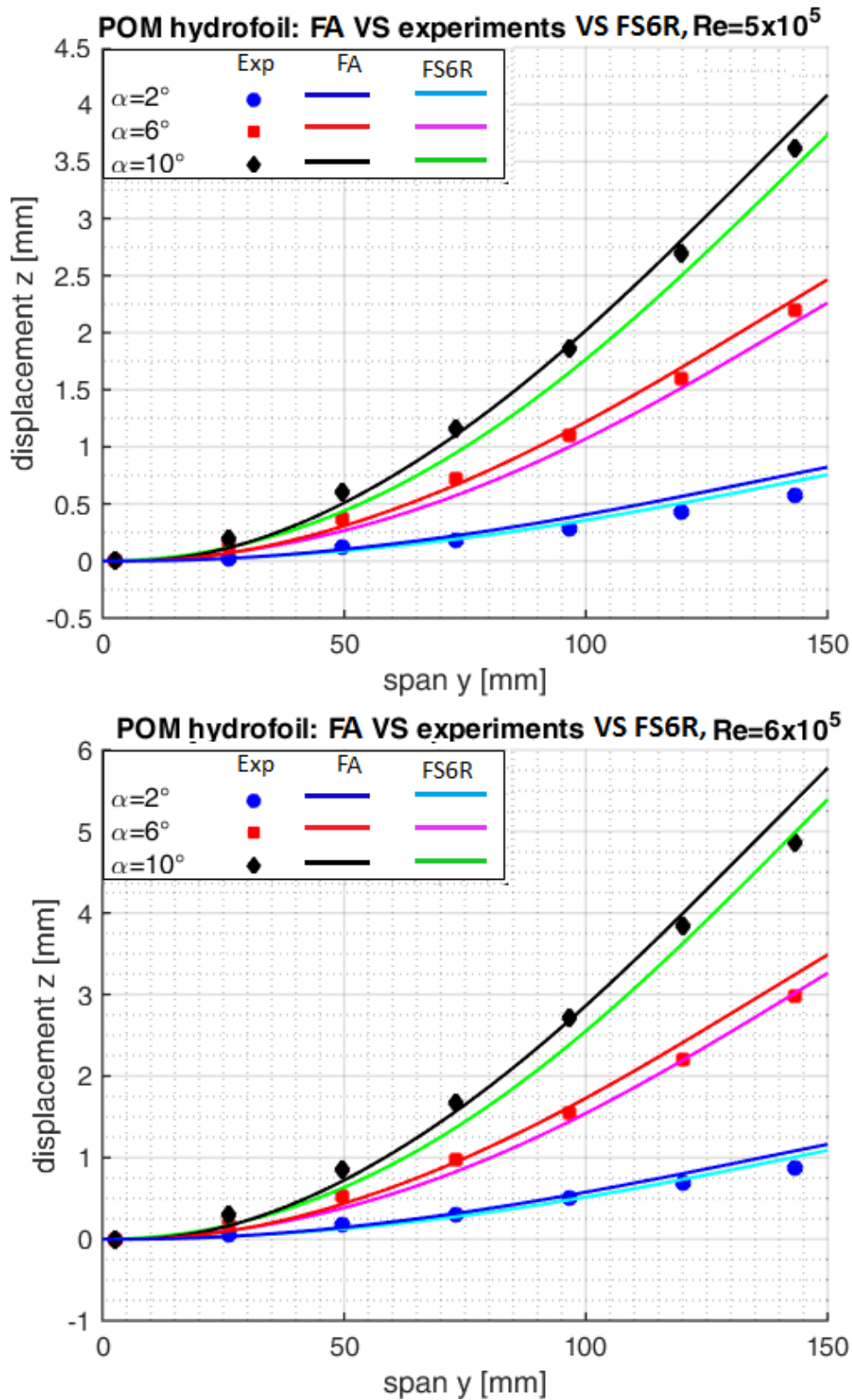
FIGURE 5.15 – Foam-Aster VS experiments VS FS6R : displacements of the POM hydrofoil, Re = 5×10^5 and Re = 6×10^5

Structure with Aster, including BTC effect.
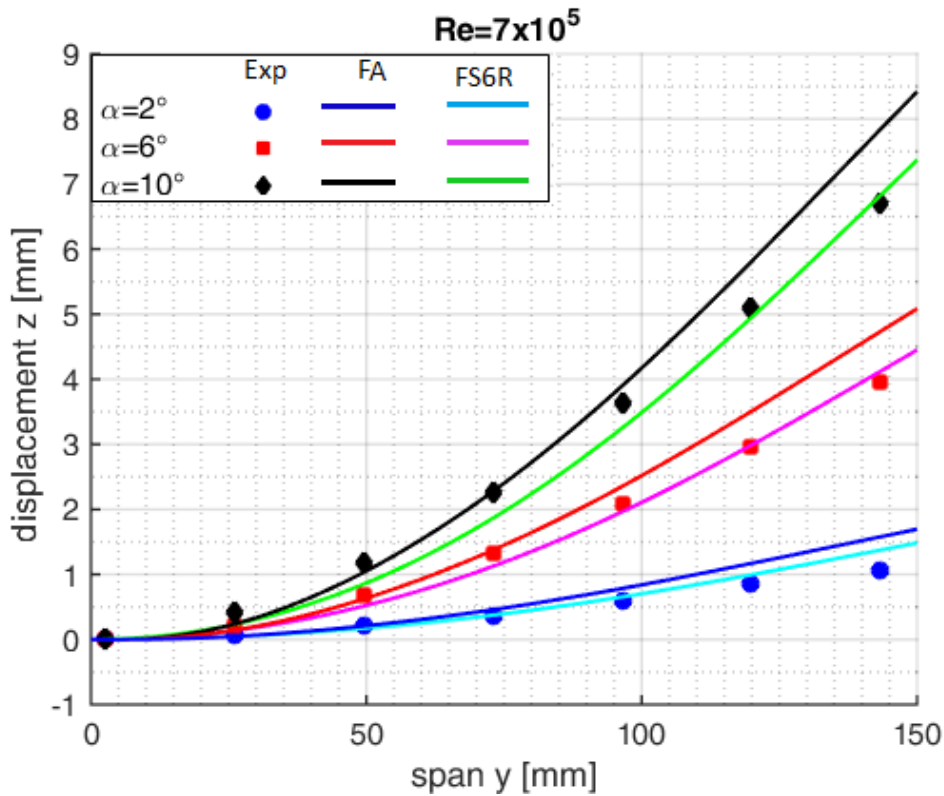
FIGURE 5.16 – Foam-Aster VS experiments VS FS6R : displacements of the POM hydrofoil, $Re = 7 \times 10^5$

5.2   Analysis of the bend twist coupling in Code_Aster : thin plate in compositeS

This section aims to analyze the BTC on composite materials with Code_Aster. The test case is a simple one, a thin plate with the dimensions of the hydrofoils : $1350mm$ long, $114mm$ width and $17.1mm$ (maximum thickness of the hydrofoils).
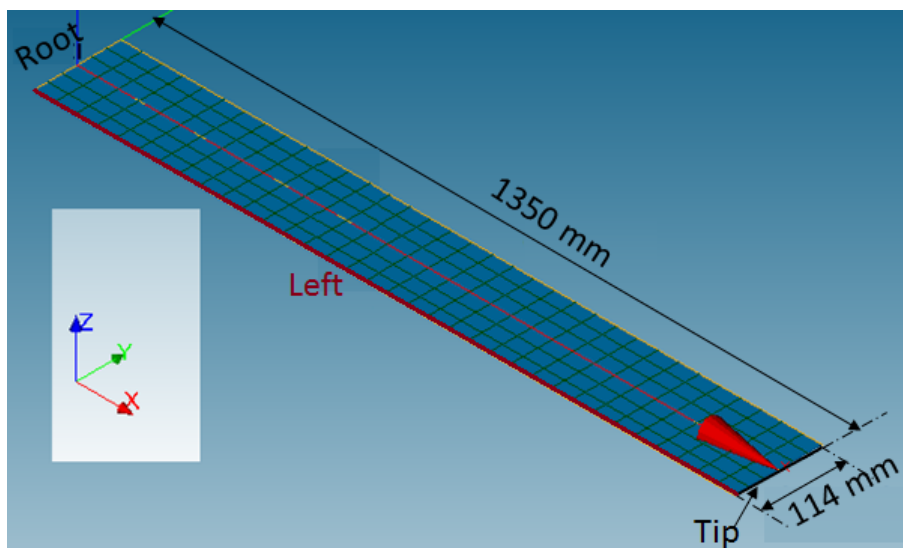
FIGURE 5.17 – Geometry of the plate used for BTC analysis with Code_Aster, $1350 \times 114 \times 17.1mm^3$.

The plate is made of stacking plies all unidirectional with the same angle in all the

layup, each ply uses the glass fiber properties $Glass_2$ presented in table 5.2.

Different layups are tested from $-90°$ to $90°$ at $10°$ steps.

The plate shown in figure 5.17 is cantilevered on the root and loaded at the tip. We impose the maximum displacement of the plate at 10% of the span corresponding to a loading force of 78.2N applied at the tip. The loading is applied downward -78.2N and its distribution is linear along the tip section. The results of displacements ant bend-twist angles are extracted on the left line and the tip section (see figure 5.17).

The middle line being the axis of rotation of the plate, the displacement recorded for orientations $\pm\theta$ will be the same. Thus, the left line is chosen to see the influence of the BTC on the displacements.

5.2.1 Results of the BTC investigations on the plate

Figure 5.18 shows the evolution of the vertical displacement of the plate along the span, extracted on the left line for various orientations of the fibers.
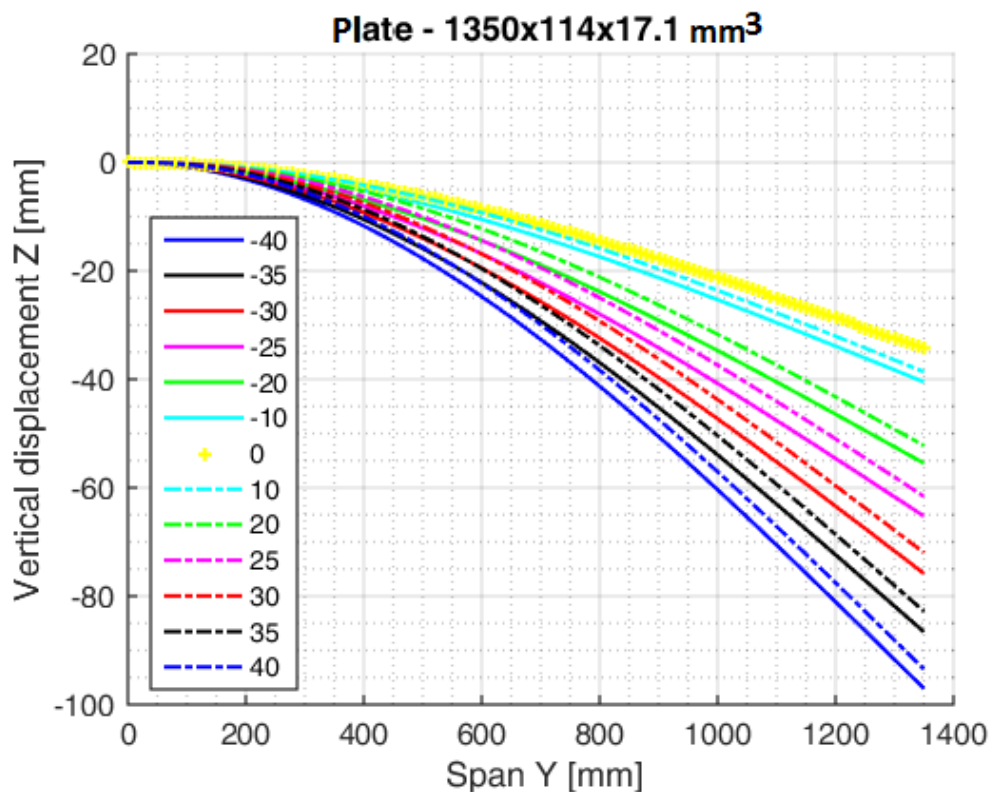
FIGURE 5.18 – Displacement of the thin plate for various orientations of the layup - left line.

The curves exhibit a well defined bending motion. The difference between the negative and positive orientations is clearly observable, highlighting the BTC. The negative orientations are higher than the positive orientations.

This observation is in agreement with the conclusions of the chapter 4 on the BTC appearance : a negative orientation gives a negative twist and a positive orientation gives positive twist. Since the applied load is negative, the displacements of the left line for the negative orientations are higher than the positive orientations. The tendency is inverted when looking at the right line and the results overlap on the middle line for $\pm\theta$ orientations.

Figure 5.19 shows the evolution of the displacement and the bend-twist angle extracted at the tip section of the plate for all the orientations tested in the layups.
The displacement curve is symmetric when the curve of the bend-twist angle is asymmetric.
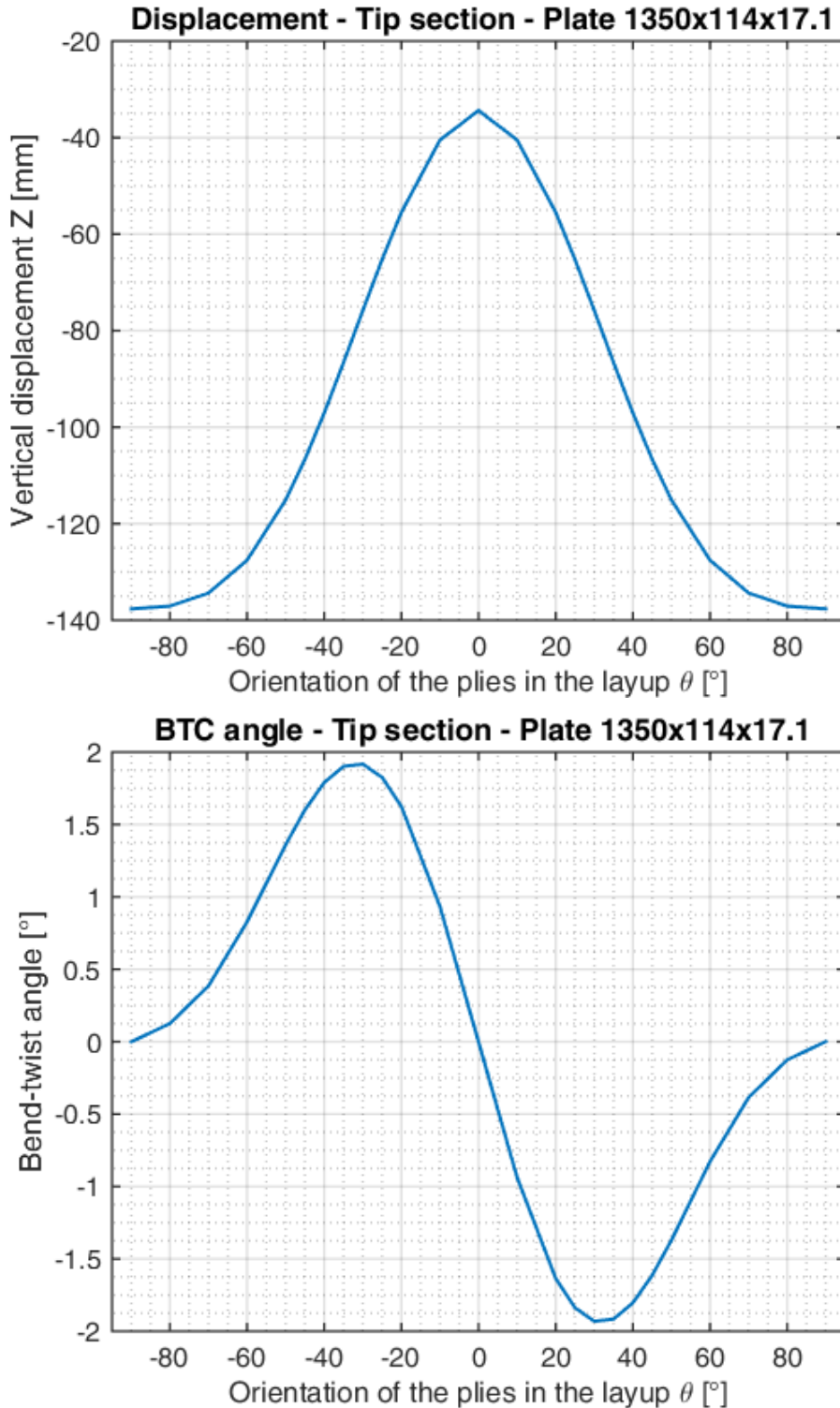
FIGURE 5.19 – Displacement and bend-twist angle extracted at the tip section of the plate for all the orientations tested.

The 0° orientation has the higher stiffness which is the longitudinal modulus of the fiber and thus gives the smallest displacement. The ±10° orientations are still stiff and their

displacement is close to 0°.

When the orientation of the fibers rises, the stiffness decreases and the minimum correspond to ±90° which give the highest displacement.

The evolution of the bend-twist angle shows : the positive orientations in the layup twist positive and the negative orientations in the layup twist negative. The orientations of 0° and ±90° give zero bend-twist angle when the maximum bend-twist angle is observed with ±30° in agreement with the literature.

As a summary of this section, Code_Aster computes very well the BTC behavior of various fiber orientations. The tendencies observed are in agreement with the experimental investigations presented in chapter 4 and the evolution of the bend-twist angle with the fiber orientations is in agreement with the literature.

5.3 Structural modeling of the composite hydrofoils in Code_-Aster

In order to reproduce as well as possible the experimental behavior of the composite hydrofoils with their sandwich section in FOAM_Aster calculation, the structural modeling must be done in a clever way.

The theoretical cross-section of the hydrofoils is a sandwich made of a web in Airex material and a laminated skin as presented in figure 5.20 when figure 5.21 shows an image of the manufacture cross-section for the layup P_1.
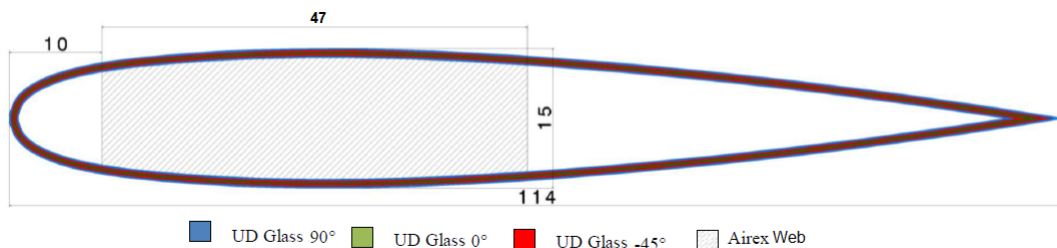
FIGURE 5.20 – Web location in the sandwich structure and layup illustration of P_2 in the thickness of the laminate skin.
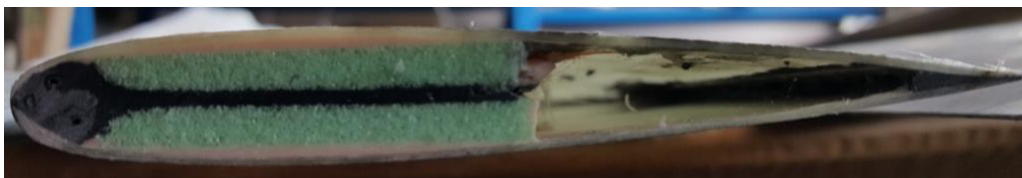
FIGURE 5.21 – Image of the final hydrofoils P_2 showing the sandwich cross-section.

The manufactured section shows some significant structural difference with the theoretical one. The gap between the leading edge an the trailing edge is full of glue. There is around 12 mm width of glue along the hydrofoil close to the trailing edge and there is also a good amount of glue in another area between the web and the trailing edge of P_1 and P_4.

Table 5.2 reminds the properties of the different materials. The white and black glues (see figure 5.21) in the hydrofoils sections are the spabond 345 whose modulus is non negligible compared to the modulus of the glass fibers.

Material	Carbon	Glass1	Glass2	Airex
E_l[GPa]	105.4	54	45	0.58
E_t[GPa]	8.6	10.4	10	0.58
G_{lt}[GPa]	3	3.9	5	
ν_{lt}	0.4	0.25	0.25	0.3
e_p [mm]	0.3	0.2	0.2	

TABLE 5.2 – Mechanical properties of the materials. The layup of P_1 uses the Glass2 when the layup of P_2 and P_3 use the Glass1.

Thus, not including the glue in the structural model will modify the stiffness distribution in the cross-section and may lead to errors in the twist motion of the hydrofoil 's sections compared to experiments, when a loading is applied.

After analyzing the manufactured hydrofoils, the simplified representation of the cross sections are presented in figure 5.22. The two configurations are chosen to reproduce more closely the observed differences on the section's structures.
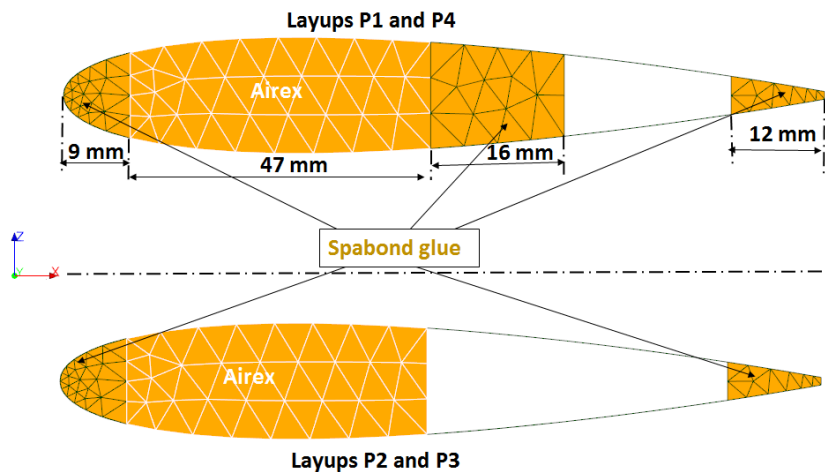
FIGURE 5.22 – Modeling of the sandwich cross-section for the different hydrofoils.

In code_Aster, the laminated skin is modeled with DKT shell elements and the layup are given with the description of the ply and the orientations (see details in tables 5.2 and 5.3). The glue and the Airex area are model with solid elements and isotropic materials.

Foils	Material	layup
P_1	Epoxy-Glass2	$[(BA_{\pm 45})_2/0_{0.5}]_{sym}$
P_2	Epoxy-Glass1	$[(90/-45/0_{0.5}]_{sym}$
P_3	Epoxy-Glass1	$[(90/45/0_{0.5}]_{sym}$
P_4	Epoxy-Carbon	$[(90/0)_{sym}]$

TABLE 5.3 – Hydrofoils layups, BA is a bi-axial ply.

To validate the structural model, the static bending tests performed on the hydrofoils with the mass $M_1 = 2.2kg$ are simulated with Code_Aster.
Figure 5.23 shows the setup of the bending test of the hydrofoils modeled in Code_Aster. The hydrofoil is cantilevered on the root and loaded close to the tip to reproduce the experimental conditions. As performed in the experiments, a vertical load is applied on the

point A_1, the center of the section located at $Y = 1250 mm$ from the root of the hydrofoil. Then, a static mechanical analysis is performed on code_Aster.
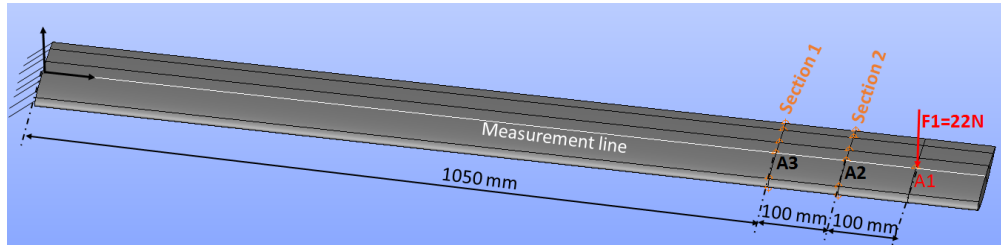
FIGURE 5.23 – Modeling of the bending test on the composite hydrofoils in Code_Aster.

The following results are computed on a continuous line along the hydrofoil skin that goes through the center of all the sections (see figure 5.23).
During the experiments, the displacement and twist were recorded for the sections S_1 and S_2, thus the points A_2 and A_3.

5.3.1 Influence of the mesh on the convergence of the results

Figure 5.24 shows the vertical displacements extracted on the point A_2 in simulations with different meshes. The vertical axis is the displacement and the horizontal axis is the number of points imposed on a section.
The figure compares the simulation to the experimental value for the four composite hydrofoils.
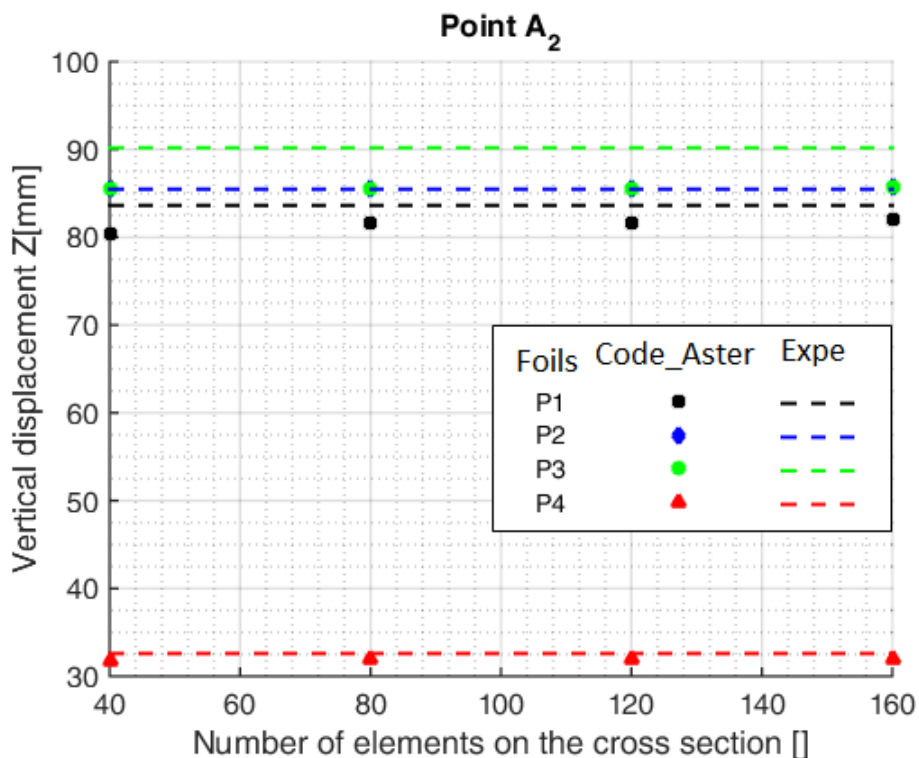
FIGURE 5.24 – Influence of the mesh on the convergence of the displacements, measured on point A_2.

The results computed with Code_Aster for the layup P_4 fits perfectly with the experiments. The results of P_1 are slightly lower than the experiments and the relative difference is very low 3.3% for the coarse mesh and decreases up to 2% with the finest mesh. Code_Aster computes the same displacement for the layups P_2 and P_3 because the sign of a ply orientation does not influences the equivalent stiffness of the laminate. The computed displacement fits very well with the experimental results of P_2 with a relative difference less than 0.3% but are 5% lower than the experimental results of P_3. This observation is explained knowing that the real stiffness of P_2 is 0.9% close to the theoretical value when the real stiffness of P_3 is 4% lower than the theoretical value.

For all the layups, the results are quite constant with the number of elements on the cross section of the hydrofoils. Since the finer is the mesh, the longer runs the calculation, we chose to work with N = 40 giving an element size of $2.85 mm$. The chosen mesh is shown in figure 5.25, it contains 116 861 volumes and 61398 faces. A mechanical static analysis on Code_Aster performed on one processor lasts 12 minutes.
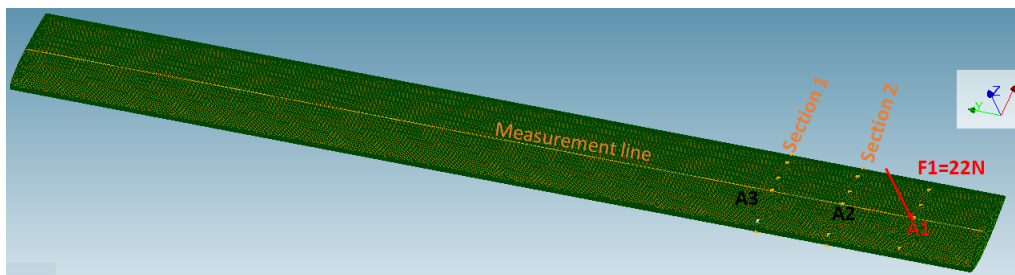
FIGURE 5.25 – Structural mesh used on the composite hydrofoils in Code_Aster.

5.3.2 Results of the bending tests : static analysis

This section presents the results of the bending tests on the four hydrofoils, simulated with Code_Aster. The vertical displacement of the hydrofoil computed on the middle line (see figure 5.25) and the bend-twist angle are discussed.

The evolution of the vertical displacement along hydrofoils span computed with Code_Aster is compared to the experiments in figure 5.26 for all the layups. As previously observed with the point A_2 (figure 5.24), the results of P_4 and P_1 fit perfectly with the experiments when the numerical results are the same for both P_2 and P_3. The simulated results of P_2 and P_3 fits well with the experimental results of P_2 The evolution of the computed twist along the entire hydrofoil and extracted on the middle line is presented in figure 5.27 and compared to the twist measured on points A_2 and A_3

The simulations are very low and around $0.14°$ at the tip. This is the order of magnitude of the experimental twist recorded for P_1 and P_4 that was neglected. Knowing that Code_Aster computes well the BTC behavior of composite materials, these results highlight the need to improve the structural model. More over, we performed the same bending test on a plate geometry similar to the hydrofoils : $1350 \times 114 \times 1 mm^3$. The thickness of $1 mm$ is the thickness of the hydrofoils composite skin. The layup contains only one orientation and several angles are tested. We applied the loading M = $2.2 kg$ in a punctual loading on the point A_1 and a surface loading on an area of $114 \times 20 mm^2$ centered on A_1. The results of the bend-twist angle came out to be dependent on the loading type. Figure
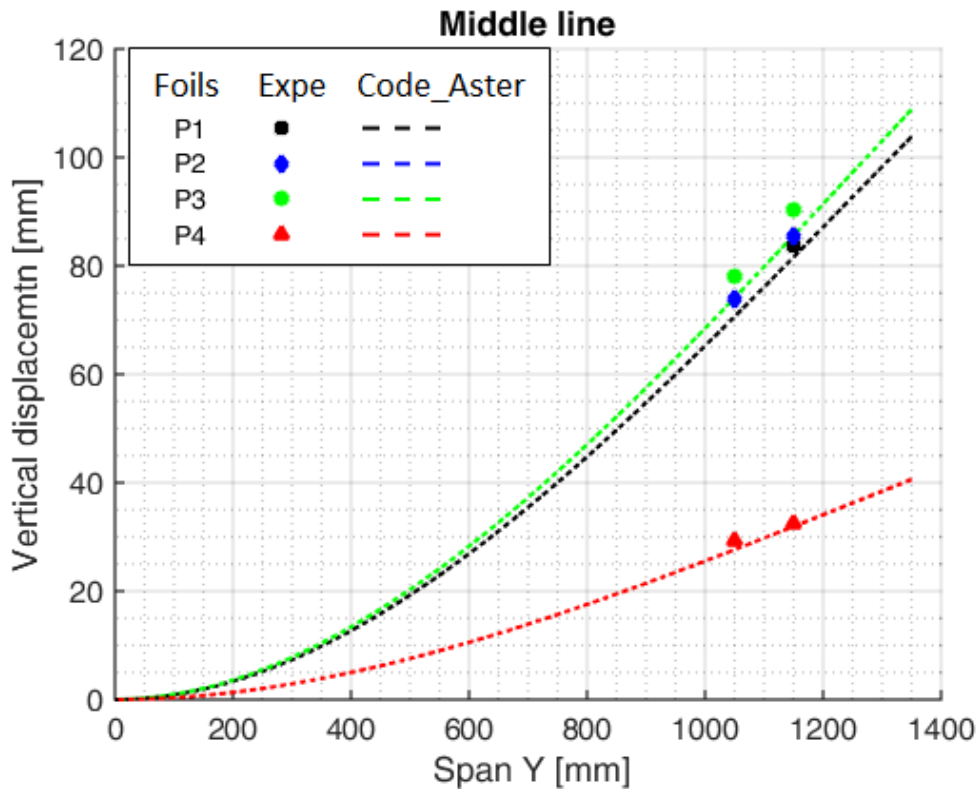
FIGURE 5.26 – Vertical displacement on the hydrofoil in static bending test-Code_Aster.
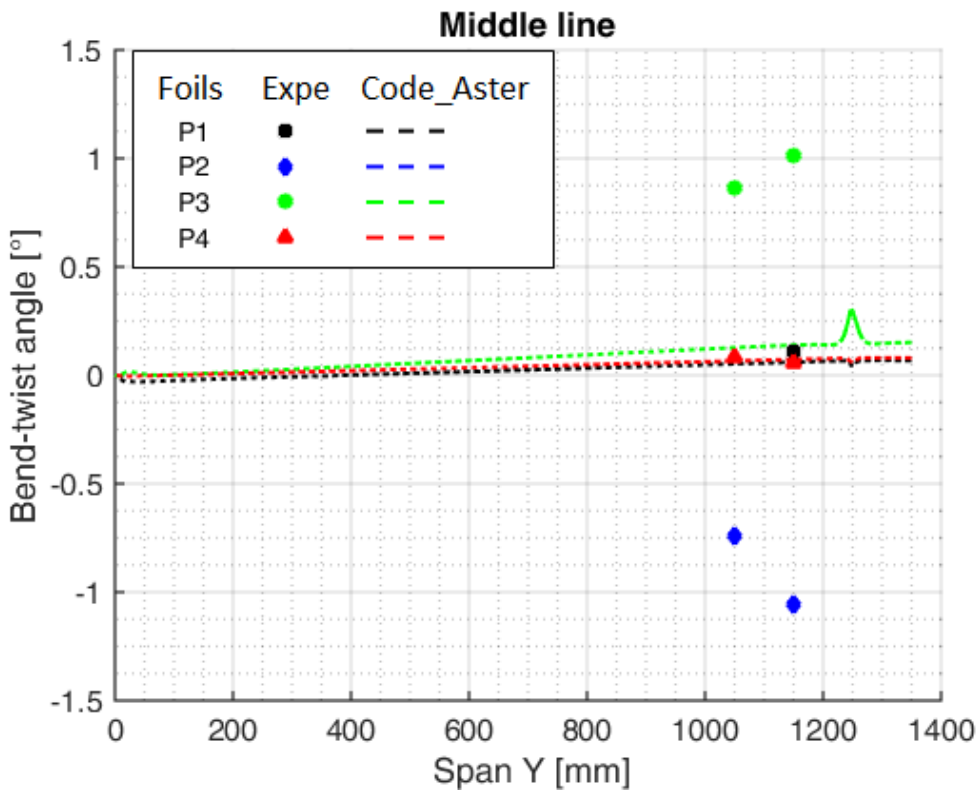
FIGURE 5.27 – Twist angle on the hydrofoil in static bending test computed with Code_Aster.

5.28 shows the bend-twist angle simulated for the same loading applied in a punctual mode versus a surface mode.

FIGURE 5.28 – Bend-twist angle of the plate $1350 \times 114 \times 1 mm^3$ in static bending test for punctual and surface loading.

No twist angle is recorded with the punctual loading when the surface loading clearly shows the different behavior with the fiber orientations. These results point out lacks in the structural model.

Hydrodynamic loading being applied on the hydrofoils as surface loading, one should expect the FSI simulations to fit the experiments. Further developments on the structural model of these hydrofoils will be investigated in future work.

5.4   Comparison of the hydrodynamic tests on the composite hydrofoils with Foam-Aster

This section presents a comparison of the simulations of Foam-Aster on the four composite hydrofoils and the experimental results.

5.4.1   Fluid model

This section describes the modeling of the hydrodynamic flume of Lorient in Open-Foam and presents its boundary conditions. Figures 5.29 to 5.31 show the fluid domain meshed and a zoom on the profile showing the boundary layer around the hydrofoil.
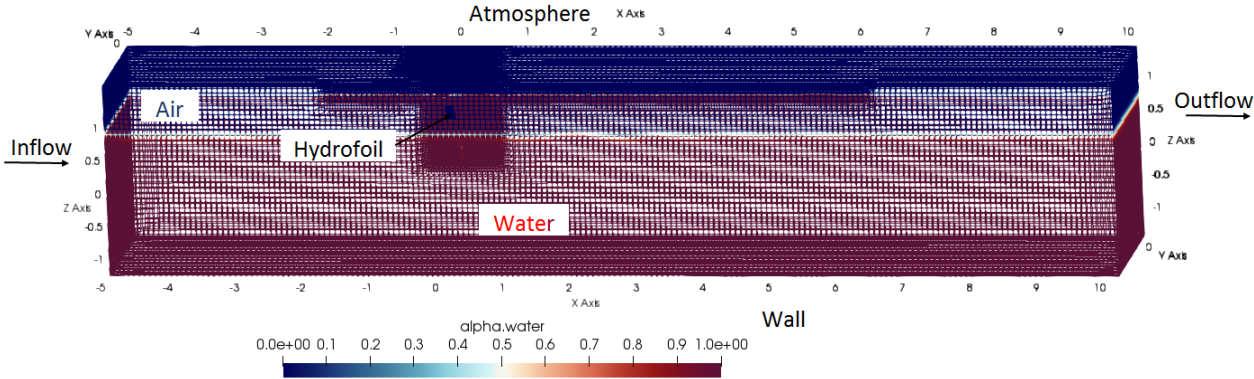
FIGURE 5.29 – Mesh of the fluid domain and zoom on the hydrofoil section mesh.

The domain is a rectangular box whose section fits the real dimensions of the flume excepts the length in the flow direction who is chosen 3 times the length of the flume. The box is $15 \times 2.5 \times 2.5 \ m^3$ and contains 7196562 hexahedra cells of unstructured mesh; the foil is placed in the same configuration of the experiments : piercing the free surface with at an angle of 45°. The figures show a refinement box around the hydrofoils and a refinement zone at the free surface interface.
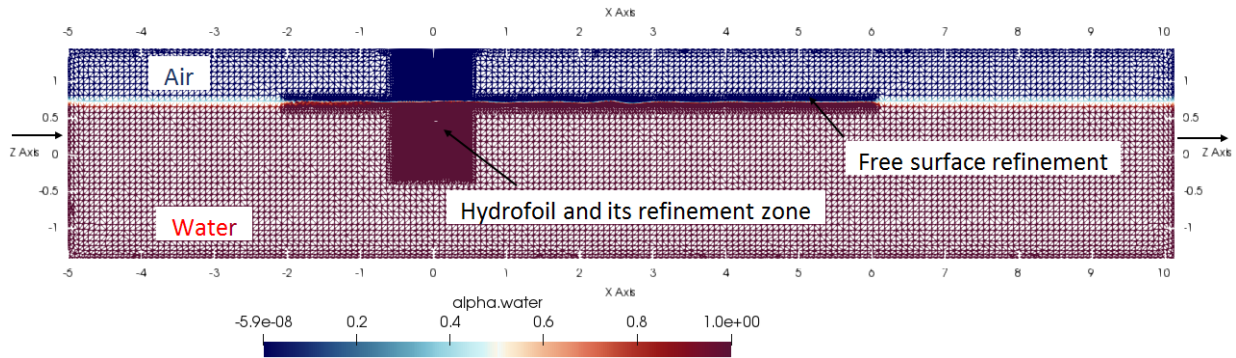
FIGURE 5.30 – Mesh of the fluid domain and zoom on the hydrofoil section mesh.
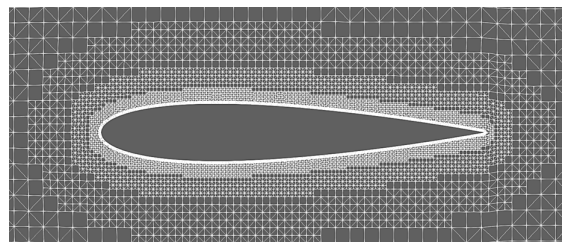
FIGURE 5.31 – Mesh of the fluid domain and zoom on the hydrofoil section mesh.

The fluid simulation carried out with the OpenFOAM solver **interFoam** uses the $K - Omega$SST for the turbulence model. We impose a non-slip boundary condition on the foil with a wall function *movingWallVelocity*. The time interval is chosen to have an initial Courant number equals to 1.

5.4.2 Hydrodynamic forces

The hydrodynamic forces computed in Foam-Aster are not given in the hydrofoil references but the the global reference system, thus, the following the comparison focuses on the lift magnitude and the drag force.

The lift force of the real-scale composite hydrofoils computed with Foam-Aster are compared to the experiments in figure 5.32.

The simulated results exhibits the same trend as the experiments. The curves are linear and the BTC 's influence is observed : lift P3< lift P_1 lift P_4< lift P_2.

The numeric results fit well with the experiments for all the hydrofoils excepts P_3. The experimental lift force of the hydrofoil P_3 is lower than the simulations up to a relative difference of 12%.

This structural difference between the theoretical section of P_3 and the manufactured real one where not pointed out in FS6R simulations because the twisting and bending stiffness used in the model were the experimental values.

The experimental bending stiffness of P_1 and P_2 are the same and that value is 0.9% close

to the theoretical bending stiffness of P_2 thus, the numerical simulation of P2 is close to the experiments.
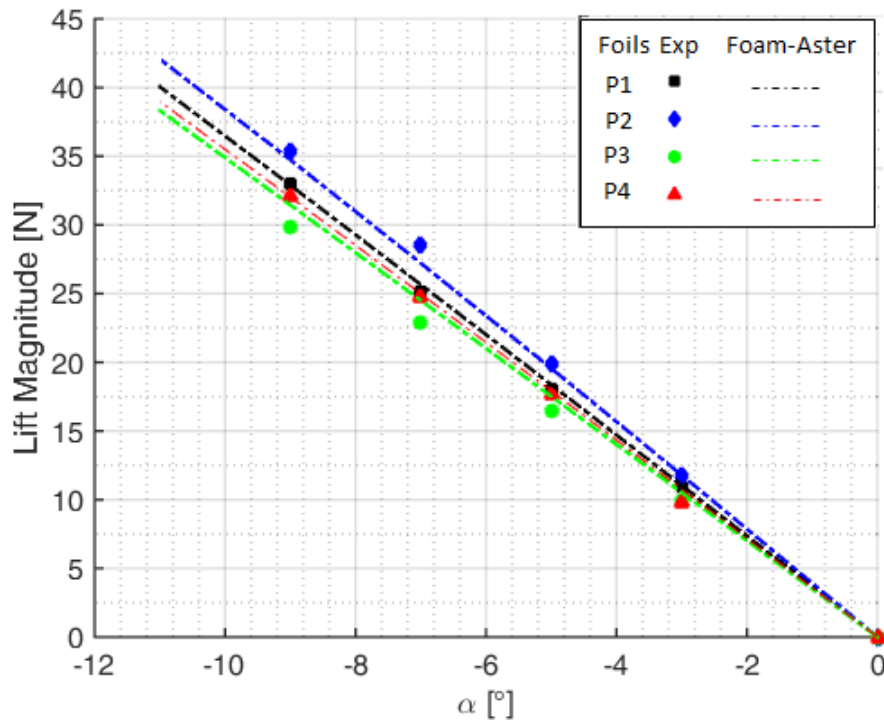
FIGURE 5.32 – Validation of Foam-Aster : lift force of the composite hydrofoils, U=0.9m/s.

The theoretic bending stiffness of P_3 is 4% higher than the experiment such as its theoretical torsional stiffness that both lead to an under estimation of the twist motion and a simulated lift force higher than the experimental value.

Figure 5.33 shows the evolution of the drag force on the four hydrofoils simulated with Foam-Aster for U=0.9m/s and several angles of attack.

The drag force of the hydrofoils has a parabolic shape and a small difference is observed between the different layups. The drag of P_4 is the highest and very close to the drag of P_1. The drag of P_3 and P_2 are very close and the smallest. The difference between the two group is lower than 5% and is likely numerical and does not correspond to a physical behavior.

5.4.3   Hydro-elastic response of the hydrofoil

This part analyses the hydro-elastic response of the hydrofoil simulated with Foam-Aster. The displacements of the hydrofoils under the hydrodynamic loading are presented in figures 5.34-5.36.

Foam-Aster simulates well the bending shape of the hydrofoils under the loading. The numeric results are in good agreement with the experiments of all the hydrofoils excepts P_3. This observation is in good agreement with the lift results. The experimental displacement of P_3 is lower than the numerical one up to 18%. These results of P_3 is linked to the overestimation of its bending and torsional stiffness.

Globally, Foam-Aster simulates well the behavior o a hydrofoil experiencing FSI and give very good accuracy for rigid structure without structural coupling such as the hydrofoils P_4 and P_1. Considering that simulations are based on the theoretical properties of the
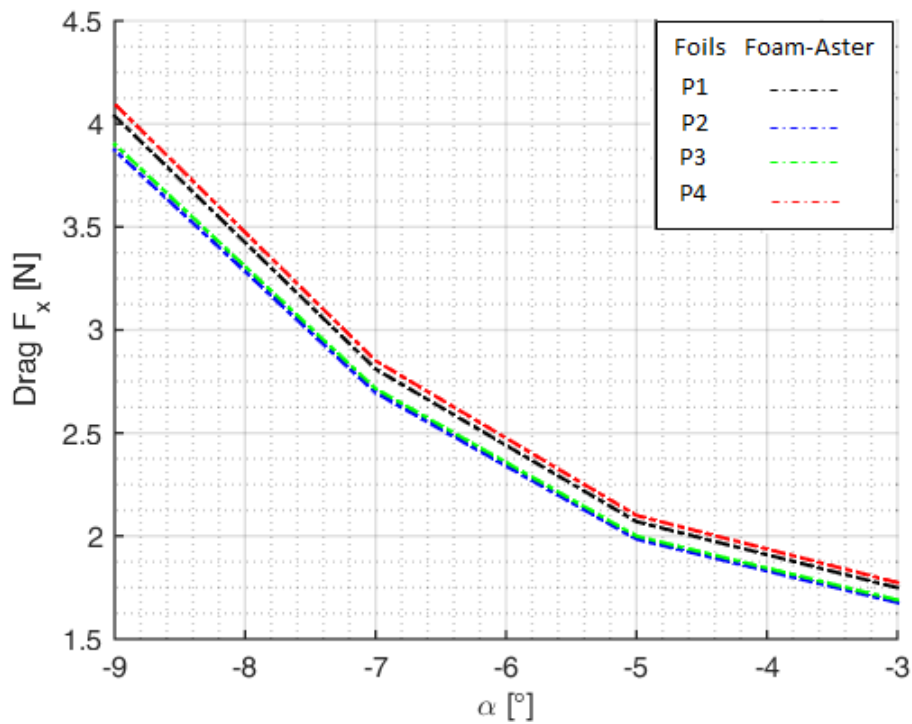
FIGURE 5.33 – Drag force simulated with Foam-Aster on the four composite hydrofoils, U=0.9m/s.
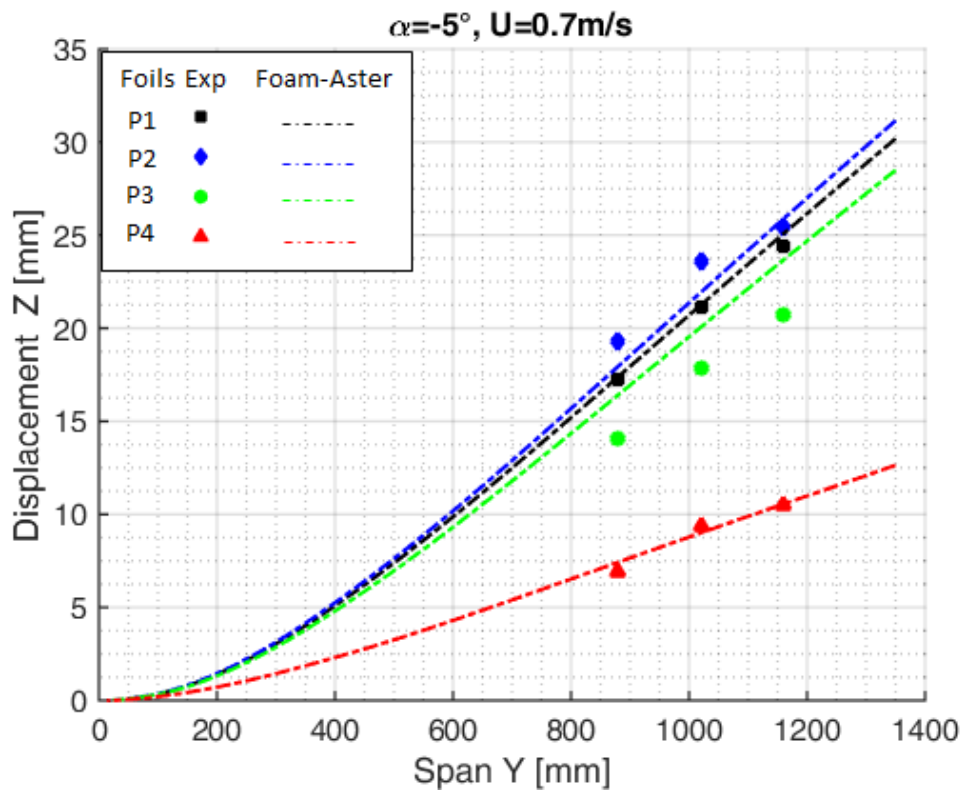
FIGURE 5.34 – Validation of Foam-Aster : Normal displacements of all the hydrofoils, $\alpha = -5°$ and $U = 0.7 m/s$.

laminates.

The difference between P_2 and P_3 shows that the coupling is able to see the influence of

the layup orientations on the twist motion as expected from the static simulations.
The discrepancies between the numeric and experimental results of P_3 highlight the influence of the manufacturing on the mechanical properties of the structure and the need of characterizing real structure to get accurate results.
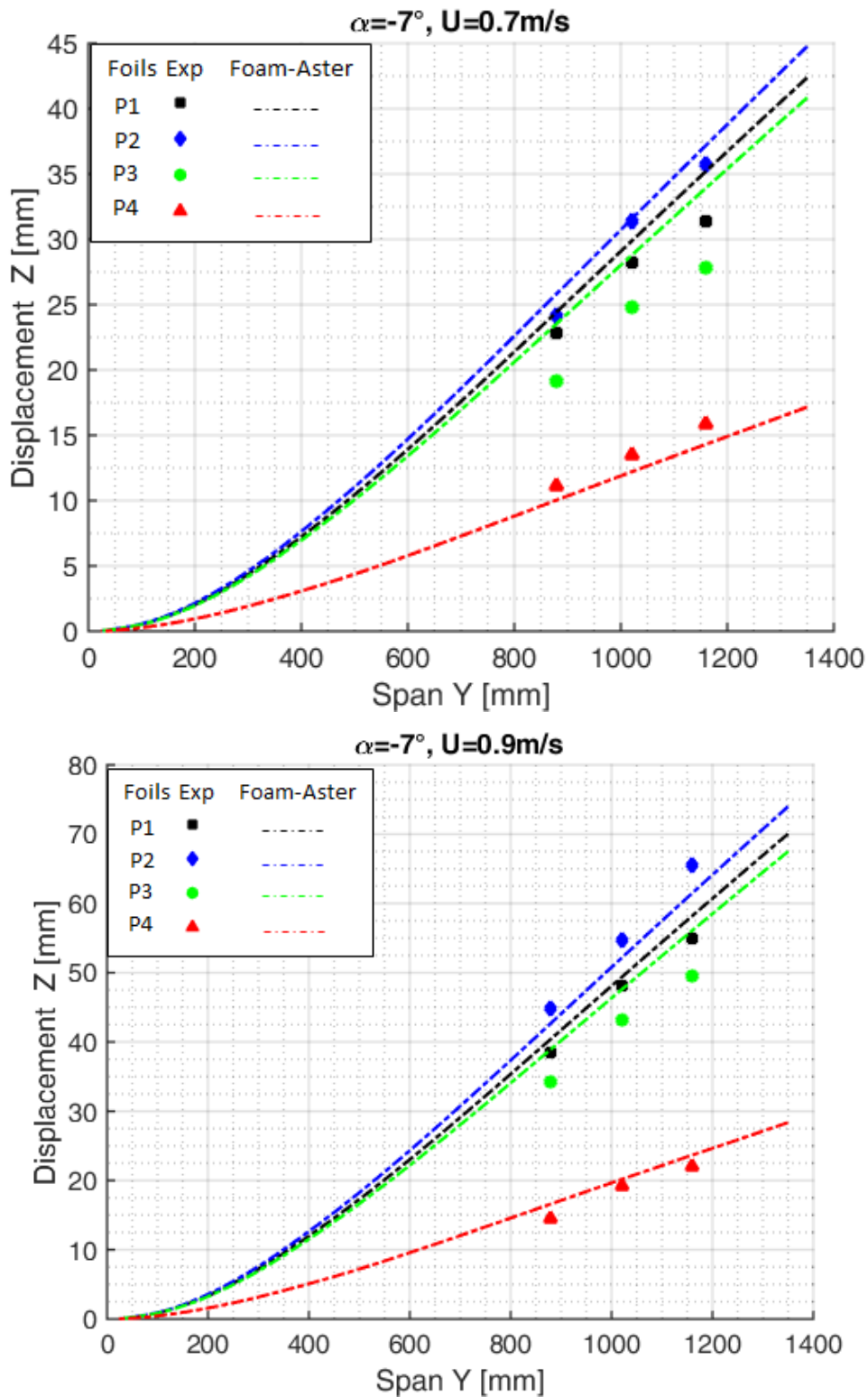
FIGURE 5.35 – Validation of Foam-Aster : Normal displacements of all the hydrofoils, $\alpha = -7°$, U = $0.7 m/s$ and U = $0.9 m/s$.
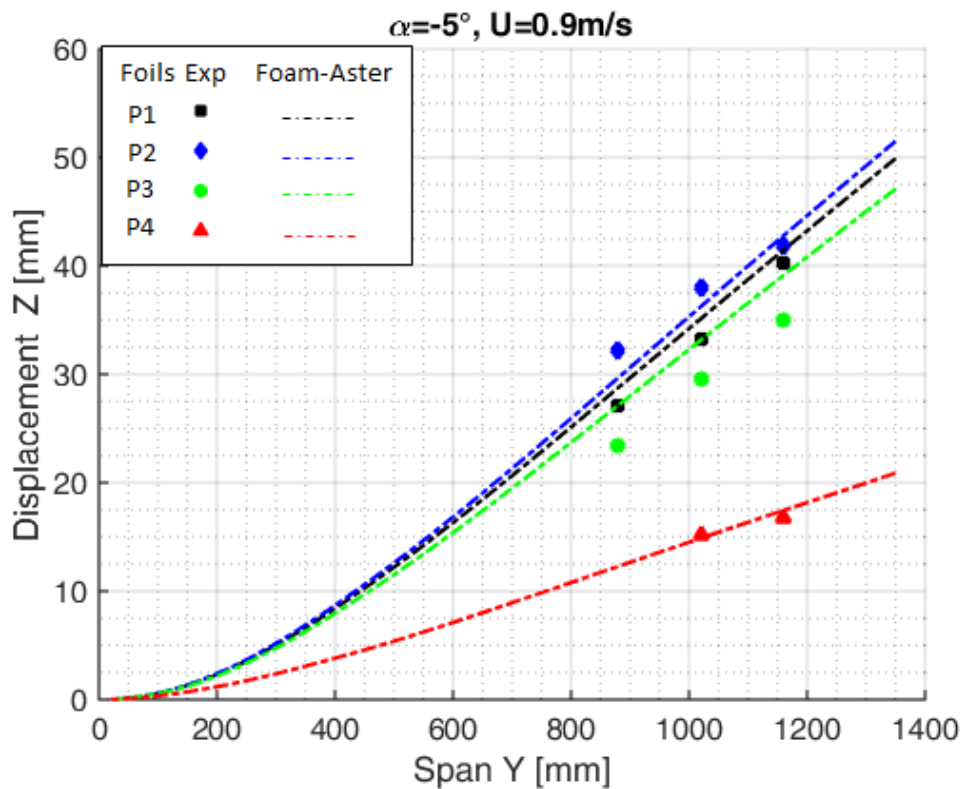
FIGURE 5.36 – Validation of Foam-Aster : Normal displacements of all the hydrofoils, $\alpha = -5°$ and $U = 0.9 m/s$.

5.4.4 Visualisation of the free surface deformation

This section shows 3D displays of the free surface from the simulations of Foam-Aster. We choose to present only the results of P_2, the observations are the same for all the layups.
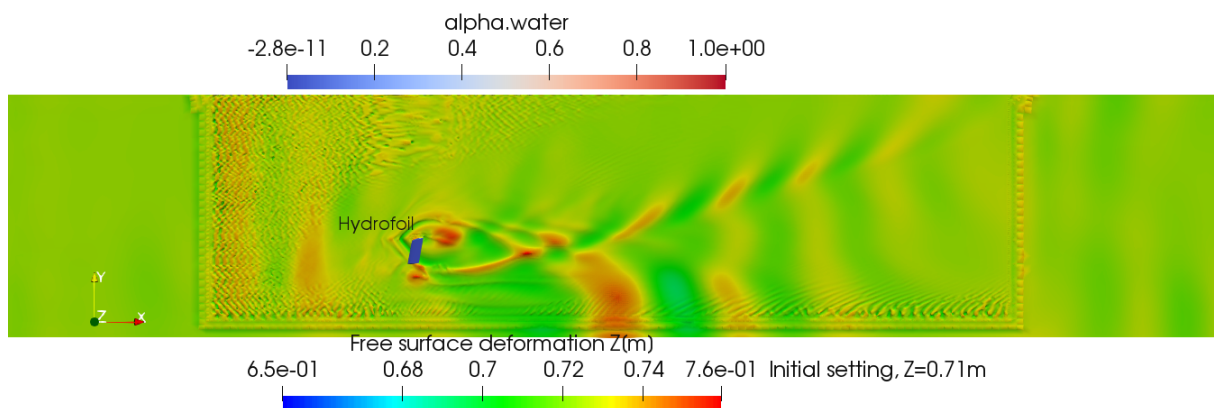
FIGURE 5.37 – Visualisation of the free surface deformation for the hydrofoil P2, $\alpha = 7°$ and U=0.9m/s.

Figure 5.37 shows the deformation of the free surface and the flow around the foil after the FSI simulation. Z is the vertical coordinate and alpha.water is the water fraction in the domain (1 for water and 0 for air). In the initial setting, the free surface coordinate was $Z = 0.71 m$.

The wake of the hydrofoil shows small waves and the flow around the hydrofoil does not

seem disturbed. The free surface height around the foil is between 0.7 and 0.72. The free
surface shape is far from the type of deformation observed in the case of swept hydrofoils
piercing the free surface. In those case the free surface deforms strongly with a creation of
a hole in its wake and depending with the flow condition ventilation can occurs.
Figure 5.38 shows other views of the free surface with the deformed hydrofoil and the
initial hydrofoil.
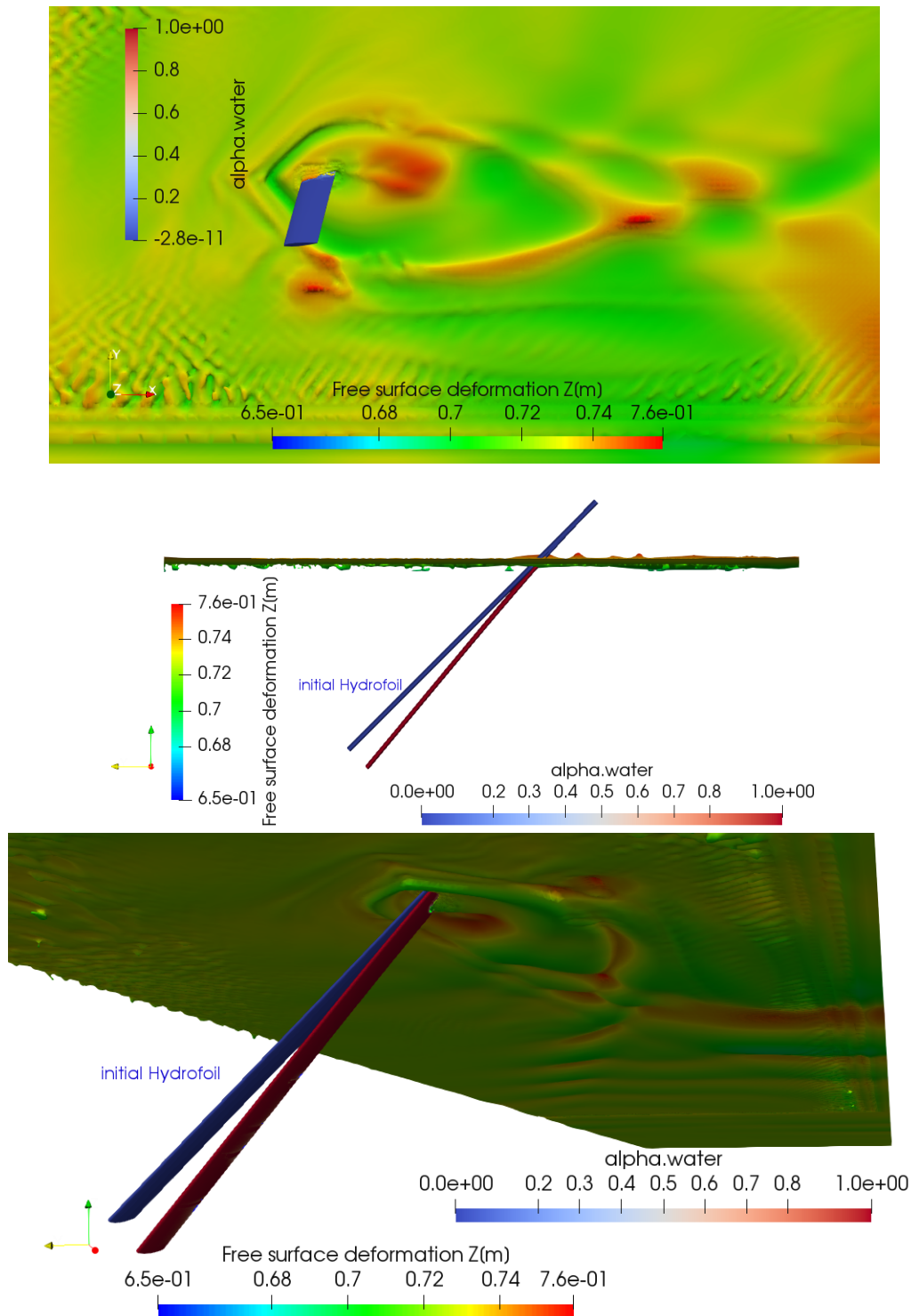
FIGURE 5.38 – Visualisation of the free surface deformation for the hydrofoil P2, including the
initial geometry $\alpha = 7°$ and U=0.9m/s.

5.4.5 Comparison of FS6R with Foam-Aster

This section compares the simulations of the high-fidelity coupling Foam-Aster to the simulations of the lower-fidelity tool FS6R.

5.4.6 Hydrodynamic forces

Figure 5.39 compares the results the three approaches on the lift force of the hydrofoils.
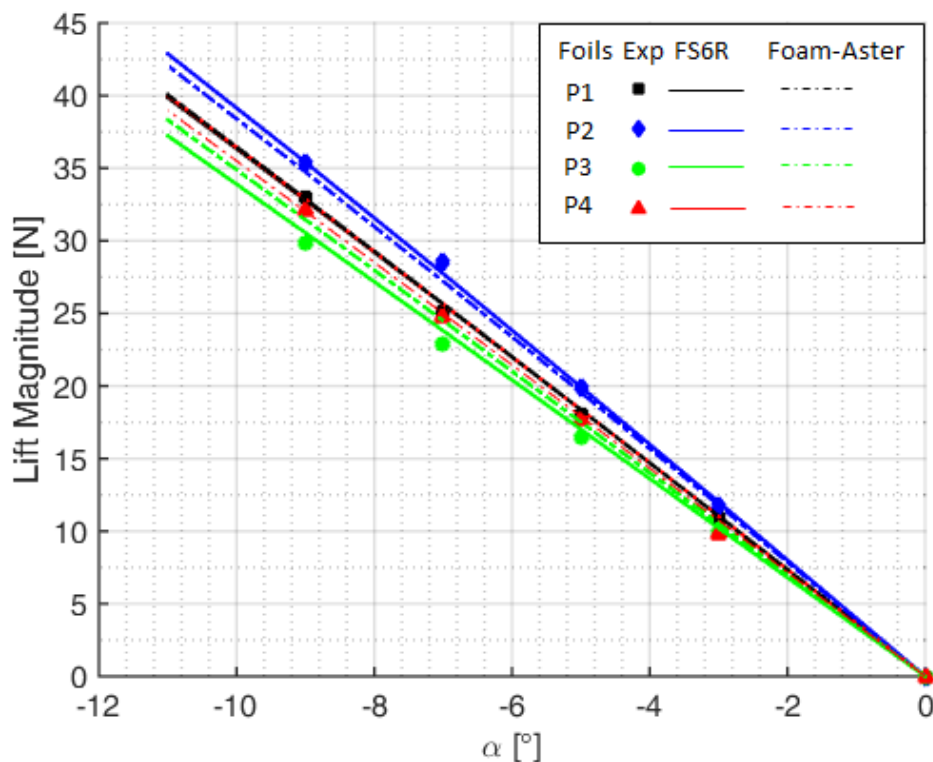
FIGURE 5.39 – FS6R vs Foam- Aster : Lift force on the four hydrofoils at flow speed U = $0.9m/s$.

The three approaches give the same trend in the results. FS6R results fits very well to the experiments when the results of Foam-Aster on the lift force are slightly lower than FS6R and the difference between both approaches less than 5% and 8% with P_3.

Figure 5.40 compares the drag force computed with FS6R to the drag force computed with Foam-Aster on the four hydrofoil. The results of the high fidelity code Foam-Aster computed as the x projection of the total pressure are 1.3 times higher than the results of FS6R.
A comparison of the drag computed from the hydrodynamic pressure (total pressure - hydro static pressure) with Foam-aster is compared to the drag of FS6R in figure 5.41. The curves overlap well for P_4 results and the both approaches gives a drag of the same amplitude for all the hydrofoils.
This observation shows that FS6R does not consider the hydro static pressure in its calculations and that component is not negligible on the drag force for the simulated cases.
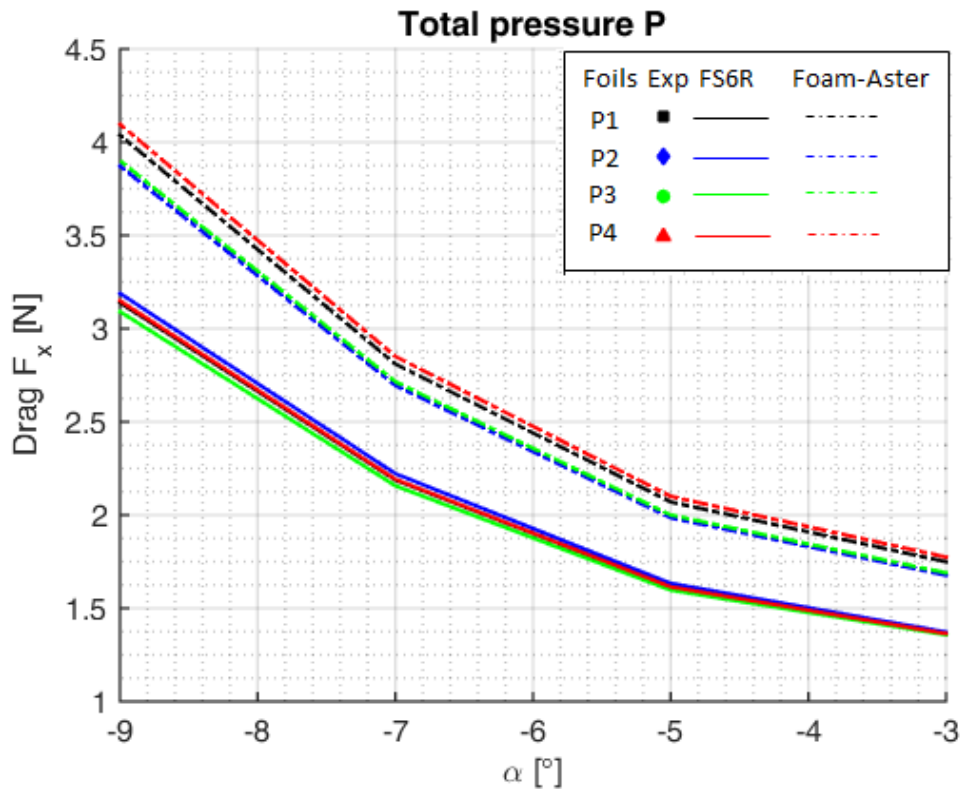
FIGURE 5.40 – Drag force computed from the total pressure of Foam-Aster VS FS6R, U $= 0.9 m/s$.
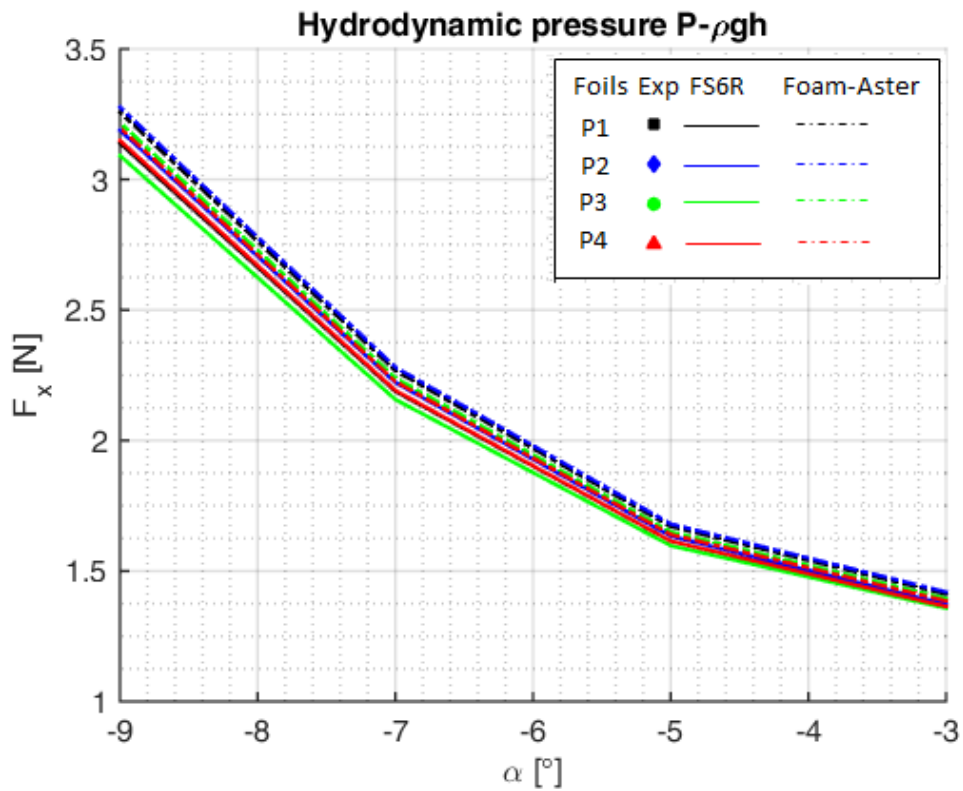
FIGURE 5.41 – Drag force computed from the hydro static pressure of Foam-Aster VS FS6R, U $= 0.9 m/s$.

5.4.7 Displacements

The displacements of the four hydrofoils from the three approaches are compared in figures 5.42 and 5.43.
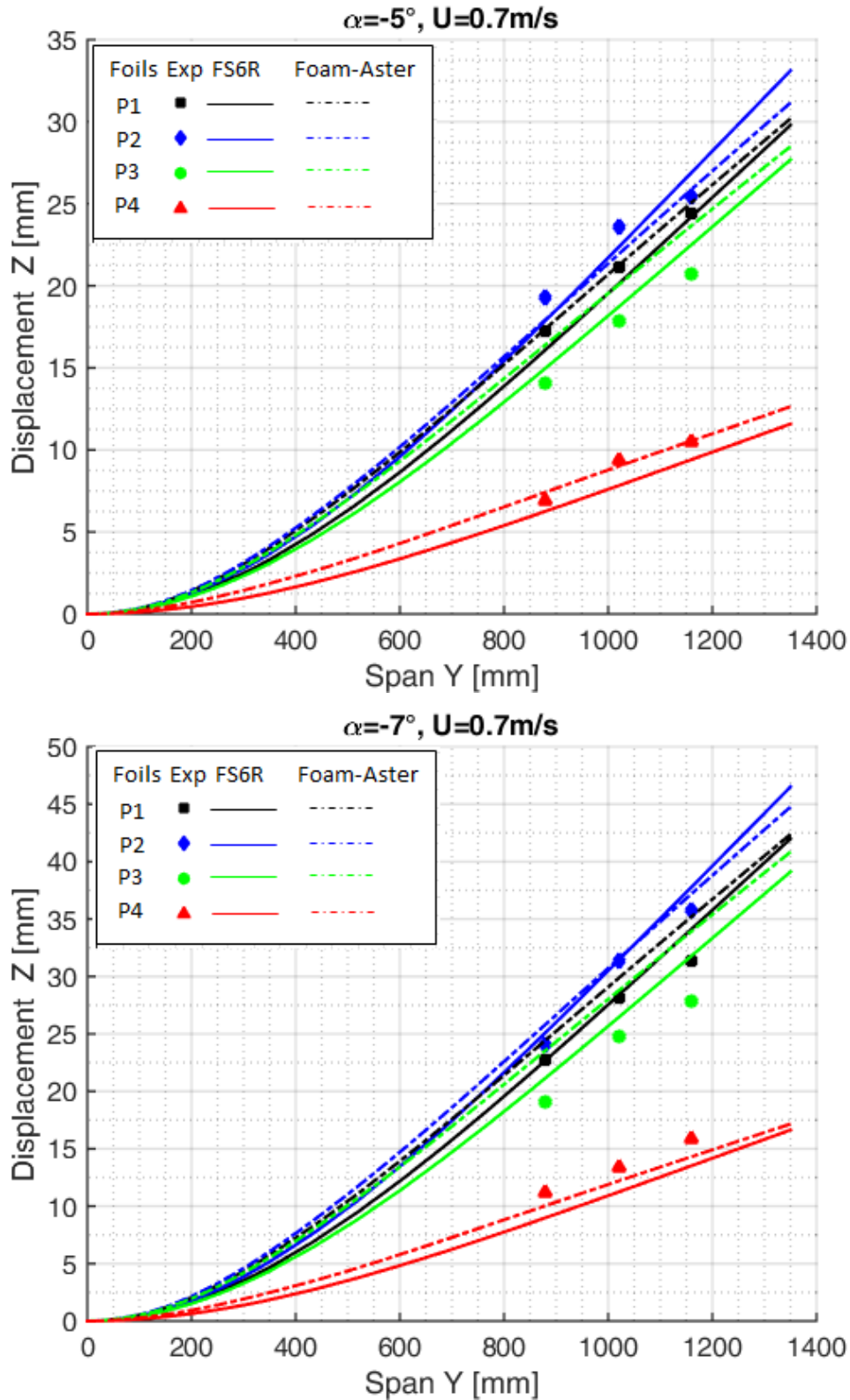
FIGURE 5.42 – FS6R vs Foam- Aster : Normal displacements of the four hydrofoils, U $= 0.9 m/s$ for $\alpha = 5°$ and $\alpha = 7°$.
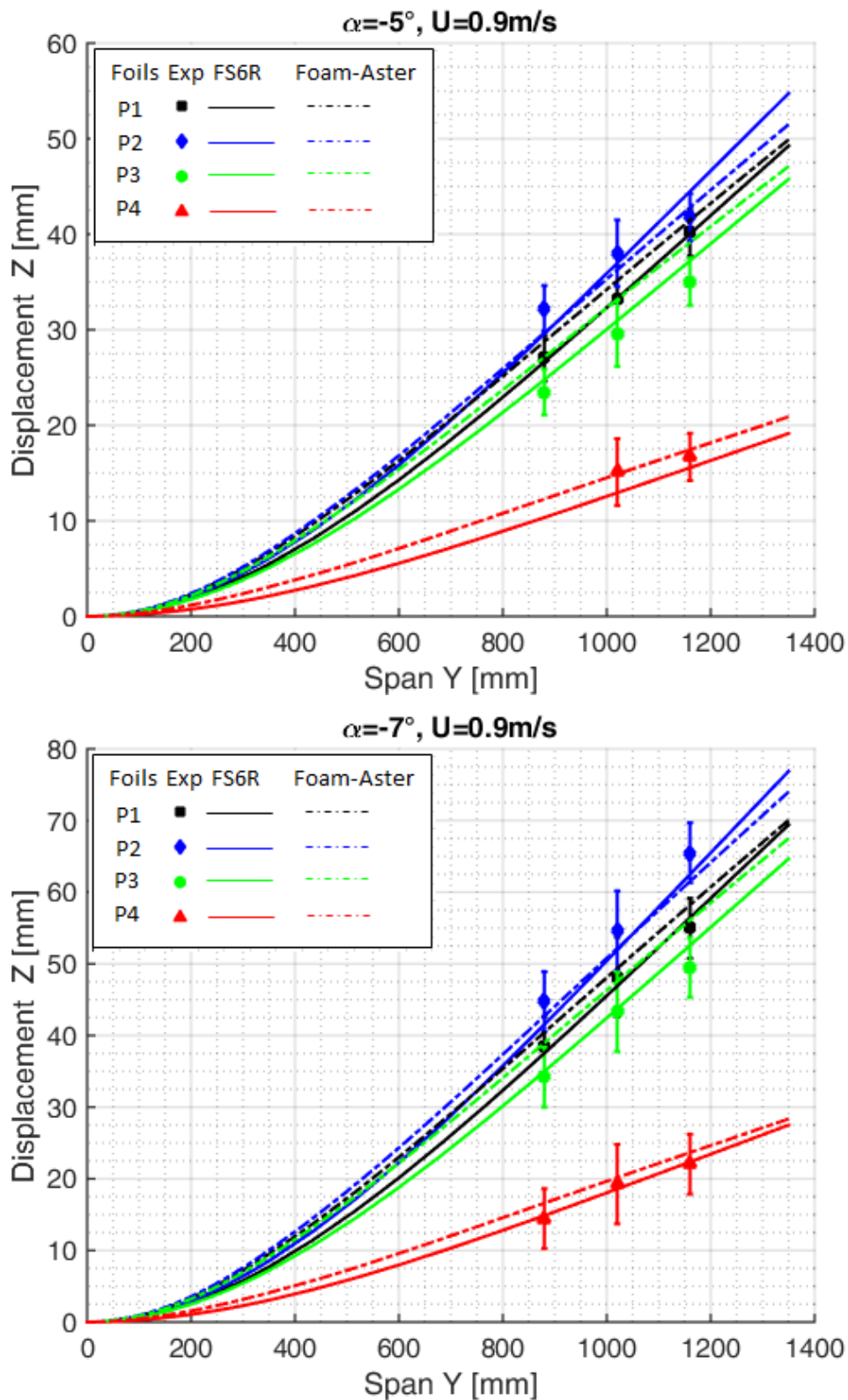
FIGURE 5.43 – FS6R vs Foam- Aster : Normal displacements of the four hydrofoils, $U = 0.9 m/s$ for $\alpha = 5°$ and $\alpha = 7°$.

The impact of the BTC on the response of the hydrofoil is observed with the two numeric approaches.

Foam-Aster results fit perfectly with the experiments for P_4 and a difference around 5% is observed with P_1. It simulates the bend-twist coupling for P_2 and P_3 but the twist angle is

underestimated and that underestimation is amplified with P_3. Thus the results computed by Foam-Aster are the less accurate for both P_2 and P_3.
The low fidelity tool FS6R performed better than the high-fidelity coupling Foam-Aster because the simulations of FS6R were computed using the measured mechanical properties of the hydrofoils obtained with the experiments when Foam-Aster simulations are based on the theoretical material properties.

Also, the high aspect ratio and the homogeneous sandwich section along the span, make fits the hypothesis of the beam theory and the potential theory.
Moreover, the surface deformation, visible experimentally where the foil is piercing the surface, is of second order due to the low AoA and flow speed. Comparison of the two numerical approaches may differ with a more complex composite structure and flow.
The difference between the both approaches are less than 10%.

5.5 Summary of the chapter

This chapter presented the numerical and experimental comparison of Foam-Aster simulations to the experiments on the results of the model scale POM hydrofoil and the composite real scale hydrofoils.
The first section discussed the POM hydrofoil and the simulations are performed with a convergence criteria of $\epsilon = 10^{-4}$. Foam-Aster computed very well the trend the results, the bending motion of the hydrofoil was well represented and the overall discrepancies were under 5%.
The comparison of Foam-Aster to the low-fidelity tool FS6R shows similar results. Foam-Aster results are slightly higher than FS6R results and Foam-Aster the most accurate between the two codes.
The second part of the chapter was dedicated to the real-scale composite hydrofoils. It started with the investigation of BTC on Code_Aster.
A static mechanical analysis is performed to simulate the bending of a composite plate made of glass fibers with the same orientation in all the plies. The results show the ability of Code_Aster to simulate the influence of the ply orientation on the twist motion of the structure. In agreement with the experimental observations, a negative angle in the layup induces a negative twist and a positive angle in the layup induces a positive twist. It was observed that the maximum bend-twist angle is obtained for ±30°.
According to the manufactured sections of the four hydrofoils, two structural modeling were proposed, one for P_1 and P_4 and the other one for P_2 and P_3. The comparison of Code_Aster simulations with the results of the bending tests performed on the hydrofoils shows that the models fit well for P_1 and P_4 and outlines other aspects for P_2 and P_3.
Due to the manufacturing process, the bending stiffness of P_3 is lower than its theoretical value, leading to an underestimation of the displacements of P_3 in the simulations of Code_Aster. The displacement of P_2 is well computed but the bend-twist angle computed for the both layup is zero. More over some simulations shows that for small loading, the bend-twist coupling behavior was sensitive to the loading type. The surface loading appears to give physical twist angle. These results outlines the need to improve the structural model and eventually the loading application on the structure. Investigations were not carried out deeply on those aspects but since the hydrodynamic loading is a surface loading, the simulations of the of the hydrodynamic experiments computes the BTC behavior.
The simulations give very good results for P_1 and P_4 for both the forces and the displace-

ments. The simulations of Foam-Aster on the drag force show that the component from the hydro static pressure is not negligible and therefore FS6R 's drag fits Foam-Aster results computed with the hydrodynamic pressure.

A difference in good agreement with the BTC behavior was observed between P_2 and P_3 results : P_2 twists negative and P_3 twist positive. The discrepancies is less than 5% for P_1 and P_4, less than 10% for P_2 and goes up to 18% for P3 mainly due to the underestimation of its bending and torsional stiffness when using the theoretical values.

A comparison of Foam-Aster to FS6R show Foam-Aster as the most accurate when looking at P_1 and P_4 but FS6R results on P_2 and P_3 fit better the experiments. This good accuracy of FS6R when using the measured characteristics of the materials highlights the importance to characterize the mechanical properties of the composite structures.

Conclusions and perspectives

> « *I don't like work, no man does.*
> *But I like what is in the work,the*
> *chance to find yourself.*
> *Your own reality, for yourself not*
> *for others.*
> *what no other man can ever know.*
> *They can only see the mere show,*
> *and never can tell what it really*
> *means.* »
>
> Joseph Conrad, Heart of
> Darkness-1899

Summary of this research work

The research work presented in this thesis was carried out in a partnership between the Research Institute of the Ecole Navale IRENAV, the foil resource center SEAIR, the IRDL laboratory and IFREMER of Brest. The aim of the study was to create for SEAIR, numerical tools to study FSI on flexibles composite hydrofoils.
The study focused on :

— The understanding of coupling phenomena between a deformable hydrofoil and a flow with a dense fluid (water) through hydrodynamic experiments.

— The mechanical characterization of structures and the understanding of the structural bending-twisting coupling appearing in hydrofoils made of composite materials.

— The implementation and validation of two numerical methods with two levels of fidelity. They both allow to adequately predict the hydro-elastic response of a flexible hydrofoil, made of isotropic or composite material with bending-twisting coupling, in a flow with fluid-structure interactions.

Two study cases are selected :

— A trapezoidal hydrofoil of 150mm span, 100mm chord at root and 30mm chord at tip ; made of Polyoxymethylene and profile section NACA0015. The foil is tested in the IRENAV cavitation tunnel for angles of attack between -10° and 10° and five Reynolds numbers between 3×10^5 and 7×10^5. An embedding disk at the root of the foil does not allow the measurement of hydrodynamic forces and the deformations of the structure are measured with a laser telemeter.

— Four plan-form hydrofoils with 1.35m span, 114mm constant chord and a NACA0015 section are made of glass and carbon fibers. The hydrofoils all have the same hydrodynamic shape but differ in their composite layups in order to study the bending-twisting coupling.

P_1 is made up of glass fibers with bi-axial plies oriented at $\pm45°$ and a unidirectional ply at $0°$. P_2 is also made up of glass fibers, it only contains unidirectional plies and the orientations are $90°$, $-45°$ and $0°$. P_3 layup is the same as P_2 and only differ with $+45°$. P_4 is made up of carbon fibers with $90°$ and $0°$ orientations.

The structures are mechanically characterized in air through bending, tensile and vibration tests. A laser telemeter allows to measure the deformations of the structures due to imposed loading. The hydro-elastic behaviour of the hydrofoils in a flow with fluid-structure interactions is studied in the IFREMER Lorient's flume. The hydrofoils are piercing the free surface and the tests are carried out with profile incidences from -10° to -13° and two Reynolds numbers : 7×10^4 and 10^5. A hydrodynamic balance fixed to the hydrofoils allows the measurement of hydrodynamic forces and a laser telemeter measures the deformations of the hydrofoils.

Two numerical coupling tools with two different level of fidelity are implemented on the basis of an iterative partitioned approach. These tools use either open source codes or codes developed within the framework of this study :

— FS6R the low-fidelity coupling is dedicated to pre-design projects uses the open source tools AVL and XFoil for the fluid part and an internal code based on beam theory by the finite element, for the structural part. A modification of the stiffness matrix used in the classical beam theory is implemented by new coupling terms in the stiffness element matrix to consider the BTC behavior.

— FOAM-Aster the high-fidelity coupling is a coupling between the open source code OpenFoam for the fluid part and Code_Aster for the structural part.

A summary of the two codes given the different inputs parameters and outputs is presented in figure 5.44. The limitations and validity of the codes is also presented.

The validation of the numerical tools is performed in two stages on the hydrofoils :

— Flexible hydrofoil made of isotropic POM material in a mono fluid flow (water).

— Flexible hydrofoil made of composite materials, piercing the free surface in a two fluid flow (water and air).

	FS6R
Fluid code	AVL+Xfoil
Structural code	In-house beam model with BTC implemented
Inputs	• Geometry: coordinates X,Y,Z of the hydrofoil's leading edge • Flow conditions: incidence α[°], velocity , fluid viscosity • Equivalent properties of the material : Young modulus, shear modulus, inertia • Coupling parameter α [%] if BTC • Mesh parameters • convergence criteria ε
Outputs	• Hydrodynamic forces and coeficients (X,Y,Z) • Displacements of the structure (normal to span Z and chordwise X) • 3D visualisation of the deformed shape
Validity	• OK for both isotropic and composite materials (if equivalent properties of the composite are given as input) • Can compute BTC if the coupling parameter of the material α [%] is given • Gives good results on simple extruded geometries such as stabilizers • Ok for geometries with moderate aspect ratio (>3) in agreement with VLM limitations
Limitations	• Swept geometries: AVL allows swept geometries but the beam code needs to be tested, validated and eventually modify • many geometries: No, not able to simulated the influence between many hydrodoils

	Foam-Aster
Fluid code	OpenFoam
Structural code	Code_Aster
Inputs	• 3D geometry of the structure: stl and bref formats • Flow conditions: incidence , fluid viscosity , turbulence model, initial conditions of the flow (velocity, pressure, turbulence fields,...) • Type of simulation: one phase-flow, multiphaseflow, phase change, ... • Mesh parameters for the fluid domain • Material properties: Young modulus, shear modulus, definition of the composite ply, Poison coefficient • Structural Mesh defined on the initial geometry • convergence criteria ε of the FSI loop
Outputs	• Hydrodynamic forces/Coefficients (X,Y,Z) • Evolution of the different flow fields (Pressure, Velocity, ...) • Displacements field of the structure (X,Y,Z) • Stress, strains fields • 3D visualisation of the entire domain fluid and structure
Validity	• OK for both isotropic and composite materials • Can compute BTC • No limitations in term of geometries and numbers (ok for many hydrofoils) • Viscous, turbulent flow
Limitations	• The model needs improvements for sandwich sections • Quasi-static simulations

FIGURE 5.44 – Summary of two coupling tools FS6R and Foam-Aster presenting the inputs, outputs as well as the limits and validity of the codes.

Summary of the results

The study of the flexible POM hydrofoil in the cavitation tunnel of IRENAV shows a bending behavior as the hydro-elastic response of the hydrofoil. No twist motion was obser-

ved, only a bending motion. The hydrofoil bends upward in agreement with the positive incidences and the bending increases with the velocity, in agreement with the lift increase. Numerical simulations with the two coupling tools are performed to verify a good convergence of the results in hydrodynamic forces and displacements through the investigation of the influence of the mesh. They were firstly validated on the basis of the displacements of the POM hydrofoil under the effect of the hydrodynamic loading, measured during the experiments.

The lift force on the POM hydrofoil computed with FS6R is compared to the simulation of Foam-Aster. The simulations are performed for all the velocities investigated and the trend of both numerical approaches are the same with Foam-Aster slightly higher than FS6R. A comparison of the lift coefficient simulated with FSI and without FSI shows that the bending motion does not modify the amplitude of the lift force but its distribution along the span is modified.

The both approaches describe with a good accuracy the trend of the hydro-elastic response of the POM hydrofoil under hydrodynamic loading . Both cases simulate a bending motion in agreement with the experiments for all the incidences. FS6R displacements is slightly lower than the experiments (relative discrepancies are less than 7%) and Foam-Aster is slightly higher (relative discrepancies are less than 4%). Globally, Foam-Aster fit the experiments better than FS6R and the difference between the both approaches is in an average of 10%.

The study of the composite hydrofoils started with their mechanical characterization to determine the bending stiffness EI and the torsional stiffness GJ. The determination of the bending stiffness compares bending, vibration and tensile tests to the laminate theory and shows that the laminate theory had the same order of amplitude with the experiments and is able to compute the results with a precision of 4% (experiments are the reference). As expected, the hydrofoil P_4 in carbon is the stiffer than the other hydrofoils in glass. It was determined that P_1 and P_2 had barely the same bending stiffness and P_3 is 4.4% smaller. The torsional modulus was different for the 4 hydrofoils in agreement with the theory : P_4 with only 0° and 90° in its layup has the lowest torsional stiffness when P_1 with its biaxial plies at $\pm 45°$ has the higher torsional stiffness. The differences between P_2 and P_3 in bending and torsional stiffness is likely due to the manufacturing process.

The bend-twist coupling (BTC) investigations on the hydrofoils shows that when P_1 and P_4 with their balanced layup don't experience a twist angle induced by a bending loading, the bend twist coupling phenomenon is highlighted with a significant amplitude for P_2 and P_3 layups : P_2 with a negative orientation in its layup experiences a negative twist and P_3 with a positive orientation in its layup is influenced with a positive twist angle.

FS6R takes as input the experimental bending and torsional stiffness and computes of the hydrofoils the results of the static experiment with a good accuracy. Code_Aster takes as input the properties of each ply of the layup and its simulations are less accurate than FS6R. The trend of the bending motion is well simulated when the bend-twist angle give results does not fit the experiments. It was determine that the accuracy of Code_Aster in the prediction of the BTC depends on the loading type. For the same applied force the surface loading gives better results that a punctual loading. A more complete analysis on the appearance of the BTC through simulations with Code_Aster showed that the optimal orientation in the composite layup to maximise the BTC effect is between 25-30°

The investigation of FSI on the composite hydrofoils in hydrodynamic experiments shows results in good agreement with the BTC observations in static tests. The angle of incidences investigated being negative, P_2 with its negative bend-twist angle becomes the most loaded and P_3 with its positive bend-twist angle becomes the less loaded. In agree-

ment with the bending stiffness of the hydrofoils, For all the configurations, the displacements of P_4 are the smallest when P_2 has the highest displacement. The difference between P_2 and P_3 is clearly observable.

The analysis of the forces also shows that when the BTC modifies the angle of attack of the hydrofoils and therefore the amplitude of the forces, the bending motion keeps the amplitude of the lift constant and only modifies its projection on the axis and therefore the bending motion will modify the equilibrium of a foiling boat. A 3D visualisation of the flow from the simulations of Foam-Aster shows the the free surface deformation was negligible and there was no ventilation phenomenon fro the configuration investigated.

The results of the forces and the displacements simulated with FS6R fit perfectly the experiments. FS6R computes very well the behavior of the composite hydrofoils experiencing FSI with BTC with a precision of 90%.

The high fidelity coupling FOAM-Aster computes perfectly the resulst of P1 and P4 that do not experience BTC. The trend of P_2 and P_3 results is relatively well predicted with 8% discrepancies on P_2 and up to 18% discrepancies on P_3. This higher difference on the simulations and experiments of Foam-Aster and experiments on P_3 is likely due to P_3 manufacturing. Static experiments shows that the bending stiffness of P_3 was lower than P_2 which is close to the theoretical value. Code_aster using theoretical thus compute the results of P_3 with the highest discrepancies.

In a global comparison, the high fidelity tool FOAM-Aster and the low-fidelity tool FS6R predict with a very good accuracy the hydro-elastic behavior of isotropic and composite hydrofoil in FSI. When the BTC is not involved FOAM-Aster is more accurate than FS6R but when the structures experience BTC behavior, FS6R appears to be more accurate the the high fidelity tool FOAM-Aster. This conclusion is only true in this validation case because FS6R takes as input the mechanical properties of the structures determined experimentally when FOAM-Aster uses theoretical value. The global difference between the both approaches are less than 10% but one should expect more discrepancies from FS6R when it comes to simulate more complex geometries (swept hydrofoil, well developed free surface effects, ...) and complex composite layup.

Perspectives

The tools have been validated for simple extruded geometries with isotropic and composite materials. From the different tests performed, we can define the limits of our different tools and the perspectives for future work.

FS6R

FS6R is a quick tool that demonstrates good ability to estimate the hydro-elastic response of a composite or isotropic and deformable hydrofoil experiencing FSI. To meet the industrial need, future work on FS6R will first focus on the validation of the tool on swept geometries and investigations on free surface effect. Three main limitations of the code have been identified :

— The calculation of the torsional modulus of composite materials : the structural code does not allow to compute the torsional modulus GJ in the case of composite material. Analytical methods are available in the literature ([62]) but their implementation and validation was out of the scope of this work.

— The determination of the bend-twist coupling percentage : the bend-twist coupling percentage is a key parameter for the method implemented in FS6R to predict the BTC. For glass and carbon fibers, the values we used were extracted from [31]. Simulation or experimental campaign on composite material must be carried out to determine an analytic expression or a well defined database for this parameter.

For the moment, FS6R is ready for the design of simple structure such as plan form hydrofoils used as rear stabilizers on SEAIR 's boats.

Foam-Aster

The high fidelity coupling Foam-Aster shows good results for the simulated cases. Being based on OpenFoam and Code_Aster both able to analyze complex fluid flow and complex geometries and materials, the coupling does not have limitations based on those criteria.
The main limitation encounter in a simulation is the high CPU time. A way to reduce the CPU time is the implementation of a relaxation factor. An attempt made in this research work gave hazardous results thus, there is a need to investigate deeply the relaxation to accelerate the convergence. Another way to reduce the computation time of Foam-Aster should be the use of FS6R results as input in the high fidelity tool. FS6R having shown a good ability to predict the hydrofoil behavior, Foam-Aster should reach the convergence faster.
Future development on Code_Aster should address two points :

— The improvement of the structural model to analyze composite sandwich structures. This may improve the prediction of the BTC behavior.

— The implementation of a structural model with a pres-tress. The aim is to have the same geometry input in the both OpenFoam and Code_Aster. The actual tool uses the non-deformed geometry as input of Code_Aster in all the iteration and the transportation of the forces from the fluid mesh to the structural mesh reduce the accuracy of the coupling.

The perspectives of this work must also consider the evolution of the industrial needs and their project constraints. Today, SEAIR is less and less interested in flexible hydrofoils and is oriented on the design of rigid hydrofoils. Having an internal tools for the structural design of composite hydrofoils, the company is therefore more oriented towards the development of the fluid calculation tools. In the current design phases, I use OpenFoam on the basis of the calculation cases implemented within the framework of this research work to carry out all the CFD studies on the appendages and the boat+appendages assembly. One of the perspectives of FS6R is the implementation of the fluid part AVL+Xfoil in the current VPP (Velocity Program Prediction) of the company.

APPENDIX A

Properties of ABS kevlar and carbon fibers and POM materials

ARAMID FIBERS / ABS COMPOSITE

REINFORCED ARAMID FIBERS ABS FOR 3D PRINTERS

APPLICATIONS

The aramid fibers / ABS composite is a specially designed blend based on Acrylonitrile Butadiene Styrene (ABS) and aramid fibers for 3D printers. The aramid fiber size distribution has been specifically selected in order fit to the standard 3D printer nozzles. The combination of a precise dosage of aramid fibers and selecting their size provide excellent features of ABS parts printed without nozzle clotting. The abrasive phenomenon is less important compared to the corresponding carbon fibers composites. Printing settings are compatible with most 3D printers equipped with heating plate.

Advantages: Light printed parts. Low warping during printing. Increased resistance to friction and shocks. The printed parts are less brittle than carbon ABS parts. Weakly flammable fibers (T°C of degradation > 500 ° C). The aramid fibers are UV and moisture sensitive.

PROPERTIES

3D PRINTING

Extrusion Temp.	250 - 270	°C
Plate Temp.	90 - 110	°C
Nozzle	0.5 (>0.4)	mm
Printing Speed	50 - 70	mm/s
Diameter	1.75 or 2.85	mm +/- 50µm
Linear Weigth (g/m)	2.50 @ Ø 1.75	6.50 @ Ø 2.85

MECHANICAL

Density	1.08	g/cm3 (ISO 1183)
Tensile Modulus	2400	MPa (ISO 527)
Flexural Modulus	2300	MPa (ISO 178)
Elong. @ Break	7.5	% (ISO 527)

THERMAL

Tg	101	°C
DTUL	90	°C
Flammability	HB	UL 94 @ 1.6mm

FILLER

Mean Length	215	µm
Mono fiber diameter	10 +/- 2	µm
Fibers > 100 µm	70	%
Fibers Population	5.0 x E6	Unit / g of filament

Color: pale yellow (native) or black.

HEALTH & SAFETY

Aramid fibers are not hazardous for health. However, as short fibers and dust, in case of peeling or sanding, aramid fiber may cause skin, eyes and respiratory tract irritation. Moreover, the low size of fibers can cause sometimes allergies. Users must wear individual protection equipment (mask, gloves…) in case of sanding or milling the printed pieces. Consult MSDS for more data. ABS can lead to COV production during the printing process (styrene derivatives). Ensure a working area equipped with air extraction or suitable protection. Always refers to MSDS prior handling.

PACKAGING
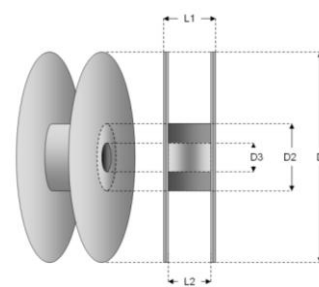
Spool	L1	L2	D1	D2	D3
500 g	55	45	200	105	52
750 g	55	45	200	105	52
1.0 kg	67	59	200	105	52
2.5 kg	100	90	300	210	52

Spools packed in individual boxes, under vacuum with desiccant. Product supplied with batch number and material traceability. Other spools are available on request (up to 25 kg).

CONTACT

NANOVIA
Smart Chemicals for Advanced Materials
ZA Saint-Paul F-22540 LOUARGAT – France
Tel: +33(0) 296 433 690 / contact@nanovia.pro
www.nanovia-technologies.com

CARBON FIBERS / ABS COMPOSITE

REINFORCED CARBON FIBERS ABS FOR 3D PRINTERS

APPLICATIONS

CF ABS is a specially designed compound of Acrylonitrile Butadiene Styrene (ABS) and carbon fibers for 3D printers. The carbon fiber size distribution was specifically selected in order to fit the standard 3 D printer nozzles. The combination of an accurate dosage of carbon fibers and their size management gave to the NANOVIA CF ABS material excellent printing characteristics without nozzle clotting and, at the same time, limiting the abrasive impact of the printing equipment. The optimized blend leads to a less brittle filament compared to the standard carbon reinforced thermoplastics usually available onto the market. With an improved tensile modulus of +35% compared to standard ABS, the printing parameters are compatible with the majority of 3D printers equipped with heating plates.

PROPERTIES

3D PRINTING

Extrusion Temp.	250 - 270	°C
Plate Temp.	90 - 110	°C
Nozzle	0.5 (>0.4)	mm
Printing Speed	70	mm/s
Diameter	1.75 or 2.85	mm +/- 50µm
Linear Weigth (g/m)	2.51 @ Ø 1.75	6.70 @ Ø 2.85

MECHANICAL

Density	1.08	g/cm3 (ISO 1183)
Tensile Modulus	2700	MPa (ISO 527)
Flexural Modulus	2700	MPa (ISO 178)
Elong. @ Break	10	% (ISO 527)
Charpy	5.18	kJ/m^2

THERMAL

Tg	101	°C
DTUL	90	°C
Flammability	HB	UL 94 @ 1.6mm

ELECTRICAL

Surface Resistivty	1.E+06	Ω.m
Resistivity	1.E+02	Ω.cm

FILLER

Mean Length	251	µm
Mono fiber diameter	7 +/- 2	µm
Fibers > 100 µm	70	%
Fibers Population	4.37 x E6	Unit / g of filament

PACKAGING

Spool	L1	L2	D1	D2	D3
500 g	55	45	200	105	52
750 g	55	45	200	105	52
1.0 kg	67	59	200	105	52
2.5 kg	100	90	300	210	52

Spools packed in individual boxes, under vacuum with desiccant. Product supplied with batch number and material traceability. Other spools are available on request (up to 25 kg).

CONTACT

NANOVIA

Smart Chemicals for Advanced Materials

ZA Saint-Paul F-22540 LOUARGAT – France
Tel: +33(0) 296 433 690 / contact@nanovia.pro
www.nanovia-technologies.com

Polyacétal (POM)

Le polyacétal ou polyoxyméthylène commercialement nommé DELRIN® (homopolymère) ou HOSTAFORM® (copolymère) est très utilisé dans les pièces techniques car il possède de très bonnes propriétés mécaniques, élasticité, résistance à la fatigue dynamique et à l'usure, Faible coefficient de frottement, bonne stabilité dimensionnelle, bon comportement à la chaleur
et au froid ainsi qu'à bon nombre de produits chimiques tels que les huiles, solvants usuels, graisses et produits pétroliers.

Propriétés	Méthode d'essai	Unités	Delrin	Hostaform
Densité	DIN 53 479	g/cm2	1.41	1.41
Absorption d'eau	ASTM D 570	%	0.16	0.22
Allongement à la rupture	DIN 53 455	%	25	25
Module d'élasticité	DIN 53 457	N/mm2	3200	2900
Résistance à la traction	DIN 53 455	N/mm2	70	65
Résistance aux chocs	DIN 53 453	KJ/m2	8	8
Dureté Rockwell	ASTM D 785	--	120	120
Usure par abrasion P=0.05N/mm2 V=0.6m/s	--	µm/km	4.6	8.9
Température de fusion	DIN 53 786	°c	175	165
Température d'utilisation en continu	DIN 52 612	°c	-50 +80°c	-50 +90°c
Conductibilité thermique	DIN 52 612	W/°c.m	0.23	0.31
Coefficient de dilatation thermique linéaire	DIN 52 326	10-5mm/°c	9	11

UTILISATIONS

Pièces de frottement:
Coussinets, paliers, bielles, fermetures à glissière...
Pièces techniques:
Engrenages, ressorts, corps de vannes, pompes, éléments pour commandes pneumatiques isolants, pignons, clips et pièces à emboîtement..

APPENDIX B

Illustration of the layup of the composite hydrofoils
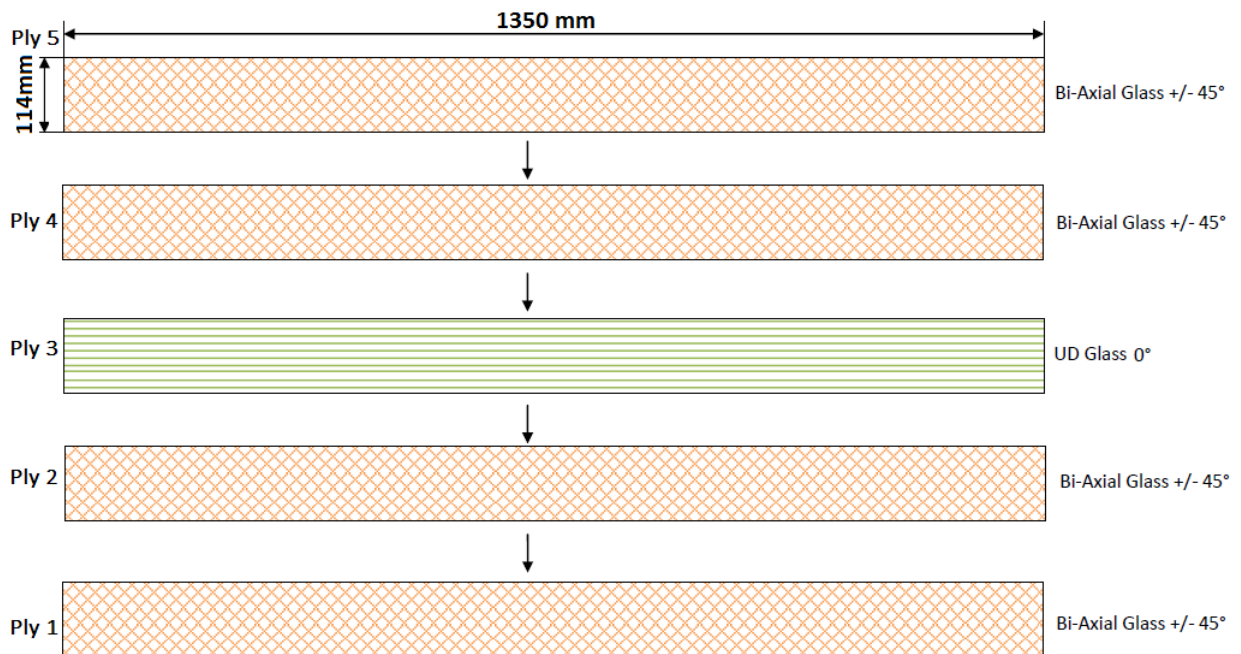
FIGURE B.1 – Orientation of the lies in the layup P_1 .
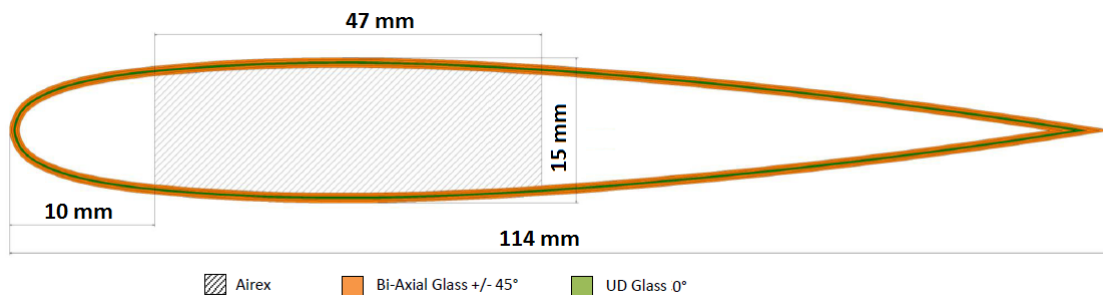
FIGURE B.2 – Web location in the sandwich structure and layup illustration of P_1 in the thickness of the laminate skin.
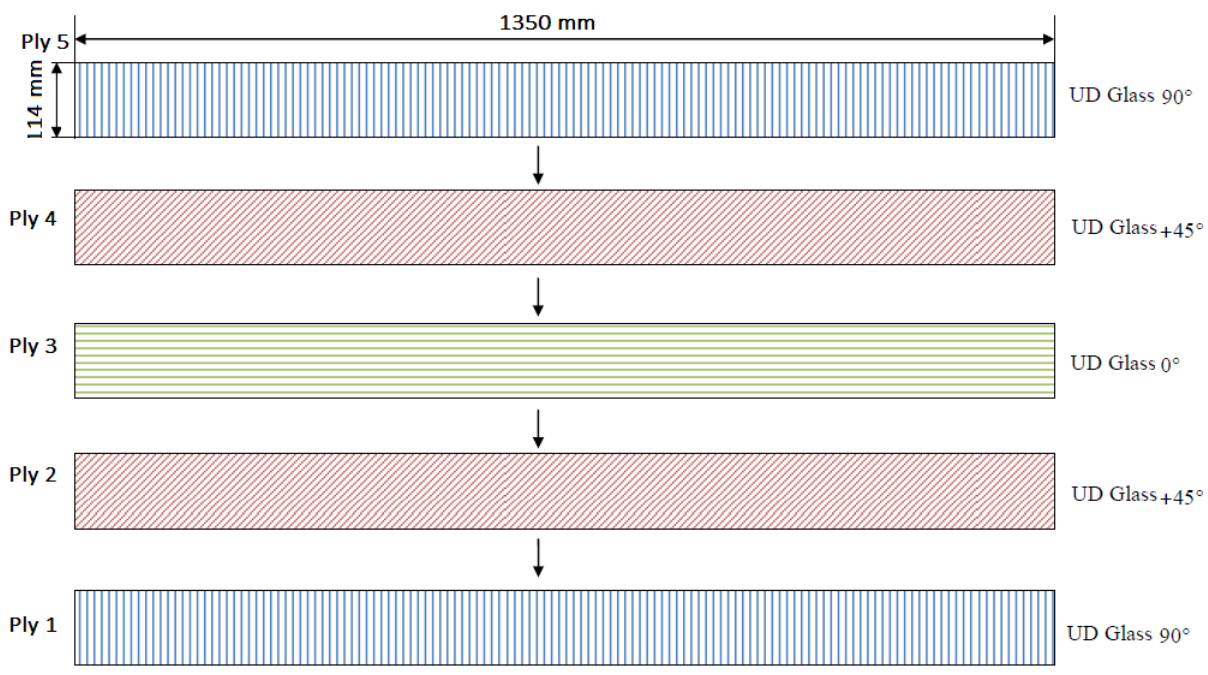
FIGURE B.3 – Orientation of the lies in the layup P_2 .
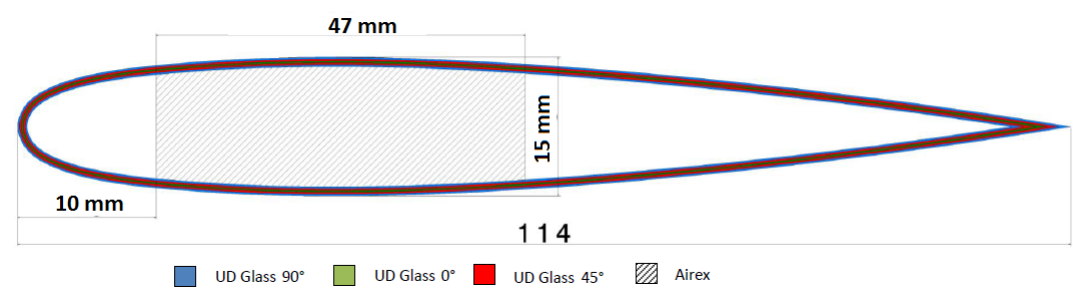
FIGURE B.4 – Web location in the sandwich structure and layup illustration of P_2 in the thickness of the laminate skin.
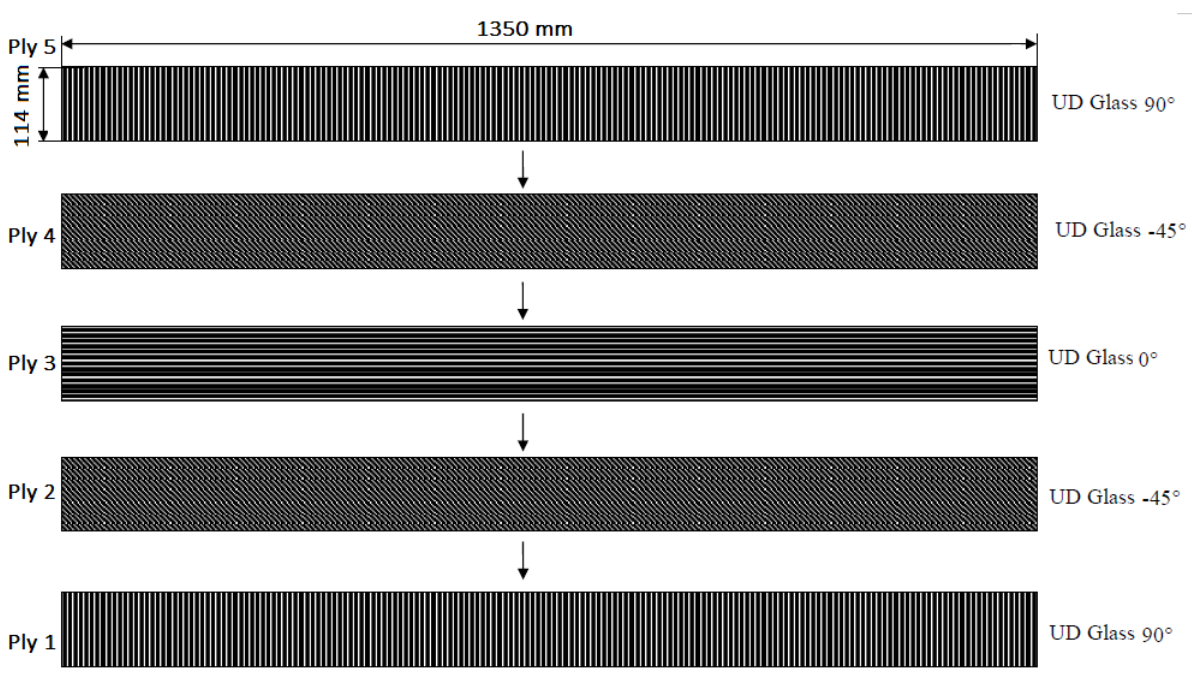
FIGURE B.5 – Orientation of the lies in the layup P_3 .
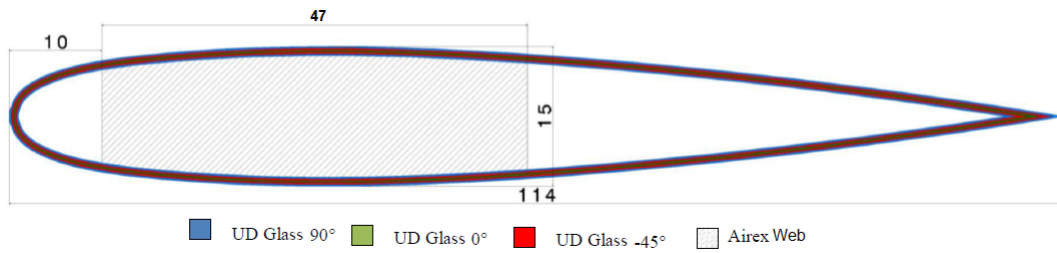
FIGURE B.6 – Web location in the sandwich structure and layup illustration of P_3 in the thickness of the laminate skin.
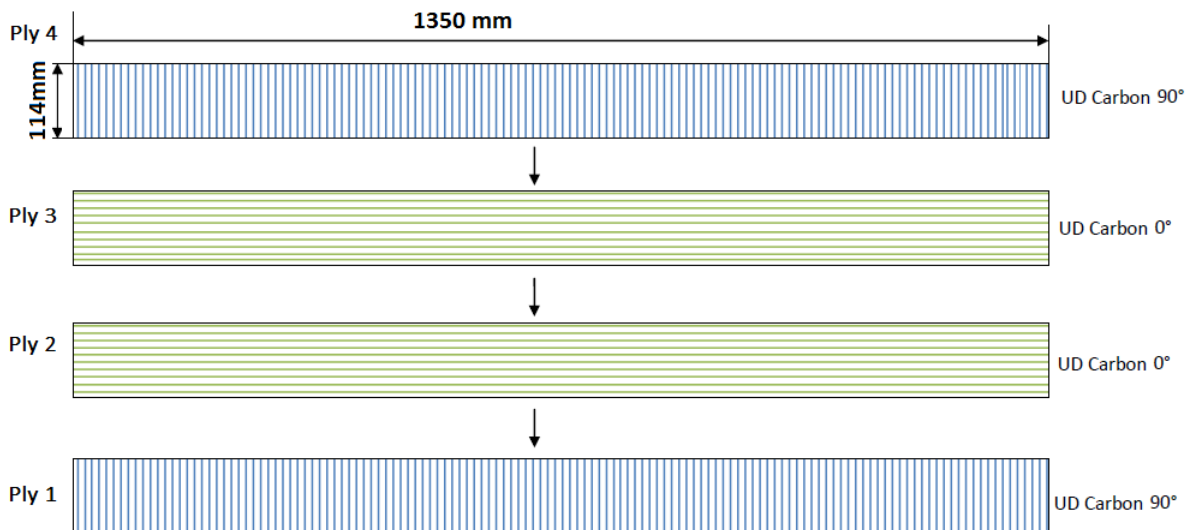
FIGURE B.7 – Orientation of the lies in the layup P_4.
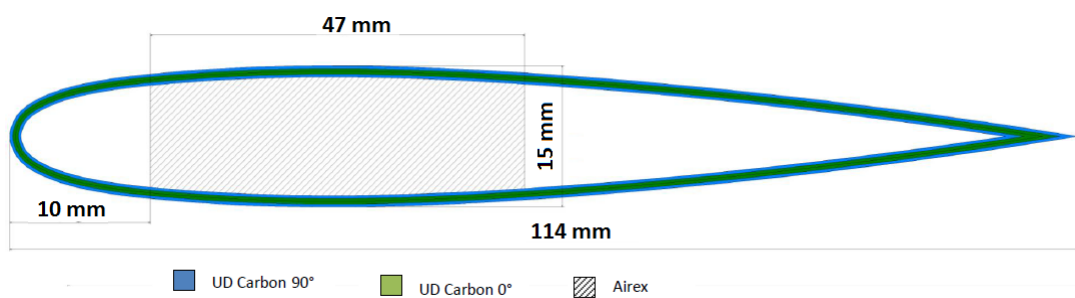
FIGURE B.8 – Web location in the sandwich structure and layup illustration of P_4 in the thickness of the laminate skin.

APPENDIX C

CALFEM functions for 3D beam analysis

Purpose:

Compute element stiffness matrix for a three dimensional beam element.
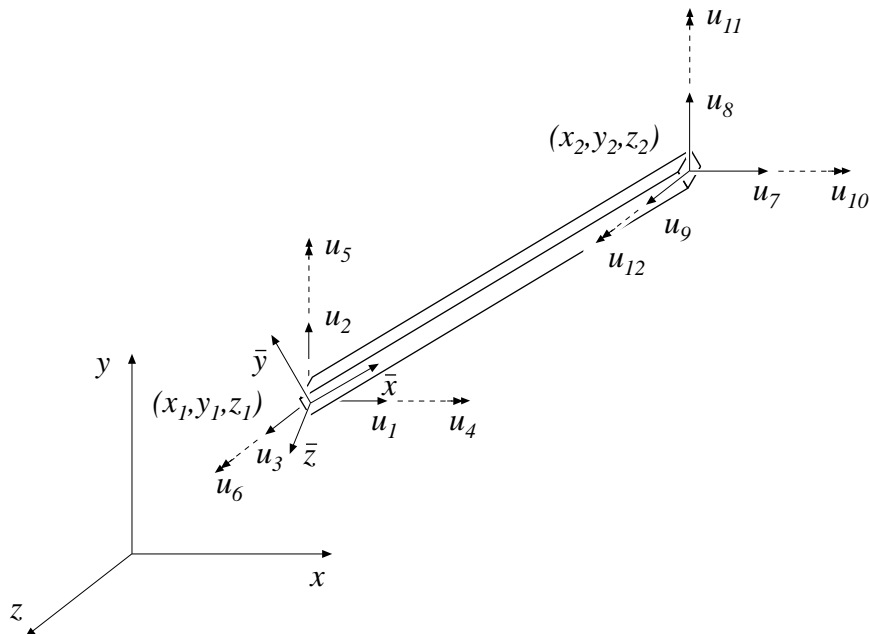
Syntax:

Ke=beam3e(ex,ey,ez,eo,ep)
[Ke,fe]=beam3e(ex,ey,ez,eo,ep,eq)

Description:

beam3e provides the global element stiffness matrix Ke for a three dimensional beam element.

The input variables

$$\begin{aligned} \mathsf{ex} &= \begin{bmatrix} x_1 & x_2 \end{bmatrix} \\ \mathsf{ey} &= \begin{bmatrix} y_1 & y_2 \end{bmatrix} \qquad \mathsf{eo} = \begin{bmatrix} x_{\bar{z}} & y_{\bar{z}} & z_{\bar{z}} \end{bmatrix} \\ \mathsf{ez} &= \begin{bmatrix} z_1 & z_2 \end{bmatrix} \end{aligned}$$

supply the element nodal coordinates x_1, y_1, etc. as well as the direction of the local beam coordinate system $(\bar{x}, \bar{y}, \bar{z})$. By giving a global vector $(x_{\bar{z}}, y_{\bar{z}}, z_{\bar{z}})$ parallel with the positive local $\bar{z}$ axis of the beam, the local beam coordinate system is defined. The variable

$$\mathsf{ep} = \begin{bmatrix} E & G & A & I_{\bar{y}} & I_{\bar{z}} & K_v \end{bmatrix}$$

supplies the modulus of elasticity E, the shear modulus G, the cross section area A, the moment of inertia with respect to the $\bar{y}$ axis I_y, the moment of inertia with respect to the $\bar{z}$ axis I_z, and St Venant torsional stiffness K_v.

The element load vector fe can also be computed if uniformly distributed loads are applied to the element. The optional input variable

$$\text{eq} = [\, q_{\bar{x}} \quad q_{\bar{y}} \quad q_{\bar{z}} \quad q_{\bar{\omega}} \,]$$

then contains the distributed loads. The positive directions of $q_{\bar{x}}$, $q_{\bar{y}}$, and $q_{\bar{z}}$ follow the local beam coordinate system. The distributed torque $q_{\bar{\omega}}$ is positive if directed in the local $\bar{x}$-direction, i.e. from local $\bar{y}$ to local $\bar{z}$. All the loads are per unit length.

Theory:

The element stiffness matrix $\mathbf{K}^e$ is computed according to

$$\mathbf{K}^e = \mathbf{G}^T \bar{\mathbf{K}}^e \mathbf{G}$$

where

$$\bar{\mathbf{K}}^e = \begin{bmatrix}
k_1 & 0 & 0 & 0 & 0 & 0 & -k_1 & 0 & 0 & 0 & 0 & 0 \\
0 & \frac{12EI_{\bar{z}}}{L^3} & 0 & 0 & 0 & \frac{6EI_{\bar{z}}}{L^2} & 0 & -\frac{12EI_{\bar{z}}}{L^3} & 0 & 0 & 0 & \frac{6EI_{\bar{z}}}{L^2} \\
0 & 0 & \frac{12EI_{\bar{y}}}{L^3} & 0 & -\frac{6EI_{\bar{y}}}{L^2} & 0 & 0 & 0 & -\frac{12EI_{\bar{y}}}{L^3} & 0 & -\frac{6EI_{\bar{y}}}{L^2} & 0 \\
0 & 0 & 0 & k_2 & 0 & 0 & 0 & 0 & 0 & -k_2 & 0 & 0 \\
0 & 0 & -\frac{6EI_{\bar{y}}}{L^2} & 0 & \frac{4EI_{\bar{y}}}{L} & 0 & 0 & 0 & \frac{6EI_{\bar{y}}}{L^2} & 0 & \frac{2EI_{\bar{y}}}{L} & 0 \\
0 & \frac{6EI_{\bar{z}}}{L^2} & 0 & 0 & 0 & \frac{4EI_{\bar{z}}}{L} & 0 & -\frac{6EI_{\bar{z}}}{L^2} & 0 & 0 & 0 & \frac{2EI_{\bar{z}}}{L} \\
-k_1 & 0 & 0 & 0 & 0 & 0 & k_1 & 0 & 0 & 0 & 0 & 0 \\
0 & -\frac{12EI_{\bar{z}}}{L^3} & 0 & 0 & 0 & -\frac{6EI_{\bar{z}}}{L^2} & 0 & \frac{12EI_{\bar{z}}}{L^3} & 0 & 0 & 0 & -\frac{6EI_{\bar{z}}}{L^2} \\
0 & 0 & -\frac{12EI_{\bar{y}}}{L^3} & 0 & \frac{6EI_{\bar{y}}}{L^2} & 0 & 0 & 0 & \frac{12EI_{\bar{y}}}{L^3} & 0 & \frac{6EI_{\bar{y}}}{L^2} & 0 \\
0 & 0 & 0 & -k_2 & 0 & 0 & 0 & 0 & 0 & k_2 & 0 & 0 \\
0 & 0 & -\frac{6EI_{\bar{y}}}{L^2} & 0 & \frac{2EI_{\bar{y}}}{L} & 0 & 0 & 0 & \frac{6EI_{\bar{y}}}{L^2} & 0 & \frac{4EI_{\bar{y}}}{L} & 0 \\
0 & \frac{6EI_{\bar{z}}}{L^2} & 0 & 0 & 0 & \frac{2EI_{\bar{z}}}{L} & 0 & -\frac{6EI_{\bar{z}}}{L^2} & 0 & 0 & 0 & \frac{4EI_{\bar{z}}}{L}
\end{bmatrix}$$

in which $k_1 = \frac{EA}{L}$ and $k_2 = \frac{GK_v}{L}$, and where

$$\mathbf{G} = \begin{bmatrix}
n_{x\bar{x}} & n_{y\bar{x}} & n_{z\bar{x}} & 0 & 0 & 0 & 0 & 0 & 0 & 0 & 0 & 0 \\
n_{x\bar{y}} & n_{y\bar{y}} & n_{z\bar{y}} & 0 & 0 & 0 & 0 & 0 & 0 & 0 & 0 & 0 \\
n_{x\bar{z}} & n_{y\bar{z}} & n_{z\bar{z}} & 0 & 0 & 0 & 0 & 0 & 0 & 0 & 0 & 0 \\
0 & 0 & 0 & n_{x\bar{x}} & n_{y\bar{x}} & n_{z\bar{x}} & 0 & 0 & 0 & 0 & 0 & 0 \\
0 & 0 & 0 & n_{x\bar{y}} & n_{y\bar{y}} & n_{z\bar{y}} & 0 & 0 & 0 & 0 & 0 & 0 \\
0 & 0 & 0 & n_{x\bar{z}} & n_{y\bar{z}} & n_{z\bar{z}} & 0 & 0 & 0 & 0 & 0 & 0 \\
0 & 0 & 0 & 0 & 0 & 0 & n_{x\bar{x}} & n_{y\bar{x}} & n_{z\bar{x}} & 0 & 0 & 0 \\
0 & 0 & 0 & 0 & 0 & 0 & n_{x\bar{y}} & n_{y\bar{y}} & n_{z\bar{y}} & 0 & 0 & 0 \\
0 & 0 & 0 & 0 & 0 & 0 & n_{x\bar{z}} & n_{y\bar{z}} & n_{z\bar{z}} & 0 & 0 & 0 \\
0 & 0 & 0 & 0 & 0 & 0 & 0 & 0 & 0 & n_{x\bar{x}} & n_{y\bar{x}} & n_{z\bar{x}} \\
0 & 0 & 0 & 0 & 0 & 0 & 0 & 0 & 0 & n_{x\bar{y}} & n_{y\bar{y}} & n_{z\bar{y}} \\
0 & 0 & 0 & 0 & 0 & 0 & 0 & 0 & 0 & n_{x\bar{z}} & n_{y\bar{z}} & n_{z\bar{z}}
\end{bmatrix}$$

The element length L is computed according to

$$L = \sqrt{(x_2 - x_1)^2 + (y_2 - y_1)^2 + (z_2 - z_1)^2}$$

In the transformation matrix $\mathbf{G}$, $n_{x\bar{x}}$ specifies the cosine of the angle between the x axis and $\bar{x}$ axis, and so on.

The element load vector $\mathbf{f}_l^e$, stored in fe, is computed according to

$$\mathbf{f}_l^e = \mathbf{G}^T \bar{\mathbf{f}}_l^e$$

where

$$
\bar{\mathbf{f}}_l^e =
\begin{bmatrix}
\dfrac{q_{\bar{x}} L}{2} \\[2mm]
\dfrac{q_{\bar{y}} L}{2} \\[2mm]
\dfrac{q_{\bar{z}} L}{2} \\[2mm]
\dfrac{q_{\bar{\omega}} L}{2} \\[2mm]
-\dfrac{q_{\bar{z}} L^2}{12} \\[2mm]
\dfrac{q_{\bar{y}} L^2}{12} \\[2mm]
\dfrac{q_{\bar{x}} L}{2} \\[2mm]
\dfrac{q_{\bar{y}} L}{2} \\[2mm]
\dfrac{q_{\bar{z}} L}{2} \\[2mm]
\dfrac{q_{\bar{\omega}} L}{2} \\[2mm]
\dfrac{q_{\bar{z}} L^2}{12} \\[2mm]
-\dfrac{q_{\bar{y}} L^2}{12}
\end{bmatrix}
$$

Purpose:

Compute section forces in a three dimensional beam element.
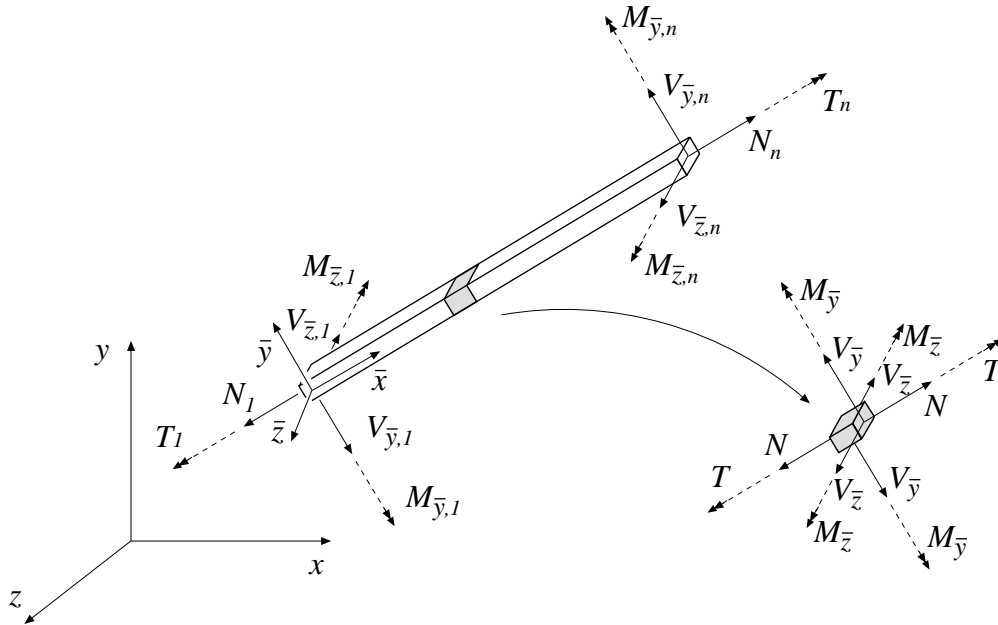
Syntax:

es=beam3s(ex,ey,ez,eo,ep,ed)
es=beam3s(ex,ey,ez,eo,ep,ed,eq)
[es,edi,eci]=beam3s(ex,ey,ez,eo,ep,ed,eq,n)

Description:

beam3s computes the section forces and displacements in local directions along the beam element beam3e.

The input variables ex, ey, ez, eo, and ep are defined in beam3e, and the element displacements, stored in ed, are obtained by the function extract. If distributed loads are applied to the element, the variable eq must be included. The number of evaluation points for section forces and displacements are determined by n. If n is omitted, only the ends of the beam are evaluated.

The output variables

$$\textsf{es} = [\, \mathbf{N} \ \ \mathbf{V}_{\bar{y}} \ \ \mathbf{V}_{\bar{z}} \ \ \mathbf{T} \ \ \mathbf{M}_{\bar{y}} \ \ \mathbf{M}_{\bar{z}} \,] \qquad \textsf{edi} = [\, \bar{\mathbf{u}} \ \ \bar{\mathbf{v}} \ \ \bar{\mathbf{w}} \ \ \bar{\boldsymbol{\varphi}} \,] \qquad \textsf{eci} = [\, \bar{\mathbf{x}} \,]$$

consist of column matrices that contain the section forces, the displacements, and the evaluation points on the local $\bar{x}$-axis. The explicit matrix expressions are

$$\textsf{es} = \begin{bmatrix} N_1 & V_{\bar{y}1} & V_{\bar{z}1} & T & M_{\bar{y}1} & M_{\bar{z}1} \\ N_2 & V_{\bar{y}2} & V_{\bar{z}2} & T & M_{\bar{y}2} & M_{\bar{z}2} \\ \vdots & \vdots & \vdots & \vdots & \vdots & \vdots \\ N_n & V_{\bar{y}n} & V_{\bar{z}n} & T & M_{\bar{y}n} & M_{\bar{z}n} \end{bmatrix}$$

$$
\text{edi} =
\begin{bmatrix}
\bar{u}_1 & \bar{v}_1 & \bar{w}_1 & \bar{\varphi}_1 \\
\bar{u}_2 & \bar{v}_2 & \bar{w}_2 & \bar{\varphi}_2 \\
\vdots & \vdots & \vdots & \vdots \\
\bar{u}_n & \bar{v}_n & \bar{w}_n & \bar{\varphi}_n
\end{bmatrix}
\qquad
\text{eci} =
\begin{bmatrix}
0 \\
\bar{x}_2 \\
\vdots \\
\bar{x}_{n-1} \\
L
\end{bmatrix}
$$

where L is the length of the beam element.

Theory:

The evaluation of the section forces is based on the solutions of the basic equations

$$
EA\frac{d^2\bar{u}}{d\bar{x}^2} + q_{\bar{x}} = 0 \qquad\qquad EI_z\frac{d^4\bar{v}}{d\bar{x}^4} - q_{\bar{y}} = 0
$$

$$
EI_y\frac{d^4\bar{w}}{d\bar{x}^4} - q_{\bar{z}} = 0 \qquad\qquad GK_v\frac{d^2\bar{\varphi}}{d\bar{x}^2} + q_{\bar{\omega}} = 0
$$

From these equations, the displacements along the beam element are obtained as the sum of the homogeneous and the particular solutions

$$
\mathbf{u} =
\begin{bmatrix}
\bar{u}(\bar{x}) \\
\bar{v}(\bar{x}) \\
\bar{w}(\bar{x}) \\
\bar{\varphi}(\bar{x})
\end{bmatrix}
= \mathbf{u}_h + \mathbf{u}_p
$$

where

$$
\mathbf{u}_h = \bar{\mathbf{N}}\,\mathbf{C}^{-1}\,\mathbf{G}\,\mathbf{a}^\mathbf{e}
\qquad\qquad
\mathbf{u_p} =
\begin{bmatrix}
\bar{u}_p(\bar{x}) \\
\bar{v}_p(\bar{x}) \\
\bar{w}_p(\bar{x}) \\
\bar{\varphi}_p(\bar{x})
\end{bmatrix}
=
\begin{bmatrix}
\dfrac{q_{\bar{x}}L\bar{x}}{2EA}\left(1 - \dfrac{\bar{x}}{L}\right) \\[2ex]
\dfrac{q_{\bar{y}}L^2\bar{x}^2}{24EI_z}\left(1 - \dfrac{\bar{x}}{L}\right)^2 \\[2ex]
\dfrac{q_{\bar{z}}L^2\bar{x}^2}{24EI_y}\left(1 - \dfrac{\bar{x}}{L}\right)^2 \\[2ex]
\dfrac{q_{\bar{\omega}}L\bar{x}}{2GK_v}\left(1 - \dfrac{\bar{x}}{L}\right)
\end{bmatrix}
$$

and

$$
\bar{\mathbf{N}} =
\begin{bmatrix}
1 & \bar{x} & 0 & 0 & 0 & 0 & 0 & 0 & 0 & 0 & 0 & 0 \\
0 & 0 & 1 & \bar{x} & \bar{x}^2 & \bar{x}^3 & 0 & 0 & 0 & 0 & 0 & 0 \\
0 & 0 & 0 & 0 & 0 & 0 & 1 & \bar{x} & \bar{x}^2 & \bar{x}^3 & 0 & 0 \\
0 & 0 & 0 & 0 & 0 & 0 & 0 & 0 & 0 & 0 & 1 & \bar{x}
\end{bmatrix}
$$

$$
\mathbf{C} =
\begin{bmatrix}
1 & 0 & 0 & 0 & 0 & 0 & 0 & 0 & 0 & 0 & 0 & 0 \\
0 & 0 & 1 & 0 & 0 & 0 & 0 & 0 & 0 & 0 & 0 & 0 \\
0 & 0 & 0 & 0 & 0 & 0 & 1 & 0 & 0 & 0 & 0 & 0 \\
0 & 0 & 0 & 0 & 0 & 0 & 0 & 0 & 0 & 0 & 1 & 0 \\
0 & 0 & 0 & 0 & 0 & 0 & 0 & 1 & 0 & 0 & 0 & 0 \\
0 & 0 & 0 & 1 & 0 & 0 & 0 & 0 & 0 & 0 & 0 & 0 \\
1 & L & 0 & 0 & 0 & 0 & 0 & 0 & 0 & 0 & 0 & 0 \\
0 & 0 & 1 & L & L^2 & L^3 & 0 & 0 & 0 & 0 & 0 & 0 \\
0 & 0 & 0 & 0 & 0 & 0 & 1 & L & L^2 & L^3 & 0 & 0 \\
0 & 0 & 0 & 0 & 0 & 0 & 0 & 0 & 0 & 0 & 1 & L \\
0 & 0 & 0 & 0 & 0 & 0 & 0 & 1 & 2L & 3L^2 & 0 & 0 \\
0 & 0 & 0 & 1 & 2L & 3L^2 & 0 & 0 & 0 & 0 & 0 & 0
\end{bmatrix}
\qquad
\mathbf{a}^e =
\begin{bmatrix}
u_1 \\
u_2 \\
\vdots \\
u_{12}
\end{bmatrix}
$$

The transformation matrix $\mathbf{G}^e$ and nodal displacements $\mathbf{a}^e$ are described in beam3e. Note that the transpose of $\mathbf{a}^e$ is stored in ed.

Finally the section forces are obtained from

$$
N = EA\frac{d\bar{u}}{d\bar{x}} \qquad\qquad V_{\bar{y}} = -EI_z\frac{d^3\bar{v}}{d\bar{x}^3} \qquad\qquad V_{\bar{z}} = -EI_y\frac{d^3\bar{w}}{d\bar{x}^3}
$$

$$
T = GK_v\frac{d\bar{\varphi}}{d\bar{x}} \qquad\qquad M_{\bar{y}} = -EI_y\frac{d^2\bar{w}}{d\bar{x}^2} \qquad\qquad M_{\bar{z}} = EI_z\frac{d^2\bar{v}}{d\bar{x}^2}
$$

Examples:

Section forces or element displacements can easily be plotted. The bending moment $M_{\bar{y}}$ along the beam is plotted by

```
>> plot(eci,es(:,5))
```

References

[1] Numerical simulations of a surface piercing a-class catamaran hydrofoil and comparison against model tests. *Chesapeak sailing yacht symposium*. vii, 17

[2] R3.01.00 ABBAS Mickaël. *Finite element method isoparametric*, 09/10/2013. 119

[3] Deniz Tolga Akcabay and Yin Lu Young. Influence of cavitation on the hydroelastic stability of hydrofoils. *Journal of Fluids and Structures*, 49 :170 – 185, 2014. 21

[4] Othmar H. Amman, Theodore von Karman, and Glenn B. Woodruff. The failure of the tacoma narrows bridge. *Technical Report*, 59,118, (1941). 30

[5] John D Anderson. *Fundamental of aerodynamics* . ISBN 0-07-237335-0. McGraw-Hill, Boston, 2001. ix, 92, 97, 98

[6] J. A. Astolfi. Contribution à l'étude du phénomène de cavitation : une approche expérimentale des conditions d'apparition et de développement de la cavitation,habilitation à diriger les recherches. 2003. 19

[7] Jean-Pierre Aubry. *Beginning with code Aster : A practical introduction to finite element method using code Aster and Gmsh*, 2013-2019. 119

[8] Benoit AUGIER. Dynamique du voilier. Cours de Master Recherche IRENAV, 2019-2020. vii, 11, 13

[9] P-E. Austrell and O. Dahlblom. *CALFEM manual, a finite element toolbox version 3.4.* x, 104, 106, 107

[10] KUDAWOO Ayaovi-Dzifa. *Pre and Postprocessing for the thin hulls out of composite materials,Clé : R4.01.01*, 17/05/2016. 123

[11] Sakir Bal. Free surface effects on 2-d airfoils and 3-d wings moving over water. *Ocean Systems Engineering*, 6 :245–264, 2016. vii, 15, 16

[12] J. Balhan. Metingen aan enige bij scheepsschroeven gebruikelijke profielen in vlakkestroming met en zonder cavitatie. *Uitgave Publicatie*, 99, 1951. 19

[13] R Balze, N Bigi, K Roncin, JB Leroux, A Nême, V Keryvin, A Connan, H Devaux, and D Gléhen. Racing. *Innovsail International Conference, Lorient, France*, pages 51–58, 2017. 4

[14] E.J. Barbero. Finite element analysis of composite materials. . CRC Press. 22

[15] Matthew Franklin Barone and Jeffrey L. Payne. Methods for simulation-based analysis of fluid-structure interaction. Rapport de recherche SAND2005-6573, Sandia National Laboratories, 2005. 35

[16] I. E. Barton. Comparison of pimple and pi -type algorithms for transient flows. In *Int. J. Numerical methods in fluids, 26,459-483*, 1998. 115

[17] Y. Bazilevs, V. M. Calo, Y. Zhang, and T. J. R. Hughes. Isogeometric fluid–structure interaction analysis with applications to arterial blood flow. *Computational Mechanics*, 38(4) :310–322, Sep 2006. 30

[18] Alexander Graham Bell. The alexander graham bell foundation. https ://agbfoundation.ca/hydrofoil/. 9

[19] M. Benaouicha. *Contribution au développement d'algorithmes de couplage en interaction fluide-structure*. Thèse de doctorat, Université de La Rochelle, 2007. 38

[20] D. Bertetta, S. Brizzolara, S. Gaggero, M. Viviani, and L. Savio. Cpp propeller cavitation and noise optimization at different pitches with panel code and validation by cavitation tunnel measurements. *Ocean Engineering*, 53 :177 – 195, 2012. 22

[21] Jean-Marie Berthelot. *Matériaux composites à Comportement mécanique et analyse des structures,* 5eme *édition* . Lavoisier, Paris, 2012. vii, 24, 27

[22] Clarich A. Franchini F. Biancolini M.E., Cella U. Multi-objective optimization of a-class catamaran foils adopting a geometric parameterization based on rbf mesh morphing. *Computational Methods in Applied Sciences*, 49 :467–482, 2018. 8

[23] Raymond L. Bisplingo. Principle of aeroelasticity. https ://aerbook.com/books/principles of aeroelasticity-7905.html. 2007. 30

[24] F. Blom. A monolithical fluid-structure interaction algorithm applied to the piston problem. *Comput. Methods Appl. Mech. Eng.,* 167 (3-4) :369–391, (1998). 36

[25] Maguire BOATS. Exocet moth. https ://www.maguireboats.com/exocet-moth-21-w.asp, 2013. 14

[26] Campagnolo F. Croce A. Bottasso, C. L. and C. Tibaldi. Optimization-based study of bend-twist coupled rotor blades for passive and integrated passive/active load alleviation. In *Wind Energy, 16, https ://doi.org/10.1002/we.1543*, 2013. 33

[27] J. Boussinesq. *Théorie de l'écoulement tourbillonant, Mem. par. div. Sav., Paris, 23.* 117

[28] Christophe Bouvet. *Dimensionnement des structures composites : applications à l'aéronautique.* ISTE Editions, January 2015. vii, 22, 23, 26

[29] Claire BREGMAN. Interaction fluide-structure. Rapport de stage, CERFACS-Arts et Métiers, Paris Tech, 2018. 4

[30] John P. Breslin and Richard Skalak. Exploratory study of ventilated flows about yawed surface-piercing struts. Technical report, NASA, 1959. 17

[31] Mark Capellaro. Design challenges for bend twist coupled blades for wind turbines and application to standard blades. In *Proceedings of Sandia Wind Turbine Blade Workshop*, 2012. x, xi, 108, 109, 158, 206

[32] Hodges DH. Cesnik CES. Vabs : A new concept for composite rotor blade cross-sectional modeling. *Journal of American Helicopter Societys*, 42(1) :27–38, 1997. 34

[33] Raymond Cointe. *Quelques aspects de la simulation numérique d'un canal à houle.* Thèse de Doctorat, École Nationale des Ponts et Chaussées, 1989. 35

[34] CompositeLab. Composite manufacturing processes. http ://compositeslab.com/composites-manufacturing-processes/open-molding/. 29

[35] Shaoshi Dai, Bassam A. Younis, and Liping Sun. Openfoam predictions of hydrodynamics loads on full-scale tlp. *Ocean Engineering*, 102 :162 – 173, 2015. 113

[36] Davy DAUBY. *Simulation d'écoulements cavitants par résolution numérique d'équations de Navier-Stokes en moyenne de Reynolds. Application à la cavitation de tourbillons d'extrémité.* Thèse de doctorat, L'Ecole Centrale de Nantes et l'Université de Nantes, 2007. 20

[37] Electricité de France. Finite element *code_aster*, analysis of structures and thermomechanics for studies and research. Open source on www.code-aster.org, 1989–2017. 4, 118

[38] R3.07.04 DE SOZA Thomas. *Éléments finis de coques volumiques*, 25/09/2013. 120

[39] Pierre Luc Delafin. *Analyse de l'écoulement transitionnel sur un hydrofoil : application aux hydroliennes à axe transverse avec contrôle actif de l'angle de calage.* Thèse de Doctorat, Ecole Doctorale des sciences de la Mer - Institut de Recherche de l'Ecole Navale, 2014. 2

[40] J. Deparday. Experimental studies of fluid-structure interaction on downwind sails. *PhD Thesis,Université de Bretagne Occidentale*, 2016. 55

[41] G. Dimitriadis. Aircraft design, lecture10, aeroelasticity, université de liege. 30

[42] Numo Miguel Diniz Dos Santos. *Numerical methods for fluid-structure interaction problems with valves.* Thèse de Doctorat, Université Pierre et Marie Curie - Paris VI, 2007. 35

[43] Mark Drela. Xfoil : An analysis and design system for low reynolds number airfoils. *Springer Berlin Heidelberg*, 54 :112, 1989. ix, 100, 101

[44] A. Ducoin and Y.L. Young. Hydroelastic response and stability of a hydrofoil in viscous flow. In *Second International Symposium on Marine Propulsors smp'11*, Allemagne, 2011. 35

[45] Antoine Ducoin. *Etude expérimentale et numérique du chargement hydrodynamique des corps portants en régime transitoire avec prise en compte du couplage fluide structure.* Thèse de Doctorat, Ecole Centrale de Nantes, 2008. 2, 21, 55

[46] Antoine Ducoin, Jacques-André Astolfi, Franã§ois Deniset, and Sigrist Jean-François. Computational and experimental investigation of flow over a transient pitching hydofoil. *European Journal of Mechanics B/ Fluids*, 28 :728 – 743, 2009. 32

[47] M. Eichhorn and al. Investigation of the fluid-structure interaction of a high head francis turbine using openfoam and code aster. In *IOP Conf. Ser. : Earth Environ. Sci. 49 072005*, 2016. 4, 109

[48] F. Axisa et J. Antunes. Modelling of mechanical systems - fluid structure interaction. butterworth-heinmann. 2007. 31, 35

[49] Odd M. Faltinsen. *Hydrodynamics of High-Speed Marine Vehicles*. Cambridge University Press, 2006. ix, 102, 103

[50] Vladimir Fedorov. Bend twist coupling effect in wind turbine blades. *PhD Thesis*, 2012. viii, 33

[51] Vladimir Fedorov, Christian Berggreen, Steen Krenk, and Kim Branner. Bend-twist coupling effects in wind turbine blades. 2012. viii, 32, 108

[52] Michael W. Findlay and Stephen R. Turnock. Development and use of a velocity prediction program to compare the effects of changes to foil arrangement on a hydrofoiling moth dinghy. 2008. 8

[53] Avellan F. Belahadji B. Billard J. Briancon Marjollet L. D.Frechou Fruman D. Karimi A. Kueny J. Franc, J. and J. Michel. La cavitation, mecanismes physiques et aspects industriels. *Presses Universitaires de Grenoble*, 1994. 20

[54] J. Franc and J. Michel. Attached cavitation and the boundary layer : experimental investigation and numerical treatment. *Journal of Fluid Mechanics*, pages 63–90, 1985. 20

[55] Fabien Gaugain. *Analyse expérimentale et simulation numérique de l'interaction fluide-structure d'un hydrofoil élastique en écoulement subcavitant et cavitant.* Thèse de Doctorat, Ecole Nationale Supérieure d'Arts et Métiers - Institut de Recherche de l'Ecole Navale, 2013. viii, 2, 3, 21, 31, 32, 52, 117

[56] Daniel Gay. *Materiaux composites; 3rd ed.* Traité des nouvelles technologies. Hermès, Paris, 1991. viii, 23, 66

[57] H. Ghassemi and A. R. Kohansal. Wave generated by the naca4412 hydrofoil near free surface. *Journal of Applied Fluid Mechanics*, 6 :1–6, 2013. 15

[58] L Marimont Giovannetti. Fluid structure interaction testing, modeling and development of passive adaptive composite foils. *PhD Thesis*, -, 2017. 34, 35

[59] L Marimont Giovannetti, J Banks, M Ledri, SR Turnock, and SW Boyd. Toward the development of a hydrofoil tailored to passively reduce its lift response to fluid load. *Ocean Engineering*, 167 :1–10, 2018. 2

[60] L Marimont Giovannetti, J Banks, M Ledri, SR Turnock, and SW Boyd. Toward the development of a hydrofoil tailored to passively reduce its lift response to fluid load. *Ocean Engineering*, 167 :1–10, 2018. 34

[61] K. Graf, A.v. Hoeve, and S. Watin. Comparison of full 3d-rans simulations with 2d-rans/lifting line method calculations for the flow analysis of rigid wings for high performance multihulls. *Ocean Engineering*, 90 :49 – 61, 2014. Innovation in High Performance Sailing Yachts - INNOVSAIL. 92

[62] S.N. Grebenyuk. The shear modulus of a composite material with a transversely isotropic matrix and a fibre. *Journal of Applied Mathematics and Mechanics*, 78(2) :187 – 191, 2014. 205

[63] P. Guiffant. Etude du comportement hydroélastique d'un hydrofoil flexible. *Technical report, Ecole Nationale des Arts et Métiers, 2015.* 55

[64] H. Jasak C. Fureby H. G. Weller, G. Tabor. A tensorial approach to computational continuum mechanics using object-oriented techniques. *Computers in Physics*, Vol. 12, No. 6, Nov/Dec 1998. Philip. 113

[65] K. Bathe H. Zhang. Direct and iterative computing of fluid flows fully coupled with structures. *K.J. Bathe (Ed.), Computational Fluid and Solid Mechanics, Elsevier, Amsterdam*, 2001. 36

[66] N. Hagemeister and R. Flay. Computational techniques used for velocity prediction of wing-sailed hydrofoiling catamarans. In *Proceedings of VII International Conference on Computational Methods in Marine Engineering MARINE*, 2017. 92

[67] N. Hagemeister and R. Flay. Velocity prediction of wing-sailed hydrofoiling catamarans. *Innovsail International Conference, Lorient, France*, pages 11–18, 2017. 96

[68] Gunt Hamburg. Ecoulement stationnaire : Cavitation. https ://www.gunt.de/images/download/cavitation-in-pumps-french.pdf. vii, 20

[69] Kooijman HJT. Bending-torsion coupling of a wind turbine rotor blade. In *Smart Rotor Project*, 1996. 33

[70] Dewey H Hodges. *Non-linear Composite Beam Theory*. 78-1-56347-697-6. American Institute of Aeronautics and Astronautics, 1, 2006. 106

[71] S. Hoerner. Some characteristics of spray alia ventilation. Gibbs and Cox ONR Contract No. NONR -507(00), 1953. 17

[72] C. Hook and A. Kermode. *Hydrofoils, by Christopher Hook and A.c. Kermode.* Pitman, 1967. 12

[73] Christopher Hook and A. C. Kermode. Pitman. Yates, a. (1967). hydrofoils, illustrations. 32s. 6d. *The Journal of the Royal Aeronautical Society*, 71(662-662) :242, 1967. 12

[74] G. Hough and S. Moran. Froude number effects on two-dimensional hydrofoils. *Journal of Ship Research*, 13(1) :53–60, 1969. vii, 15, 16

[75] Ming-Chen Hsu, David Kamensky, Yuri Bazilevs, Michael S. Sacks, and Thomas J. R. Hughes. Fluid–structure interaction analysis of bioprosthetic heart valves : significance of arterial wall deformation. *Computational Mechanics*, 54(4) :1055–1071, Oct 2014. 30

[76] http ://www.wolfdynamics.com. Finite volume method : A crash introduction. http ://www.wolfdynamics.com/wiki/fvm_crash_intro.pdf. 114, 115

[77] H. Jasak. *Error Analysis and Estimation for the Finite Volume Method with Applications to Fluid Flows.* Ph.d thesis, Imperial College of Science, Technology and Medicine, London, 1996. x, 113, 114

[78] Jonathan S. Pitt Jason P. Sheldon, Scott T. Miller. Methodology for comparing coupling algorithms for fluid-structure interaction problems. *World Journal of Mechanics*, 4 :54–70, 2014. viii, 36, 37

[79] Christian Jacquot Antoine Leroy Bernard Peseux et al. Jean-Pierre Basset, Patrice Cartraud. *Introduction à la résistance des matériaux*. Ecole d'ingénieur, Nantes, France, 2007. 49

[80] R. M. Jones. *Mechanics of Composite materials, Second edition*. Taylor and Francis, ISBN 156032712X, 1999. 23

[81] Emricka Julan. *Simulation numérique du choc laser pour la mise en compression en présence de l'état initial dû au soudage*. Thèse de Doctorat, aboratoire de Mécanique des Structures Industrielles Durables - EDF Eectricté de France, 2014. 4

[82] Robert H. Scanlan K. Yusuf Billah. Resonance, tacoma narrows bridge failure, and undergraduate physics textbooks. *Journal of Fluid Mechanics*, 59,118, (1991). 30

[83] C. Kassiotis. Nonlinear fluid-structure interaction : A partitioned approach and its application through component technology. *Université Paris-Est, Ecole doctorale MODES,153p., 20 Novembre 2009*. 39

[84] G Ketterman. Foil en l. https ://foils.wordpress.com/2008/11/12/foils-en-t-ou-foils-en-v/, 2005. 14

[85] Dieter Scholz Kinga Budziak. *Aerodynamic Analysis with Athena Vortex Lattice (AVL)*. Master project, MSME,Department of Automotive and Aeronautical Engineering Hamburg University of Applied sciences, 2015. 92, 97

[86] Alexandra Lelong. *Etude expérimentale du comportement hydroélastique d'une structure flexible pour différents régimes d'écoulement*. Thèse de Doctorat, Ecole Doctorale des sciences de la Mer - Institut de Recherche de l'Ecole Navale, 2016. viii, 2, 21, 46, 54, 55

[87] C. LIU. *Wake Vortex Encounter Analysiswith Different Wake Vortex ModelsUsing Vortex-Lattice Method*. Master of science thesis, Delft University of Technology, Faculty of Aerospace Engineering, 2007. 97

[88] D. Lobitz and P. Veers. Load mitigation with bending/twistcoupled blades on rotors using modern control strategies. In *Wind Energy, 6, https ://doi.org/10.1002/we.74*, 2003. 33

[89] Veers P. Lobitz, D. and D. Laino. Performance of twistcoupled blades on variable speed rotors, tech. rep. In *Sandia National Labs, Albuquerque, NM (US); Sandia National Labs., Livermore, CA (US)*, 1999. 33

[90] Aerocraft Inc. Marc Drela, MIT Aero Astro. Harold Youngren. *AVL :Extended Vortex Lattice Model-3.36 User Primer*, last update 12 Feb 17. 97, 100

[91] Cambridge MA Marc Drela, MIT Press. *Flight Vehicle Aerodynamics, Flight Vehicle Aerodynamics*, 2014. 92

[92] F. R. Menter. Two-equation eddy-viscosity turbulence models for engineering applications. *AIA A JOURNAL*, VOL. 32, NO. 6. 117

[93] Vizinho R. Silvestre M. Pascoa J. Morgado, J. Xfoil vs cfd performance predictions for high lift low reynolds number airfoils. 2016. 102

[94] Liu Moubin and Z.L. Zhang. Smoothed particle hydrodynamics (sph) for modeling fluid-structure interactions. *Science China : Physics, Mechanics and Astronomy*, 62 :984701, 02 2019. 37

[95] Lahcen Ait Moudid. *Couplage Fluide Structure pour la simulation numérique des écoulements fluides dans une conduite à parois rigides ou élastiques, en présence d'obstacles ou non. Sciences de la Terre.* Thèse de doctorat, Université d'Artois, 2007,Français, tel-00341094. 4, 37

[96] Canadian Navy. Hydrofoils, boat. https ://www.oldlifemagazines.com/september-27-1954-life-magazine.html. vii, 10

[97] M O. and A Kayran. Investigation of the effect of bending twisting coupling on the loads in wind turbines with superelement blade definition. *Journal of Physics : Conference Series*, 524(1) :012040, 2014. 33

[98] OpenCFD. *OpenFOAM user Guide, version6,https ://OpenFOAM.org,* 10th July 2018. 113

[99] Chopra I. Panda B. Dynamics of composite rotor blades in forward flight. vertica, 11(1/2) :187-210. 1987. 33

[100] S. V. Patankar and . B. palding. A calculation procedure for heat, mass and momentum transfer in three-dimensional parabolic flows. In *Int. J. Heat Mass Transfer, 15, 1787-1806,* 1972. 115

[101] PLOE Patrick. *Surrogate-based Optimization of Hydrofoil Shapes using RANS simulations.* Thèse de doctorat, Université de Bretagne Loire, 2018. vii, 9, 13, 17

[102] J. Penrose, D. Hose, C.J. Staples, I. Hamill, I. Jones, and D. Sweeney. Fluid structure interactions : coupling of CFD and FE. In *18th CAD-FEM User's Meeting - International Congress on FEM Technology,* 2000. 35

[103] Laetitia Pernod, Antoine Ducoin, Hervé Le Sourne, Jacques-André Astolfi, and Pascal Casari. Experimental and numerical investigation of the fluid-structure interaction on a flexible composite hydrofoil under viscous flows. *Ocean Engineering*, 194 :106647, 2019. 32

[104] Giridhar R. and al. Improving airfoil drag prediction. *34th Wind Energy Symposium, AIAA SciTech, 4-8 January 2016, San Diego, California, USA*, 54 :112, 2016. ix, 100, 102

[105] Wolfram Raither, Andrea Bergamini, and Paolo Ermanni. Profile beams with adaptive bending–twist coupling by adjustable shear centre location. *Journal of Intelligent Material Systems and Structures*, 24(3) :334–346, 2013. 34

[106] Richard Stone Rothblum. *Investigation of methods of delaying or controling ventilation on surface piercing struts.* Thesis, The University Leeds , 1977. 18

[107] Nacra Sailing. Nacra f20 fcs. https ://www.nacrasailing.com/project/nacra-f20-fcs/, 2015. vii, 12

[108] Scipy.org. *SciPy V1.3.2 Reference Guide : scipy.interpolate.griddata*, 9 Nov. 2019. 111

[109] SEAIR. Au large de lorient, un bateau à moteur vole. https ://www.la-croix.com/France/Au-large-Lorient-bateau-moteur-vole-2018-02-15-1300914129, 2018. vii, 11

[110] P. E. Shen, Yi Dimotakis. Influence of surface cavitation on hydrodynamic forces. In *Proceedings of American Towing Tank Conference, 22nd, Canada*, 1989. 21

[111] J-F. Sigrist. Méthodes numériques de calculs couplés fluide/structure : Cas du fluide s'écoulant. In *Techniques de l'Ingénieur*. Techniques de l'Ingénieur, 2010. 38

[112] Alexander R. Stäblein. *Analysis and Design of Bend-Twist Coupled Wind Turbine Blades*, pages 67–80. Springer International Publishing, Cham, 2016. 33

[113] Morten Hartvig ; Verelst David Robert Stäblein, Alexander R. ; Hansen. *Modal Properties and Stability of Bend-Twist Coupled Wind Turbine Blades*. Wind Energy Science, 2017. 34

[114] M. Sudre and J. Barrau. Determination du tenseur complet des contraintes dans des poutres composites. In $10^{\grave{e}me}$ *Journées nationales sur les composites ;10 :847-856*, 1996. 33

[115] Lakshman Anumolu Suraj S. Deshpande and Mario F. Trujillor. Evaluating the performance of the two-phase flow solver interfoam. *Computational Science and Discovery*, Vol. 5, No. 1, 2012. 4

[116] A. Taufik, J. Barrau, and F. Lorin. Composite beam analysis with arbitrary cross section. In *Composite Structures, 44(2/3) :189-194*, 1999. 33

[117] Tayfun E. Tezduyar, Sunil Sathe, Ryan Keedy, and Keith Stein. Space-time finite element techniques for computation of fluid-structure interactions. *Computer Methods in Applied Mechanics and Engineering*, 195(17) :2002 – 2027, 2006. Fluid-Structure Interaction. 36

[118] Alain THEBAULT. L'hydroptère Rocket va tenter de battre le record du monde de vitesse en mer. https ://www.la-croix.com/France/Au-large-Lorient-bateau-moteur-vole-2018-02-15-1300914129, 2014. vii, 12

[119] R3.07.03 Thomas DE SOZA. *Shell elements : modelizations DKT, DST, DKTG and Summarized*, 13/05/2013. x, 122, 123

[120] W. A. Wall. U. Kûttler. Fixed-point fluid-structure interaction solvers with dynamic relaxation. *Springer. p.61-72, 2008*. 39

[121] Paul Veers, Donald Lobitz, and Gunjit Bir. Aeroelastic tailoring in wind-turbine blade applications. *Technical report Sandia National Labs., Albuquerque, NM (US)*, 1998. 34, 108

[122] Guillaume VERDIER. Le principe des foils en un schéma. oÃ¹ le basculement de la quille constitue une étape préalable essentielle. https ://www.ouest-france.fr/vendee-globe/vendee-globe-foils-quilles-deux-poids-des-mesures-4588630, 2016. vii, 8

[123] D. R. Verelst and T. J. Larsen. Load consequences when sweeping blades a case study of a 5 mw pitch controlled wind turbine. In *Tech. Rep. Ris-R-1724(EN), Ris National Laboratory for Sustainable Energy3*, 2010. 33

[124] J. Vierendeels, K. Dumont, and P.R. Verdonck. A partitioned strongly coupled fluid-structure interaction method to model heart valve dynamics. *Journal of Computational and Applied Mathematics*, 215(2) :602 – 609, 2008. Proceedings of the Third International Conference on Advanced Computational Methods in Engineering (ACOMEN 2005). 36

[125] Berdichevsky VL. Variational-asymptotic method of shell theory construction. 43(4) :664–687, 1979. 34

[126] Lianzhou Wang, Chunyu Guo, Pei Xu, and Yumin Su. Analysis of the performance of an oscillating propeller in cavitating flow. *Ocean Engineering*, 164 :23 – 39, 2018. 21

[127] Yu Wenbin, V. Vitali, Hodges Dewey, and Xianyu Hon. Validation of the variational asymptotic beam sectional analysis (vabs). *American Institute of Aeronautics and Astronautics Journal*, 40, No. 10 :2105–2113, 2002. 34

[128] Joseph M. Wetzel. Ventilation of bodies piercing a free surface. In *Second Symposium on Naval Hydrodynamics, Office of Naval Research*, 1958. 17

[129] S. Widnall. *Lecture notes based on J. Peraire Version 2.0,Lecture L3 - Vectors, Matrices and Coordinate Transformations*. 16.07 Dynamics. 25

[130] Clé : U4.42.03 Xavier DESROCHES. *Opérateur DEFI_COMPOSITE*, 02/02/2012. 123

[131] Y. L. Young, C. M. Harwood, F. Miguel Montero, J. C. Ward, and S. L. Ceccio. Ventilation of lifting bodies : Review of the physics and discussion of scaling effects. *Applied Mechanics Reviews*, 69 :012040, 01 2017. 010801. 18

[132] Yin L Young, Nitin Garg, Paul A Brandner, Bryce W Pearce, Daniel Butler, David Clarke, and Andrew W Phillips. Load-dependent bend-twist coupling effects on the steady-state hydroelastic response of composite hydrofoils. *Composite Structures*, 189 :398–418, 2018. 34

[133] Y.L. Young. Fluid-structure interaction analysis of flexible composite marine propellers. *Journal of Fluids and Structures*, 24(6) :799 – 818, 2008. 35

[134] W. Yu, D. Hodges, and J. Ho. Variational asymptotic beam sectional analysis - an updated version. *International Journal of Engineering Science*, 59 :40–64, 2012. 34

[135] C. Yvin. Couplage fluide-structure par une chaîne de calculs open-source. Thèse de Master, ENSIETA - Sirehna, 2010. viii, 4, 35, 37, 38, 109

[136] D. Zenkert and M. Battley. *Foundation of fibre composites/notes fo the course : Composite lightweight structures,*. Technical university of Denmark, second edition, 2006. 23

Titre : Etude Expérimentale et Numérique des Interactions Fluide-Structure sur des Hydrofoils Flexibles en Composite

Mots clés : Code_Aster, Couplage flexion-torsion, Hydrofoils, Interactions fluide-structure, Matériaux composites, OpenFoam.

Résumé : En vol, l'hydrofoil subit de grandes déformations qui impactent fortement son chargement hydrodynamique. Cette thèse vise à développer pour SEAIR des outils numériques qui modélisent les interactions fluide-structure sur des hydrofoils flexibles en composites et qui seront validés par des tests expérimentaux.

Deux campagnes expérimentales sont menées : la première est réalisée dans le tunnel hydrodynamique de l'IRENAV sur une maquette réduite d'hydrofoil en matériau isotrope (le PolyOxométhylène "POM") et un télémètre laser mesure les déplacements de l'hydrofoil. La deuxième campagne est réalisée sur quatre hydrofoils de taille réelle en matériau composites. Des essais sont effectués en air pour caractériser leurs propriétés mécaniques et pour étudier le couplage flexion-torsion. Les essais hydrodynamiques sont effectués dans le canal hydrodynamique d'IFREMER Lorient. Une balance hydrodynamique mesure les forces et un télémètre laser mesure les déplacements.

Deux outils de couplage présentant deux niveaux de fidélité sont développés dans ce travail. L'outil basse fidélité FS6R dédié à l'analyse d'avant-projet est un couplage entre AVL corrigé en viscosité par Xfoil pour le calcul des fluides, et un code développé en interne sur la base de la théorie des poutres pour les calculs de structure.

L'outil haute-fidélité est un couplage entre les outils open-source OpenFoam pour le calcul des fluides et Code_Aster pour l'analyse structurelle. Il permet un calcul complet des domaines fluide et structure et l'utilisation de géométries complexes. Les deux algorithmes de couplage reposent sur une méthode partitionnée, synchrone et itérative. Ils sont validés dans un premier temps sur le déplacement d'hydrofoil en matériau POM, simulé dans un domaine à une phase fluide et une seconde validation est effectuée sur les forces hydrodynamiques et les déplacements des hydrofoils composites simulés dans un domaine à deux phases fluides avec calcul de surface libre.

Title: Experimental and Numerical Study of Fluid-Structure Interactions on Flexible Hydrofoils in Composites

Keywords: Bending-twisting coupling, Code_Aster, Composite materials, Fluid-Structure Interactions, Hydrofoils, OpenFoam

Abstract: When flying, the hydrofoil presents large deformations which impact significantly its hydrodynamic loads. This thesis aims to develop for SEAIR numerical coupling tools validated by experimental tests, that model Fluid-Structure Interactions on flexible composite hydrofoils. Two experimental campaigns are carried out: the first one is performed on a model scale hydrofoil made of the isotropic material PolyOxoMethylene "POM". These experiments are carried out in the hydrodynamic tunnel of IRENAV and a telemeter laser is used to measure the displacements of the hydrofoil. The second campaign is performed on four composite hydrofoils having the same hydro-dynamic shape but different composite layups. Several tests are performed in air to characterize their mechanical properties and to investigate the bending-twisting coupling. Hydrodynamic tests on the composite hydrofoils are carried out on the hydrodynamic flume of IFREMER Lorient.

A hydrodynamic balance is used to measure the hydrodynamic forces and a telemeter laser is used to measure the displacements. Two coupling tools of two level of fidelity are developed in this work. The low-fidelity tool FS6R dedicated for pre-design analysis is a coupling of the code AVL corrected by Xfoil for the fluid calculation, and an in-house code developed on beam theory for the structural analysis. The high-fidelity tool is a coupling between the open-source tools OpenFoam for the fluid calculations and the Code_Aster for the structural analysis. It allows a complete calculation of the fluid and structural domains and the use of complex geometries. The both coupling algorithms stand on a partitioned method, synchronized and iterative. They are first validated on the displacement of the POM hydrofoils simulated in a one-phase fluid domain and a second validation is performed on the hydrodynamic forces and displacements of the composite hydrofoils simulated in a two-phase fluid domain with free surface calculation.